The University Of Sheffield.

Amending soils with basalt: evidence for rock weathering, mineral precipitation, and soil organic carbon stabilisation

Miss Amy Louise Lewis

A thesis submitted in partial fulfilment of the requirements for the degree of Doctor of Philosophy

The University of Sheffield
Faculty of Science
School of Biosciences

September 2022

Acknowledgements

"He has also set eternity in the human heart; yet no one can fathom what God has done from beginning to end" – Ecclesiastes 3:11

Completing a PhD is often thought of as a 'solo pursuit', as it is an 'independent project', but the culmination of these *c.* 3.5 years of work would not have been possible without the guidance, support and kindness of so many people. However, this PhD process has been much more than this thesis, regardless of its outcome.

I've been very lucky over my PhD to work with a large range of people from a variety of scientific (and occasionally business) backgrounds and interests. Some have helped me academically, some have shown me the practicalities of science, others have kindly provided me with data and some have helped me keep the 'bigger picture' close in my mind.

I'd firstly like to thank my supervisors: David Beerling, Binoy Sarkar, Mark Hodson and Simon Kemp. Each have their own interests and expertise and I'm grateful to have been able to call on them for advice, guidance and support during my PhD. I'd also like to give thanks to Jonathan Leake, who, while not a formal supervisor has provided me with advice to further my project.

One of the main reasons I wanted to come to Sheffield to study my PhD was that I really liked the idea of working as part of a larger research team. I've been grateful for what I've been able to learn (and occasionally contribute) to discussions as part of the LC^3M and thoroughly enjoyed working with all those who have worked there, so thank you to you all.

In particular, I'd like to thank Maria Val Martin for her encouragement, her passion for fighting climate change and her inspiration as a mother, research fellow, as a person active in her local community. I'd also like to thank Lyla Taylor for her ever-insightful advice and for always willing to go 'above and beyond' in her support for me and I'm sure for many other colleagues, and for continually pushing me scientifically, and Derek Bell for interesting scientific discussions and encouragement. I'd also like to thank Debbie Hill for all her encouragement and support in both a personal and professional capacity.

I'd also like to thank Michelle Roe who kindly hosted me (providing comfortable accommodation, great food and wonderful hospitality) during my stays at the BGS.

I'd like to give especial thanks to the three wonderful friends I'd met at the LC^3M: Mike Kelland, Peter Wade and Karen Bailey. All of whom have provided me with wonderful friendship throughout my PhD. We've had many good laughs as well as many deep and important conversations, scientific or otherwise. They have been integral to my enjoyment at the University of Sheffield.

An especial thanks belong to those who have known me the longest – my mum and dad. Gosh, the unconditional love and support they have shown me throughout my life is quite overwhelming to think of. I'm so grateful to have the relationship I have with them, with them. Especial thanks also belong to my sister, Samantha, who always listens to me. I would never have thought when I was 14 or 16 that I could ever get this far, and am quite sure I only have because of you three have always been at the side lines cheering me on.

Of all the people who have been with me, I would finally like to thank my wonderfully supportive and loving fiancé, Rory McBride. Life comes with joy and challenges and during the challenges I've had during my PhD, Rory, you have been an anchor and a support and helped me turn challenges into opportunities. Your rational thinking has bought me back to Earth from the sky or the depths when I've needed it and you've helped me live a life that has been so much more than basalt! You've shown me new life and you've given me some of the most treasured of all my memories. You've encouraged me and supported me in all my endeavours, scientific and otherwise. Truly, I am undoubtedly blessed to have shared this time with you. Thank you for everything.

There are countless others who have also played a big role in my time here in Sheffield – family, friends and mentors both old and new. I'm sorry I have not listed you all here.

But from whom do all these blessings come? And the countless more blessing that I am without time and resource to account for? Our heavenly Father, the Lord Jesus Christ who intercedes and the Holy Spirit who have all sustained me, strengthened me, shaped me, challenged me, comforted me. But, above all else they have shown a very flawed human unfailing, unending, eternal love and grace. Praise and thanksgiving for all these things listed above belong to God! *'Now to the*

King eternal, immortal, invisible, the only God, be honor and glory for ever and ever. Amen.' - 1 Timothy 1:17

Specific scientific contributions (see abbreviations)

More specifically, I'd like to thank the following people for their help and scientific contributions to my PhD:

Mike Kelland – providing samples for Chapter 3 and 4 and data for Chapter 4.

Dimitar Epihov – providing CEC for Chapter 5.

Ian Mounteney – training and some sample preparation for XRD and BET surface area analysis, support while staying at the BGS (Chapter 2, 3 and 5).

Simon Kemp – training and support with XRD, providing TGA data (Chapter 2 and 3).

Neil Bramall and Heather Grieveson – collecting ICP-OES data (Chapter 2).

Kalu Davies, Kok Loong Yeong, Mike Masters, Mike Kelland, – supplying basaltic quarry fines samples (Chapter 2).

Robert Henderson, Rich Affeldt, Thomas Vanacore, Jeremy Sewell, Elvina Timothy and Kalu Davies – providing information on quarry processes.

Lyla Taylor – running RTM using the ShARC supercomputer at Sheffield (Chapter 2).

Gren Turner and Jeremy Rushton – training and advice for SEM analysis (Chapter 2 and 3).

Binoy Sarkar – providing data for flask dissolution experiment (Chapter 3).

Deborah Hammond – conducting XPS analysis and providing advice on XPS data interpretation (Chapter 3).

Francis Clegg – Allowing me to use his laboratory to conduct DRIFTS analysis, advice on DRIFTS and providing clay mineral spectra, and for much encouragement at clay mineral conferences (Chapter 3).

Christina Larkin, Grace Andrews and Rachael James – for leachate data from Flitcham Farm Field Demonstrator (Chapter 5).

Christina Larkin – support and help in getting a COVID-19 extension.

Robert Ashurst – Training and support for particle size analysis (Chapter 2, 3 and 5).

Robert Hanson – Training and support for FTIR-ATR analysis (Chapter 3).

Robert Moorehead – Training and support for XRF studies (Chapter 3).

Ellen Allwood – Access and training on Centrifuge Heraeus Megafuge 40 for sequential extractions (Chapter 3, 4 and 5)

David Wilson – Organising and collecting Li isotope data (Chapter 4).

John Fletcher – Producing polished blocks for SEM-EDS analysis (Chapter 2).

Irene Johnson – Training in Sheffield School of Biosciences laboratories.

Dave Johnson – Technical support (2018-2019) (mostly Chapter 2).

Karen Bailey – Technical support (2018-2022).

Abbreviations

Terms

CDR – Carbon Dioxide Removal

SCS – Soil Carbon Sequestration

OC – Organic Carbon

SOC – Soil Organic Carbon

Techniques

FTIR-ATR – Fourier Transform Infrared – Attenuated Total Reflectance

DRIFTS – Diffuse Reflectance Fourier Transform Spectroscopy

SEM – Scanning Electron Microscopy

SEM-EDS – Scanning Electron Microscopy – Energy Dispersive Spectroscopy

XRD – X-ray Diffraction

XRF – X-ray Fluorescence

XPS – X-ray Photoelectron Spectroscopy

BET – Brunauer, Emmet, Teller (surface area analysis)

SSA – Specific Surface Area

Declaration

I, Amy Louise Lewis, confirm that the Thesis is my own work. I am aware of the University's Guidance on the Use of Unfair Means (www.sheffield.ac.uk/ssid/unfair-means). This work has not been previously presented for an award at this, or any other, university.

Where others have been involved in data collection for the work presented in this thesis, acknowledgement has been made in text and also in the Acknowledgements section.

Some of this thesis has been previously published.

The contents of Chapter 2, *'Effects of mineralogy, chemistry and physical properties of basalts on carbon capture potential and plant-nutrient element release via enhanced weathering'* was taken from a paper of the same name. The full reference is given below:

> Lewis, A.L., Sarkar, B., Wade, P., Kemp, S.J., Hodson, M.E., Taylor, L.L., Yeong, K.L., Davies, K., Nelson, P.N., Bird, M.I., Kantola, I.B., Masters, M.D., DeLucia, E., Leake, J.R., Banwart, S.A., Beerling, D.J., 2021. Effects of mineralogy, chemistry and physical properties of basalts on carbon capture potential and plant-nutrient element release via enhanced weathering. Appl. Geochemistry 132, 105023.

Regrettably, some errors were identified in the paper after publication. The corrected values are documented in this thesis, and a corrigendum was in press at the time of submitting this thesis for examination.

In this paper, I collected most of the characterisation data (Simon Kemp collected TGA data, Neil Bramall collected the ICP-OES data) and updated the geochemical model referenced in the paper with the relevant parameters. The models were then mostly ran by Lyla Taylor on the ShARC Supercomputer at the University of Sheffield to speed up the runtime for simulations. The majority of the paper was written by myself, with other authors helping with editing and guidance. As with other chapters in my PhD, the experiment design was designed by myself with help from other supervisors (and in this case, authors).

This paper is fully represented in Chapter 2, but the XRD mineralogy and particle size of the Blue Ridge metabasalt were originally presented in Blancs et al (2020):

> Blanc-Betes, E., Kantola, I.B., Gomez-Casanovas, N., Hartman, M.D., Parton, W.J., Lewis, A.L., Beerling, D.J., DeLucia, E.H., 2021. In silico assessment of the potential of basalt amendments to reduce N2O emissions from bioenergy crops. GCB Bioenergy 13, 224–241. https://doi.org/https://doi.org/10.1111/gcbb.12757

And the XRD mineralogy and some SEM-EDS analysis of basaltic glass were also originally presented in Kelland et al (2020):

> Kelland, M.E., Wade, P.W., Lewis, A.L., Taylor, L.L., Sarkar, B., Andrews, M.G., Lomas, M.R., Cotton, T.E.A., Kemp, S.J., James, R.H., Pearce, C.R., Hartley, S.E., Hodson, M.E., Leake, J.R., Banwart, S.A., Beerling, D.J., 2020. Increased yield and CO2 sequestration potential with the C4 cereal Sorghum bicolor cultivated in basaltic rock dust-amended agricultural soil. Glob. Chang. Biol. n/a. https://doi.org/10.1111/gcb.15089

In Chapter 5, the mineralogical characterisation of the Middleton basalt was presented in the following article:

> Kantzas, E.P., Val Martin, M., Lomas, M.R., Eufrasio, R.M., Renforth, P., Lewis, A.L., Taylor, L.L., Mecure, J.-F., Pollitt, H., Vercoulen, P. V, Vakilifard, N., Holden, P.B., Edwards, N.R., Koh, L., Pidgeon, N.F., Banwart, S.A., Beerling, D.J., 2022. Substantial carbon drawdown potential from enhanced rock weathering in the United Kingdom. Nat. Geosci.

In this paper, I was only involved in characterising the mineralogy.

In addition, some of this work had been presented internally within the School of Biosciences, at the Clay Mineral Group – Research in Progress meeting in 2019 and at the EUROCLAY conference in 2019.

Amy Louise Lewis

Abstract

Enhanced rock weathering (ERW) is a CO_2 removal (CDR) technology which utilises one of Earth's natural CO_2 regulators to remove CO_2 from the atmosphere via silicate weathering. One ERW method aims to accelerate rock weathering by applying finely crushed, fast weathering silicate rocks to cropland soils. Basalt: an abundant, fast-weathering rock readily available in a finely crushed form as a by-product of the aggregate industry as 'basaltic quarry fines' is a prime candidate for ERW.

There is limited, direct evidence for understanding how basalt grains weather and the fate of Al, Fe and Mn released during weathering when basalt is applied to soils. These weathering products could stabilise organic carbon (OC) in soils, preventing its release into the atmosphere as CO_2, therefore increasing basalt's CDR potential via ERW. The interaction of basalt's weathering products with OC during ERW is also unknown. Broadly, the aims of this thesis were to: (1) characterise different basaltic quarry fines and assess their CDR potential via weathering, (2) investigate how basalt grains weather in soil solution, (3) assess changes to Al, Fe and Mn soil sinks after basalt amendment and (4) assess evidence for OC stabilisation after basalt amendment into cropland soils. Using six commercially available basaltic quarry fines and samples from two ERW experiments, a range of techniques including: geochemical modelling, chemical extractions, mineralogical characterisation, surface area characterisation and elemental analysis were used to investigate these aims.

The thesis identified a large range in CDR potential between the quarry fines and chemical analysis identified the leaching of alkaline and alkaline-Earth metals during weathering. Several increases in Al, Fe and Mn were also identified as a result of basalt amendment and the use of either conventional or organic fertiliser. However, there was limited evidence to suggest that basalt amendment significantly affected OC that had interacted with Al, Fe or Mn ions/precipitates.

Table of Contents

Table of Figures (shortened titles)

Table of Tables (shortened titles)

1. Introduction

1.1. Brief literature review

1.1.1. Climate change and CO_2 removal (CDR) strategies

The UNFCCC Paris Agreement aims to limit human-caused climate warming to less than 1.5°C above pre-industrial temperatures. This requires urgent phase-down of CO_2 emissions (IPCC, 2018, 2021), and large-scale deployment of safe, effective and environmentally acceptable CO_2 removal (CDR) strategies, on the order of up to 2-10 $GtCO_2\ yr^{-1}$ (gigatons of carbon dioxide per year) by 2050 (Rockström *et al.*, 2017; Mercure *et al.*, 2018).

There is evidence to suggest that no single CDR strategy will be able to sustainably draw down the 2-10 $GtCO_2\ yr^{-1}$ that has been predicted as being needed to be removed from the atmosphere to limit global warming to 1.5°C above pre-industrial temperatures (Fuss *et al.*, 2018). Instead, an array of strategies is required to remove enough CO_2 to meet the targets set out in the UNFCCC Paris Agreement. There are several CDR strategies actively being investigated in terms of potential, cost and longevity including: afforestation, bioenergy with carbon capture and storage (BECCS), biochar, direct air capture and carbon storage (DACCS), ocean fertilisation, soil carbon sequestration (SCS) and enhanced rock weathering (ERW) (Fuss *et al.*, 2018; Minx *et al.*, 2018; Nemet *et al.*, 2018). The costs, longevity and CDR potential of these strategies are summarised in Table 1.1.

Overall, there are large uncertainties associated with potential CDR with each of these strategies, with up to one order of magnitude difference in the predicted CDR of several of these strategies (e.g. BECCS and DACCS). The longevity of the CDR strategies also varies substantially from decades to centuries for afforestation and soil carbon sequestration to being potentially permanent in the case of BECCS and DACCS. The deployment of certain CDR technologies are also predicted to weaken several of Earth's natural C sequestration feedbacks (e.g. strong confidence that ocean and land C sequestration will be weakened in DACCS). Furthermore, certain CDR strategies are also predicted to increase the emissions of other greenhouse gases (e.g.

increased N_2O in BECCS, increased volatile organic carbon (VOC) in BECCS, DACCS and afforestation) (IPCC, 2021).

Relative to other technologies, ERW is predicted to remove substantial quantities of CO_2 (2-4 $GtCO_2$ yr^{-1}) and once removed, the CO_2 will have a long residence time (10-100,000 years, Table 1.1). ERW also does have the disadvantages of significantly weakening ocean and land C sequestration via Earth system feedbacks or by increasing N_2O or volatile organic carbon (VOC) emissions (IPCC, 2021).

This thesis focuses on ERW as a CDR strategy.

Table 1.1 – A comparison in CDR potential, cost and longevity of different CO_2 removal (CDR) strategies. Unless specified, all data is from Fuss *et al.* (2018).

Technology	Description	Predicted CDR ($GtCO_2\ yr^{-1}$)	Cost ($\$\ t\ CO_2^{-1}$)	Longevity
Afforestation/reforestation	Planting and replanting of trees.	0.5-3.6	2-150	Decades to centuries
Bioenergy with carbon capture and storage (BECCS)	Producing bioenergy, then capturing CO_2 –released during energy production and storing the captured CO_2 underground.	0.5-5	15-400	Potentially permanent
Biochar	Applying pyrolyzed organics (i.e. organics which are thermally degraded in the absence of oxygen) to soils to increase carbon stocks and improve soil fertility.	0.5-2	60-100	Decades to Centuries
Direct air capture and carbon storage (DACCS)	Using chemical membranes to remove atmospheric CO_2.	0.5-5	30-1000	Potentially permanent
Soil carbon sequestration (SCS)	Changing land management techniques to increase soil organic carbon content, thus preventing CO_2 respiration from soils.	Up to 5	-40 - 100	Decades to centuries
Enhanced rock weathering (ERW)	Artificially accelerating the natural weathering processes to draw down CO_2.	2-4	80-180[1]	10 to 100-thousand years

[1] Taken from Beerling *et al.* (2020).

1.1.2. Enhanced Rock Weathering

Enhanced rock weathering aims to accelerate a natural carbon sequestration process driven by chemical weathering of silicate rocks (Seifritz, 1990; Lackner *et al.*, 1995). During the chemical weathering of silicate rocks, dissolved atmospheric CO_2 forms aqueous species that accelerate the dissolution of silicate phases (minerals and glasses – which make up silicate rocks) via proton consumption to generate bicarbonate (Eq. 1.1). Eventually, this bicarbonate is transported to the oceans via runoff where it is stored in a stable form for time scales of 10,000 to 100,000 years (Renforth and Henderson, 2017):

$$CaMgSi_2O_6 + 4CO_2(g) + 6H_2O \rightarrow Mg^{2+} + Ca^{2+} + 2H_4SiO_4 + 4HCO_3^- \quad \text{(Eq. 1.1)}$$

The generated bicarbonate (HCO_3^-) must be charge balanced with cations to remain stable in solution. Divalent (Mg^{2+} and Ca^{2+}) and monovalent (Na^+ and K^+) cations which are released from silicate rocks during weathering are essential to charge balance the negative bicarbonate ion (HCO_3^-) in solutions in the ERW conceptual model. If any of these cations are removed from the solution (i.e. by biota, or through adsorption to soil clays), bicarbonate may be outgassed from the solution as CO_2 into the atmosphere, and therefore this released CO_2 will not have contributed to CDR via weathering.

The bicarbonate and cations that are generated via the weathering reactions may also be precipitated as carbonates (with concomitant release of $CO_{2(g)}$), depending on solution pH, which leads to a net of 1 mol of CO_2 being captured for every 2 mol of CO_2 consumed in the silicate weathering reaction (Eq. 1.2):

$$Ca^{2+} + 2HCO_3^- \rightarrow CaCO_3 + H_2O + CO_2(g) \quad \text{(Eq. 1.2)}$$

Generally, the chemical weathering of minerals can be described as being a function of their surface area, dissolution rate constant and various solution parameters. These solution parameters include: pH (solution pH with a greater deviation from pH 7 increases the weathering rate), temperature (hotter reaction temperatures increase the weathering rate) and the amounts of elements which comprise a mineral in solution (lower concentrations of the elements which comprise the mineral in the reaction solution increases the weathering rate). This

is described in the generalised description of mineral dissolution (Eq. 1.3) (Palandri and Kharaka, 2004; Declercq and Oelkers, 2014):

$$\frac{dm}{dt} = -SA \cdot \begin{bmatrix} A_{acid} e^{\frac{-E_{acid}}{RT}} \cdot a_{H+}^{n_{acid}} \cdot (1 - SR) \\ + A_{neutral} e^{\frac{-E_{neutral}}{RT}} \cdot (1 - SR) \\ + A_{base} A e^{\frac{-E_{base}}{RT}} \cdot a_{H+}^{n_{base}} \cdot (1 - SR) \end{bmatrix} \text{(Eq. 1.3)}$$

Where *m* is the number of moles of the mineral, *t* is time (in seconds, s), *SA* is the reactive surface area (m^2), *A* is the pre-exponential factor (the rate constant) of the acid, neutral and base mechanism (mol m^{-2} s^{-1}), *E* is the activation energy (of the acid, neutral and base dissolution mechanism, J mol^{-1}), *R* is the gas constant for water (8.31, J mol^{-1} K^{-1}), *T* is the temperature (in Kelvin, K), *a* is the ion activity of hydrogen (H^+), *n* is the reaction order (for the acid, neutral and base dissolution mechanism), and *SR* is the saturation ratio. Mineral dissolution slows down as the SR increases.

ERW seeks to accelerate silicate weathering by exploiting some of the parameters, as described in the previous paragraph, which affect rock dissolution. There are several ways in which rock weathering can be accelerated, which are summarised in Hartmann *et al.* (2013). These applications include: (1) spreading fast-dissolving silicate powders onto the terrestrial surface to enhance natural rates of chemical weathering (e.g. Schuiling & Krijgsman, 2006), (2) adding reactive minerals to the open ocean (e.g. Köhler *et al.*, 2013) (3) spreading fast weathering materials over coastal zones (e.g. Schuiling & de Boer, 2013) and (4) pumping high-pCO_2 into rock formations to accelerate natural weathering (Matter *et al.*, 2016).

Out of those four applications, the first three utilise enhanced surface area by either pre-crushing material (1, 2 and 3) or using coastal physical weathering processes to accelerate weathering (3). The effect of the amounts of elements within constituent minerals that have weathered into a solution is taken advantage of in application (2) and (3) where a build-up of elements is prevented by weathering materials in a large water body like the ocean. Application (4) lowers the solution pH by the increased pCO_2 being injected into rock formations.

Recent attention in ERW research has focused on one way of using application (1) by applying crushed silicate to cropland areas (Kantola *et al.*, 2017; Beerling *et al.*, 2018; Kelland *et al.*, 2020). Beerling *et al.* (2018) details several practical reasons for using croplands as a reactor for ERW including: a large land area (nearly 11% of total land area is used for crop production) and the readily available infrastructure and machinery suitable for spreading silicate materials onto croplands (e.g. from liming practices). By adding crushed silicate to cropland areas, weathering is not only accelerated by increased surface area but it is also accelerated by the higher concentrations of carbonic acid in soils (via higher pCO_2 concentrations from root and microbe respiration (Nan *et al.*, 2016)). Figure 1.1 illustrates how ERW on croplands could work.

This thesis focuses on the application of ERW principles to cropland soils.

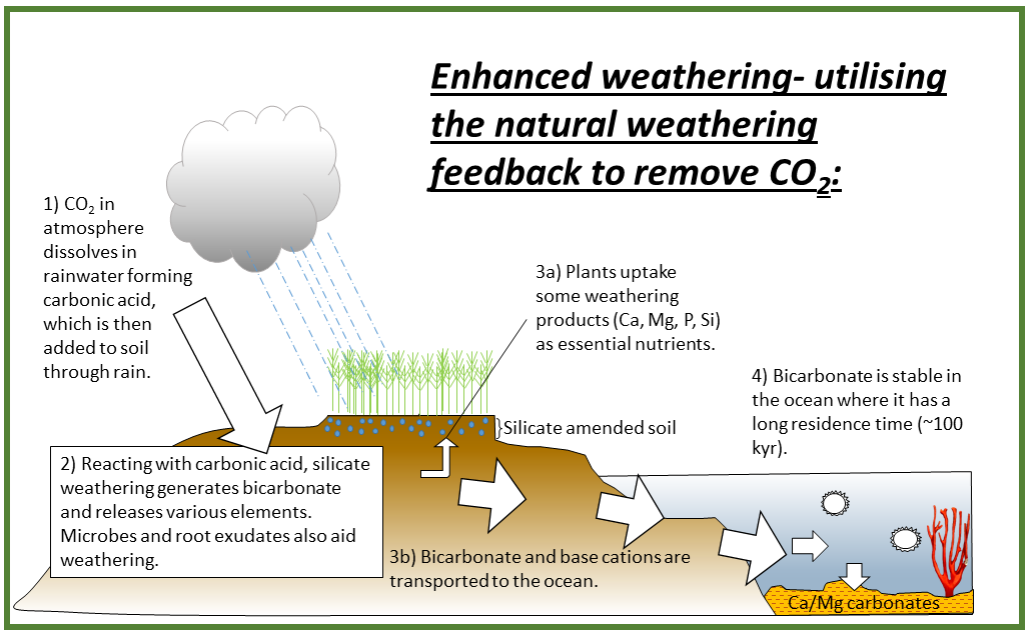

Figure 1.1 – Enhanced rock weathering in cropland areas. Adapted from Beerling *et al.* (2018).

1.1.3. Silicate candidates for ERW

Silicate rocks comprise *c.* 90% of the rocks exposed at the Earth's land surface (White, 2003). However, not all silicate rocks are suitable for ERW applications. Sedimentary and metamorphic silicate rocks comprise *c.* 79.1% of the land surface (Amiotte Suchet, Probst and Ludwig, 2003) but are typically low in Ca and Mg so are unsuitable for ERW. Any Ca and Mg minerals present in sedimentary and metamorphic rocks are more likely to be confined to slow-

weathering clay minerals which would have precipitated out of a solution during incongruent chemical weathering or via replacement and diffusion during metamorphic reactions.

While they comprise a lower proportion of the total land area (*c.* 5.2%, Amiotte Suchet *et al.*, 2003), mafic igneous rocks are considered more suitable for ERW because they typically contain significant concentrations of Ca and Mg compared to acidic igneous rocks (Figure 1.2).

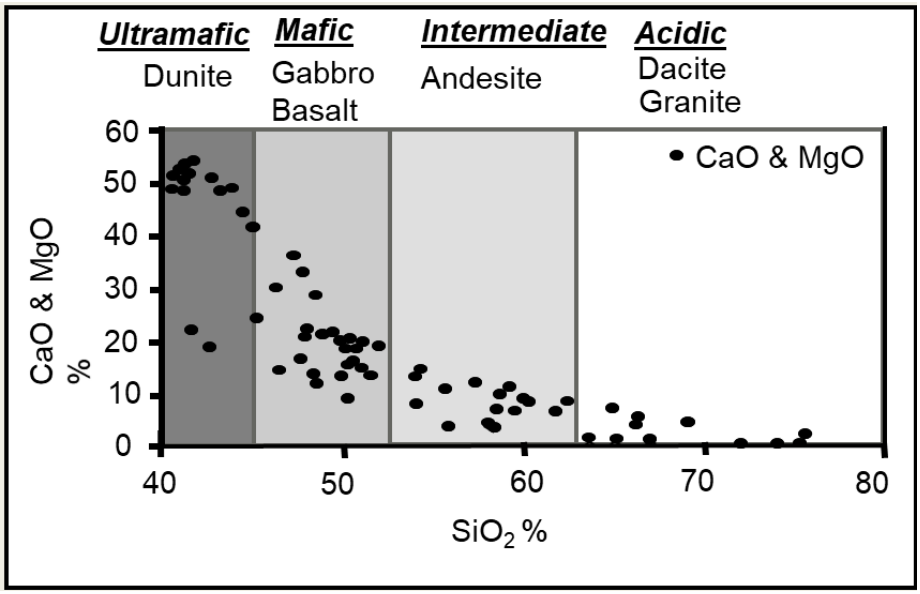

Figure 1.2 – %CaO and MgO in igneous rocks. Diagram modified from Renforth (2012).

Much of the early ERW studies considered the application of single minerals for ERW. One such mineral is olivine: an 'essential mineral' (i.e. 'a mineral component of a rock that is necessary to the classification and nomenclature of the rock, but that is not necessarily present in large amounts.' (Mindat, 2022)) in ultramafic rocks with a high Mg content and very fast weathering rate (Palandri and Kharaka, 2004). Given the high Mg content of olivine, it has a large potential for CDR: 0.8-0.9 tonnes of CO_2 could be removed from the atmosphere per tonne of olivine weathered (Beerling *et al.*, 2018). However, olivine typically hosts high concentrations of potentially toxic metals Ni and Cr which can accumulate in soil profiles (Renforth, Pogge von Strandmann and Henderson, 2015) which may make it unsuitable for ERW application.

Another fast weathering mineral that has been investigated is wollastonite ($CaSiO_3$): a fast weathering pyroxenoid mineral (Palandri and Kharaka, 2004) that can form during contact metamorphism of limestone. The application of wollastonite to cropland systems has shown a significant potential to remove CO_2 from the atmosphere – up to 39.3 t CO_2 ha^{-1} when high quantities of wollastonite were amended into soils (221 tonnes wollastonite ha^{-1}) (Haque *et al.*, 2019; Kelland *et al.*, 2020). More modest amounts of CDR at 0.13 t CO_2 per ha^{-1} were identified after 3.44 t wollastonite was applied to a forested catchment system in New Hampshire, USA after 15 years of weathering (Taylor *et al.*, 2021).

A drawback of using wollastonite is that its resource size is much too small to be applied on a large scale. Resources of wollastonite have been identified in North America, Europe, China and India (Haque *et al.*, 2019). However, Taylor *et al.* (2021) that given an application rate of 50 t ha^{-1} (a value frequently cited for f), the global wollastonite reserve could cover less than only 25,000 km^2 (e.g. land area of UK = 242,495 km^2). The limited resource size of wollastonite makes it unsuitable for large-scale global deployment of ERW.

Artificial silicates (e.g. demolition waste and steel slags) have also been considered for ERW (Beerling *et al.*, 2020; Kantzas *et al.*, 2022). Both steel slag and demolition waste have high concentrations of Ca (steel slags = 25-27 wt.% Ca (Proctor *et al.*, 2000); demolition waste = 11-13% Ca (Moreno-Pérez *et al.*, 2018)). Both materials have a large resource, with 5.8-8.3 billion tonnes of legacy steel slag and production rate of 1.4-5.9 billion tonnes yr^{-1} of demolition waste (Renforth *et al.*, 2011). Both resources have proven high potential for CDR strategies in reactor settings, but there is evidence that steel slags can leach metals at potentially toxic concentrations into soils (O'Connor *et al.*, 2021) and generate extremely alkaline (pH = 12) leachate solutions (Mayes, Aumônier and Jarvis, 2009). Further work is suggested to be necessary to assess the long-term effects of steel slag amendment into cropland soils on environmental and human health (O'Connor *et al.*, 2021).

Given toxicity related issues associated with olivine and artificial silicates and resource issues associated with wollastonite, the mafic rock basalt is considered as a prime candidate for ERW (Beerling *et al.*, 2018, 2020). Basalt is a

fast-weathering, Ca- and Mg-rich and abundant silicate rock. Basalt is defined by the International Union of Geological Sciences as having between 45 and 52 wt.% SiO_2 and less than 5 wt.% alkalis (K_2O and Na_2O) (Le Maitre *et al.*, 2002). The major constituent minerals of basalt (pyroxenes and plagioclase feldspar) typically weather faster, and can therefore potentially capture CO_2 faster, than minerals commonly found in granitic or sedimentary rocks (e.g. quartz, K-feldspar, muscovite) (Palandri and Kharaka, 2004).

While basalt typically has a lower CDR potential relative to olivine and wollastonite (between 0.2-0.6 t CO_2 t $basalt^{-1}$ (Renforth, 2012 and Figure 1.2)), model simulations have predicted that globally, at an application rate of 50 t ha^{-1}, basalt amendment has the potential to remove between 2.7 and 27 $GtCO_2$ from the atmosphere by 2100 (Taylor *et al.*, 2016). Recent simulations assessing the potential of ERW in the UK alone estimated that ERW could remove between 6-30 Mt CO_2 yr^{-1} which accounts for around 45% of current UK CO_2 emissions (Kantzas *et al.*, 2022).

Basalt is extremely abundant: it comprises 5.2% of the Earth's surface (Amiotte Suchet, Probst and Ludwig, 2003) and is frequently exposed as large, voluminous deposits known as large igneous provinces (LIPs) which may have individual greater than 1 million km^2 (Ross *et al.*, 2005; Bryan *et al.*, 2010). Not only abundant, basalt is also frequently mined for the aggregate industry. During the crushing of rock into suitably sized gravel for the aggregate industry, a fraction of quarry fines (typically 0-4 mm) are generated (Renforth *et al.*, 2011). These fines are too small to be used by the aggregate industry and the 3 billion tonnes that are generated each year (Renforth *et al.*, 2011) could be suitable for application to fields (Beerling *et al.*, 2018). The use of crushed rock eliminates the requirement for rocks to be crushed, thus removing the most energy intensive step in the ERW supply chain, improving the efficiency of the CO_2 removal (Renforth, 2012; Moosdorf, Renforth and Hartmann, 2014; Beerling *et al.*, 2020).

Basalt could also be used as a fertiliser. Basalts inherently constitute P, K, Ca, Mg, Fe and P (GERM, 2000) which are released into the soil solution during weathering which may then be available for plant-uptake. Soil health has been shown to improve following basalt amendment with increased soil pH, cation

exchange capacity, and soil Ca, Mg and K in tropical soils (D'Hotman and De Villers, 1961; Gillman, Burkett and Coventry, 2002; Anda, Shamshuddin and Fauziah, 2013). Crop yield has also been shown to improve following basalt amendment. In experiments which tested basalt amendment for CDR potential, crop yields have increased by up to 21±9.4 % (Kelland *et al.*, 2020). The release of Si during basalt weathering is also hypothesised to replenish Si stocks which become depleted when plant residues are not returned to the soils (Beerling *et al.*, 2018).

1.1.4. Potential sinks for elements released during basalt weathering in soils

The main aim of applying basalt to croplands for ERW is to release cations from basalt that can neutralise the negative charge of the bicarbonate ion (HCO_3^-) so that the bicarbonate is balanced and retained in solution. However, the ions released during weathering may not accompany bicarbonate. Instead, some ions may be retained in soils by bonding with clays and organic carbon via exchange reactions (Kelland *et al.*, 2020), taken up by plants and microbes (Kelland *et al.*, 2020; Epihov *et al.*, 2021), or precipitated as secondary phases in soils or on basalt particles (basalt grains). The precipitation of secondary minerals as a potential consequence of basalt amendment has been suggested (Slessarev *et al.*, 2022; Vicca *et al.*, 2022), but to the authors' knowledge, the precipitation of secondary phases associated with ERW has not been previously evidenced experimentally.

Both Al and Fe, which can be released into soil solution during basalt weathering, are immobile at circumneutral pH conditions and are therefore likely to be removed from the solution by precipitation (Pourbaix, 1974). While there has been no directly applicable experimental evidence for the precipitation of secondary minerals as a result of basalt amendment to an agricultural field site, the transformation of basalt over geological time has shown precipitation of several secondary phases. Research has shown that over a 4.1-million-year timescale, basalt pedogenesis transformed primary minerals (e.g. plagioclase feldspar, diopside) into poorly crystalline weathering products: allophane ($Al_2O_3•(SiO_2)_{1.3\text{-}2}•((H_2O))_{2.5\text{-}3}$), microcrystalline gibbsite ($Al(OH)_3$) and ferrihydrite ($(Fe^{3+})_2O_3•0.5H_2O$) (Chorover, Amistadi and Chadwick, 2004). Then,

over time, these poorly crystalline weathering products were transformed into crystalline minerals such as kaolinite ($Al_2(OH)_4Si_2O_5$), gibbsite ($Al(OH)_3$) and goethite (FeO(OH)) (Chorover, Amistadi and Chadwick, 2004). Therefore, it could be expected that as the amended basalt weathers, these Al and Fe phases will form in soils. Although, the length of time it will take for these phases to form in the context of ERW is unknown. However, the surface area of the basalt grains relative to basaltic bedrock is much higher and it could be expected to increase dissolution rates (e.g. Eq. 1.3 and Palandri and Kharaka (2004)). Increased dissolution rates may result in higher supersaturation of Al and Fe phases and thus enhance their rate of precipitation from solution.

1.1.5 Potential stabilisation of organic carbon and synergy between ERW and SCS

The secondary phases mentioned in the previous section have sites of charge, and therefore may not only be sinks for Al and Fe but could also bond with other elements (e.g. exchangeable ions Ca, Mg, K and Na) and soil compounds including organic carbon. Secondary phases may stabilise organic carbon either: (1) by stabilising organic carbon via adsorption to charged sites (e.g. Kaiser and Zech, 2000; Jagadamma *et al.*, 2014; Chen *et al.*, 2017; Singh *et al.*, 2017) or (2) as co-precipitants which incorporate organic carbon into their chemical structure (e.g. Tamrat *et al.*, 2019).

Once organic carbon interacts with inorganic materials via either adsorption or co-precipitation, the organic carbon is chemically protected against microbial degradation (i.e. it is not respired as CO_2). The retention of organic carbon in soils is desirable both for preventing CO_2 entering the atmosphere and as such, is another CDR strategy called soil carbon sequestration (SCS), as briefly summarised in Table 1.1. SCS aims to increase total carbon in soils by reducing losses of CO_2 from respiration and disturbances, mainly through changes in land management (The Royal Academy of Engineers and The Royal Society, 2018). Current data suggests that SCS has a moderate CO_2 removal potential: between 0.3 – 3.0 $GtCO_2\ yr^{-1}$ (Table 1.1, Fuss *et al.*, 2018). Functionally, the retention of organic carbon in soils is also desirable. The depletion of soil organic carbon can lead to degraded soil quality, reduced biomass productivity and reduced water

quality (Lal, 2004), all of which affect global food and water supplies (IPCC, 2021).

There is a wealth of evidence that demonstrates that increased soil organic carbon content is correlated to the accumulation of secondary phases such as clay minerals and short range order phases (SROs) (Sarkar *et al.*, 2018; Rasmussen *et al.*, 2018; Mikutta *et al.*, 2006; Eusterhues, Rumpel, and Kögel-Knabner, 2005; Kleber *et al.*, 2005). Furthermore, Rasmussen et al (2018) assessed the correlation between soil organic carbon and several environmental factors which are considered to be correlated to the amount of soil organic matter in different soils including: mean annual precipitation, mean annual temperature, potential evapotranspiration/mean evapotranspiration, pH, exchangeable Ca, poorly crystalline Fe and Al (oxalate-extractable), crystalline Fe (dithionite-extractable) and clay fraction and silt fraction. Of each of these variables, the most important for organic carbon stabilisation were the amounts of poorly crystalline Al and Fe, and exchangeable Ca (Rasmussen *et al.*, 2018).

Basalt is an abundant source of Al (6.9-8.0 wt.%), Fe (5.3-7.5 wt.%) and Ca (5.4-7.4 wt.%) (Sarbas, 2008; Kelland *et al.*, 2020) and basalt weathering reactions will release Al, Fe and Ca into soil that can form the poorly crystalline phases and increase exchangeable Ca to increase soil organic carbon. Basalt also contains trace Mn, which has been shown to be important for organic carbon dynamics in soils (Li *et al.*, 2021). There is therefore a strong indirect evidence base that suggests that amending soils with basalt for ERW will also, in time, increase soil organic carbon and therefore could be a facilitator for SCS.

1.2. Knowledge gaps

1.2.1. Basalt and its complex mineralogy

While basalt is considered to be a prime candidate for ERW, the use of basalt adds an additional layer of scientific complexity to ERW because basalt is a rock composed of a mixture of minerals compared to an individual mineral such as olivine or wollastonite.

Complexity is added because basalt mineralogy can vary depending on which tectonic environment the basalt has formed in. Diagnostically, basalt

contains pyroxene- (e.g. diopside and augite) and plagioclase feldspar-group minerals (e.g. andesine, labradorite, bytownite and anorthite) (Wilson, 1989). Basalt also, however, contains several accessory minerals depending on the melt chemistry before crystallisation. Faster weathering olivine group minerals will form in Fe and Mg rich magmas, whereas hydrated magmas may contain amphibole group minerals. Under acidic weathering conditions, the difference in rate constant between olivine and amphibole minerals can vary by one order of magnitude (Palandri and Kharaka, 2004). Rapid quenching of the melt can lead to basaltic glass formation (Allen *et al.*, 1981). Poorly crystalline glasses have been shown to weather more rapidly than crystalline minerals of similar chemical compositions (Wolff-Boenisch, Gislason and Oelkers, 2006). In addition, several secondary minerals may form (e.g. clay minerals such as saponite, various zeolites) during hydrothermal alteration and weathering of basalts (Kristmannsdottir, 1979). Both clay minerals and zeolites weather up to five orders of magnitude slower than pyroxenes, plagioclases, olivines and amphiboles in acidic conditions (Palandri and Kharaka, 2004).

These differences of weathering rate constants of up to five orders of magnitude between pyroxenes, amphiboles and clay minerals crudely illustrate how basalt mineralogy may affect the rate of CDR. An appreciation for the different mineralogy of basalts has been shown in modelling studies which have assessed the CDR potential of two different basalts characterised as a faster weathering alkaline basalt (containing more olivine) and a slower weathering tholeiitic basalt (containing no olivine) (Taylor *et al.*, 2016; Beerling *et al.*, 2020). However, these results do not reflect the presence of basaltic glass or secondary phases which may have formed during weathering or hydrothermal alteration.

Furthermore, given the dependence of weathering rates of materials on surface area, the surface areas of basaltic quarry fines that are used in ERW studies are also important. There is a good rationale for utilising the quarry fines produced by the mining industry as a by-product rather than crushing fresh material, however, there could be differences in quarry sorting processes which could affect particle size and surface area. A handful of studies have measured the surface areas of igneous material including dolerite (Rigopoulos *et al.*, 2016), andesite and dacite (Dalmora *et al.*, 2020a) and tephra from amethyst mining

(Korchagin, Caner and Bortoluzzi, 2019). While the characterisation of surface area is useful, the studies lack quantitative mineralogical interpretation which is essential for understanding the CDR potential and the release of elements from these materials (including nutritional elements P and K).

While both mineralogy and surface area are known to be important parameters influencing mineral and rock dissolution, the relative importance of the two factors for weathering are not known. If the relative importance of the two factors is known, then more guided decisions can be made about: (1) where to source basaltic quarry fines from and (2) if further crushing of material to generate finer particle sizes is warranted.

The CDR potential of a material is not the only factor which will be affected by the weathering rate of minerals. The mineralogy and surface area of a material will also affect the amount of Al and Fe that will be released from the rock and that could be precipitated as secondary minerals which can then interact with organic carbon.

Given the importance of these properties in calculating mineral dissolution, it is therefore imperative to characterise the mineralogy, chemistry, surface area and particle size of basalts in order to assess: (1) CDR potential, (2) their relative importance for CDR and (3) nutrient potential.

1.2.2 Lack of understanding of grain-scale interactions between basalt grains and soil solutions

The mineralogical composition and surface area of basaltic quarry fines can be inputted into geochemical models which simulate weathering in a bulk soil solution to assess the CDR potential and elemental release from materials. Published geochemical models track the dissolution of specific mineral phases within complex mineral mixtures and the fate of elements once released into solutions. The geochemical models have the potential to track several elemental sinks including: the retention of elements on organic and inorganic exchange sites, uptake of elements by crops and the precipitation of secondary minerals out of the soil solution (e.g. Kelland *et al.*, 2020). Basalt amendment has been demonstrated through mesocosm experiments to increase crop yield, the uptake of elements by plants and increase the retention of cations in soils (Kelland *et al.*,

2020), and increases in yield have also been observed in Poblador *et al.* (2022). To the author's knowledge, at the time of writing, there are no studies which have experimentally observed the precipitation of Al and Fe secondary phases in the bulk soil in an ERW context.

The bulk soil is a very useful pool to study as it allows researchers to track the overall effect of basalt amendment on soils. In reality, however, the bulk soil pool consists of several microenvironments which will have a variety of unique geochemical processes driving their development. At least two important microenvironments exist within a soil that has been amended with basalt: the bulk soil and the area directly surrounding the basalt grain. Given the high pH basalt (*c.* pH 9 (Korchagin, Caner and Bortoluzzi, 2019)) and the relative ease of weathering of basaltic minerals compared to other common soil minerals (e.g. quartz, clay minerals – Palandri & Kharaka, (2004)), the solution surrounding the basalt grains is likely to be of a higher pH than the bulk and contain higher concentrations of ions that have been released into solution by weathering reactions. These differences in microenvironment will affect which geochemical processes can occur. In particular, at higher pH, Al-hydroxide phases are less likely relative to Fe-hydroxide phases to precipitate whereas the converse is true in a lower pH bulk soil.

At present, geochemical modelling of ERW in soils has not accounted for a basalt grain microenvironment. Mineral dissolution is expressed simply within current geochemical models, only accounting for the stoichiometric loss of minerals within the basalt grains as a function of time. The models cannot account for the further breakdown of minerals by biota (e.g. mycorrhizal fungi – which have been shown to preferentially colonise basalt over soil particles (Quirk *et al.*, 2012)) nor do they account for the preferential leaching of weaker-bonded elements from basaltic minerals, as is hypothesised by Oelkers (2001). While it is beyond the scope of the work presented in this thesis to improve geochemical models, it is worth noting that the models cannot be used to determine if these processes occur and to what extent they affect CDR.

There has been limited work investigating the basalt grain microenvironment experimentally in an ERW context. Limited work has

considered changes to the basalt grains by characterising both the bulk elemental change of basalt grains retrieved from an ERW experiment and the interaction between basalt bags and mycorrhizal fungi (Kelland *et al.*, 2020). However, the potential precipitation of secondary minerals and retention of organic carbon have not been previously determined in ERW experiments at either bulk or grain scale.

If secondary mineral precipitation could be a key sink for Al and Fe released during basalt amendment, determining where this precipitation is occurring (i.e. on the basalt grains vs the pre-existing soil matter) could be important for understanding how basalt weathers, and ultimately removes CO_2 from the atmosphere, when applied to a soil environment.

1.2.3. Identifying sinks for Al, Fe and Mn, and their association with organic carbon in bulk soils

As mentioned in the previous section, some sinks for Al, Fe and Mn are considered in geochemical models. Several different secondary phases have been used as Al and Fe sinks in geochemical modelling including: gibbsite, amorphous Al, allophane and kaolinite as an Al-sink, and amorphous Fe-hydroxide and goethite as an Fe sink (Dontsova *et al.*, 2009; Pohlmann *et al.*, 2016; Taylor *et al.*, 2016, 2021; Beerling *et al.*, 2020; Kelland *et al.*, 2020). Pyrolusite (MnO_2) was used as a Mn sink in Kelland *et al.* (2020). Currently there is no consensus of which secondary minerals to use in geochemical models, though the duration which the model is run for may affect the precipitate used (i.e. poorly crystalline minerals for short term time scales, crystalline phases for longer-term time scales). Even though the precipitation of these secondary phases is accounted for in geochemical models, the association of organic carbon with those phases (presumably via adsorption) is not accounted for in geochemical models.

The adsorption of Al, Fe and Mn to humic substances is also an important sink in soil systems. It is not, however, possible to model the co-precipitation of Al, Fe and Mn with organic carbon in the current geochemical modelling set-up. This is because PHREEQC (Parkhurst and Appelo, 2013), the geochemical modelling software frequently used for ERW modelling (e.g. Kelland *et al.*, 2020; Beerling *et al.*, 2020; Taylor *et al.*, 2015), does not have the capability to model these processes. It is also not currently possible to model the adsorption of Fe or

Mn to humic surfaces, however, the adsorption of Al to humic surfaces has been incorporated into recent water-shed scale models using PHREEQC (Erlandsson *et al.*, 2016).

Both the precipitation of secondary phases and subsequent organic carbon adsorption to these newly precipitated phases, along with the association of organic carbon with Al, Fe and Mn ions via humic substance interaction are important processes within the soil systems. They could represent key sinks for Al, Fe, Mn and organic carbon which have not yet been studied in the context of ERW. Although it is not currently possible to model some of the geochemical processes, it is important to quantify these Al, Fe, Mn and organic carbon sinks so that their relative importance in ERW processes can be considered. By studying these Al, Fe, Mn and organic carbon sinks, the potential synergy between ERW and SCS can also be investigated.

1.2.4. Experimental need for secondary phase precipitation and organic carbon stabilisation at field demonstrator scale

There is a need to understand these processes at the field demonstrator scale. While more challenging than conducting experiments at smaller mesocosm scale, the assessment of these techniques in field trial set-ups is crucial because it is hoped that ERW will be deployed to fields on a large scale. However, field-trials are exposed to uncontrolled weather conditions, unhomogenised soil structure and uneven distribution of basalt which can make the identification of evidence for CDR, secondary mineral precipitation and organic carbon stabilisation difficult. To help understand the extent to which these processes can occur, it is important to study them at the mesocosm experiment scale where environmental (e.g. temperature and precipitation) and experimental conditions (e.g. the distribution of basalt within the soil profile, soil particle size etc.) can be controlled or at least measured. However, the effort towards understanding these processes cannot stop at the mesocosm scale. Instead, evidence from mesocosm-scale experiments should be compared to evidence from field-scale ERW demonstrators.

At present, to the author's knowledge, there has been no study to date which has analysed the precipitation of secondary phases and their association with organic carbon at the field scale, in an ERW experiment.

1.3. Thesis aims and chapter outline

This thesis comprises six chapters in total, including a general introduction, four experimental chapters and a general discussion. The main research questions addressed in this thesis and the interconnectivity of the chapters are summarised in Figure 1.3.

Given the knowledge gaps outlined in the previous section, this thesis aims to address the following questions:

1. How do the mineralogical and surface area characteristics affect CDR potential of basaltic quarry fines?
2. How do basalt grains weather in soil solutions?
3. Does organic carbon associated- and secondary precipitated- Al, Fe and Mn increase in soils and on grains following basalt amendment?
4. Is there evidence for increased organic carbon stabilisation following basalt amendment?

Each chapter is outlined below:

Chapter 1 provides a general introduction to ERW, including the rationale for using basalt in ERW and the largely unexplored potential synergy between ERW and SCS through the precipitation of secondary Al, Fe and Mn phases which can stabilise soil organic carbon. Key knowledge gaps are also identified in: (1) basalt characterisation, (2) grain-scale basalt weathering in the soil environment and (3) secondary phase precipitation in soils following basalt amendment. Chapter 1 also outlines the aims of this thesis.

Chapter 2 addresses the complex mineralogy and surface areas associated with basalt quarry fines. Firstly, the mineralogy, chemistry, particle size and surface area of six basaltic quarry fines are characterised in this chapter. Then, these characterisations are inputted into a reactive transport model to simulate weathering in an agricultural soil, and are assessed in terms of (1) CDR and (2)

nutrient release. The results from these models are also used to try to predict (1) future weathering based on rock chemistry and surface area and (2) P and K release during weathering.

Chapter 3 aims to assess evidence of (1) chemical weathering, (2) precipitation of secondary phases and (3) potential organic carbon stabilisation on basalt grains which were applied to an ERW experiment and then extracted after the experiment finished. Grains were taken from a mesocosm experiment which featured four treatments (NPK, NPK + basalt, Manure and Manure + basalt).

Chapter 4 aims to quantify several sinks for basalt weathering products (Al, Fe and Mn) and their association with organic carbon in the bulk soil environment. Metal-organic carbon complexes and the association of organic carbon with SRO phases are considered in this chapter. The samples analysed in this chapter were from the same experiment as used in Chapter 3.

Chapter 5 has the same aims as Chapter 4, but data is collected from a different experiment. The samples analysed in this chapter came from an ERW field demonstrator site on an alkaline soil.

Chapter 6 is a general discussion which brings together the data and interpretations from Chapters 2, 3,4 and 5, and uses the independent conclusions from each of these chapters to determine areas for further study.

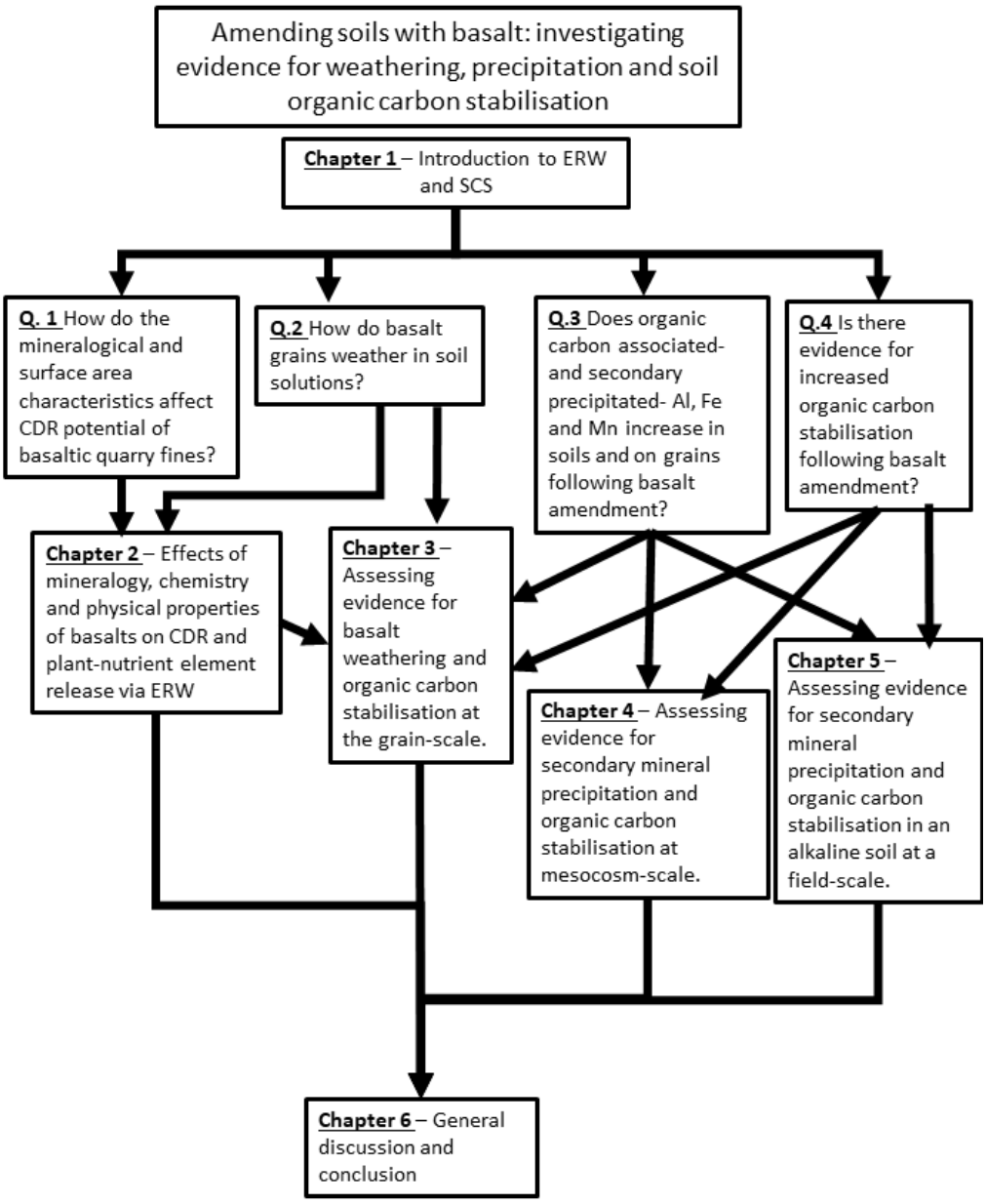

Figure 1.3 – Visual aid describing the overview of this thesis, in terms of overarching questions and interconnectivity between chapters. CDR = carbon dioxide removal ERW = enhanced rock weathering; SCS = soil carbon sequestration.

2. Effects of mineralogy, chemistry and physical properties of basalts on carbon capture potential and plant-nutrient element release via enhanced weathering

2.1. Introduction

The UNFCCC Paris Agreement aims to limit human-caused climate warming to less than 1.5°C above pre-industrial temperatures. This requires urgent phase-down of CO_2 emissions (IPCC, 2018), and large-scale deployment of safe, effective and environmentally acceptable CO_2 removal (CDR) strategies, on the order of up to 2–10 $GtCO_2\ yr^{-1}$ by 2050 (Rockström *et al.*, 2017; Mercure *et al.*, 2018). Enhanced rock weathering (ERW) is a proposed CDR strategy that involves accelerating natural carbon sequestration processes driven by chemical weathering of silicate rocks (e.g. Seifritz, 1990; Lackner *et al.*, 1995). During chemical weathering of silicate rocks, dissolved atmospheric CO_2 forms aqueous species that accelerate the dissolution of silicate phases (minerals and glasses) with proton consumption to generate bicarbonate (Eq. 1.1). Eventually, this bicarbonate is transported to the oceans via runoff where it is stored in a stable form for approximately 100,000 years (Renforth and Henderson, 2017):

$$CaMgSi_2O_6 + 4CO_2(g) + 6H_2O \rightarrow Mg^{2+} + Ca^{2+} + 2H_4SiO_4 + 4HCO_3^- \quad \text{(Eq. 1.1)}$$

Bicarbonate carbon may be precipitated as pedogenic carbonates, depending on soil pH, which leads to a net of 1 mol of CO_2 being captured for every 2 mol of CO_2 consumed in the silicate weathering reaction (Eq. 1.2):

$$Ca^{2+} + 2HCO_3^- \rightarrow CaCO_3 + H_2O + CO_2(g) \quad \text{(Eq. 1.2)}$$

Land-based ERW can involve amending forest (Köhler, Hartmann and Wolf-Gladrow, 2010; Taylor *et al.*, 2016; Strefler *et al.*, 2018) and cropland (Kantola *et al.*, 2017; Beerling *et al.*, 2018, 2020) soils with finely-crushed silicate rocks. Basalt, an abundant, fast-weathering, Ca- and Mg-rich, silicate rock, is considered a prime candidate for ERW (Beerling *et al.*, 2018, 2020). The major constituent minerals of basalt (pyroxenes, olivine and plagioclase feldspar)

typically weather faster, and can therefore potentially capture CO_2 faster, than minerals commonly found in granitic or sedimentary rocks (e.g. quartz, K-feldspar, muscovite) (Palandri and Kharaka, 2004). Finely crushed basalt is an abundant by-product of the aggregate and mining industry and there is growing recognition of its potential to improve soil health and support crop production (D'Hotman and De Villers, 1961; Gillman, Burkett and Coventry, 2002; Ramos *et al.*, 2019; Kelland *et al.*, 2020). The increased reactive surface area per unit volume of crushed basalt accelerates dissolution compared to natural *in situ* outcrops. Basalt weathering also liberates inorganic plant nutrients, including Ca, Mg, Fe, K, P and micronutrients (e.g., Mo), that could support crop production and generate alkalinity to reverse soil acidification caused by agricultural production (Hartmann *et al.*, 2013; Kantola *et al.*, 2017; Beerling *et al.*, 2018). If crop biomass is not returned to fields following harvest, major cations taken up from the soil (Ca^{2+}, Mg^{2+}, K^{+}) during growth will be unavailable to contribute to CDR via alkalinity production in soil porewaters (Banwart, Berg and Beerling, 2009).

Basalts are commonly formed following eruption in a variety of tectonic environments, and differences in petrogenesis result in a range of mineralogical compositions. Other mafic rocks, dolerite and gabbro, are formed during magmatic intrusions. Dolerite more commonly forms in smaller 'sheet-like' intrusions like sills and dykes, while gabbro forms in larger intrusions. Basalt diagnostically contains pyroxene- (e.g. diopside and augite) and plagioclase feldspar-group minerals (e.g. andesine, labradorite, bytownite and anorthite) (Wilson, 1989). The identity and proportion of accessory minerals may also vary, depending on the melt chemistry (e.g. olivine from Fe- and Mg-rich magmas, amphibole from hydrated magma). Rapid quenching of the melt can lead to basaltic glass formation (Allen *et al.*, 1981). Secondary minerals (e.g. saponite, various zeolites) may form during hydrothermal alteration and weathering of basalts (Kristmannsdottir, 1979).

The dissolution rate of minerals is a function of their surface area and dissolution rate constants as well as temperature and solution composition, including pH. Mineral dissolution rate is described in Eq. 1.3 (Palandri and Kharaka, 2004; Declercq and Oelkers, 2014):

$$\frac{dm}{dt} = -SA \cdot \begin{bmatrix} A_{acid} e^{\frac{-E_{acid}}{RT}} \cdot a_{H+}^{n_{acid}} \cdot (1 - SR) \\ + A_{neutral} e^{\frac{-E_{neutral}}{RT}} \cdot (1 - SR) \\ + A_{base} A e^{\frac{-E_{base}}{RT}} \cdot a_{H+}^{n_{base}} \cdot (1 - SR) \end{bmatrix}$$

(Eq. 1.3)

Where *m* is the number of moles of the mineral, *t* is time (in seconds, s), *SA* is the surface area, *A* is the pre-exponential factor (the rate constant) of the acid, neutral and base dissolution mechanism, *E* is the activation energy of the acid, neutral and base dissolution mechanism, *R* is the gas constant for water (8.31, J mol^{-1} K^{-1}), *T* is the temperature in Kelvin, K, *a* is the ion activity of hydrogen (H^+), *n* is the reaction order for the acid, neutral and base dissolution mechanism, and *SR* is the saturation ratio. In addition to mineralogy, surface area (SA, Eq. 1.3) is a crucial variable in the dissolution rate equation and is controlled by particle size, particle roughness, and mineralogy (Brantley, White and Hosdson, 1999; Parry *et al.*, 2015). The particle size of crushed rocks varies depending on the rock composition and processing procedures used by mining companies and is the most energy intensive step in the ERW supply chain (Hartmann *et al.*, 2013; Moosdorf, Renforth and Hartmann, 2014; Beerling *et al.*, 2020). However, utilizing mineralogically suitable silicate quarry fines from mining companies will reduce the dependency on energy intensive crushing. These fines are also recognized as valuable feed-stocks for sequestering CO_2 to assist in developing strategies for carbon neutral mining (Power *et al.*, 2014).

This chapter reports the detailed mineralogical (X-ray diffraction; XRD), chemical (Scanning Electron Microscopy - Energy Dispersive Spectroscopy; SEM-EDS and Inductive Coupled Plasma - Optical Emission Spectroscopy; ICP-OES), particle size (laser particle size analysis and mass fraction sieving) and surface area (Brunauer, Emmet, Teller (BET)-N_2 adsorption) characteristics of six basaltic quarry fines from mining companies that are being trialled across a worldwide network of large-scale ERW-CDR field-trial sites are reported. Then,

the mineralogical and surface area data are inputted into a reactive transport model (RTM) to: (1) evaluate the relative importance of mineralogy and particle surface area for CDR, (2) derive a function to predict the CDR potential of a basalt based on its chemical composition and surface area, and (3) track the release of essential plant nutrients P and K during dissolution to determine the potential of ERW with basalt to substitute for P and K fertilizers derived from finite high-grade mineral reserves (Elser and Bennett, 2011; Amundson *et al.*, 2015; Ciceri, Manning and Allanore, 2015; Amann and Hartmann, 2019; Beerling *et al.*, 2020).

2.2. Methods

In this chapter, basaltic quarry fines from six commercial quarries were studied. The basalt formed during hotspot and crustal extension-related episodes (Oregon, Tichum, Cragmill and Hillhouse) and island arc magmatism (Tawau). The Blueridge is a metamorphosed basalt, forming from medium temperature and pressure regional metamorphism (Blue Ridge) (Table 2.1). Several of the basaltic quarry fines investigated in this chapter were not formally classified as basalts, but they are mostly mafic in character. Therefore, for simplicity, all basaltic quarry fines are collectively referred to as basalts, with the exception of the Blue Ridge which is referred to as a metabasalt. All basalts, except the Blue Ridge metabasalt, were processed following conventional crushing and screening techniques at the quarry sites (Table 2.1). The Oregon basalt underwent additional on-site processing through air-extraction systems, limiting the abundance of finer particles (<75 μm). The Blue Ridge metabasalt comprised fine dust collected from the air during the commercial crushing process.

Table 2.1 – Origin and geological background of the commercially available basalts analysed.

Material	Geological Setting, (age)	Reference	Country of origin	Source and Supplier	Size fraction	Mining technique	Source
Blue Ridge	Metamorphosed basalt-Potentially part of the Catoctin greenstone. Virginia, USA, (Neo-Proterozoic)	USGS (2019)	USA	Purchased from Rock Dust Local LLC, Bridport, Vermont, USA	<1.34 mm	Collected as fine dust from crushing stages and baghouse dust collection from hard-rock drilling processes.	Mineralogy (X-Ray Diffraction) and particle size distribution, published in Blanc-Betes *et al.* (2021)
Cragmill	Whin Sill (Dolerite) Emplacement, Pennsylvanian, (Carboniferous)	Sabine *et al.* (1954)	UK	Donated by CEMEX Group, Cragmill, Northumberland	<4 mm (<15% > 4 mm)	Jaw and cone crushed, then sorted by screening.	This chapter
Hillhouse	Intrusive analcime gabbro, (Carboniferous).	Kirstein *et al.* (2006)	UK	Donated by Hillhouse Quarry Group, Dundonald, Troon	<4 mm	Jaw and cone crushed, then sorted by screening.	This chapter
Oregon	'Prineville Chemical Type Unit' of the Columbia River Basalt Group, (Middle Miocene).	Smith and Hayman (1987)	USA	Purchased from Central Oregon Basalt Products LLC, Madras, Oregon, USA	<1.18 mm	Crushed and sorted by screening. Ultrafines removed via dust handling system.	Mineralogy (X-Ray Diffraction) and glass chemistry (SEM-EDS) published in Kelland *et al.* (2020)
Tawau	Associated with Magmatic-arc volcanism, (Pleistocene).	Tahir *et al.* (2010)	Malaysia	Donated by Onika Quarry Co., Tawau, Sabah, Malaysia	<5 mm (<3% > 5 mm)	Jaw and cone crushed, then sorted by screening.	This chapter
Tichum Creek	Associated with continental-mantle plume magmatism, (Miocene).	Stephenson *et al.* (2007)	Australia	Donated by Boral Quarries, Tichum Creek, Queensland, Australia.	<4.75 mm	Jaw and cone crushed, then sorted by screening.	This chapter

2.2.1. Basalt chemistry and mineralogy

For chemical and mineralogical analyses, basalt samples were pulverized in a Fritsch Pulverisette agate ball mill (Fritsch International, Oberstein, Germany), then ground further using a pestle and mortar to homogenise the sample to <125 μm. The elemental chemistry analysis was conducted by Mr N Bramall at the University of Sheffield. Elemental Chemistry was determined using Inductively Coupled Plasma - Optical Emission Spectroscopy (ICP-OES) (Faculty of Science, University of Sheffield) on HF-digested powdered samples of 0.25 g. The spectrometer was calibrated with elemental standards between 1 and 25 mg L^{-1} (Spex Certiprep, Rickmansworth - UK), with typical accuracy within ±2% error of the measured value.

The mineralogy of the basaltic quarry fines was determined by the author using X-ray diffraction (XRD) analysis at the British Geological Survey (BGS) Keyworth laboratories. Samples were spiked with 10 wt.% corundum (Al_2O_3), micronised to aid quantitative analysis and spray-dried from an ethanol suspension at 80°C to ensure random orientation of mineral phases (Hillier, 1999). Measurements were conducted using a PANalytical X'Pert Pro diffractometer (Malvern Panalytical Ltd., Malvern, UK) equipped with Co-Kα radiation (λ = 1.78896 Å) and operated at 45 kV and 40 mA. Front-loaded powder mounts were scanned from 4.5–85°2θ at 2.06°2θ/minute. Crystalline mineral phases were identified using PANalytical HighScore Plus software (v. 4.8) coupled to the International Centre for Diffraction Data PDF-4+ database (International Centre for Diffraction Data (ICDD), 2019). Crystalline mineral and amorphous material quantification was completed using the Rietveld refinement technique within the same HighScore Plus software package using crystallographic information from the Inorganic Crystal Structure Database (Hellenbrandt, 2004; Inorganic Crystal Structure Database (ICSD), 2019) following the methodology in Kemp *et al.* (2016a).

2.2.1.1 Clay mineralogy

Fine fraction separations and further XRD analyses were conducted to definitively identify any clay minerals present and therefore aid the powder mount interpretations. The clay-sized (<2 μm) fractions were isolated by settling and dried following the protocol of Kemp *et al.* (2016b). The dried clay separates (*c.* 20 mg) were weighed into test tubes with *c.* 0.5 mL of deionised water and 2 drops of 0.1 M calcium chloride hexahydrate ($CaCl_2.6H_2O$) and ultrasonicated for 1 h to fully disperse the particles. The resulting suspensions were pipetted onto zero-background silicon crystal substrates to produce oriented mounts. The mounts were then slowly dried at room temperature to prevent cracking.

The clay separates were characterised by subjecting the oriented mounts to standard diagnostic tests and repeated XRD scans from 2° to 40°2θ at 1.02°2θ $minute^{-1}$: (1) after air-drying, (2) after overnight ethylene glycol (EG) solvation at 55°C (smectite identification), and (3) after heating to 550°C for 2 hours (kaolinite identification) (Moore and Reynolds, 1997). XRD traces were interpreted by comparison of sample peak *d*-spacings and relative intensities with standard values (Moore and Reynolds, 1997).

2.2.2 Scanning electron microscopy

Scanning electron microscopy (SEM) was used to assess the textural characteristics of the samples including morphology, sizes and the relative relationships between the different grains; chemical compositions were also determined. For this, the basalt particles were mounted in epoxy resin blocks and polished prior to analysis. Detailed mineralogical observations were made on both the polished blocks and on stub-mounted samples. The polished blocks were produced by Mr J Fletcher at the British Geological Survey. Both blocks and stubs were carbon coated to approximately 25 nm thickness in an Agar AGB7367A automatic SEM carbon evaporation coater, prior to analysis.

Image acquisition for both polished block and stub-mounted sample analysis was performed using a FEI QUANTA 600 SEM at the BGS laboratories, operating at an accelerating voltage of 20 kV. For polished block analysis, analysis took place using a beam current of 2.3 nA and under high vacuum conditions ($<1x10^{-4}$ Torr). Reduced beam currents of 0.081 and 0.31 nA were used for imaging the stub-mounted samples under high vacuum conditions with the exception of the Tichum basalt which frequently developed charge when imaged under high vacuum and was subsequently imaged in low vacuum mode. Energy Dispersive X-ray Spectroscopy (EDS) analysis was conducted using an Oxford Instruments X-MAX large area (50 mm^2) silicon drift detector (SDD), running with Oxford Instruments INCA (v4) software. The EDS system was used to identify and semi-quantitatively measure the elements (from atomic number 5 (B) to 92 (U)) at the selected point of interest with a detection limit of 0.2 to 0.5 wt.% for most elements. Images were obtained with secondary electron (SE) and backscatter electron (BSE) imaging techniques.

Minerals were identified from mineral form observations and EDS spectra. Minerals with solid solution chemistries (e.g. feldspar), containing appreciable trace elements (e.g. pyroxenes), or that were rare (e.g. titanite), were identified through comparison of measured elemental weight percentages to those of known minerals using Webmineral Element Composition Search (Webmineral, 2019).

Chemical data from point analyses were compiled into R (R Development Core Team, 2018) to compute the average composition of the different mineral types identified using SEM-EDS. The EDS analyses are considered semi-quantitative and as a result were normalised to ideal mineral formulae reported in the Handbook of Mineralogy (Anthony *et al.*, 1995). Elements with concentrations below 1% were discounted from the mineral formula calculation. Amorphous phases, interpreted as basaltic glass, were normalised to Si concentrations. The average measured mineral compositions obtained from SEM-EDS were used to select appropriate crystallographic information files for XRD

quantification from the Inorganic Crystal Structure Database (Hellenbrandt, 2004; Inorganic Crystal Structure Database (ICSD), 2019).

2.2.3 Particle size analysis

Particle size analysis was conducted so that geometric surface area could be calculated. Two methods were used: (1) mass fraction sieving on entire basalt samples, and (2) laser particle size analysis of a sieved <75 μm fraction. Mass fraction sieving was carried out to determine the distributions of larger particles (>75 μm) likely to be missed by laser particle size analysis due to rapid particle settling. Data from both methods were combined, with particles identified to be larger than 75 μm from laser particle size analysis discounted from the overall particle size distribution. Geometric specific surface area (SSA) was calculated as described in Kelland *et al.* (2020) (see Supplementary Information, Table S3 in Kelland *et al.* (2020)).

2.2.3.1. Mass fraction sieving

Representative sub-samples, between 30 and 40 g (18-20 g Blue Ridge), were produced by coning, quartering, and riffle-splitting. A smaller mass of the Blue Ridge metabasalt was used as its comparatively fine-grain size clogged the sieves. Samples were sieved through 4000, 2000, 1000, 500, 250, 180, 125 and 75 μm sieves using a Retsch AS200 sieve shaker for 5 min (2 × 5 minutes for the Blue Ridge to prevent clogging) and the mass of each size fraction recorded.

2.2.3.2. Laser particle size analysis

The <75 μm mass fraction was riffle split to produce a representative sample and particle size was determined using a Horiba LA950 Partica Laser Scattering Particle Size Analyser (Horiba UK Ltd, Northampton, UK). The samples were fully dispersed into suspension using 0.1 M sodium hexametaphosphate solution and ultra-sonication for 1 minute before measurement.

2.2.4 Basalt BET surface area analysis

The specific surface area of the samples was determined using N_2 adsorption and application of the BET isotherm (Brunauer, Emmett and Teller, 1938). For this, the samples were sieved to <4 mm prior to analysis to fit into the measurement tubes. The <4 mm fraction was split into *c.* 2.5 g subsamples using a riffle splitter. Subsamples were degassed overnight in a Micrometrics VacPrep 061 Sample Degas System at 60°C and *c.* 200 mTorr to remove residual water and gas. The sample weight after degassing was recorded and incorporated into surface area calculations. Surface area analyses were conducted using a Micromeritics Gemini VI 2385C system at the BGS laboratories, calibrated with a carbon black standard. The samples were run on a 10-adsorption pressure point program between 0.001 and 0.150 P P_0^{-1} with an equilibration time of 10 seconds. Three subsamples of each basalt were measured to assess sample variation by calculating standard error.

2.2.5. Thermogravimetric analysis (TGA)

TGA analyses were conducted by Mr S Kemp at the British Geological Survey. The analyses were carried out using a Mettler-Toledo TGA/SDTA851^e simultaneous thermal analysis system coupled to a Pfeiffer Vacuum ThermoStar mass spectrometer to identify and quantify carbonate minerals present in the basalts. Prior to commencing analyses, the TGA/SDTA system was calibrated using the specified Indium/Aluminium (In/Al) melting test. Zero runs were completed for empty 150 µL platinum crucibles.

For sample analysis, *c.*75 mg portions of each powdered sample were heated in 150 µL platinum crucibles through a ramped heating program of 30 to 500˚C at a heating rate of 50˚C minute^{-1}, followed by 500 to 1000˚C at 10˚C minute^{-1}, followed by an isotherm at 1000 ˚C for 10 minutes to ensure complete reaction. A gas flow of 40 mL minute^{-1} N_2 (99.998% pure, not oxygen-free) was maintained throughout. Analyses were controlled and TGA output traces were interpreted using the Mettler STAR^e software suite. The presence and

quantification of the different carbonate species was determined to a high resolution (*c.*100 ppm/0.01%) by comparison with empirically-derived standard weight losses and temperatures.

2.6. Reactive transport modelling

As stated at the end of the introduction, the modelling aimed to calculate: (1) the mass transfer rate of cations from the constituent minerals of the basalt to aqueous solution, (2) the resultant alkalinity release to solution and CDR potential during the initial 15 years of dissolution for each of the six basaltic quarry fines (Table 2.1), (3) the projected cumulative CDR after 30 years of basalt dissolution, and (4) P and K release over time via mineral dissolution. The long-term simulations were run for 30 years to account for rapidly weathering minerals dominating dissolution in the initial stages of reaction as well as a longer-term contribution from slower weathering minerals.

The model used in this chapter was originally published in Kelland *et al.* (2020). Modifications to the code used in this model were made by the author, following discussion with supervisors and other advisors. Most of the simulations were then ran on the ShARC supercomputer by Dr L Taylor. The model was developed with the PHREEQC (Parkhurst and Appelo, 2013) modelling code and a standard geochemical reaction database (Amm_T&H.dat) (Appelo and Postma, 2004). This choice of geochemical reaction database was different to the one used in Kelland *et al.* (2020). In Kelland *et al.* (2020), the T_H.dat (Appelo and Postma, 2013) was used because it incorporates the wateq4f.dat database which is frequently used in PHREEQC modelling with complexation constants for metals binding with particulate organic matter and humate/fulvate species. The database used in this chapter (Amm_T-H.dat) also decoupled the NO_3/NH_4. While studying the changes to nitrogen speciation in soil solutions was not an important component of this thesis, it does more accurately replicate nitrogen in agricultural soil solutions and subsequent processes.

The model parameters were based on the properties of a UK clay loam agricultural soil, described fully in Kelland *et al.* (2020). The clay-loam soil parameterised RTM was used to simulate 1-D vertical flow and transport, and release of cations from the reactions between basalt and soil solution in a 50 cm deep soil profile, represented as ten 5 cm deep computational cells. Basalt was added in the top 25 cm of the profile to simulate the plough layer mixing depth used in the mesocosms set up in Kelland *et al.* (2020) from which this model was initially designed. The 1-D RTM simulates the dissolution of powdered basalt in the top five soil cells (25 cm) equivalent to a field application of 50 tonnes ha^{-1} at 25°C in an initial mildly acidic soil solution. The pH of the soil solution was modified in this chapter from the measured leachate that was used in Kelland *et al.* (2020) to the measured soil pH cited in Kelland *et al.* (2020) of pH 6.6. Soil pH was chosen instead of leachate pH because it was thought to be more realistic of the porewater conditions that the basalt grains would have been exposed to. The background soil solution is assumed to reflect the background weathering of soil minerals in the absence of basalt amendment (background soil solution can be found in Table A1), and is also equilibrated with the average annual CO_2 pore gas partial pressure observed at each soil depth in rain-fed maize fields (Nan *et al.*, 2016). The soil profile was assigned an average net infiltration rate of 763 mm yr^{-1} with water filled porosity of 0.2, both of which were determined experimentally in Kelland *et al.* (2020). At each time step (4.9 days), the soil column was replenished with fresh soil solution, of the initial soil pore water composition, which entered at the column surface. This flow rate was calculated from irrigation-leachate data over the growth period of the sorghum crop in Kelland *et al.* (2020). The biogeochemical sinks for the elements released during weathering are: (1) sorption to solid phases (e.g. cation exchange capacity of clay; sorption to organic matter and to hydrous ferric oxide), (2) reversible precipitation-dissolution of the secondary mineral phases amorphous $Al(OH)_3$, SiO_2 and $Fe(OH)_3$, and (3) the annual uptake of elements (120 days per year) by the sorghum crop. All of these processes were inputted via standard PHREEQC code commands. The sorption of elements to solid phases were implemented in the

model using the EXCHANGE block (for inorganic exchange) and SURFACE (for exchange onto organic matter and hydrous ferric oxide). EQUILIBRIUM_PHASES was used simulate the precipitation of secondary phases The uptake of elements by the sorghum crop was implemented as a kinetic phase, via the RATES and KINETICS blocks.

The proportions of minerals and amorphous material (glass) present in the basalts were determined from normative calculations based on XRD measurements on basalt powder and elemental composition of rock grains based on SEM-EDS analyses, together with TGA determination of the traces of calcite identified in the basalts. No basaltic glass was identified in the SEM-EDS analysis of the Cragmill basalt. Therefore, the chemical formula for basaltic glass was taken from Oelkers and Gislason (2001) for this basalt. The chemical kinetic rates of irreversible mineral dissolution were calculated using the generalised rate law for water and acid- and base-catalysed reactions (Eq. 1.3) and the corresponding rate constants taken from the compilation of Palandri and Kharaka (2004) with the exception of basaltic glass. Given the effect of sulphate on Al speciation, and sulphate concentration in the background soil porewater (50.78 μM L^{-1}, Table A1) and for consistency with the model used in Kelland *et al.* (2020), dissolution rate constants were taken from Flaathen *et al.* (2010) which built upon the rate constants originally developed by Oelkers and Gislason (2001). The reaction of soil pore fluids with calcite was calculated as thermodynamic mineral solubility equilibria (i.e. using EQUILIBRIUM_PHASES), as calcite has the potential to react reversibly with the soil solution on timescales considered in this model unlike silicate minerals. The reacting surface area of all kinetic mineral phases was assigned proportionally to their relative abundance in each basalt, however, as an equilibrium phase no reacting surface area term could be attributed to calcite. The measured SSAs (from N_2-BET measurements) were used in these simulations, as well as a range of standardised SSAs (i.e. basalt dissolution was modelled using the same surface area for each basalt) from 0.1-10 $m^2 g^{-1}$. These standardised surface areas range from the upper-limit of calculated geometric

surface areas, calculated from particle size distributions, to the upper BET surface areas that were determined in this chapter.

At the time of writing this chapter, there were no published dissolution rate laws for the mineral phases titanite, epistilbite, analcime and spinel. However, these minerals contribute only trace quantities of Ca and Mg to the mineral chemical composition of the basalts. Equilibrium constants used to calculate the saturation ratios (SR in Eq. 1.3) were sourced from the THERMODDEM database (Blanc *et al.*, 2012) with the exception of those for labradorite and augite, which were taken from Taylor *et al.* (2015), and the basaltic glass equilibrium constants which were taken from Aradóttir *et al.* (2012).

CDR via ERW of crushed basalt applied to soils occurs from alkalinity production as CO_2 released by soil biota respiration dissolves in pore fluids to form carbonic acid. The pore fluids then percolate through the soil and react with silicate minerals to release cations (Ca^{2+}, Mg^{2+}, Na^{+}, K^{+}) with concomitant increase in alkalinity, as described in Eq. 1.1. Transfer of the increased load of cations and alkalinity produced from ERW to the oceans via surface runoff and river transport results in increased marine CDR. Ocean chemistry reduces the CO_2 removal efficiency (η) via this pathway. Based on average ocean temperature (17°C), salinity (35%) and dissolved pCO_2 of 400 μatm, η is calculated to equal 0.86, to give 1.72 moles of CO_2 removed per mole of divalent cation added to the ocean (Renforth and Henderson, 2017). The CDR was calculated from the generation of cations in the ERW simulations and removal efficiency, as follows (Eq. 2.1):

$$CDR = \eta \cdot \sum (mol\ monovalent\ cations)$$

$$+2\eta \cdot \sum (mol\ divalent\ cations) \quad \text{(Eq. 2.1)}$$

The model also simulated the dissolution of carbonate phases contained within the basalt rock and precipitation of carbonate minerals in the soil and

leachate (Eq. 1.2) and their effects on CDR. However, on the time scales of the simulations in this chapter (15 years), there was no net precipitation of carbonate in the soil system.

Possible outgassing of CO_2 during stream water transport (if it occurs) is not considered. However, it would not reduce alkalinity because it does not add or remove any acid. Thus, unless acid is added to the streams, alkalinity will remain conserved while being transported to the marine environment where it ultimately contributes to long-term (*c.* 100,000 year timescale) CDR (Renforth and Henderson, 2017). Carbonate precipitation/dissolution during groundwater transport of weathered products to receiving streams is related to residence time of waters draining arable land, and the presence of carbonate precipitation inhibitors, such as soluble reactive phosphate, suspended material, and dissolved organic matter (Neal, 2002). Furthermore, the production of low-molecular-weight organic acids by microbes and root systems could inhibit mineral weathering reactions (Fakhraei and Driscoll, 2015), thus potentially reducing CDR (Taylor *et al.*, 2021). Consideration of these aspects of the carbonate system is beyond the scope of the present 1-D RTM modelling. Accessory calcite present in the basalts was treated in the same way (Table 2.3), and its influence on CDR potential was subtracted from the results retrospectively (see Table 2.5).

The release of P and K were simulated using mineral dissolution fluxes from the model output to calculate the cumulative release of P and K over time. The mass transfer of P within the relatively more rapidly dissolving accessory mineral apatite (Palandri and Kharaka, 2004) (identified using XRD, Figure 2.2) was calculated from the amount of apatite within the rock and multiplying that by the proportion of bulk minerals which had dissolved during each time step. The calculation used to determine P release is summed up in Eq. 2.2.

$$P_{(i)} = TMW_{(i)} * \%apatite \qquad \text{(Eq. 2.2)}$$

Where $P_{(i)}$ is the phosphorus released at time step *i*, the $TMW_{(i)}$ is the total mineral weathering from time = 0 until time step *i*, and the %apatite is the wt.% apatite as determined from XRD.

K release was calculated from data on the dissolution of K-bearing minerals in the model at each time step. The release of K was calculated at each time step by identifying the amount of a K-bearing mineral that dissolved from the model (outputted directly from the model), and then multiplying it by the amount of K which a K-bearing mineral contained based on mineral chemical compositions determined via SEM-EDS analysis (Table A2).

2.3. Results

2.3.1. Rock type classifications

The chemistry and mineralogy of the basalts from the six sites (Table 2.1) were compared using Total Alkaline Silica (TAS) (le Bas *et al.*, 1986) and Quartz, Alkali feldspars, Plagioclase feldspars and Feldspathoid (QAPF) (Streckeisen, 1974) plots (Figure 2.1a and b respectively). Comparisons with both TAS and QAPF classifications confirm that the basalts are generally typical of Large Igneous Provinces (LIPs) (25 locations, of 1354 data points) which host large (>1000 km^3) amounts of basalt (Bryan *et al.*, 2010). According to the TAS classification, Cragmill and Hillhouse are basalts, Oregon and Tichum are basanites and Tawau is a basaltic andesite (Figure 2.1a). Under the QAPF scheme, the diverse mineralogy of the six basalts result in Hillhouse and Cragmill being classed as basalt/andesite and Tichum, Oregon and Tawau classed as phonolitic tephrite, latite and dacite, respectively (Figure 2.1b). The high silica and quartz concentrations of Tawau (Figure 2.1a, 2.1b) is typical of its island-arc origin (Table 1). The Blue Ridge metabasalt (Table 2.1) represents a chlorite-actinolite metabasalt and is unsuitable for both the TAS and QAPF classifications (Robertson, 1999).

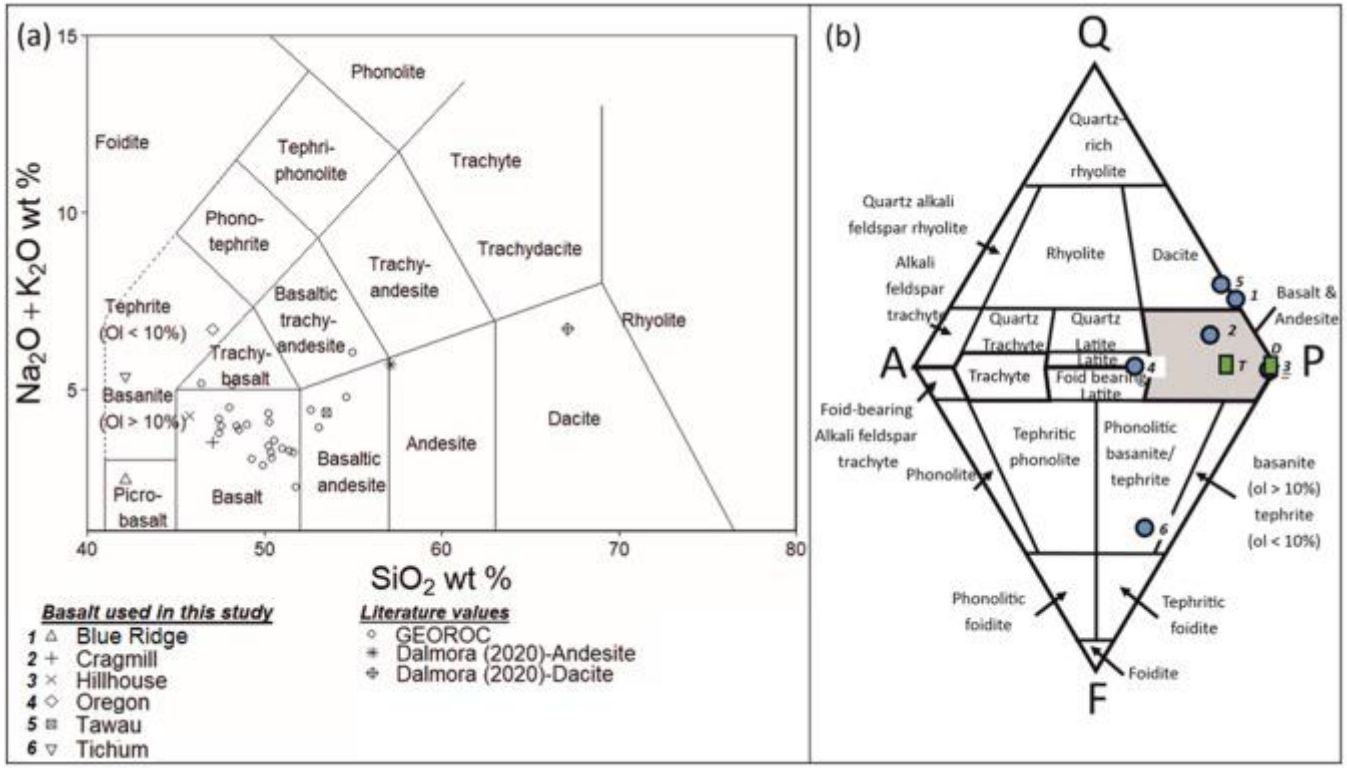

Figure 2.1 – Total Alkaline Silica (TAS) (a) and Quartz Alkali Plagioclase Feldspathoid (QAPF) (b) classifications of the six basaltic quarry fines studied. Circles in Figure 2.1a denote average alkaline ($Na_2O + K_2O$ wt.%) and SiO_2 wt.% data collated from continental flood basalts and large igneous provinces (n = 25) from the GEOROC database (Sarbas, 2008). In Figure 2.1b, numbers for each basalt are shown in the legend of Figure 2.1a, with the exception of T and D (position marked with green squares) which correspond to basalt used in model simulations in Taylor *et al.* (2016) and dissolution experiments in Dontsova *et al.* (2014) respectively.

2.3.2. Mineralogical analyses

The detailed mineralogy of the six basalts and chemical composition of minerals derived from SEM-EDS analyses are summarised in Figure 2.2 and Table A2 respectively. Basalts produced through crustal extension have a higher proportion of faster weathering minerals (including olivine, augite and plagioclase; Tichum, Hillhouse, Cragmill and Oregon, between 46.7 and 82.0 wt.%, Table 2.2) when compared to those produced at convergent margins (e.g. Tawau) which contain a significant proportion of slower weathering minerals (quartz and hydrothermal clay minerals (e.g. smectite (saponite), 24.9 wt.% slow weathering minerals, Table 2.2)). Relative to the other basalts, the Blue Ridge metabasalt has a smaller proportion of fast weathering minerals (11.6 wt.%, Table 2.2).

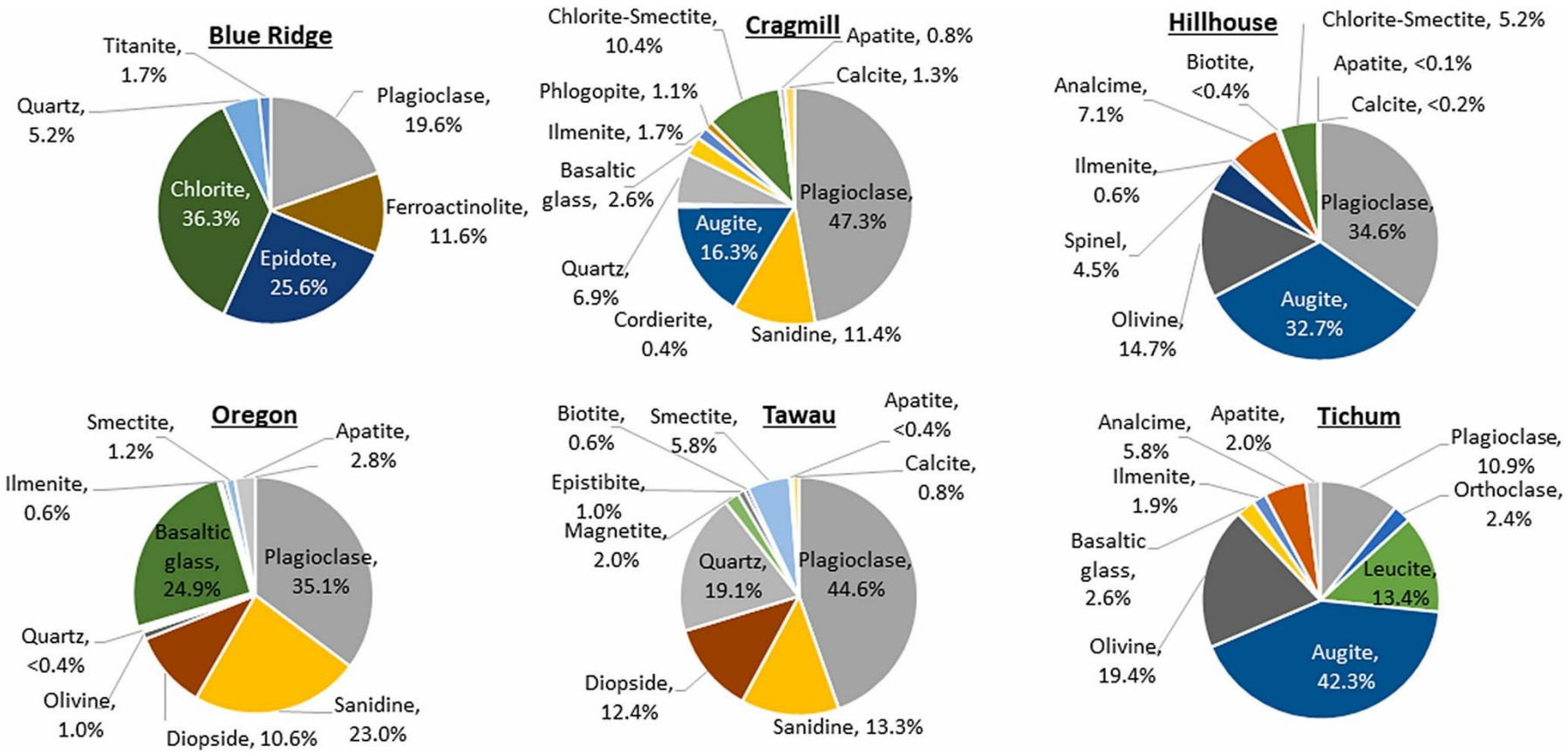

Figure 2.2 – Mineralogy of basalts studied as determined by XRD analysis. Analyses are given in wt.%. For clarity, plagioclase minerals are not differentiated in these pie charts, but chemical analyses (Table A2) identify albite in the Blue Ridge; labradorite in the Cragmill, Hillhouse and Tawau; andesine in the Oregon and Tichum.

Table 2.2 – Rate constants of the minerals identified in the basalts, and the relative proportions of fast, medium and slow weathering silicate minerals. Rate constants are taken from Palandri and Kharaka (2004). BR = Blue Ridge; C = Cragmill; HH = Hillhouse; O = Oregon; Ti = Tichum; Ta = Tawau.

Reactivity grouping (from rate constants)	Mineral	Rate constant, A, H^+	Rate constant, A, H_2O	Relative proportion of 'mineral reactivity' groupings (based on rate constants), %					
Silicate minerals				**BR**	**C**	**HH**	**O**	**Ti**	**Ta**
Fast				11.6	66.6	82.0	70.6	86.1	57.0
	Plagioclase (Ca/Na rich)								
	- Labradorite[a]	-7.87	-11.47						
	- Andesine[a]	-8.88-10.16	-10.91						
	Ferroactinolite	-8.40	-10.6						
	Leucite	-6.00	-9.20						
	Diopside	-6.36	-11.11						
	Augite	-6.82	-11.97						
	Olivine	-6.85	-10.64						
	Basaltic glass	-3.30	-11.85						
	Cordierite	-3.80	-11.20						
Medium				81.5	11.4	-	23.0	2.4	13.3
	Plagioclase (Na-rich)								
	- Albite[b]	-10.16	-12.56						
	Epidote	-10.60	-11.99						
	Clinochlore	-11.11	-12.52						
	Sanidine	-10.06	-12.41						
	Orthoclase	-10.06	-12.41						
Slow				5.2	17.3	5.2	1.6	-	24.9
	Quartz	-13.99	-16.29						
	Chlorite-Smectite	-12.71[b]	-14.41[b]						
	Smectite	-12.71	-14.41						
	Kaolinite	-11.31	-13.18						
Unknown				-	-	11.5	-	5.8	1.0
	Analcime	NA[c]	NA[c]						
	Epistibite	NA[c]	NA[c]						
	Spinel	NA[c]	NA[c]						
Other minerals/ trace silicates									
Fast	Calcite	-0.30	-5.81						
	Apatite	-3.73	-8.00						
	Ilmenite	-8.35	-11.16						
	Hematite	-9.39	-14.60						
	Magnetite	-8.59	-10.78						
Medium	Biotite	-9.84	-12.55						
Unknown	Titanite	NA[c]	NA[c]						
	Phlogopite	NA[c]	-12.40						

[a] Mineralogical analyses identify the plagioclase feldspars as: albite in the Blue Ridge; labradorite in the Cragmill, Hillhouse and Tawau; andesine in the Oregon and Tichum.
[b] Assuming dissolution rate constant of montmorillonite.
[c] The author is not aware of dissolution rate data for these minerals.

The relatively fast weathering minerals, Ca/Na-plagioclase and pyroxene, occur in all samples except the Blue Ridge metabasalt (Figure 2.1), with abundances varying by a factor of 4–5. Ca/Na-plagioclase in these basaltic quarry

fines was present as labradorite and andesine (Table A2). The fast-weathering silica-poor feldspathoid, leucite, was present in high concentrations (13.4 wt.%, Figure 2.2) in the Tichum basalt. Leucite has a significantly higher weathering rate than feldspars (Tole *et al.*, 1986; Palandri and Kharaka, 2004). Olivine, another fast weathering mineral commonly found in basaltic rocks, varied between 1.0 wt.%. and 19.4 wt.% in the Oregon, Hillhouse and Tichum basalts. An XRD-identified amorphous phase, interpreted as fast-weathering basaltic glass from back-scattered electron imaging observations, contributes 24.9 wt.% to the Oregon basalt (Kelland *et al.*, 2020). Fast weathering actinolite (also referred to as ferroactinolite), converted from pyroxene during metamorphic reactions (Fyfe, Turner and Verhoogen, 1959) was identified in the Blue Ridge metabasalt at 11.6 wt.%.

Several medium weathering-rate minerals, formed during metamorphic reactions that convert pyroxenes to epidote and chlorite (Fyfe, Turner and Verhoogen, 1959), are present in the Blue Ridge metabasalt. Additionally, plagioclase was present in the Blue Ridge metabasalt as Na-plagioclase, which dissolves *c.* 2 orders of magnitude slower than the Ca/Na-rich plagioclase minerals observed in all other basaltic quarry fines identified in this study. Slower-dissolving K-feldspars, orthoclase and sanidine, vary in abundance between 2.3 wt.% and 23 wt.% in Tichum, Tawau, Cragmill, and Oregon, but are lacking in the Blue Ridge metabasalt and Hillhouse basalt. Slow weathering quartz and several secondary minerals were identified in the studied basaltic quarry fines. Quartz was present in the Tawau (19.1 wt.%), Cragmill (8.4 wt.%) and Blue Ridge (5.2 wt.%) basalts. Secondary minerals, such as clays and zeolites, are present in all the samples apart from the Blue Ridge metabasalt. The Cragmill and Hillhouse basalts contain clinochlore (a chlorite group mineral) associated with pyroxene and olivine alteration (Figure A1 and A2). Saponite (an Fe-Mg smectite, 5.8 wt.%) was identified in the Tawau basalt by both XRD and SEM-EDS. Iron oxides identified by XRD as either ilmenite-hematite (Tichum, 1.9 wt.%; Cragmill, 1.6 wt.%; Hillhouse, 0.6 wt.%; Oregon, 0.6 wt.%) or magnetite (Tawau, 2.0 wt.%) were present in most basalts. SEM-EDS analyses also indicate the presence of an iron oxide phase in the Blue Ridge metabasalt. The Ca-Ti-silicate titanite ($CaTiSiO_5$) comprises 2.0 wt.% of the Blue Ridge

metabasalt, as confirmed by earlier analysis (USGS, 2019). TGA analysis identified 0.173-1.249 wt.% calcite in all six basalts (Table 2.3).

Table 2.3– Calcite concentrations derived from thermogravimetric analysis (TGA).

Basalt	Calcite (wt.%)
Blue Ridge	0.540
Cragmill	1.249
Hillhouse	0.195
Oregon	0.173
Tawau	0.642
Tichum	0.223

During mineral dissolution, elements important for plant nutrition including phosphorus (P) and potassium (K) are released into the soil solution (Beerling *et al.*, 2018; Pratt *et al.*, 2020). Apatite, the mineral source of P in the basalts used in this chapter, is identified in all basaltic quarry fines with the exception of the Blue Ridge metabasalt, with concentrations varying 28-fold between 0.1 and 2.8 wt.%. The essential nutrient K is hosted in K-feldspar (Oregon, Cragmill, Tichum and Tawau), biotite (Hillhouse and Tawau), phlogopite (Cragmill) and leucite (Tichum). The abundance of K bearing minerals varied by two orders of magnitude from 0.6 to 35.1 wt.%.

2.3.3. Particle sizes, surface area and clay minerals

Measured particle size distributions (Figure 2.3) were used to calculate *p*80 values, i.e. the mesh size through which 80% of particles will pass. These varied by a factor of 10 between the six basalt samples. This wide range reflects differences in the mining and screening (sieving) processes (Table 2.1) that each quarry site uses to produce the basalt used in this chapter. The *p*80 values for the Oregon basalt and Blue Ridge metabasalt were smallest because they were passed through finer sieves during production (1.18 and 1.34 mm respectively) compared to the 4–5 mm sieves used for processing the other basalts (Table 2.1).

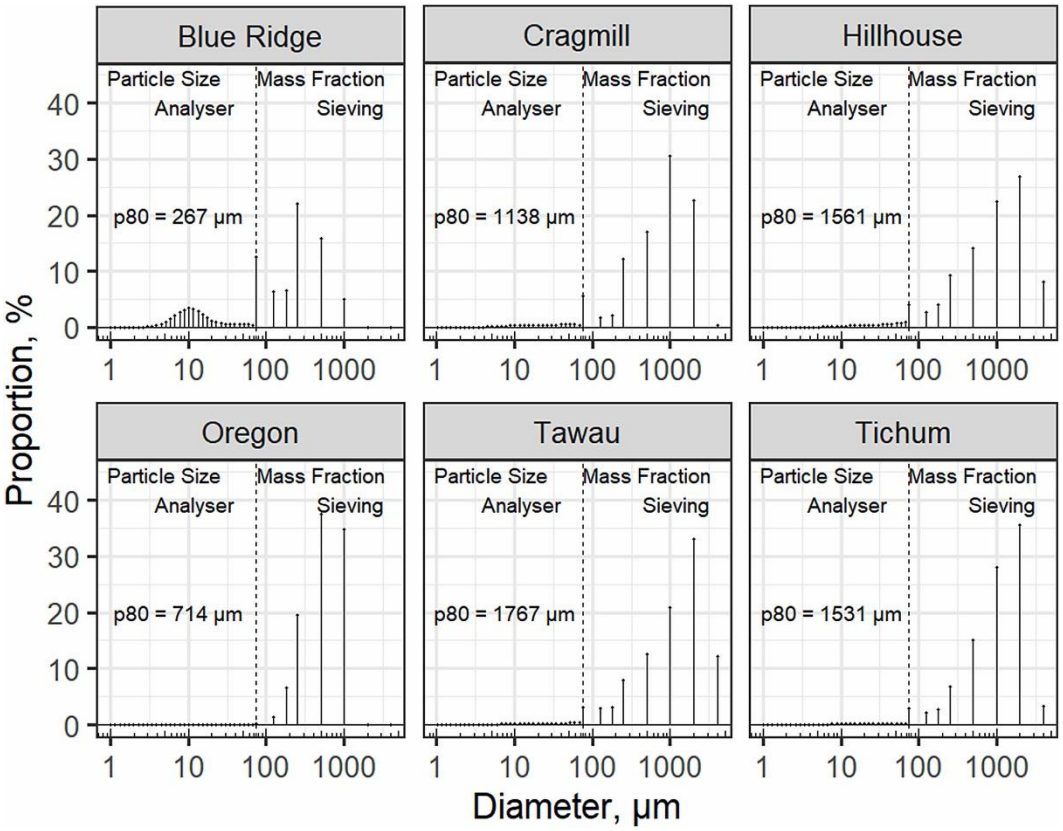

Figure 2.3 – Basalt particle size distributions, as determined with a particle analyser (<75 µm) ($n \geq 5$ samples per basalt) and from mass fraction sieving (>75 µm) ($n = 4$ samples per basalt). Analysis from the particle size analyser provides the proportion of total concentration of particles, while mass fraction sieving provides the proportion of the total weight. The cumulative density functions for each basalt, from which the *p*80 was determined, are given in the Figure A3.

BET SSA (Table 2.4) values generally fall within the range of those reported for commercially available basaltic quarry fines (4.8–10 $m^2 g^{-1}$) (Rigopoulos *et al.*, 2016; Ponce-Lira *et al.*, 2017; Dalmora *et al.*, 2020a). These basalts included dolerite mined from the Troodos ophiolite in Cyprus (8.4 $m^2 g^{-1}$) (Rigopoulos *et al.*, 2016), macro-porous basaltic tephra from Mexico (9.6 $m^2 g^{-1}$) (Ponce-Lira *et al.*, 2017), and dacite (4.9 $m^2 g^{-1}$) and andesite (10 $m^2 g^{-1}$) from Brazil (Dalmora *et al.* 2020a).

Table 2.4 – Whole rock specific surface areas (SSA) as determined by N_2-adsorption and the BET isotherm (BET SSA) (± standard error), mean particle sizes (Geometric SSA) and surface roughness.

Sample	BET SSA, m^2g^{-1}	Geometric SSA, m^2g^{-1}	Surface Roughness, λ
Blue Ridge	1.02 ± 0.014	0.077	13.21
Cragmill	1.01 ± 0.052	0.018	55.84
Hillhouse	1.39 ± 0.072	0.015	92.85
Oregon	14.54 ± 0.29	0.006	2423.23
Tawau	2.73 ± 0.057	0.011	248.76
Tichum	10.30 ± 0.396	0.01	1029.83

Clay-sized particles (<2 μm), which comprise a relatively small proportion of each basalt, are likely important controls on the BET SSA. Secondary clay minerals typically have high relative surface areas compared to primary minerals (Brantley and Mellott, 2000; Dogan *et al.*, 2006; Sakizci, 2016), due to their small particle sizes and the accessibility of interlayers and pores to the nitrogen molecules used in the measurements. A small proportion (<0.08%) of clay-sized particles were identified in the basalts through laser particle size analysis. XRD traces of clay-sized separates variously detected chlorite, kaolinite, illite and smectite in the basalts (Figure 2.4). The broad peak widths of the smectite basal spacings, particularly shown on the Oregon and Tichum basalt diffraction traces, are indicative of relatively small crystallites (e.g. Moore and Reynolds, 1997) which contribute to their high BET values (14.5 m^2 g^{-1} and 10.3 m^2 g^{-1}, respectively). XRD traces of these basalts also show a very broad background curvature between *c.* 25–40°2θ (Figure 2.4) indicative of amorphous silicate material with smaller, short range-ordered crystallites with high surface area.

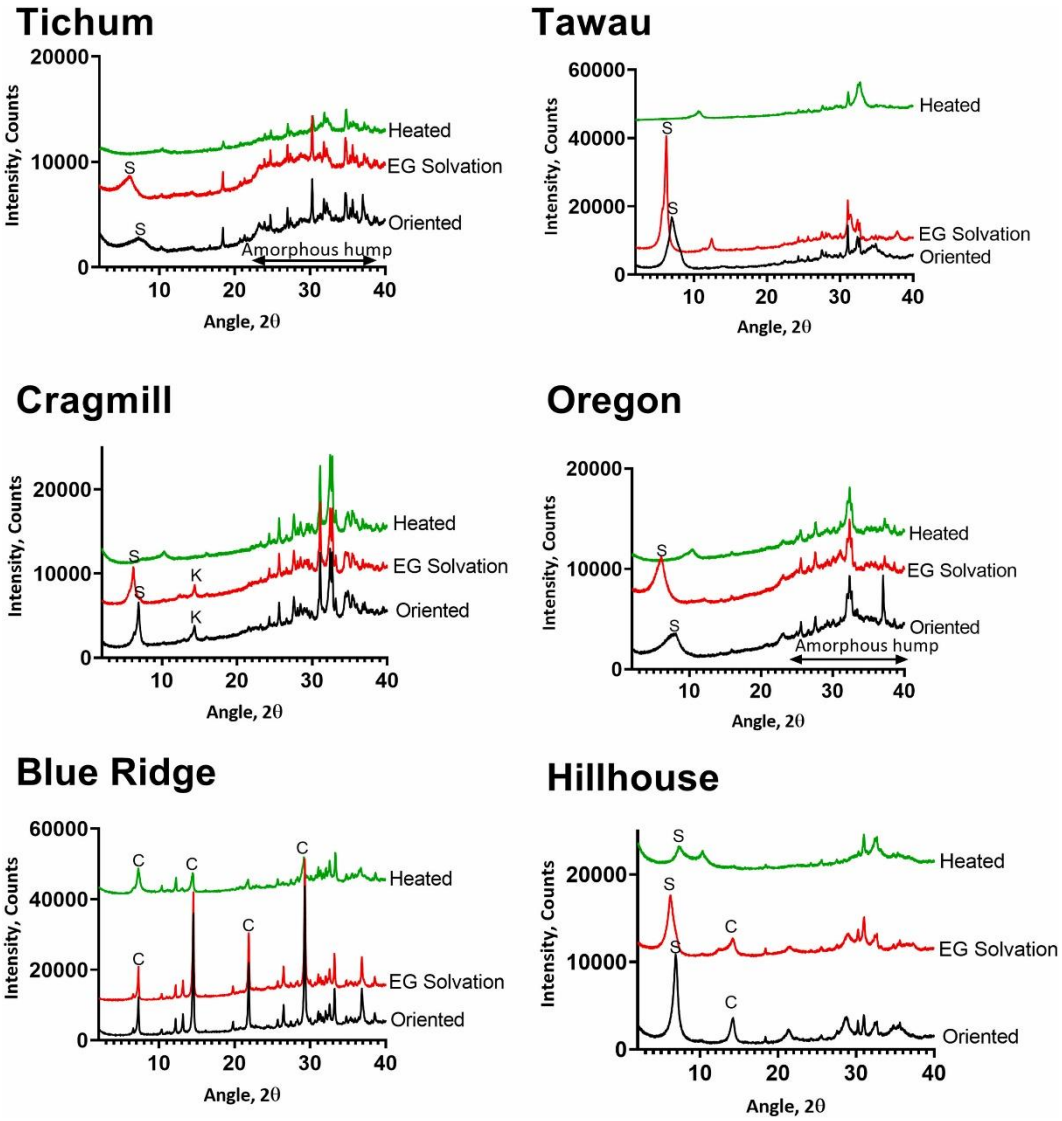

Figure 2.4 – XRD traces for the clay-sized fraction (<2 μm) of each basalt. Diagnostic clay mineral peaks are labelled: S; smectite, C; chlorite'; K; kaolinite, I; illite. EG = ethylene glycol.

SEM micrographs of representative rock fragments of all six basalts (Figure 2.5) show that grain surfaces in the Tichum and Oregon basalts exhibit cracks, the walls of which will contribute to the higher BET surface areas (Figure 5a and 5b). In contrast, the Blue Ridge and Cragmill basalts (Figure 2.5c and 2.5d) have relatively smooth grains. SEM imaging also revealed fine particles adhering to the surface of larger grains of all six basalts, with high concentrations of fine particles observed in the Hillhouse basalt (Figure 2.5e) and along planar structures in the Tawau basalt (Figure 2.5f). These fine particles (<1 μm diameter) may play a role in BET SSA differences, though their abundance cannot be accurately quantified using the laser particle size analysis because of their small diameter.

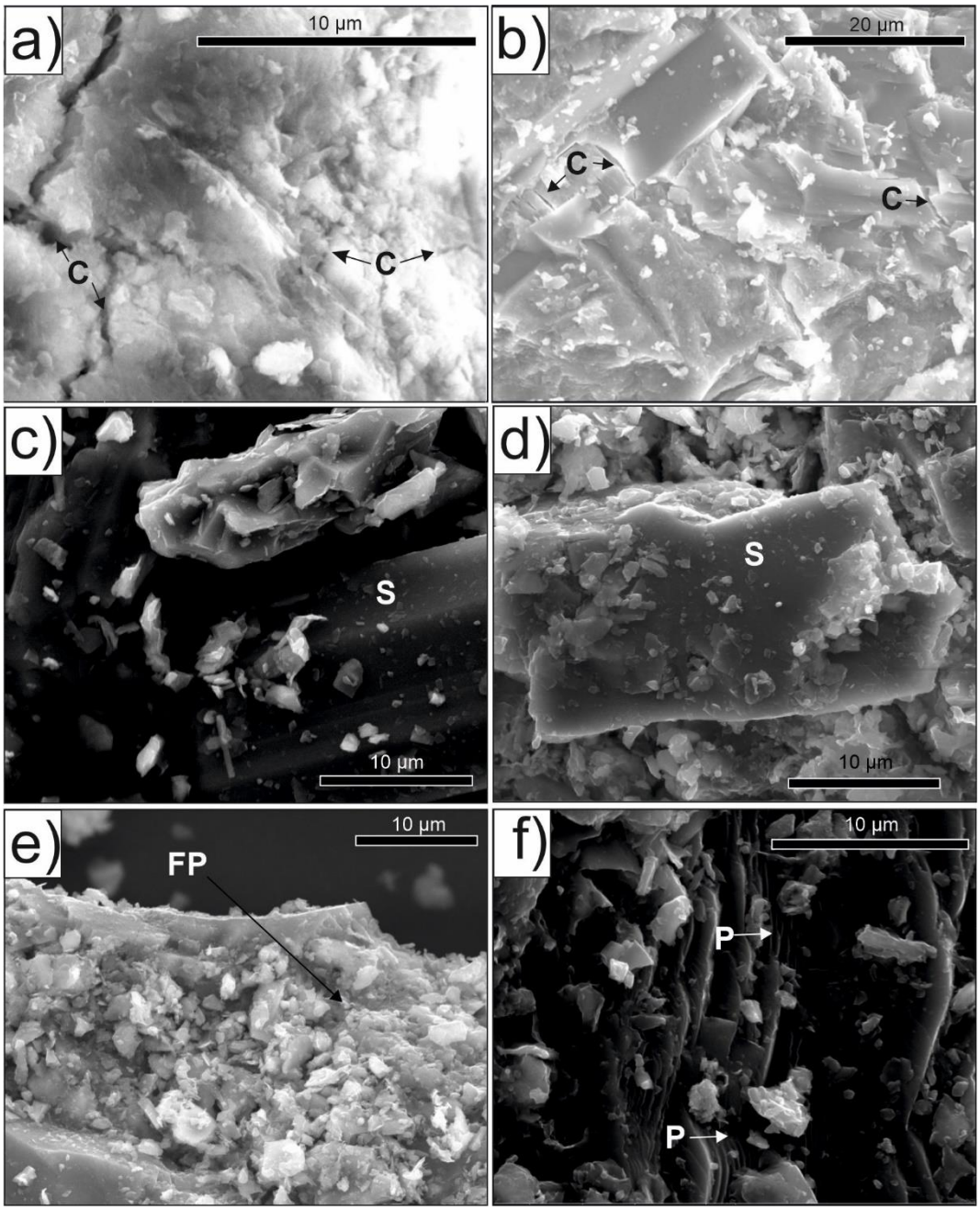

Figure 2.5 – Secondary Electron Micrographs of basaltic quarry fines used in this chapter. Cracks (denoted C) are shown in grains from the Tichum and Oregon basalts (Figure 2.5a, b respectively), compared to relatively smooth grains (denoted S) observed in the Blue Ridge and Cragmill basalts (Figure 2.5c, d respectively). High concentrations of fine particles (denoted FP) are observed in the Hillhouse basalt (Figure 2.5e) and planar structures (denoted P) in the Tawau basalt (Figure 2.5f).

The surface roughness (λ) for the six basalts is presented in Table 2.3. The surface roughness was calculated by dividing the measured BET SSA (S) by the geometric SSA (s) values. The geometric SSA values were calculated from the particle size data (Figure 2.3) using the equations developed in Kelland *et al.* (2020) (see Table S3 of Kelland *et al.* (2020)).

Surface roughness values can vary because of differences in the actual shape of particles, grain topography, grain cracking (Lee and Parsons, 1995; Hodson, Lee and Parsons, 1997; Hodson, 1998), the presence of fine (<1 μm) particles, and porosity effects. The surface area that is available to potentially react with aqueous solutions increases with surface roughness with, in theory, a proportional increase in dissolution rate. The λ of the six basalts varied by two-orders of magnitude between 13 (Blue Ridge) and 2423 (Oregon) (Table 2.3). The Oregon and Tichum basalts had the highest BET values due to the presence of smaller crystallites (Figure 2.4) and disrupted surface topography (Figure 2.5); they also had the highest λ values. In general, λ values are comparable in magnitude to literature values, e.g. basaltic glass powder with a diameter of 45–125 μm had a λ of *c.* 6-206 after ultrasonic cleaning to remove fine particles (Wolff-Boenisch *et al.*, 2004).

2.4. Discussion

2.4.1. RTM simulated CDR from basalts

The potential CDRs of different basalts used for ERW in relation to mineralogy and surface areas with the same agricultural clay-loam soil; a common soil type in Europe and North America. The author recognises that different soil types will likely give different responses and that results should therefore be considered illustrative and comparative between the basalts used in this study. However, they allow for comparison between the CDR potential of each characterised basalt and to assess the relative importance of both mineralogy and surface area for ERW.

RTM simulations are presented assuming the formation of amorphous $Al(OH)_3$, as the secondary mineral sink for Al. This results in higher solution Al

concentrations, and little basaltic glass dissolution. Assuming gibbsite formation, as the sink for Al, greatly reduces solution Al concentration, and leads to higher basaltic glass dissolution as the rate law for basaltic glass dissolution incorporates the ion activity of aqueous Al^{3+}. Whilst gibbsite can be found in utisols, inceptisols and andisols it is more common as a detectable phase in highly weathered tropical soils and tends to form in Si-poor environments once Si is separated from Al (Huang *et al.*, 2002). Consequently, amorphous Al hydroxide was used in these simulations as a baseline case. The CDR and weathering of minerals when gibbsite was used as an Al sink can be found in the Figures A4, A5.

Calculated CDR potential from our 1-D RTM simulations over 15 years of basalt dissolution following a single application varied widely between 1.3 – 8.5 t CO_2 ha^{-1} for the basaltic quarry fines produced by commercial quarries (i.e. using the mineralogy and BET SSA of each of the respective basalts) (Figure 2.6a). As expected, the two basalts with the highest CDR potential after 15 years of weathering (Figure 2.6a, Hillhouse and Tichum) contained the highest proportion of fast-weathering minerals; olivine, augite and lecuite (Figure 2.2, Figure 2.7a and b; Table 2.2 and Table 2.5). Diopside, another pyroxene-group mineral, dissolves most rapidly in the Tawau and Oregon basalts (Figure 2.7a and b), and is also present, but in smaller quantities than augite, in the Hillhouse and Tichum basalts (Figure 2.2). Actinolite dissolves most rapidly of the metamorphic minerals in the Blue Ridge metabasalt (Figure 2.7a and b).

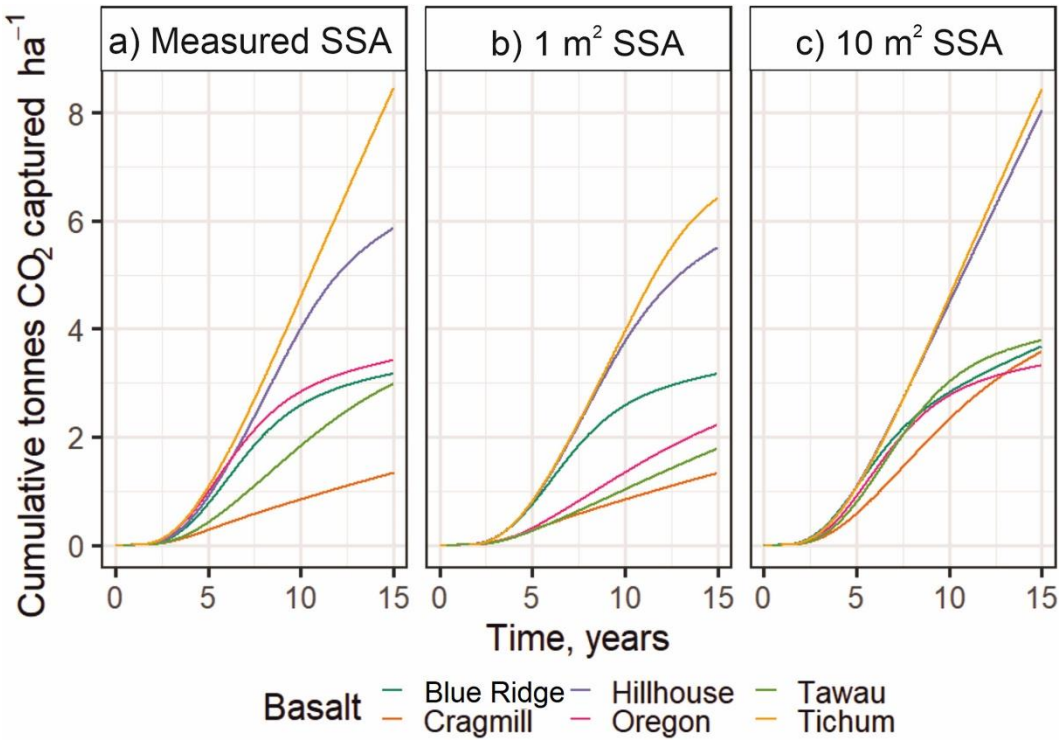

Figure 2.6 – Cumulative carbon dioxide removal (CDR) after weathering each material over a fifteen-year period under (a) measured specific surface area (SSA) (from BET analyses), (b) a standardised SSA of 1 m^2 g^{-1} and (c) a standardised SSA of 10 m^2 g^{-1}. These results do not account for reduced CDR from calcite weathering (Table 2.3). Potential reductions in CDR are given in Table 2.5.

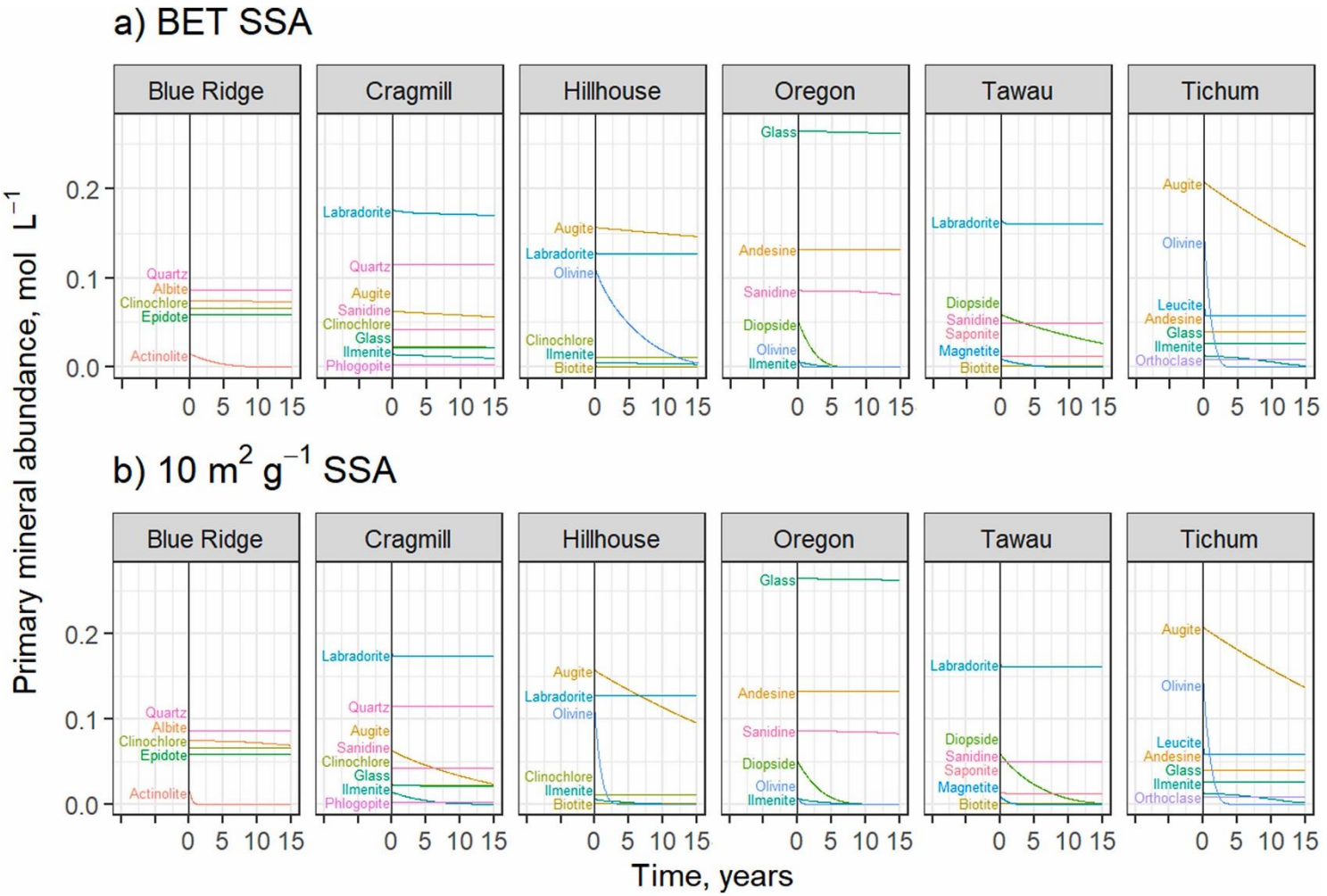

Figure 2.7 – Modelled mineral concentration of the basalts over time using the (a) measured BET specific surface area (SSA) regime and (b) 10 m^2g^{-1} SSA. The y axis shows the moles of each mineral phase per unit volume of reacting solution in the soil cells containing basalt with the initial value calculated from XRD analysis. The profiles for smectite (Oregon) and quartz Tawau and Oregon) were removed from this figure to make the image and labelling clearer and are shown in Figure A6. These minerals were unreactive under the conditions used in this model.

Table 2.5– Comparison and ranking of the carbon dioxide removal (CDR) and agronomic value of each basalt. The RTM results used measured BET surface areas in the simulations. Agronomic value indicates the % cost saving per ha resulting from P and K release from the first year of ERW and complimentary reductions to average UK spring wheat P and K fertiliser application of 14.8 and 36.4 kg ha^{-1} respectively predicted.

	CDR value				**Agronomic value**	
Material	Short term (15 yr) CDR				P-fertiliser substitution	K-fertiliser substitution
	Value – total cation flux from column, t CO_2 ha^{-1}	Value – subtracting CDR from calcite in column, t CO_2 ha^{-1}	Rank	Proportion of fast weathering minerals, %	% ha^{-1}	% ha^{-1}
Tichum Creek	8.5	8.5	1	86.1%	>100%	>100%
Hillhouse	5.9	5.9	2	82.0%	56%	44%
Oregon	3.4	3.4	3	70.6%	>100%	24%
Blue Ridge	3.2	3.1	4	11.6%	0%	0%
Tawau	3.0	2.9	5	57.0%	66%	1%
Cragmill	1.4	1.1	6	66.6%	26%	2%

Increasing the surface area in the 1-D RTM of the basalts with measured lower surface areas (i.e., Blue Ridge, Cragmill, Hillhouse and Tawau) to 10 m^2 g^{-1} (as might be achieved by additional milling for example), increased the potential CDR three-fold after fifteen years (Figure 2.6c), despite surface area increasing by a factor of 4-10. These results suggest that for some basalts, mineralogy and mineral chemistry limit the maximum CDR attainable over short time scales rather than surface area (Table 2.5). Thus, increasing the surface area for slow-weathering basalts (e.g. through energy intensive grinding) prior to field application in an ERW context may not be warranted in terms of additional gains in CDR.

The RTM results based on basalt mineralogy and SSA over a 30-year RTM simulation time horizon (Figure A7) can be compared with the theoretical CDR potential of the same basalts based on their cation content. The 30-year RTM simulation time was used to account for the effects of both the fast- and slow-weathering minerals present in the basalts. Theoretical CDR is described by the term R_{CO_2}, which is defined as the ratio of tonnes of CO_2 captured per tonne of rock mass weathered (Eq. 2.3) (Renforth, 2012):

$$R_{CO_2} = \frac{M_{CO_2}}{100}\left[\left(\frac{\%CaO}{M_{CaO}} + \frac{\%MgO}{M_{MgO}}\right)\cdot\omega + \left(\frac{\%Na_2O}{M_{Na_2O}} + \frac{\%K_2O}{M_{K_2O}}\right)\cdot 0.5\omega\right] \quad \text{(Eq. 2.3)}$$

where M_{CaO}, M_{MgO}, M_{Na_2O}, M_{K_2O} and M_{CO_2} represent the molecular masses of CaO, MgO, Na_2O, K_2O and CO_2 respectively. %CaO, %MgO, %Na_2O and %K_2O represent the oxide concentrations in the basalt in question and ω represents the additional drawdown from cation flux into the ocean (approximately 1.72). Regression of CDR (Figure A8), as determined using the RTM simulations over a 30-year time horizon against R_{CO_2} and SSA for five basalts (excluding the Blue Ridge metabasalt) yielded the relationship (Eq. 2.4, $r^2 = 0.82$, $p = 0.00004$):

$$\text{CDR potential} = \exp\left(4.4 + 0.7 \cdot log_{10}(SSA) - \frac{9.5}{\sqrt{R_{CO_2}\cdot 50}}\right) \quad \text{(Eq. 2.4)}$$

where the CDR potential is expressed in t CO_2 ha^{-1} 30 yrs^{-1} per basalt application with a single baseline application rate of 50 t ha^{-1} at time = 0. R_{CO_2} is calculated from Eq. 2.3 based on the bulk elemental analyses of the same basalts (Table 2.6) and SSA is in m^2 g^{-1}. CDR potential therefore represents the maximum value based on 30 years of weathering, and simulated dissolution kinetics demonstrate reduced CDR beyond 30 years (Figure A7).

Table 2.6 – HF-digested ICP-OES whole rock geochemical data expressed as either wt.% or mg kg^{-1}. R_{CO_2} values are also given, as calculated from Eq. 2.3.

Element	Unit	Oregon	Cragmill	Tichum	Blue Ridge	Tawau	Hillhouse
Si	%	22.0	22.0	19.7	19.8	25.0	21.4
Al	%	5.81	5.65	4.91	4.80	6.24	7.00
Ca	%	4.08	5.97	6.28	6.09	4.16	6.72
Mg	%	1.30	1.89	2.80	1.82	1.30	5.86
Fe	%	6.93	8.65	7.91	8.55	4.22	7.11
K	%	2.51	0.844	0.902	0.327	1.47	0.948
Na	%	2.72	1.85	3.18	1.53	1.91	2.31
Ti	%	1.36	1.41	1.32	1.07	0.30	0.85
P	%	0.6420	0.1290	0.333	0.0862	0.0545	0.1080
Mn	%	0.160	0.140	0.137	0.160	0.088	0.123
Ba	%	0.2050	0.0317	0.0462	0.0142	0.0219	0.0336
Ce	mg kg^{-1}	83.2	53.3	59.2	<16.0	180.0	<80.0
Co	mg kg^{-1}	18.4	39.2	49.2	49.8	18.6	<40.0
Cr	mg kg^{-1}	34.8	68.1	214.0	154.0	51.4	350.0
Cu	mg kg^{-1}	27.6	52.8	52.4	52.8	27.2	<40.0
La	mg kg^{-1}	33.1	28.4	39.7	<16.0	21.9	<40.0
Ni	mg kg^{-1}	17.8	49.4	192.0	142.0	17.9	195.0
Sr	mg kg^{-1}	296	419	828	209	331	456
V	mg kg^{-1}	398	484	357	409	201	231
Zn	mg kg^{-1}	148.0	144.0	147.0	138.0	70.6	99.2
Zr	mg kg^{-1}	105.0	112.0	144.0	22.4	20.8	<80.0
R_{CO_2} *values*							
R_{CO_2} CaO + MgO		0.12	0.17	0.21	0.17	0.12	0.31
R_{CO_2} CaO + MgO + Na_2O + K_2O		0.15	0.19	0.24	0.19	0.14	0.33

Using R_{CO_2}, particle size and mineralogy, an equation was developed to convert the R_{CO_2}, based on widely available (and easily measured) rock chemistry to an equivalent mineralogy-based CDR for a range of initial SSAs. Applying Eq. 2.4 to the chemical data for 1,345 mafic rock samples from 25 LIPs from the GEOROC database (Sarbas, 2008) using a surface area of 1 m^2 g^{-1} predicted a CDR potential range of 3.9-8.2 t CO_2 ha^{-1} 30 yrs^{-1} with a median of 5.9 t CO_2 ha^{-1} 30 yrs^{-1} (Figure 2.8a). The Tichum and Hillhouse lie beyond the upper limit of this range, while the Oregon, Blue Ridge, Tawau and Cragmill fall below this range. None of the basalts used in this study fall close to the median predicted CDR of basalts from LIPs. Increasing the surface area to 10 m^2 g^{-1} increased the range of CDR potential of the basalts from the large igneous provinces to between 7.8 and 16.5 t CO_2 ha^{-1}, with a median of 11.8 t CO_2 ha^{-1} (Figure 2.8b). Overall, these results display the probable range of CDR of rocks that are classified as basalts, both those that are available commercially and those in large igneous provinces.

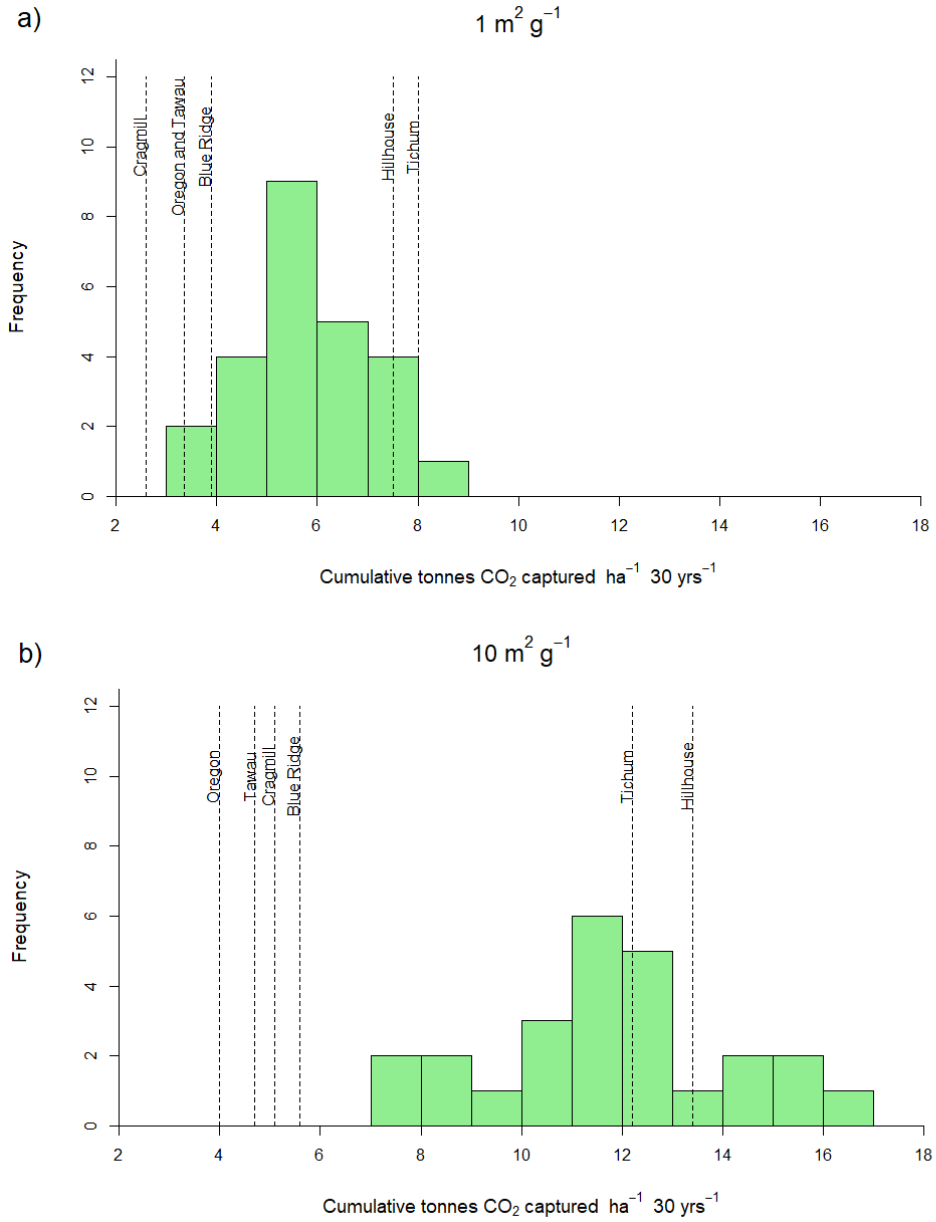

Figure 2.8 – Histogram showing the predicted CDR potential of basalts from average Ca, Mg, K and Na concentrations of 25 large igneous provinces taken from the GEOROC database (Sarbas, 2008) using (a) a 1 m^2 g^{-1} standardised surface area and (b) a 10 m^2 g^{-1} standardised surface area. The predicted CDR was calculated using CDR potential $=$ exp $(4.4 + 0.7 \cdot log_{10}(SSA) - \frac{9.5}{\sqrt{R_{CO_2} \cdot 50}})$ (Eq. 2.4). This expression is derived from a regression of five basalts across a range of surface areas (0.1 m^2g^{-1}- 10 m^2g^{-1}), is given in Figure A8. Dashed lines show the cumulative CDR of the basalts after 30 years of weathering.

2.4.2. RTM simulated P and K-release

Given the high cost of rock-derived P and K fertilizers (Amundson *et al.*, 2015), the potential for P and K release by basalt weathering to replace them was explored. The P and K concentrations in the basalts studied here varied ten-fold (Table 2.6), with P hosted primarily in apatite (trace P was also observed in basaltic glass (see Wolff-Boenisch *et al.*, 2004; Dontsova *et al.*, 2014; Kelland *et al.*, 2020) and K in K-feldspar (Hillhouse, Oregon, Cragmill, Tichum, Tawau), biotite (Hillhouse and Tawau), phlogopite (Cragmill) and leucite (Tichum). Although the Blue Ridge metabasalt contains P and K (Table 2.6), no apatite was detected through XRD analyses (Figure 2.2) and no K-bearing minerals were detected (Table A2). As a result, no P or K source minerals could be considered in the RTM simulations. For all other basalts, the 1-D RTM was used to simulate P and K release by mineral dissolution with either the BET SSA as the surface area term or a SSA of 10 $m^2 g^{-1}$ (Figure 2.9a and b). While the element release after five years of weathering was plotted, the release of elements and cost savings referred to in the rest of this section refer to values which were calculated after one year of weathering. This is because farmers typically fertilise their fields with P and K fertiliser every year.

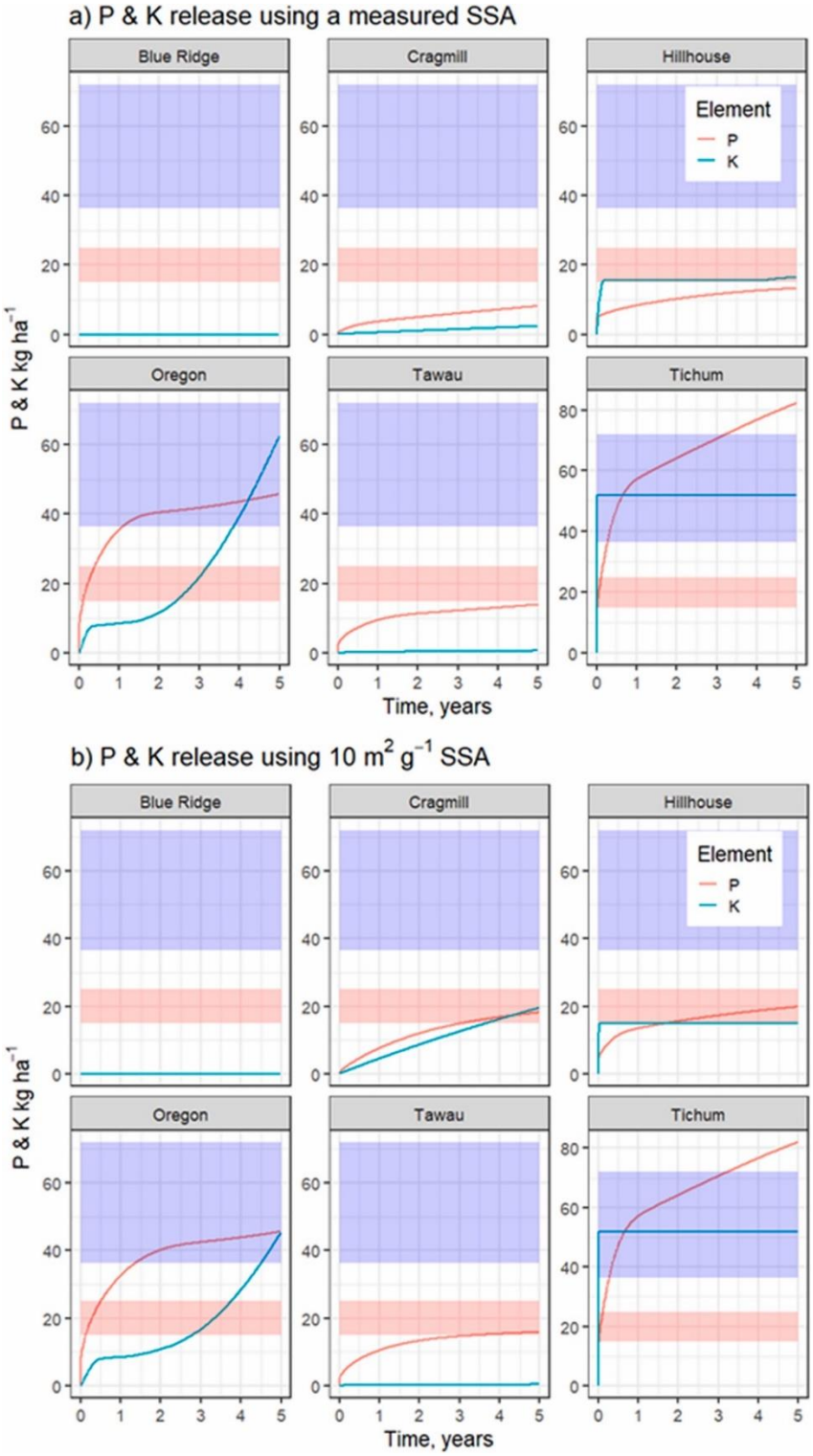

Figure 2.9 – Cumulative P and K release from the six basaltic basaltic quarry fines analyzed in this study after 5 years of mineral weathering, as determined from the reactive transport model using (a) measured specific surface area (SSA) (from BET measurements) and using (b) a standardised 10 m^2g^{-1} SSA. Shaded red and blue areas represent average P (14.8 to 26.2 kg P ha^{-1}) and K (36.4 to 72.7 kg K ha^{-1}) fertiliser application rates respectively for tillage crops in the UK, based on data from DEFRA (2020).

A comparison was made between the simulated release rates of P and K and the typical annual application rates for arable cropping systems in the UK (Figure 2.9a). Average P-fertiliser application rates for tillage crops in the UK (Supporting Information Table A3) range between 14.9 and 26.2 kg P ha^{-1} (DEFRA, 2020), and are 16.6 kg P ha^{-1} in the USA. Wheat, the most widely grown crop in the UK (DEFRA, 2020), is fertilised with an average of either 15 or 25 kg P ha^{-1} depending on when the crop is sown (spring or winter respectively). According to the RTM simulations, weathering of Oregon and Tichum basalts after a year could supply sufficient P for spring wheat in the UK, given BET SSAs. Cragmill, Hillhouse and Tawau basalts could supply between 26% and 66% of the P provided by conventional fertilisers with a single ERW treatment. Repeated annual ERW rock dust applications could therefore potentially replace relatively more expensive P-fertilisers.

For K, annual fertiliser application rates for major tillage crops in the UK vary between 36.4 and 72.7 kg K ha^{-1} (DEFRA, 2020) (Table A3), with the fertiliser application rate for spring wheat in the UK (36.4 kg K ha^{-1}, DEFRA 2020) and USA (30.6 kg ha^{-1}, USDA 2019) at the lower end. Simulation results demonstrate that, unlike for P, only the Tichum basalt is a major source of K after 1 year of weathering, supplying 53 kg K ha^{-1} (Figure 2.9a). This is equivalent to over 100% of UK and USA spring wheat application rates. The Hillhouse and Oregon basalts are also predicted to release K equivalent to significant proportions of K applied as fertiliser after one year of weathering (44% and 24% of the winter wheat K fertiliser rates respectively). The solubility of K-bearing minerals phases is initially limited by the accumulation of dissolution products from relatively rapidly dissolving pyroxenes and olivine (Figure 7a, b). K-release could therefore likely continue over the long-term, replacing small amounts of K fertiliser over a long period of time.

In addition to wheat production in temperate climates, oil palm plantations in tropical regions represent *c.*18 million ha of land across the tropical rainforest biome (Skiba *et al.*, 2020) which has an ideal climate (moist and warm) for ERW. Oil palms are fertilised with P and K to improve yield, at recommended rates of up to 14 kg ha^{-1} and 204 kg ha^{-1} respectively (Ng *et al.*, 1999). As a result, the

model simulations suggest that the 'lower P' basalts (e.g. Hillhouse, Cragmill and Tawau) could substitute P fertilisation. K fertiliser however, which is frequently under applied relative to these recommended rates in Indonesia (Woittiez *et al.*, 2018), still requires substantial application of K fertiliser.

Focusing on P release from basalt amendment, ERW could substitute for P-fertiliser application, reduce costs (Beerling *et al.*, 2018), and reduce reliance on high-grade mineral sources of these elements, over which there has been concern about the long-term sustainability of supplies (Elser and Bennett, 2011; Ciceri, Manning and Allanore, 2015). Considering the mass of basalt from eight major volcanic provinces around the world, the average P_2O_5 concentrations from these provinces (Table A4) and assuming that annually 45 million tonnes of P fertiliser, as P_2O_5, is applied globally (Cordell and White, 2014), the global reserve of P in basalt could be used as a fertiliser resource for 2.14 million years. If just 0.05% of this basalt could be sourced as an agricultural rock amendment, basalt could substitute P fertiliser globally for *c.* 425 years.

Conventional P fertilisers cost between \$364–432 US t^{-1} in the UK (AHDB, 2020) and \$406–430 t^{-1} in the USA (Quinn, 2020). Taking the UK average application rate for spring wheat, then the replacement of P fertiliser applications by basalt amendment at 50 t ha^{-1} has a cost offset potential of \$111–432 US t^{-1} P fertiliser in the UK and similar cost savings in the USA at \$99-430 US t^{-1}. An average application rate of 14.8 kg P ha^{-1}, would correspond to savings in the cost of applying basalt powder in the range \$8–29 US ha^{-1}. Considering P fertiliser rates in the USA of 16.6 kg P ha^{-1}, cost savings vary between \$6-26 US ha^{-1}. Fertiliser costs are quoted as \$350 t^{-1} (UK) (AHDB, 2020) and \$363 t^{-1} (USA) (Quinn, 2020). For the K release from the Hillhouse, Oregon and Tichum basalts, the fertiliser savings range between \$79–\$350 US t^{-1} (\$3–\$23 ha^{-1}), depending on the K content of the basalt. Estimated costs for net CDR with ERW on croplands accounting for energy demand and costs of rock mining and grinding, and transportation and spreading costs are approximately *c.* \$170 t^{-1} CO_2 yr^{-1} for the USA and Europe (Beerling *et al.*, 2020). Given approximate net CDR rates of around 4 t CO_2 ha^{-1} for these regions, this yields a cost of CO_2 removed per ha of

$680. Set against these CDR costs, a potential cost offset from supplementing or replacing fertilisers with basalt is relatively small, around *c.* 5%.

2.5. Conclusions

Detailed mineralogical and chemical analyses of six basalts from a worldwide range of sites are reported and used in 1-D RTM soil profile ERW simulations set-up with an illustrative clay-loam agricultural soil to undertake comparative potential CDR calculations. For a single baseline application rate of 50 t ha^{-1} of crushed basalt, this procedure gives CDR potentials of between 1.3 and 8.5 tonnes of CO_2 ha^{-1} after 15 years of weathering. Faster weathering minerals that are rich in Ca and Mg, such as olivine and augite, dominate CDR potential, particularly during the early stages of dissolution. Selecting basalts with favourable mineralogy and mineral chemistry will be key to optimising the near-term performance of ERW for CDR. The RTM-predicted CDR potential did not increase linearly with the amount of reactive surface area of rock used in the model, increasing by up to a factor of *c.* 2, despite a factor of 10 increase in surface area. Further processing a basalt (i.e. grinding) to increase its CDR potential therefore also warrants consideration of basalt mineralogy. Simulated P release may be sufficient to fully or partially substitute for typical P fertiliser applications depending on crop type.

The 1-D RTM approach is based on a real agricultural soil, but does not account for changes in hydrology associated with seasonal changes in precipitation nor replicate P dynamics (i.e. the direct weathering of phosphorus minerals; sorption of P to exchangers) in soils. Ultimately these effects require investigation with further detailed reactive transport modelling of basalt weathering and interaction with plants and water flow in whole soils throughout the depth of the profile, together with data from field-scale trials of ERW over a period of several years. Areas of further investigation are also discussed in the General Discussion (Chapter 6).

3. Assessing evidence for basalt weathering and organic carbon stabilisation at the grain-scale

3.1. Introduction

The use of basalt rock amendments for cropland-based Enhanced Rock Weathering (ERW) as an effective, safe and environmentally acceptable CO_2 removal (CDR) strategy is outlined in Chapter 1 and 2. When the basalt is amended into cropland soils, it reacts with the surrounding soil solution and releases elements through weathering reactions. The released elements could be subjected to one of several pathways: CDR (Renforth and Henderson, 2017), retained on cation exchange sites by clays and organic carbon (OC) (Kelland *et al.*, 2020), used by plants and microbes (Kelland *et al.*, 2020; Epihov *et al.*, 2021), or precipitated as secondary phases in soils or on grains.

Studying secondary phase formation could be important, particularly at mildly acidic/circumneutral pH's where Al and Fe are immobile (Pourbaix, 1974), as secondary phases could account for missing sinks which have not yet been considered in ERW mass balances. Secondary phases contain sites of electrical charge which can retain soil components including OC. Secondary phases may stabilise OC as either: (1) co-precipitants, forming directly in the presence of OC and incorporating OC into the chemical structure (e.g. Tamrat *et al.*, 2019) or (2) by stabilising OC via adsorption to charged sites (e.g. Kaiser and Zech, 2000; Jagadamma *et al.*, 2014; Chen *et al.*, 2017; Singh *et al.*, 2017).

Once OC interacts with inorganic materials via either adsorption or co-precipitation, the OC structure changes (Oades, 1988) and is less available to soil biota (i.e. it is not respired and converted to CO_2). A wealth of evidence demonstrates that increased soil organic carbon (SOC) content in soils is related to the accumulation of secondary phases such as clay minerals and short range order phases (SROs) (Sarkar *et al.*, 2018; Rasmussen *et al.*, 2018; Mikutta *et al.*, 2006; Eusterhues, Rumpel, and Kögel-Knabner, 2005; Kleber *et al.*, 2005).

Despite basalt grain weathering being hypothesised to drive changes in several soil parameters, limited work has considered the effects of basalt

amendment into soils on basalt grains themselves. Work considering how basalt grains may interact with soil solution has been limited to studies of bulk elemental change of basalt grains retrieved from an ERW experiment (Kelland *et al.*, 2020). In reality, though, in the ERW conceptual model (outlined in Chapter 1 and 2), the bulk soil could be divided into at least two distinct components: soil and rock amendment.

When studying bulk soil (e.g. soil and basalt combined) alone, the processes occurring within the basalt grains (e.g. on the surface or within cracks that have formed within the basalt) are not considered. There could be some processes which occur exclusively on the basalt grains which are not easily accounted for if just studying the bulk soil. Some processes that are occurring exclusively in the soil could also be 'diluted' by the presence of basalt grains which comprise *c.* 4-5% of the bulk soil when basalt is amended at a rate of 50 t ha^{-1} (see Section 4.3.10). For example, basalt might have a lower cation exchange capacity than bulk soil. Therefore, studying basalt grains amended into soils as well as the bulk soil itself, whether for secondary precipitants or a host of other parameters, could prove important in producing a full mass balance of elements within the basalt amended soil system and gaining a more complete picture of processes occurring in basalt amended soils.

While there is a lack of data directly applicable to ERW, a wealth of work has studied basalt transformation during dissolution or weathering at both: (1) flask dissolution scale (e.g. Wolff-Boenisch, Gislason and Oelkers, 2006; Dontsova *et al.*, 2014) to determine kinetic rate laws and (2) field scale weathering in the context of pedogenesis (e.g. Chorover, Amistadi and Chadwick, 2004). At both flask and field scales, 'bulk-' (e.g. pH, elemental/compound concentrations) and 'micro-' characteristics (e.g. site and target specific weathering areas) have been studied.

In bulk scale dissolution experiments, the precipitation of secondary phases has rarely been considered because experiments are frequently carried out at far-from-equilibrium conditions which inhibit secondary phase precipitation. However, Stockmann *et al.*, (2013) found that calcite precipitated on diopside surfaces is porous, thus allowing contact between the basalt grain surface and the

reacting solution. Similarly, laboratory experiments have found that the precipitation of Fe-oxides on feldspar grain surfaces does not affect feldspar dissolution as the precipitates were porous (Hodson, 2003). In addition, recent work on lithium isotope fractionation occurring during secondary phase formation under varying environmental conditions has identified several secondary precipitants from basalt dissolution including: vermiculite, nontronite, saponite (Goût *et al.*, 2021).

Surface chemistry is predicted to change during mineral dissolution. According to the general description of mineral dissolution set out in Oelkers (2001), less weakly bonded elements (e.g. Na and K) are released from mineral structures before the strongest bonds within a silicate mineral structure (the Si-O bonds) are broken. Oelkers (2001) description predicts the release of elements from a mineral structure in the following order: Na and K, Ca, Mg, Al and Si. Such trends are frequently observed at micro-scale for the common basaltic minerals after flask dissolution using XPS (X-ray Photoelectron Spectroscopy) (Schott and Berner, 1985; Muir *et al.*, 1990; Zakaznova-Herzog *et al.*, 2008; Schott *et al.*, 2012; Stockmann *et al.*, 2014). Nugent *et al.* (1998) also identified the precipitation of Al-oxides via XPS on feldspar grains recovered from soils. Additionally, small (5 and 200 nm) co-precipitant colloids of poorly ordered Fe, Al, Si and C bonds are predicted to form in soil solutions following biotite weathering, following flask-dissolution studies conducted by Tamrat *et al.* (2019). These secondary phases could be retained on soil substrates, including, in the ERW system, basalt grain surfaces.

At the field-scale, over a 4.1-million-year time scale, basalt pedogenesis transformed primary minerals into poorly crystalline weathering products, identified as short SROs: allophane, microcrystalline gibbsite and ferrihydrite. Then, SROs were transformed into crystalline minerals such as kaolinite, gibbsite and goethite (Chorover, Amistadi, and Chadwick, 2004). This trajectory transforming primary minerals to SROs then crystalline minerals could be assumed to occur as the basalt applied for ERW weathers over time. However, the length of time it will take for these phases to form as a result of basalt grain weathering in soils is unknown but these phases could form more quickly given

the increased surface area of basalt grains amended into soils compared to a basaltic bedrock. In the context of basalt grain pedogenesis it is also unknown where secondary phases may form: in the surrounding bulk soil or on basalt surfaces.

When amending soils with basalt, new soil is generated. A study has shown that relative to soils developed on other rock types, soils developed on basaltic bedrock could stabilise OC via secondary phase formation (Heckman *et al.*, 2018). Compared to rhyolite, granite and dolostone bedrock, soils developed on a basaltic bedrock had a higher proportion of secondary Fe-oxides (up to 4.1-fold higher) and higher specific surface areas (up to 2.5 times higher). Moreover, the OC that is stabilised in basaltic soils is considered to have significantly longer residence times – between 1.7- and 3.0-fold higher than soils forming on other bedrocks.

Basalt also contains abundant Al and Fe which are both key to forming the co-precipitants and secondary phases described earlier. However, basalt may already contain charged secondary phases prior to field application. Clay minerals were identified in five out of six of the basalt quarry fines described in Chapter 2 (between 1.2 wt.% - 10.4 wt.%). Other workers have shown weathered basalts can possess non-negligible cation exchange capacities of up to 59.8 cmolc kg^{-1} (Korchagin, Caner, and Bortoluzzi, 2019).

While the primary rationale for selecting basalt as a fast weathering rock is for CDR via ERW (as described in Chapter 2), evidence from previous workers strongly suggests that basalt weathering could increase OC in soils. To test this suggestion is it imperative, however, to determine where sites for OC accumulation will develop – in the soil or on basalt grains. This chapter focuses on whether charged sites for OC stabilisation will develop on basalt grains.

This chapter studies basalt grains and quartz retrieved from mesh bags emplaced in an ERW experiment, where *Sorghum bicolor* has been grown in a clay-loam agricultural soil that has been subjected to two different fertiliser regimes: (1) conventional NPK + basalt and (2) organic manure + basalt.

Evidence of (1) grain weathering, (2) secondary phase formation and (3) OC stabilisation is assessed.

Evidence for the aforementioned processes were determined from a variety of both bulk and microsite techniques including: X-ray Fluorescence (XRF) to assess bulk chemical changes, XPS to probe surface chemical characteristics and Fourier Transform Infrared (FTIR) spectroscopy to assess elemental functional groups (indicative of phases). In addition, a set of chemical extractions was used to assess the amount of Al and Fe associated with OC by (1) co-precipitation and (2) adsorption to crystalline and non-crystalline secondary phases. Additionally, scanning electron microscopy (SEM) and geochemical modelling were used to assess physical changes and the potential for secondary phase precipitation, respectively.

Given the limited directly applicable data for comparison and the complex heterogeneity of basalt (as shown in Chapter 2), a subset of the analysis techniques was applied to basalt grains from a set of closed, flask dissolution experiments where grains reacted in an OC matrix (from a compost extract) for up to eight weeks. The flask experiment was used to: (1) identify how basalt dissolves in the absence of biota and (2) help assess if any of the chemical trends identified in the basalt grains retrieved from the soil could have been the result of soil particles being transported into the mesh bags which contained basalt grains (see Section 3.2.2). While the experimental set up of this flask dissolution experiment differs from the conditions that the grains in the ERW experiment were subjected to (e.g. abiotic vs biotic, closed vs open system, soil + basalt and basalt only), the flask experiment may supplement the interpretation of basalt grains extracted from the growth experiment.

Based on the background and methods described above, the following hypotheses were tested:

(1) There will be evidence of elemental release from the basalt grains (e.g. from the decrease in Mg, Ca, Al and Na and relative to Si) from the surface chemistry

data generated using XPS and XRF data, because the grains will have dissolved in the soil columns.

(2) Evidence of elemental release will be more pronounced in the NPK + basalt treatment relative to the Manure + basalt treatment because the former will release nitric acid into the environment which weathers the basalt grains faster.

(3) There will be evidence of weathering products on grain edges because the grains are both dissolving and interacting with the soil solution (containing weathering products). Given the short time frame of the experiments, the weathering products are likely to be amorphous rather than crystalline.

(4) There will be evidence of calcite precipitation because of the flux of Ca ions from weathered minerals and the elevated pH surrounding the basalt grains.

(5) OC concentrations of the grains will increase as a result of OC stabilisation. The mechanism for stabilisation will be via co-precipitation rather than the formation of SROs and subsequently adsorbed OC.

(6) More OC will be stabilised in the Manure + basalt treatment relative to the NPK + basalt treatment because of the higher OC concentrations present in the Manure + basalt treatment because of the added manure.

3.2. Materials and methods

3.2.1. Basaltic material

The basalt used within this experiment was a highly processed version of the Oregon basalt, as described in Chapter 2. Further processing was conducted to create a more refined grain size distribution with a higher reactive surface area. The processing of the Oregon basalt was completed by PhD student Mr M Kelland and Dr D Johnson.

The Oregon basalt, as purchased from Cascade Minerals (Central Oregon Basalt Products LLC), was further crushed in a Fritsch Pulverisette agate ball mill. At three minute intervals, the basalt was removed from the ball mill and sieved through a 53 μm sieve. Any remnant grains > 53 μm were further crushed in the ball mill. Once enough basalt was crushed to < 53 μm, it was ultrasonically washed with ethanol (99% absolute, Sigma Aldrich) to remove sub-1.5 μm particles which could not be accurately measured using laser particle size analysis. The particles were left in ethanol for one hour, being stirred every 10 minutes, before the suspension was left to settle for 13 hours to, in theory, settle out any particles > 1.5 μm, as according to Stokes Law (Stokes, 1851). This process was carried out twice to try and remove as many fine particles as possible in case any particles < 1.5 μm had settled to the bottom of the column and were thus still incorporated in the washed sample.

Particle size was then measured on a HORIBA Partica with four replicates, to the same protocol as described in Section 2.3. Analysis determined that 92% of the particles were below 51 μm and had a median particle size of 17.7 μm (Figure 3.1a). The mineralogy of this newly produced basalt was also determined, in accordance with methods described in Section 2.1. The mineralogy is shown in Figure 3.1b. Overall, the mineralogy of this processed basalt is similar to the commercially available Oregon basalt (Section 3.2), though with considerably more basaltic glass (+14 wt.%), and lower plagioclase and sanidine. While the basalt was sourced from the same quarry, the Oregon basalt described in Chapter 2 was purchased on a separate occasion to the basalt

described in this Chapter. Additionally, if minerals broke differently during the ball-mill grinding, some of the minerals may have become 'overground' and subsequently been washed out of the material during the washing stage. Heterogeneity in the quarry's lithology likely explains the aforementioned mineralogical differences, though the additional sample preparation may also have had an effect on the mineralogy.

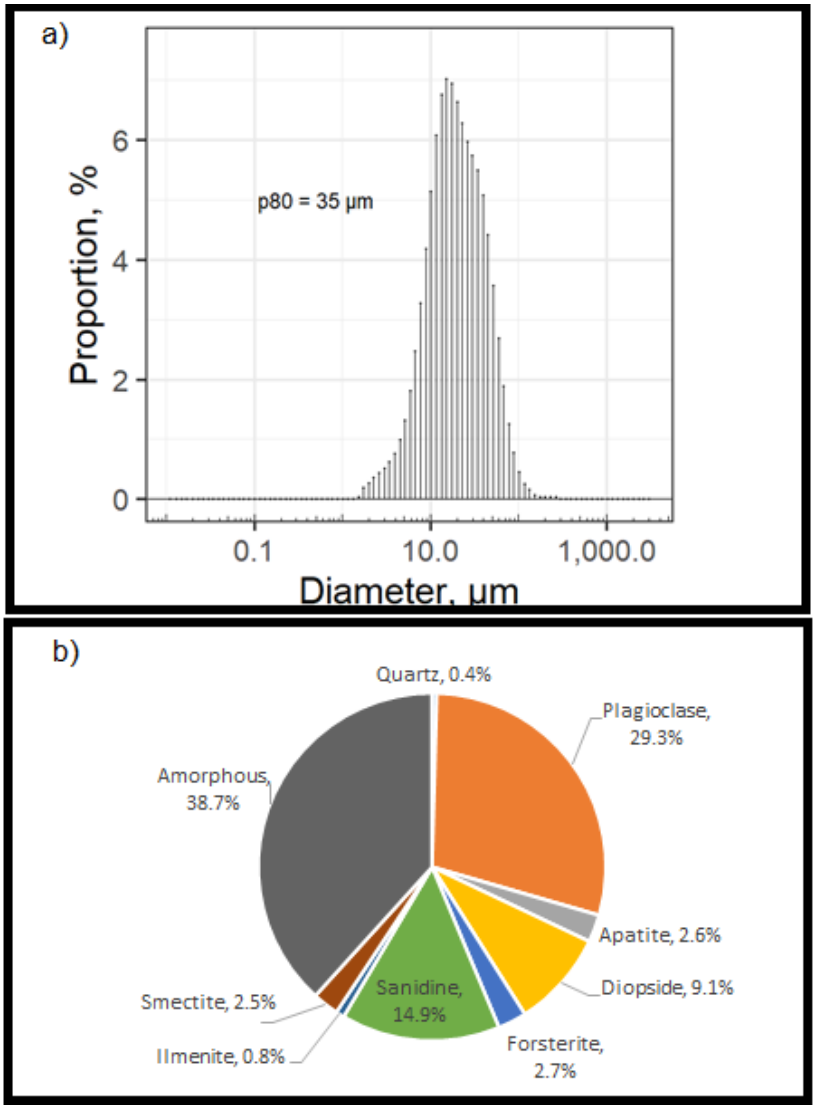

Figure 3.1 – Particle size distribution (a) and mineralogy (b) of the Oregon basalt used in this chapter.

3.2.2. Mesocosm experiment design

The mesocosm experiment was designed and conducted by Mr M Kelland, Dr B Sarkar, Dr D Johnson and Dr P Wade, as part of Mr M Kelland's PhD thesis (Kelland, in prep). Overall, the mesocosm experiment was designed to investigate the effect of a conventional NPK or an organic manure fertiliser, combined with basalt on plant yield, CDR and soil health parameters (Kelland, in prep). The experiment had four treatments: (1) NPK, (2) NPK + basalt, (3) Manure and (4) Manure + basalt. Each treatment consisted of seven replicates. A summary of the experimental design is detailed below.

A set of 50 cm column weathering reactors were used in the mesocosm experiment. The design of these weathering reactors used in the mesocosm experiments is summarised in Kelland *et al.* (2020) (Figure S1a of Kelland *et al.* 2020). Each weathering reactor was filled with 8.252 kg of soil. This soil was collected from the Game and Wildlife Conservation Trust, Allerton Project, Leicestershire (Latitude 52.611286 °N, Longitude 0.831559 °W). The initial soil was identified as a mildly acidic clay loam (soil pH = 6.45; Clay 29.04%, Silt 34.30%, Sand 36.66%). Once the soil was collected, it was comminuted by hand without drying. During the comminution, stones and invertebrates were removed. The soil was sieved to 2 mm and was not compressed when it was applied to the soil column and therefore had a low bulk density (0.91 kg L^{-1}).

Basalt and manure were amended into the top 12 cm of soil within the column (accounting for *c.* 1.98 kg soil) and is referred to the 'amended layer'. Only treatments containing manure and/or basalt had their respective treatments mixed into the amended layer by hand to generate a homogeneous distribution. If treatments contained manure or basalt, then 18 g of cattle manure and 91 g of the refined Oregon basalt (see Section 3.2.1) was added to each treatment respectively, equivalent to 10 t ha^{-1} manure and 50 t ha^{-1} of basalt. Of the 91 g of basalt added to the basalt treatment, 4.25 g of this basalt was added in mesh bags (see Section 3.2.3) rather than being homogeneously mixed. The NPK fertiliser was made up by mixing analytical grade urea, diammonium phosphate and potassium chloride. In the treatments using NPK as a fertiliser, 3.46 g of a

250:414:490 N:P:K fertiliser mix was applied as a powder to the top of the soil column.

The experiment was conducted in a growth room within the Sir David Read Controlled Growth Facility at the University of Sheffield. The growth period of the experiment lasted for 115 days followed by 14 months and 20 days of fallow period. Relative humidity and CO_2 concentrations were maintained at 75% and 400 ppm, respectively. The photosynthetically active radiation was set to 800 μmol photons m^{-2} s^{-1}. Day and night temperatures of 25°C and 17°C were used until the end of the growth period, and day and night temperatures of 5°C and 3°C were used until day 235. The hours of daylight also varied throughout the experiment: 18 hr days were implemented from day 1-60 followed by 10 hr days until the end of the experiment.

3.2.3. Mesh bag construction, placement and retrieval

To recover the basalt grains after the experiment, the basalt grains were placed in mesh bags constructed by Dr D Johnson and Mr M Kelland. Seventeen nylon mesh bags (mesh size = 35 μm) containing 0.25 g of basalt each, amounting to a total of 4.25 g of the 91 g total basalt per column, were constructed. The bags were placed within the soil and basalt amended layer during Mr M Kelland's mesocosm experiment, which is described in Section 3.2.2. In addition to the basalt bags, five quartz bags containing 0.25 g of analytical grade quartz ($p80$ = 250 μm), which acted as a control for chemical processes in comparison with basalt, were also added to the experiment.

Bags were retrieved from the experiments 14 months after the experiment was finished. During this time, the bags remained in the soils at 4°C except for when the soils were used in a CO_2 respiration experiment. As mentioned in the previous section, the experiment had four treatments: (1) NPK, (2) NPK + basalt, (3) Manure, (4) Manure + basalt, with each treatment consisting of seven replicates. However, as this chapter is investigating interactions between soil solutions and basalt, only the NPK + basalt and Manure + basalt treatments were

studied in this chapter. An initial basalt sample of the refined Oregon basalt, as described in Section 3.2.1 (referred to as 'Initial basalt'), was also studied to assess differences before and after weathering.

Post-experiment, the mesh bags were oven-dried at 50°C with their contents still in them and then stored in polyethylene bags until the basalt or quartz from the contents of all the mesh bags were compiled into one independent sample per column, and stored dry at room temperature prior to analysis. None of the basalt grains were cleaned prior to analysis.

Occasionally, independent samples from specific column reactors are referred to throughout this chapter. When this is the case, samples are referred to as 'CX', where 'C' is the column and 'X' is the independent sample reference.

3.2.4. Basalt-compost dissolution experiment design

The flask dissolution experiment was designed by Dr B Sarkar and conducted by Dr D Johnson and Dr B Sarkar.

In the experiment, the grains were weathered in a compost extract which was produced by adding 100 g of compost to 2 L of reverse osmosis (RO) water. The solution was left to stand for three weeks with the stopper of the bottle loosely closed to prevent the system becoming anaerobic. After being produced, the compost extract was filtered through a 0.22 μm filter, using a Buckner funnel. Then, sodium azide was added to the extract to produce a solution of 1% concentration before being autoclaved – both steps were employed to inhibit microbial activity and thus prevent microbial degradation of OC.

For the experiment, 30 mL of the compost extract was mixed with 1± 0.0008 g of the Oregon basalt (as described in Section 3.2.1) in a 50 mL Mini Bioreactor with an air-permeable lid (CORNING, USA). The permeable lids were used to maintain an ambient CO_2 level inside the Mini Bioreactor, so that CO_2 consumed during weathering reactions can be replaced. The centrifuge tubes were then placed on a rotatory shaker (Bibby Scientific Stuart Rotator Disk BS3) at a speed of 2 rpm and an angle of 60° to gently agitate the basalt grains and prevent

saturation developing around the grain edges. The temperature in the room that the experiment was left varied between 22–24°C and such a difference was not likely to cause a significant difference in the weathering rate. The experiment ran for 56 days (eight weeks), with sacrificial sampling taking place at: day 1, day 2, day 4, day 7 and then at weekly intervals.

The solution produced after 1 week of weathering was used for geochemical modelling experiments. pH and electrical conductivity (EC) were obtained on undiluted, unfiltered samples using a Jenway 3540 Bench Combined Conductivity/pH Meter (Jenway, Cole-Palmer, UK). Prior to carbon and cation analysis, samples were filtered through a 0.45 μm filter. The dissolved carbon (DC) and dissolved inorganic carbon (DIC) were obtained using a Shimazdu TOC-L Total Organic Carbon Analyser (Shimazdu, Japan), with dissolved organic carbon (DOC) calculated by subtracting the DIC from the DC of each sample. Cation concentrations were determined using Inductive Coupled Plasma-Mass Spectrometry (ICP-MS) on a Thermo-Fisher iCAP-Q at the University of Nottingham. For the ICP-MS analysis, major elements (Na, Mg, K and Ca) were calibrated between 10-30 ppm, and minor elements between 20-100 ppb.

The grains analysed in this chapter were removed after week eight. Once extracted, they were thrice washed with UPW (ultra-pure water) before being centrifuged, freeze dried and then stored in high density polyethylene bottles with a polypropylene cap. UPW was used instead of RO water for the washing of grains because its higher purity.

3.2.5. X-ray Fluorescence (XRF)

X-ray Fluorescence was completed at the Royce Discovery Centre at the University of Sheffield. The XRF was conducted to determine whole-rock elemental chemistry of grains recovered from the mesh bags. All analysis was conducted on Li-borate fused beads – with one bead produced for each independent sample. Three independent samples of the Initial basalt and seven samples of both NPK + basalt and Manure + basalt representing each column were made.

Li-borate fused beads were produced by mixing *c.* 0.5 g of basalt sample with *c.* 10 g of pure grade anhydrous lithium tetraborate with lithium iodide (99.50% $Li_2B_4O_7$:0.05% LiI - Claisse, Quebec City, Canada). Weights were recorded to 0.1 mg precision. Fuse beads were made in a LeNeo Fuser (Claisse, Quebec City, Canada), melting the basalt and Li-Tetraborate at 1065 °C in a 95% Pt:5% Au crucible.

XRF analysis was then conducted using a PANalytical Zetium DY 2018 using the Wide Ranging Oxide (WROXI) data collection and analysis programme to measure O, Na, Mg, Al, Si, P, S, K, Ca, Ti, V, Cr, Mn, Fe, Ni, Cu, Zn, Zr, Ba, Hf and Pb. Each fused bead was analysed three times and then these three measurements were averaged to produce one result for each independent sample to be used in treatment-based statistical analysis. Data were exported in Element wt.%, and later converted to Oxide wt.%.

Upon sample analysis, relatively large (*c.* 1 wt.%) proportions of kaolinite were identified from DRIFTS (Diffuse Reflectance Infrared Fourier Transform Spectroscopy) data and interpreted as soil contamination. The rationale for this interpretation is discussed fully in Section 3.4.1.1. Kaolinite ($Al_2Si_2O_5(OH)_4$) comprises both Al and Si, and as it was not possible to determine how much of the Al_2O_3 and SiO_2 originated from the kaolinite contamination, the Al_2O_3 and SiO_2 concentrations were subtracted from the XRF data and the relative proportions of all other elements were recalculated and renormalised to 100%. For completeness uncorrected Al_2O_3 and SiO_2 concentrations are provided in Section 3.3.2.

While there were seven Li-borate beads made for the NPK + basalt treatment, only five measurements were considered reliable and used in statistical analysis. Two samples (C9 and C11), were discounted because they were collected during a period when the instrument was frequently malfunctioning during use. All other samples collected for XRF were collected before the malfunctioning (in November and December 2021) while the samples from C9 and C11 were not collected at this time because the instrument broke during data collection (13th December 2021). After this point, the instrument has been in-and-

out of service. During the period that this chapter was written (until March 2022), the instrument was not producing reliable results so it was not possible to either: (1) recollect data or (2) conduct a comparative study between the data collected before the 13th December compared to data collected on the same samples after the 1st March. If the instrument had been operational, a replicated study would have been set up on a sub-set of the samples from all the treatments and reanalysed to test if there were any chemical differences between samples ran before and after the machine malfunctioned were comparable.

Basic statistics (e.g. mean and SE) were computed in R (R Development Core Team, 2018) and advanced statistics (ANOVA with Gabriel post-hoc test) were completed in SPSS (IBM Corp, 2020).

3.2.6. X-ray Photoelectron Spectroscopy (XPS)

All XPS analysis was performed at the Sheffield Surface Analysis Centre, based in the Department of Chemistry at the University of Sheffield. The sample analysis was conducted by Dr D Hammond (Experimental Officer), and interpretation of the data was completed by the author, with advice from Dr D Hammond. XPS is an expensive technique – therefore for each of the fertiliser treatments, only three independent samples were taken from the seven available samples. For the NPK + basalt and Manure + basalt treatments, samples from three columns were randomly selected (for NPK + basalt: C8, C10, C13 and Manure + basalt: C24, C25, C28), as well as three subsamples from the Initial basalt which were treated as independent samples. The Org 8 sample was taken from the flask dissolution experiment after 8 weeks of dissolution, though only one replicate was used so results are considered illustrative and qualitative.

Prior to analysis, samples were mounted by pushing the grains into indium foil. The grains and indium foil were electrically isolated from the sample holder by the use of a paper label between the sample holder and the double sided carbon tape used to hold down the indium foil. The analyses were carried out using a Kratos Supra instrument with a monochromated aluminium source. Survey scans were collected between 1200 to 0 eV binding energy, at 160 eV pass energy, 1 eV intervals, and 300 seconds/sweep with one sweep being

collected. High-resolution Na 1s, Fe 2p, O 1s, Ca 2p, C 1s, P 2p, Si 2p, and Al 2p scans were also collected at 20 eV pass energy and 0.1 eV intervals for each analysis point over an appropriate energy range, with one 300 second sweep for all spectra except C 1s (2 sweeps), Fe 2p (3 sweeps, due to the greater energy range to be covered) and P 2p (2 sweeps). All surface elemental data described in the Results section (Section 3.1) were taken from the high-resolution scans, with the exception of Mg. Instead, Mg concentrations were taken from the Mg 2p peak collected in the survey scan because no high-resolution scans were collected for the Mg 2p peak.

The data collected were calibrated in intensity using a transmission function characteristic of the instrument to make the values instrument independent. The data can then be quantified using theoretical Schofield relative sensitivity factors modified to account for instrument geometry, variation in penetration depth with energy and the angular distribution of the photoelectrons. The high resolution spectra were all calibrated in eV by fixing the main C 1s peak to be 285.0 eV. The data have been analysed using CasaXPS software (Fairley *et al.*, 2021).

For each independent sample, two areas of 700 µm by 300 µm were analysed. The chemical data collected from the two arein accordance with independent sample were averaged for use in the statistical analysis. The kaolinite contamination would have influenced the surface Al, Si and O concentrations, similar to how the whole-rock chemistry would have been influenced by Al_2O_3 and SiO_2 concentrations. Al, Si and O concentrations were therefore subtracted from the XPS data and the relative proportions of all other elements were recalculated. For completeness, uncorrected Al and Si concentrations are provided in Section 3.3.1.

A Kruskal-Wallis non-parametric test for variance analysis was used to assess variance followed by a Dunn post-hoc test to compare pairwise significance in the elemental concentrations between each treatment combination. These analyses were completed in R (R Development Core Team, 2018)

3.2.7. Fourier Transform Infrared (FTIR) Spectroscopy

3.2.7.1 Diffuse Reflectance Infrared Fourier Transform Spectroscopy – DRIFTS

All DRIFTS spectra were collected in the Materials and Engineering Research Institute at Sheffield Hallam University. DRIFTS was conducted on the same three samples that were used for the XPS analysis. Additionally, three quartz samples, from grains emplaced in mesh bags (from columns C10 (NPK + basalt) and C24 (Manure + basalt), as well as an 'Initial quartz' sample) to similar depths of the mesh bags containing the basalt, and a soil sample were also characterised using DRIFTS.

DRIFTS spectra were collected using a Thermo Nicolet Nexus spectrometer and a Graseby Specac 'Selector' DRIFTS accessory along the spectral range of 700-4000 cm^{-1} with a spectral resolution of 4 cm^{-1}. 64 scans from each sample were collected, then averaged by the collection software: Omnic 6.1. Samples at 5 wt.% (0.015 g) were ground with KBr (0.285 g) (FT-IR grade, <99% trace metals, Sigma Aldrich) for 1 minute using a pestle and mortar. Care was taken to reproduce the same pressure applied to each sample. The resulting mixtures were also reproducibly packed into the sampling cups. Before analysis, samples were sparged for 2 minutes using dried, CO_2-free air then analysed immediately to remove any adsorbed water vapour or CO_2 which adhered to the sample's surface. A fresh background scan of KBr was also produced before each sample was run, which was later corrected by subtracting the background from the scan which included the sample.

The corrected spectra baselines were then corrected in bulk using Quasar spectroscopy software (Toplak *et al.*, 2021) to correct the background using a positive rubber band correction using the 'Pre-process Spectra' function. Where appropriate, average spectra were calculated in the built in 'Spectra' function.

3.2.7.2 Attenuated Total Reflectance (ATR) Spectroscopy

ATR spectra were collected on a Bruker Alpha Platinum ATR at the Department of Chemistry, University of Sheffield. For each spectrum, 24 scans were collated. Spectra were collected to a resolution of 4 cm^{-1} wavenumbers and

in transmission mode. In total six spectra were taken from the 14 independent samples (seven NPK + basalt, seven Manure + basalt), and twelve spectra were taken for the Initial basalt. More samples were taken for the Initial basalt to gain a more representative analysis of it as it was being used for comparative purposes. Similar to the DRIFTS spectroscopy, data was collated in the Quasar spectroscopic software (Toplak *et al.*, 2021), though baseline corrections were conducted using a negative rubber band correction.

3.2.8. Thermogravimentric Analysis with Mass Spectrometry (TGA-MS)

TGA-MS was conducted by Mr S Kemp at the British Geological Survey, Keyworth. The TGA-MS was run on three samples, one from each treatment (Columns C8 for NPK + basalt, C24 for the Manure + basalt treatment, and the Initial basalt). The methodology for TGA-MS can be found in Section 2.2.5.

3.2.9. Sequential extractions

3.2.9.1. Extraction procedure

The set of sequential extractions, adapting from the methodology Heckman, Lawrence and Harden (2018) and Gabriel, Kellman and Prest (2018) were conducted to quantify pools of: (1) water soluble OC, Al, Fe and Mn, (2) complexed Fe, Al, Mn with OC, (3) poorly crystalline Fe, Al, Mn and associated OC and (4) crystalline Fe, Al, Mn and associated OC in the basalt grains. UPW, 0.1 M Na-pyrophosphate, 0.1 M hydroxylamine hydrochloride and 0.5 M Na-dithionite with 0.05 M HCl were used to extract each of the respective pools. Some of the limitations of the sequential extraction methodology used in this chapter can be found in Section 6.6.1.

For the Initial basalt and samples extracted from the fertiliser treatment experiment (i.e. NPK + basalt and Manure + basalt), 0.25 g and 0.5 g of sample respectively were weighed into a 50 mL polypropylene centrifuge tube. Weights of both tubes and sample were recorded. In line with the XRF analysis, three independent samples were measured of the Initial basalt, and seven for both the NPK + basalt and Manure + basalt treatments.

The first extraction was the UPW extraction, implemented using a ratio of 1:30 basalt:UPW, mass:volume. Once added to the centrifuge tube, the tube was weighed and vortexed for 20 s using a Medline Scientific Vortex and placed overnight for 16 hours on a Bibby Scientific Stuart Rotator Disk SB3 at an angle of 50° and speed of 20 rpm. After 16 hours, the samples were centrifuged firstly on a Centrifuge Heraeus Megafuge 40 at 4800 g for 15 minutes to settle to sediment into a pellet at the bottom of the centrifuge tube, before being re-centrifuged using a Sigma 4-16 KS at 13,000 g for 15 minutes to settle out smaller colloids.

Once centrifuged, the supernatant was pipetted off. Firstly, a 33% volume subset of supernatant was removed and retained for OC analysis. During trial experiments, it was found that trace amounts of OC were leached from 0.2 µm and 0.45 µm syringe filters and therefore samples were analysed without prior filtering. The samples therefore represented Total Organic Carbon (TOC), rather than DOC. After this aliquot was removed, a further 33% volume of the sample was removed and filtered using a 0.2 µm filter for ICP-MS analysis. To avoid damaging the basalt pellet at the bottom of the centrifuge tube, the remnant supernatant was left in the bottom of the centrifuge tube to dry into a moist pellet in an oven at 60°C. Details of how this remnant supernatant was taken into account in terms of calculations is provided in the final paragraph of this section. In addition, sometimes the moist pellet became dry in the oven with some samples becoming drier than others. This was particularly prevalent in the UPW-extractions and on occasion, in samples from other extractions, the moist pellet became dry in the oven due to the differential temperatures within the oven. On these occasions, the samples were gentle rehomogenised using a glass rod, taking care to avoid abrasion of the PP tube.

The process was then repeated with the other extractants. For both the second and third extractions, Na-pyrophosphate and hydroxylamine hydrochloride respectively, a ratio of 1:40 basalt:extractant was used. In both of these extractions, after centrifuging, 50% of the supernatant was pipetted off and saved for TOC analysis, and a further 25% removed for ICP-MS analysis. The final 25% of sample was left to dry in the oven at 60°C. The Na-dithionite with 0.05 M HCl extraction was conducted in two parts. Firstly, a 1:30 basalt: Na-

dithionite ratio suspension was produced in the centrifuge tube to react overnight (16 hours) and then centrifuged to the same protocol as described above. After centrifugation, all the Na-dithionite was removed (±1%). Then a ratio of 1:10 basalt:0.5 M HCl was added to the centrifuge tubes and placed on the rotating shaker for 2 hrs. After centrifugation, the Na-dithionite extract and HCl wash were combined to produce one analytical sample for each independent sample.

To account for carryover in later extractions, the proportion of remnant supernatant from the previous extraction was multiplied by the concentrations of the given element from the previous extractions, and then this value was subtracted from the total concentration measured on the extraction in question. For example, the reported values given for the Na-pyrophosphate-extractable pool ($NaPy_{real}$) was calculated by subtracting the concentration of the UPW-extractable pool (UPW_{real}) remnant multiplied by the amount of UPW-extract remaining in the bottom of the centrifuge tube ($UPW_{rem.supernatant}$) from the measured Na-pyrophosphate concentration ($NaPy_{measured}$). As an example, the value reported in this thesis for the Na-pyrophosphate extraction can be explained by the following equation (Eq. 3.1):

$$NaPy_{real} = NaPy_{measured} - (UPW_{real} \cdot UPW_{rem.supernatant})$$

(Eq. 3.1)

3.2.9.2. Extractant analysis

TOC analysis was carried out using the setting to measure non-pulverised organic carbon (NPOC) on a Shimazdu TOC-L Total Organic Carbon Analyser (Shimazdu, Japan), calibrated to a 1-25 ppm range. Every 10 samples, 1 and 25 ppm OC standards were run to assess accuracy, along with one blank sample (of UPW water) to calculate sample carry over. Four injections were taken for each independent sample. The first injection was discarded as carry-over and the final three were later averaged out to produce one analytical value per independent sample per extraction.

The detection limit of the instrument was determined to be 0.2 mg L^{-1}, machine precision was within 1.43% and accuracy was 122%. Precision and accuracy were determined by measuring five replicates of 12 concentrations prepared using potassium hydrogen phthalate from 0.5 mg L^{-1} OC to 5 mg L^{-1}

OC. The precision was determined by firstly calculating the minimum and maximum values from the five replicates of the 12 concentrations which were prepared. This difference was then divided by the mean value from the respective prepared concentration, and the median value from this analysis was then reported. Accuracy was calculated as a percentage of the ratio from the measured concentration to the 'expected' concentration.

Dissolved element analysis was conducted using ICP-MS on a Thermo-Fisher iCAP-Q at the University of Nottingham. Prior to analysis, samples were filtered through a 0.2 µm filter to remove colloidal particles and acidified to a concentration of 2% HNO_3. Major elements (Na, Mg, K and Ca) were calibrated between 10-30 ppm, and minor elements between 20-100 ppb.

Both OC and dissolved elemental data were then compiled and analysed using simple statistics in R (R Development Core Team, 2018) and more advanced statistics (e.g. ANOVA with a Gabriel post-hoc test) were completed using the SPSS statistical package (IBM Corp, 2020).

3.2.10. Scanning Electron Microscopy

Scanning Electron Microscopy was conducted on carbon-coated stubs, using the same methods as detailed in Chapter 2 (Section 2.2), on the same three samples that were characterised using DRIFTS and XPS.

3.2.11. Geochemical modelling

Geochemical models were used to predict the saturation index (SI) and ion activities of phases and species predicted to form and be present, respectively, under natural conditions of the flask dissolution experiment, as described in Section 3.2.4. Two solutions were studied: (1) the initial compost extract solution and (2) the solution after one week of basalt weathering in the compost extract, as summarised in Table 3.4. The solution chemistry from the flask dissolution experiment is assumed to be somewhat representative of the solution microenvironment directly surrounding the basalt grain.

The PHREEQC geochemical modelling software was used (Parkhurst and Appelo, 2013). For this, PHREEQC was run in R using the 'PHREEQC' package

(De Lucia and Kühn, 2013) alongside the tidyphreeqc package (Dunnington, 2020). The Amm_T-H.dat database (Appelo and Postma, 2004) was primarily chosen for: (1) consistency between modelling throughout this thesis (e.g. reactive transport modelling in Chapter 2) and (2) to distinguish between organic and inorganic carbon input (by attributing OC to 'Humate' and inorganic C to 'C'. Elemental data (Al, Ba, Ca, Fe, K, Li, Mg, Mn, Na, Si, Sr, Zn, S, Cu, Ni, V and B), along with TOC and TIC were also inputted into the model. The model temperature was set to 21°C, and pH modelled along a gradient from 5-9, at 0.1 pH unit increments. Given that pH could be considered the most dynamic geochemical variable, by using a pH gradient it was possible to determine the likelihood of mineral precipitation at a variety of pHs. The model can be found in Appendix B.

3.2.12. Additional porewater data

In the discussion of this chapter (Section 3.4), occasionally, the pH and nitrate bulk porewater measurements taken during the growth experiment which the basalt bags were deployed into are referred to in the data interpretation section. This data is found and described in full in Chapter 4, with methodology found in Section 4.3.8 and results in Section 4.4.5.

3.3. Results

3.3.1 Surface elemental chemistry (XPS)

3.3.1.1. Initial, NPK + basalt and Manure + basalt treatment

It was mentioned in the XPS methods (Section 3.2.6) that there was evidence that the soil mineral contamination significantly skewed the surface chemistry measurements for Al and Si, data for these elements are presented here for completeness of data in Figure 3.2. In the uncorrected dataset, there are significant differences in Al and Si concentrations between unweathered basalt (Sample = Initial basalt) and basalt grains extracted from the two fertiliser treatments (Samples = NPK + basalt and Manure + basalt). Relative to the Initial basalt (Initial basalt = 4.5 At.% Al), surface Al increased by 1.8 At.% ($p = 0.031$) and 1.5 At.% ($p = 0.022$) for Manure + basalt and NPK + basalt treatments

respectively. Conversely, surface Si (Initial basalt = 21.9 At.% Si) decreased by 2.4 At.% ($p = 0.059$) and 2.2 At.% ($p = 0.022$) for NPK + basalt and Manure + basalt treatments respectively, when compared to the Initial basalt. No significant differences in surface Al and Si between the NPK + basalt and Manure + basalt treatments ($p = 0.893$ for Al; $p = 0.686$ for Si) were observed.

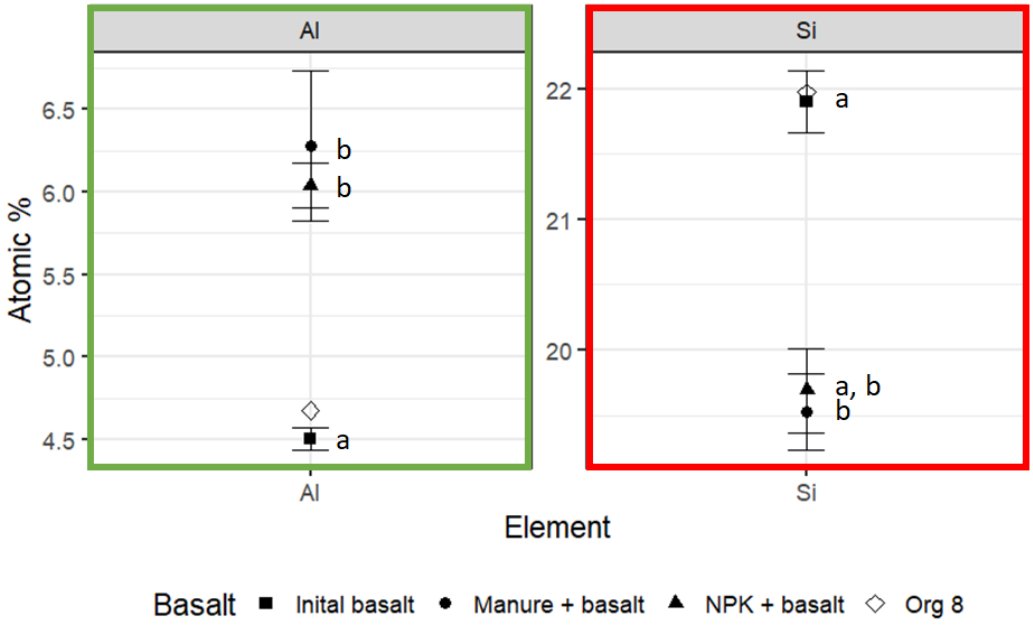

Figure 3.2 – Surface elemental abundance of Al and Si as inferred from X-ray Photoelectron Spectroscopy (XPS) of the original XPS dataset for each treatment. Points represent mean, and error bars represent ± standard error. n = 3 for each treatment except Org 8, where only one replicate was measured. Letters a and b correspond to statistical significance groupings ($p < 0.05$), as determined using Kruskal Wallis with Dunn post-hoc test. Green box highlights increase in concentration in fertiliser treatments relative to the Initial basalt and red box indicates a decrease in concentration in fertiliser treatments relative to the Initial basalt.

From this point on, the XPS data refers to corrected data with recalculated elemental concentrations once Al, Si and O were removed from the dataset. The corrected XPS data is summarised in Figure 3.3. As the sum of the Al, Si and O concentrations ranged between 73.7 and 81.0 At.% of the surface elements from analysis, the calculated At.% values of the remaining elements are large, but should only be considered comparative between the elements shown within Figure 3.3 (C, Ca, Fe, K, Mg and Na). There were no significant differences observed between the surface Ca and C concentrations between each treatment.

Ca concentrations decrease from 13.0 At.% in the Initial basalt by up to 4.0 At.%. ($p = 0.007$) in the NPK + basalt and by 3.0 At.% ($p = 0.080$) in the Manure + basalt treatment. Conversely, C concentrations increase from an Initial C concentration of 30.0 At.% by an average of 12.2 At.% ($p = 0.022$) in the Manure + basalt treatment and by an average of 8.4 At.% in the NPK + basalt treatment ($p = 0.178$). Clear separations between the NPK + basalt and Manure + basalt treatments are observed in both C and Ca in Figure 3.3, but these differences are not significant ($p = 0.345$ for both C and Ca).

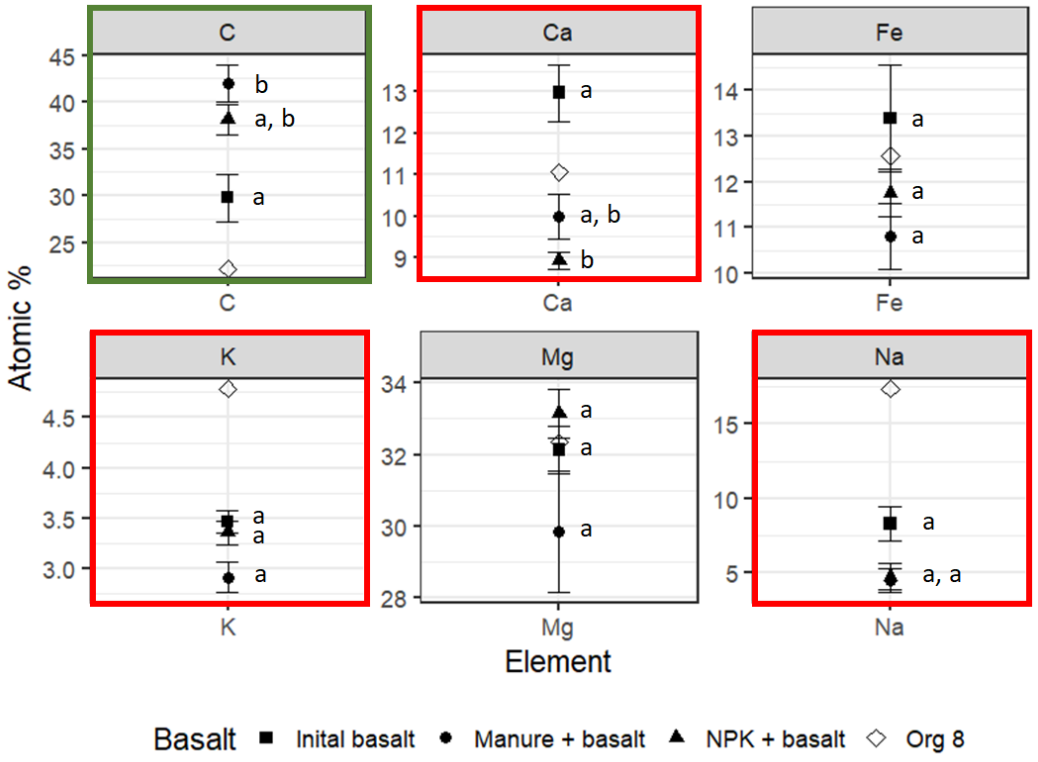

Figure 3.3 – Surface elemental abundance of X-ray Photoelectron Spectroscopy (XPS), recalculated once Al, Si and O concentrations were removed, for each treatment. Points represent mean, and error bars represent ± standard error. N = 3 for each treatment except Org 8, where only one replicate was measured. Letters a and b correspond to statistical significance groupings ($p < 0.05$), as determined using Kruskal Wallis with Dunn post-hoc test. Green box highlights a concentration increase in fertiliser treatments relative to the Initial basalt and red box highlights concentration decrease in fertiliser treatments relative to the Initial basalt.

Na concentrations also decreased by similar proportions in the fertiliser treatments relative to the Initial basalt but had a lower significance. Values decreased from the mean Initial basalt Na concentration of 4.7 At.% by 3.6 At.% ($p = 0.080$) and 3.8 At.% ($p = 0.059$) for the NPK + basalt and Manure + basalt treatment respectively. There was a different response to K concentrations between the two fertiliser regimes with the mean K concentration decreasing by 0.6 At.% ($p = 0.059$) in the Manure + basalt treatment and by only 0.1 At.% ($p = 0.590$) in the NPK + basalt treatment. There was no significant difference between the K concentrations of the two fertiliser treatments ($p = 0.178$) despite the large differences in mean concentrations.

Neither Fe or Mg concentrations significantly changed (Figure 3.3), and while P concentrations were measured, they were too low to be accurately detected using XPS.

3.3.1.2. Comparison with basalt from basalt microenvironment dissolution experiment

As mentioned in the methods Section 3.2.6, only one replicate was measured for the Org 8 experiment, so it was not possible to compare mean values between the Org 8 and other sample groups. However, when the upper and lower limits of two standard deviations (2σ) from the mean value of the measured elements in the Initial basalt were calculated (Table 3.1), only Na and K concentrations were outside the mean$\pm 2\sigma$.

Table 3.1 – Mean At.% of elements ±2σ (2σ = 2 standard deviations) of the Initial basalt compared with the At.% of elements in the Org 8.

Element	Initial basalt mean, At.%	σ, At.%	Range (Mean ± 2σ)	Org 8, At.%	Within 2σ?
Al, Si and O removed					
C	29.78	4.36	21.05 - 38.50	22.20	FALSE
Ca	13.00	1.19	10.61 - 15.35	11.06	FALSE
Fe	13.39	2.03	9.34 - 17.45	12.57	FALSE
K	3.46	0.20	3.06 - 3.87	4.79	TRUE
Mg	32.13	1.17	29.80 - 34.46	32.34	FALSE
Na	8.26	2.02	4.22 - 12.30	17.40	TRUE
Original data					
Si	21.90	5.89	21.08 – 22.72	21.97	FALSE
Al	4.51	1.96	4.27 – 4.74	4.68	FALSE

3.3.1.3. Binding environment data

SEM-BSE imaging revealed both poly- and mono-mineralic grains of differing chemical compositions (Figure 3.4). Differences in chemical composition will affect the degree of charging disproportionally across elements, and therefore once all the XPS HR scans are calibrated to the C1s peak (HR scan of the 1s orbital in C), different grains will charge-correct differently and the 'bulk sample' charge correction may then differ for different elements. As all HR scans were calibrated to the C1s peak, peak positions typically observed for the C1s peak naturally coincide with expected peak positions. However, assuming Ca and Fe will be bonded to O, highly likely given the silicate rock type, the peak positions of Fe and Ca were 1.7 and 1.2 eV higher respectively when compared to commonly published peak positions (Ni and Ratner, 2008; Grosvenor *et al.*, 2004). Both Na and Al peaks were also observed to be up to 0.2 eV different from expected values (Kloprogge *et al.*, 2006), though was considered permissible due to wide and small peak sizes. While the variable charge still makes it possible to obtain surface elemental chemistry, it proved impossible to assess changes in binding environments which are identified through changes in peak positions.

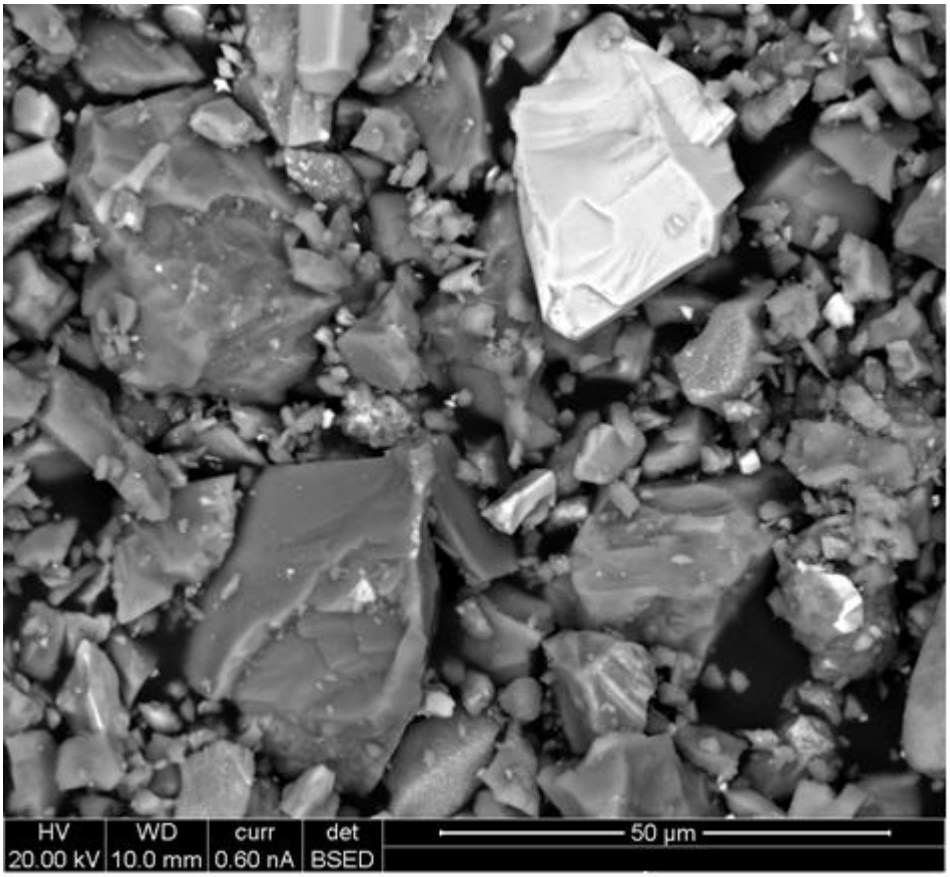

Figure 3.4 – Exemplary backscattered electron image of Initial basalt demonstrating the chemical heterogeneity of the basalt grain as evidenced by the differing contrast between grains. Lighter areas represent minerals with heavier elements (e.g. higher Fe, Mg concentrations while darker areas represent minerals with lighter elements (e.g. higher Si, Al). Image taken from stub 'Initial-C'.

Out of all of the elements analysed, distinct changes to the binding environment of the basalt grains could only be identified in the C1s high resolution scan. As detailed in the surface elemental data above, once basalt was applied to the soil, the surface OC increased by up to 12.2 At.%. Three distinguished carbon binding environments were identified: C=C, O-C=O and C-O-C. In all groups, the highest concentrations in each binding environment were observed in the Manure + basalt treatment, followed by the NPK + basalt treatment then the Initial basalt treatment and lastly, the Org 8 sample. Even though there was separation between each treatment for the different binding environments (Figure 3.5), only the Manure + basalt treatment is significantly different to the Initial basalt in the O-C=O groups ($p = 0.022$). No other significant results were identified between the treatments.

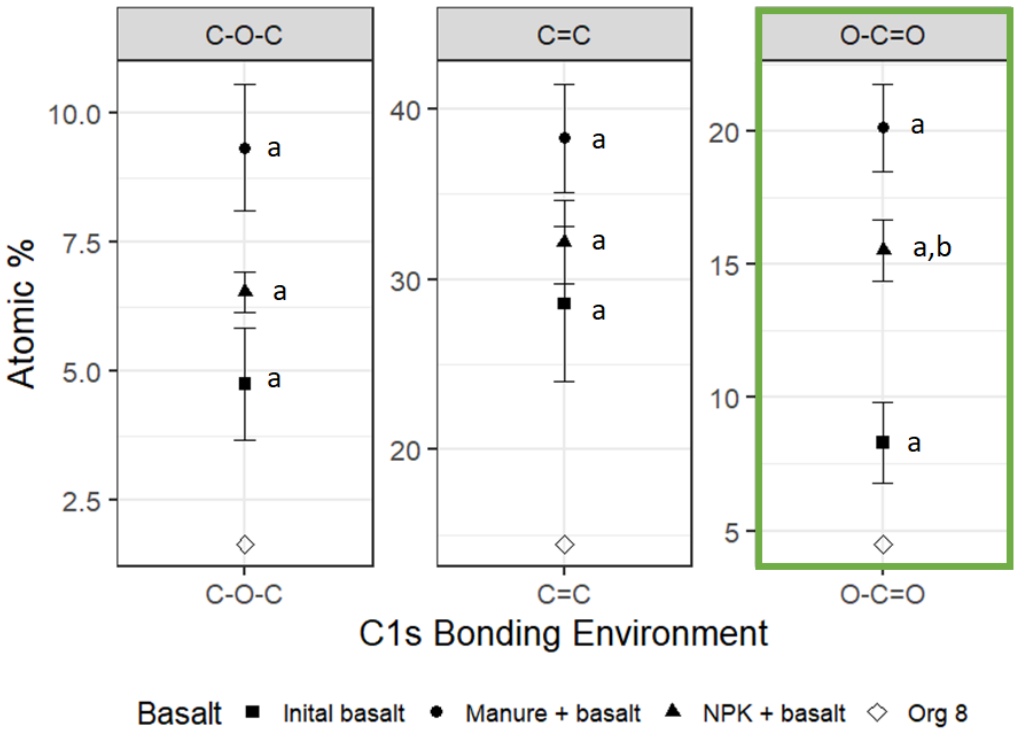

Figure 3.5 – Graph summarising the C1s bonding environment inferred from X-ray Photoelectron Spectroscopy (XPS) for each treatment. Point values represent the mean, and error bars show ± standard error. N = 3 for each treatment except Org 8, where only one replicate was taken. Letters a and b correspond to statistical significance groupings ($p < 0.05$), (e.g. a and b are significantly different; a and a are not significantly different), as determined using Kruskal Wallis with Dunn post-hoc test. Green box highlights increase relative in the fertiliser treatments relative to the Initial basalt.

The relative proportions of the three carbon binding environments, however, were not consistent between treatments (Figure 3.5, Figure 3.6 and Table 3.2). In the Initial basalt, C=C bonding dominates with a small proportion of O-C=O and C-O-C bonds. The ratio between the O-C=O and C-O-C bonding compared to C=C bonds were measured at 0.29 and 0.16 compared respectively. The O-C=O and C-O-C bonds increase in basalt grains extracted from both fertiliser treatments. The proportions of O-C=O bonds increase to 0.53 and 0.48, and C-O-C bonds to 0.24 and 0.21 in the Manure + basalt and NPK + basalt respectively (Table 3.2).

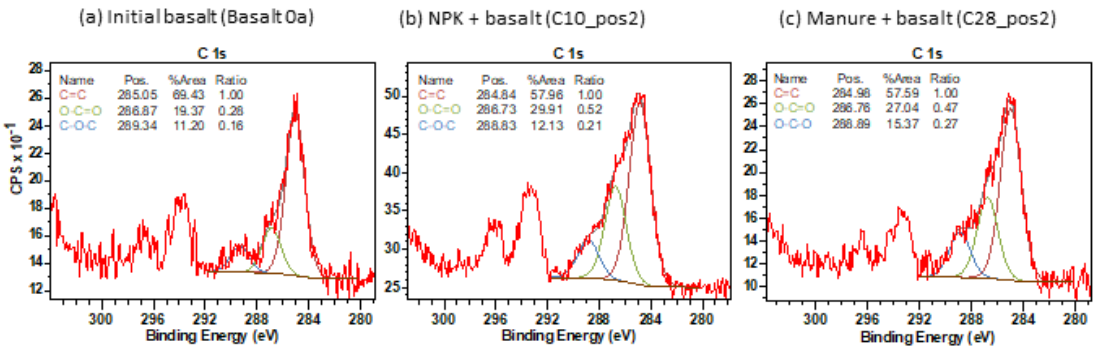

Figure 3.6 – Representative C1s spectra for the Initial basalt (a), the NPK + basalt spectrum (b) and the Manure + basalt spectrum (c). Peak position (Pos.), %Area of the C1s peak and the ratio between each binding environment are provided in the table appended to each spectrum. The reference spectra (i.e. Basalt 0a) are provided for completeness of data.

Table 3.2 – Mean ratios of different carbon binding environments observed in the XPS data.

Basalt	C=C:O-C=C:C-O-C
Initial	1:0.28:0.16
Manure + basalt	1:0.47:0.27
NPK + basalt	1:0.52:0.21

Both Fe and Al binding environments were also considered though it was not possible to interpret the peak position of different binding environments due to their off-set peak position as a result of differential charging (see Figure 3.4 and related text). The candidates for secondary phase formation ($Al(OH)_3$ and $Fe(OH)_3$ species) each have peaks which are very similar to each other, varying by between 0.2-0.5 eV (Grosvenor *et al.*, 2004; Kloprogge *et al.*, 2006) and close to the spectral resolution of the high resolution scans (0.1 eV).

3.3.2. Bulk chemistry (XRF)

Similar to the XPS results, Si and Al concentrations from the uncorrected XPS dataset are presented first for completeness of data (Figure 3.7). Relative to the Initial basalt, mean Al_2O_3 concentrations increased by 0.1 wt.% and 0.07 wt.% in the Manure + basalt and NPK + basalt treatments respectively ($p <$

0.001). However, there were no significant differences observed between any of the treatments for SiO_2 ($p < 0.705$).

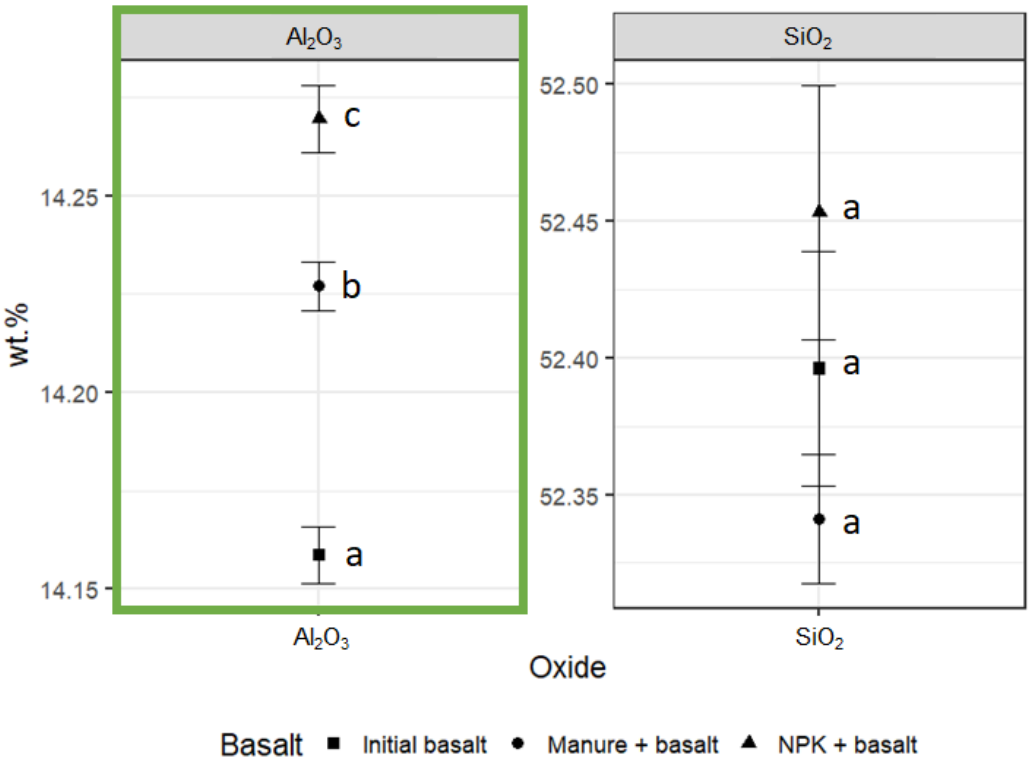

Figure 3.7 – Graph summarising X-ray Fluorescence (XRF) data for each treatment for Al_2O_3 and SiO_2 of the original XPS dataset for each treatment. Point values represent the mean, and error bars show ± standard error. N = 7 for the fertiliser treatments (NPK + basalt and Manure + basalt) and n = 3 for the Initial basalt sample. Letters a, b and c represent statistically significant groupings when considering a significance level of $p < 0.05$ (e.g. a and b are significantly different; a and a are not significantly different), as determined using an ANOVA and Gabriel post-hoc test. Green box highlights increase in the fertiliser treatments relative to the Initial basalt.

The corrected XRF oxide data are summarised in Figure 3.8. Only Mn_3O_4 showed significant differences between the three treatments, decreasing by 0.04 wt.% ($p < 0.001$) and 0.03 wt.% ($p < 0.001$) for the NPK + basalt and Manure + basalt treatments respectively, with a significant difference between the two fertiliser treatments ($p = 0.013$).

Several oxides also show differences when the Initial basalt is compared to both fertiliser treatments. Fe_2O_3 increased by an average of 0.71 and 0.47 wt.%

in the NPK + basalt and Manure + basalt treatments respectively ($p = 0.001$ and $p = 0.008$, respectively). MgO and Na_2O concentrations all decrease when the Initial basalt is compared to the fertiliser treatments. In the NPK + basalt treatment, concentrations of these elements decrease by 1.23 wt.% ($p < 0.001$) and 2.51 wt.% ($p = 0.001$) respectively. In the Manure + basalt treatment, these concentrations decrease by 1.11 wt.% ($p = 0.001$) and 1.91 wt.% ($p = 0.005$) wt.% for MgO and Na_2O respectively.

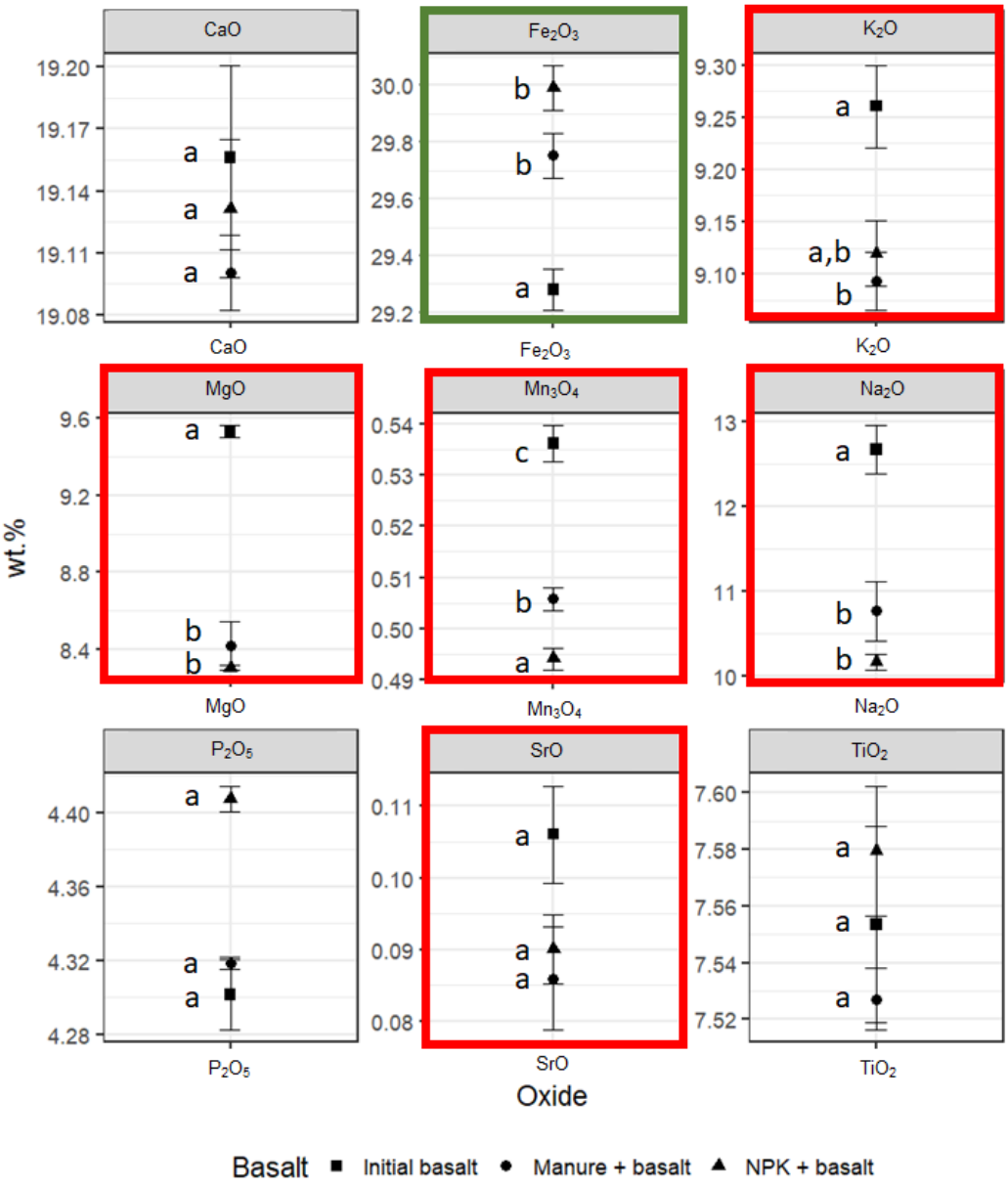

Figure 3.8 – Graph summarising corrected X-ray Fluorescence (XRF) data for each treatment for all measured oxides, with the exception of Al_2O_3 and SiO_2. Point values represent the mean, and error bars show ± standard error. N = 7 for the fertiliser treatments (NPK + basalt and Manure + basalt) and n = 3 for the Initial basalt sample. Letters a, b and c represent statistically significant groupings when considering a significance level of $p < 0.05$, as determined using an ANOVA and Gabriel post-hoc test. Green box highlights increase in fertiliser treatments relative to the Initial basalt and red box highlights decrease in fertiliser treatments relative to the Initial basalt.

Additionally, when comparing the Initial basalt relative to the NPK + basalt, P_2O_5 concentrations increase significantly by 0.028 wt.% ($p < 0.001$), while K_2O concentrations decreased significantly in the Manure + basalt

treatment relative to the Initial basalt by 0.167 wt.% ($p = 0.014$). There were no significant differences in: TiO_2 ($p < 0.797$) and SrO ($p < 0.430$).

3.3.3. Infrared spectroscopy

While FTIR-ATR did not prove successful in identifying any differences between Initial basalt and basalt grains from both fertiliser regimes (Figure 3.9), DRIFTS identified two additional peaks at 3696 cm^{-1} and 3621 cm^{-1} which are diagnostic of kaolinite, amounting to an estimated *c.* 1 wt.% (Geddes, 2006). Kaolinite produces a set of four peaks at 3699, 3669, 3655 and 3621 cm^{-1} (Madejová, 2003) indicative of νAl_2OH (Vingiani *et al.*, 2010), with the peaks at 3699 and 3621 cm^{-1} having roughly equal yet relatively higher intensities (Figure 3.8 and 3.9). In both basalt and soil spectra, the 3621 cm^{-1} peak is much more intense than the 3699 cm^{-1} indicative of an overlapping montmorillonite peak below (Figure 3.10 and 3.11). In addition to the kaolinite and montmorillonite peaks, a broad peak at 3561 cm^{-1} is indicative of the Fe-rich clay mineral nontronite (Figure 3.10 and 3.11), from $\nu Fe^{3+}{}_2OH^-$ (Madejová, 2003; Vingiani *et al.*, 2010) though this is present in all treatments and likely represents the smectite identified through XRD (Figure 3.1). The kaolinite and montmorillonite peaks were also identified in quartz mesh bags (Figure 3.10 and 3.11).

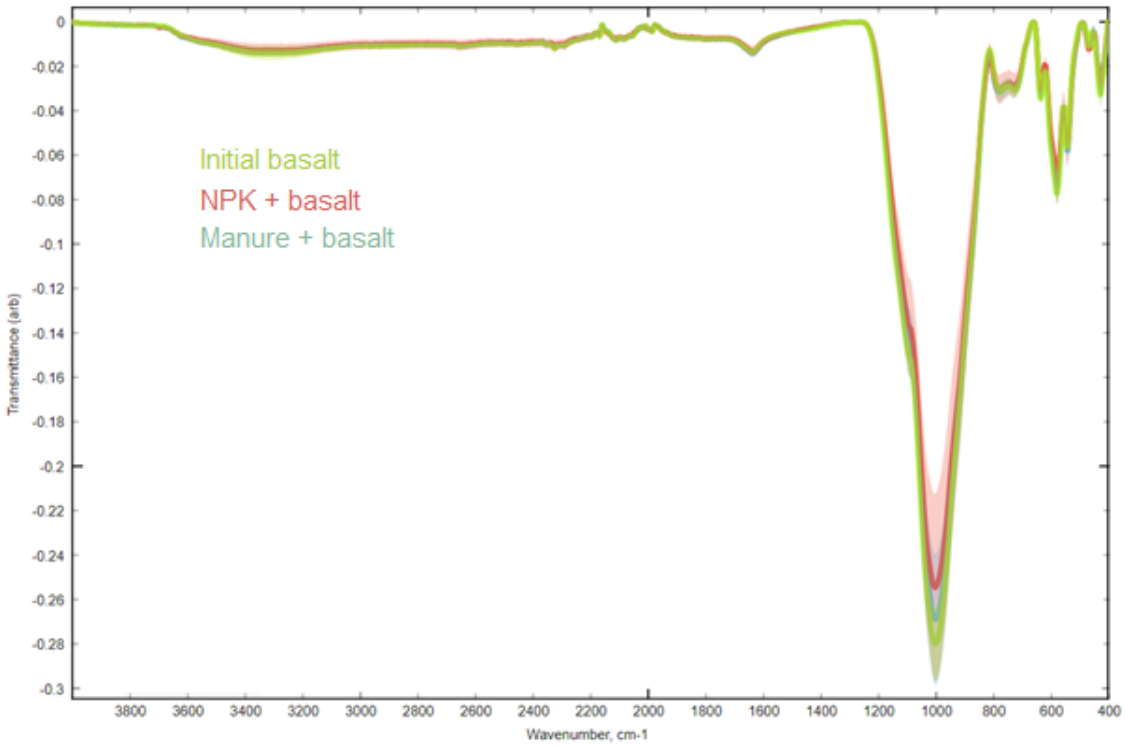

Figure 3.9 – Average Fourier Transform Infrared – Attenuated Total Reflectance (FTIR-ATR) spectra for the Initial basalt (n = 12), NPK + basalt (n = 42) and Manure + basalt (n = 42) treatments. Shaded area around each spectra represents ± standard error.

DRIFTS soil spectra identified several OC peaks and functional groups including C=C and C=O bonding at wavenumbers *c.* 1626-1996 cm^{-1} (Figure 3.10). The DRIFTS spectra of the basalt grains show some OC originally present - specifically at the 2920 and 2851 cm^{-1} (Figure 3.10a). Though, while the basalt bags were exposed to the soil environment, no additional carbon peaks were detected between the initial and treated samples, nor did the intensity of OC peaks increase. Conversely, the intensity of the 2918 and 2849 cm^{-1} C-H stretching peaks did increase in the quartz bags (Figure 3.10c).

ATR spectra of the manure added to the experiment (Figure 3.12) identified several functional groups: C-H (2917 and 2848 cm^{-1}), O-H (3263 cm^{-1}) stretching bands, along with C=O or C=C (1710 and 1631 cm^{-1}). In addition, C=C bands and O=C bands were also observed at 1720 and 1631 cm^{-1} respectively. No C≡C or C≡N bands were observed in the manure sample. Despite being exposed to manure; the basalt grains extracted from the Manure + basalt treatment showed none of the additional manure peaks (Figure 3.10a).

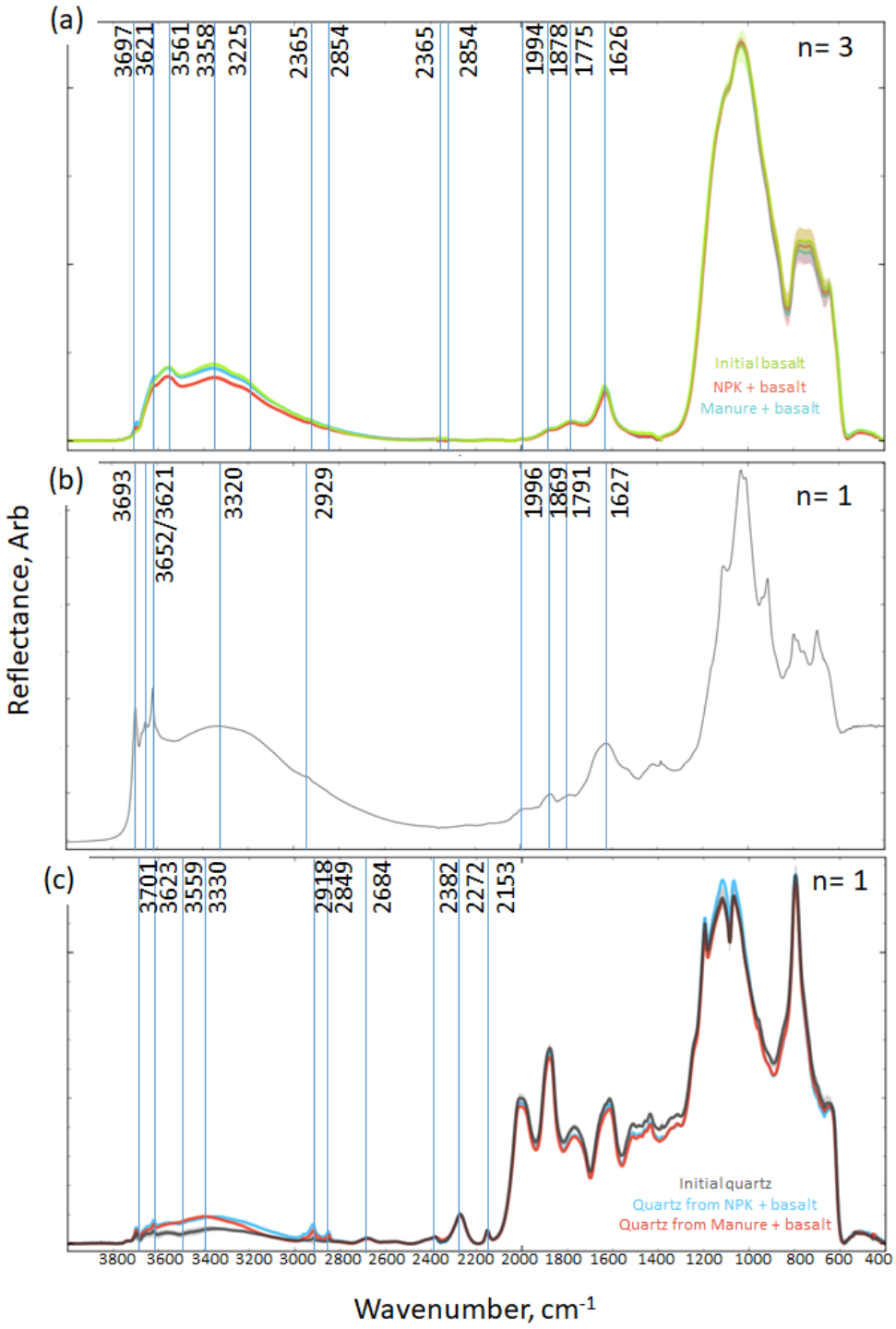

Figure 3.10 – Diffuse Reflectance Infrared Spectroscopy (DRIFTS) spectra of: basalt bags (a), initial soil (b) and quartz bags (c). Panel (a) consists of the average spectrum (n=3) with uncertainty represented in the shaded areas (standard deviation), while panels (b) and (c) show one spectrum per treatment only.

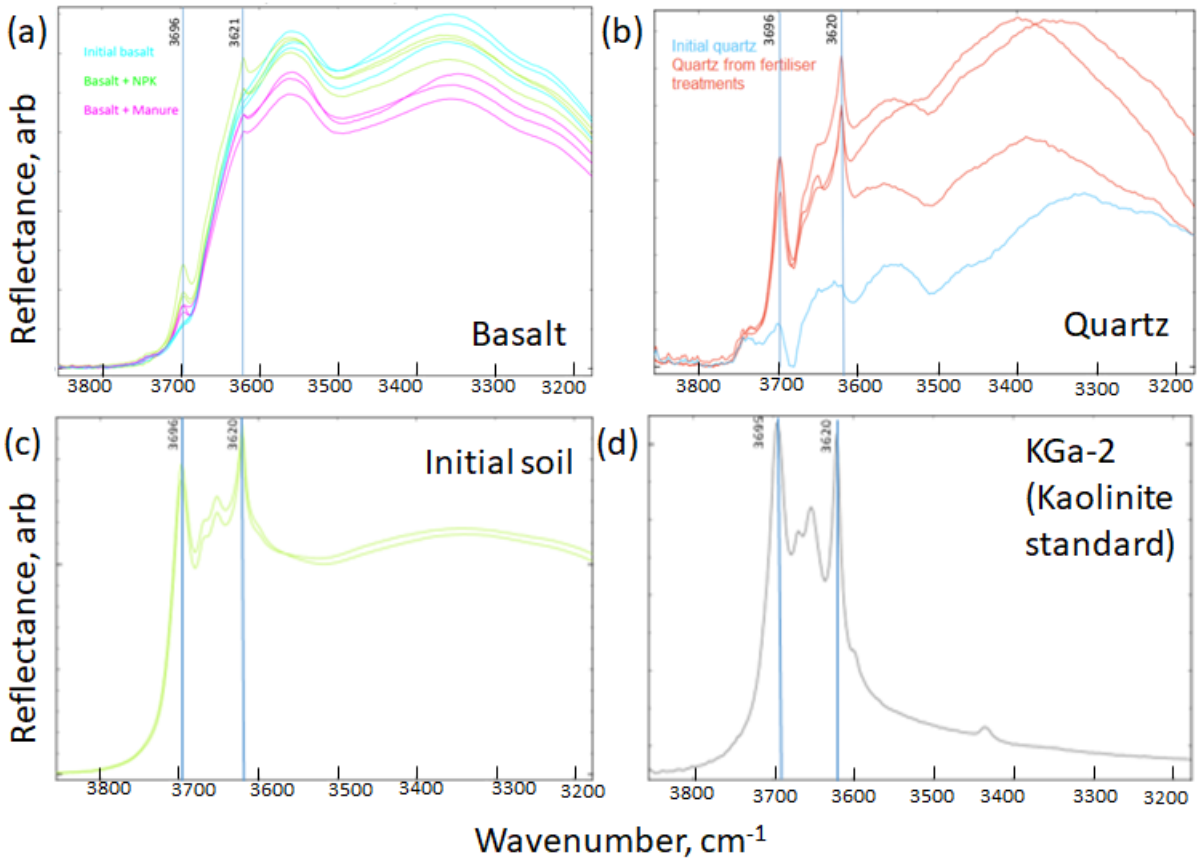

Figure 3.11 – Diffuse Reflectance Infrared Fourier Transform Spectroscopy (DRIFTS) spectra of the high wavenumber regions of: (a) basalt from mesh bags and Initial basalt, (b) quartz from mesh bags and Initial quartz, (c) Initial soil and (d) a pure clay kaolinite sample (KGa-2 from Clay mineral repository, Virginia, USA).

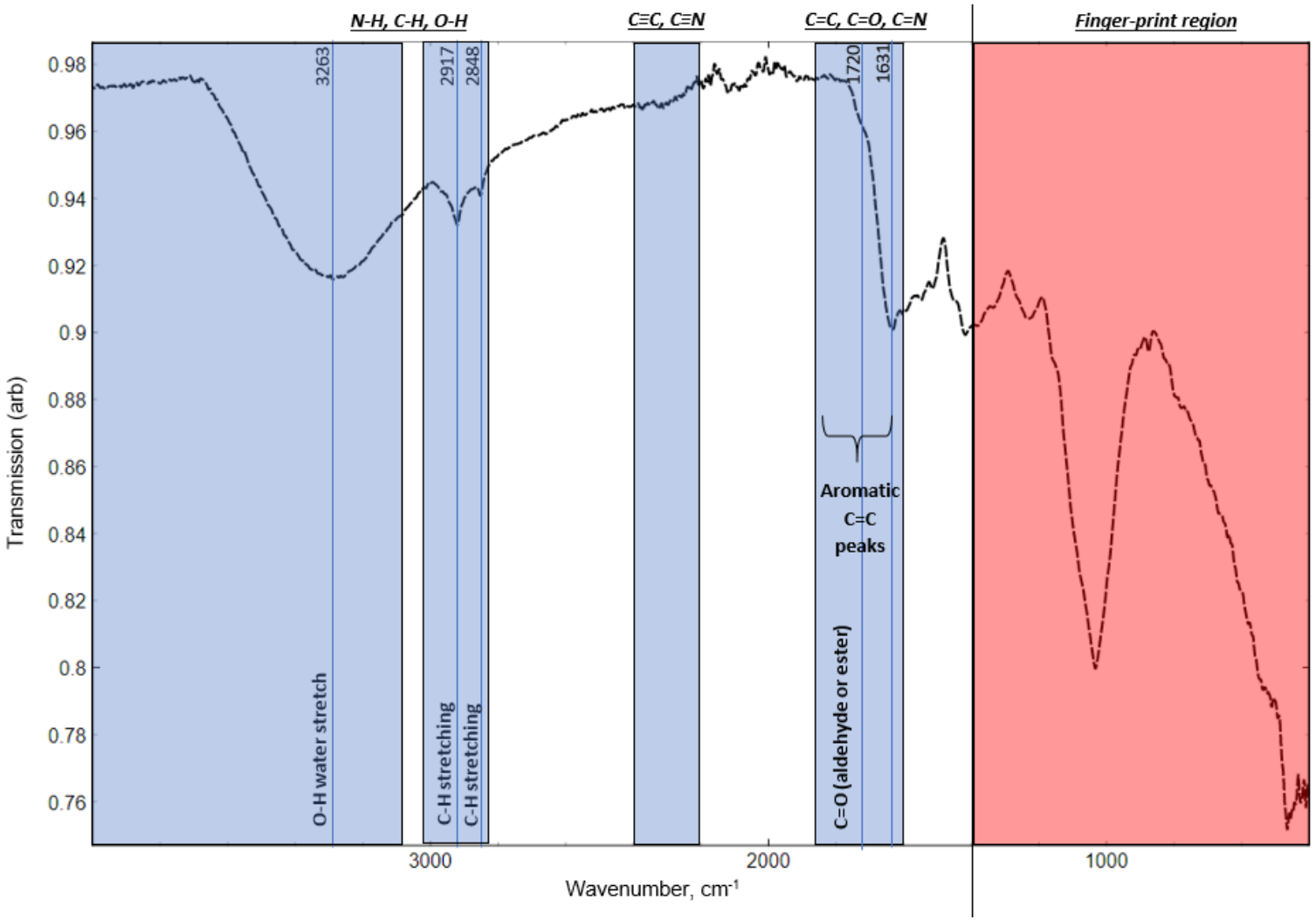

Figure 3.12 – Fourier Transform Infrared-Attenuated Total Reflectance (FTIR-ATR) spectra of the manure fertiliser applied to the Manure + basalt fertiliser treatment. Peak wavenumber and bond interpretation are labelled. The fingerprint region (from 400-1200 cm^{-1}) cannot be accurately determined because there are typically many overlapping peaks between Si-O and C-O groups which makes distinctions between the peaks difficult.

3.3.4. Sequential extractions

All results are summarized in Figures 3.13.

The mean values for the UPW-extractable fraction were negligible for Al and Fe – between 0.002–0.007 mg Al g basalt^{-1} and between 0.003–0.019 mg Fe g basalt^{-1} (Figure 3.13). There were significant increases in UPW-extractable Al and Fe in both fertiliser treatments relative to the Initial basalt ($p < 0.016$ for Al, $p < 0.005$ for Fe). UPW-extractable OC concentrations ranged from 0.30–0.35 mg OC g basalt^{-1}, though there were no significant differences between treatments ($p < 0.88$).

Extractable Al and Fe from the Na-pyrophosphate extraction, inferred as the humus adsorbed/complexed fraction, increased significantly in both fertiliser treatments relative to the Initial basalt (Al = $p < 0.001$, Fe = $p < 0.001$) (Figure 3.13). Na-pyrophosphate extractable Fe and Al was higher in the NPK + basalt treatment compared to the Manure + basalt treatment. Mean Al values increased by 1.2-fold and 1.3-fold and mean Fe values increased up to 1.7-fold and 2.4-fold, for Manure + basalt and NPK + basalt respectively relative to the Initial basalt. In quantitative terms, Na-pyrophosphate extractable Al and Fe attached to the basalt grains represent an additional sink of up to 0.03 mg Al g basalt^{-1} and of up to 0.18 mg Fe g basalt^{-1}. Na-pyrophosphate-extractable OC, however, was not significantly different between treatments – varying by 0.27–0.29 mg OC g basalt^{-1} ($p < 0.94$) (Figure 3.13).

There were no significant differences observed between the Initial basalt and either fertiliser treatment when assessing hydroxylamine hydrochloride-extractable Fe or Al, operationally defined as dissolving the poorly-crystalline phases (Figure 3.13) ($p < 0.441$ for Fe and $p < 0.368$ for Al). A significant difference was, however, observed between the NPK and Manure + basalt treatments because hydroxylamine hydrochloride-extractable Al decreased in the NPK + basalt treatment but increased in the Manure + basalt treatment ($p < 0.033$). However, compared to the Initial basalt mean OC concentrations increased significantly ($p < 0.029$) by 0.023 and 0.057 mg OC g basalt^{-1} for the NPK + basalt and Manure + basalt grains respectively (Figure 3.13). The OC

extracted from both fertiliser treatments were also significantly different from each other ($p < 0.001$).

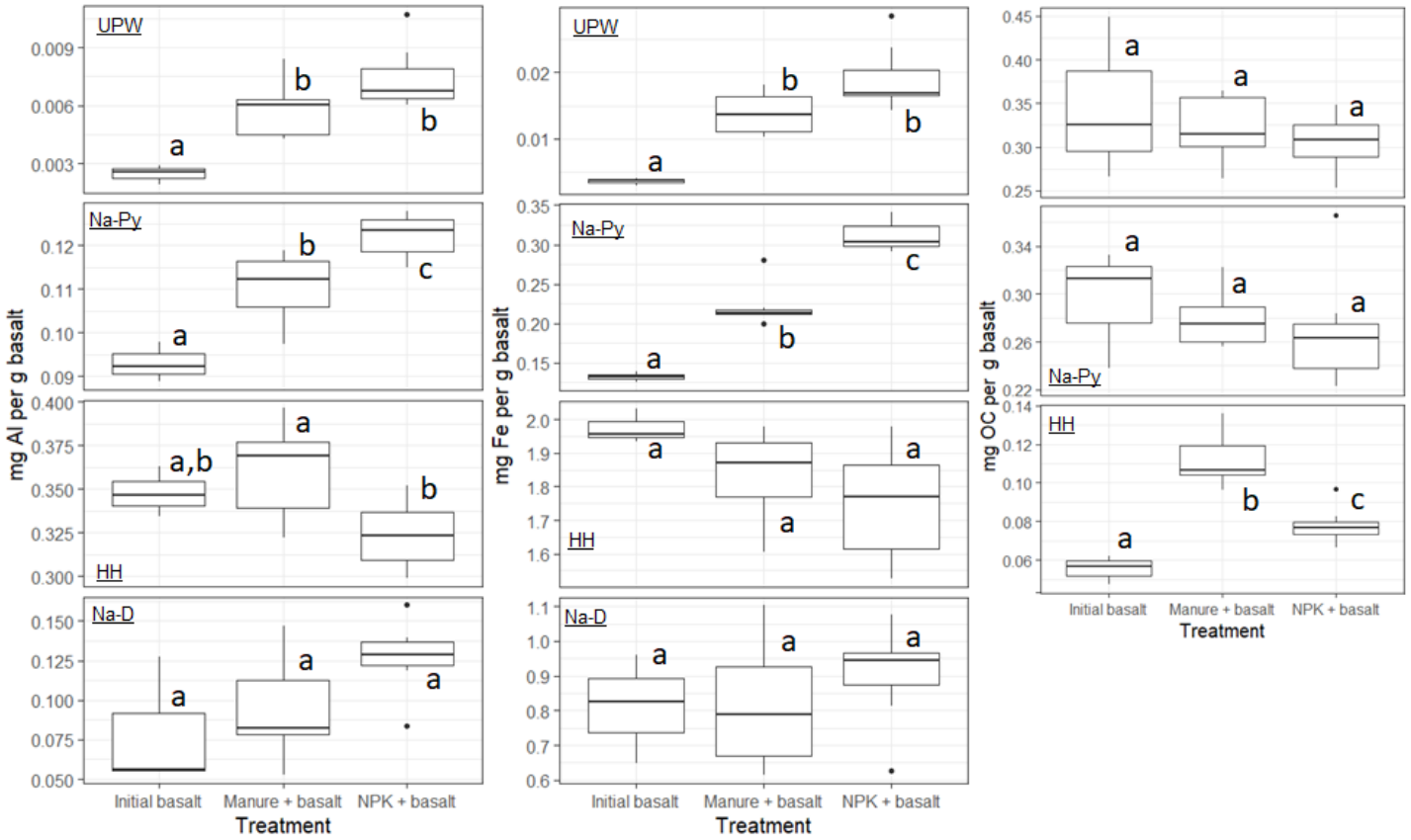

Figure 3.13 – Extractable-Al, -Fe and -organic carbon (-OC) fractions for the Initial basalt grains (n = 3), Manure + basalt (n = 7) and NPK + basalt (n = 7) fertiliser treatments. Letters are used to differentiate significant differences between different treatments (e.g. a and b are significantly different; a and a are not significantly different.) UPW = Ultra-pure water (water soluble); Na-Py = Na-pyrophosphate (humus adsorbed/complexed); HH = hydroxylamine hydrochloride (poorly crystalline); Na-D = Na-dithionite (crystalline).

No significant differences were observed in the Na-dithionite-extracts (crystalline pool) in either the extractable Al, Fe or OC (Figure 3.13). In fact, no Na-dithionite-extractable OC was measured, as evidenced by the negative values. These negative values are thought to have originated from the subtraction calculation from the sequential subtraction (Eq. 3.1), whereby after each extraction the remnant supernatant from the previous extraction is subtracted out (see Section 3.2.9.1).

Mn associated with each of the four extractions decreased in both treatments relative to Initial basalt (Figure 3.14) with the exception of the Na-dithionite-extractable pool where no significant differences were observed. Significant decreases in both fertiliser treatments relative to the Initial basalt were observed in the UPW-, Na-pyrophosphate- and hydroxylamine hydrochloride-extractable fractions ($p < 0.001$).

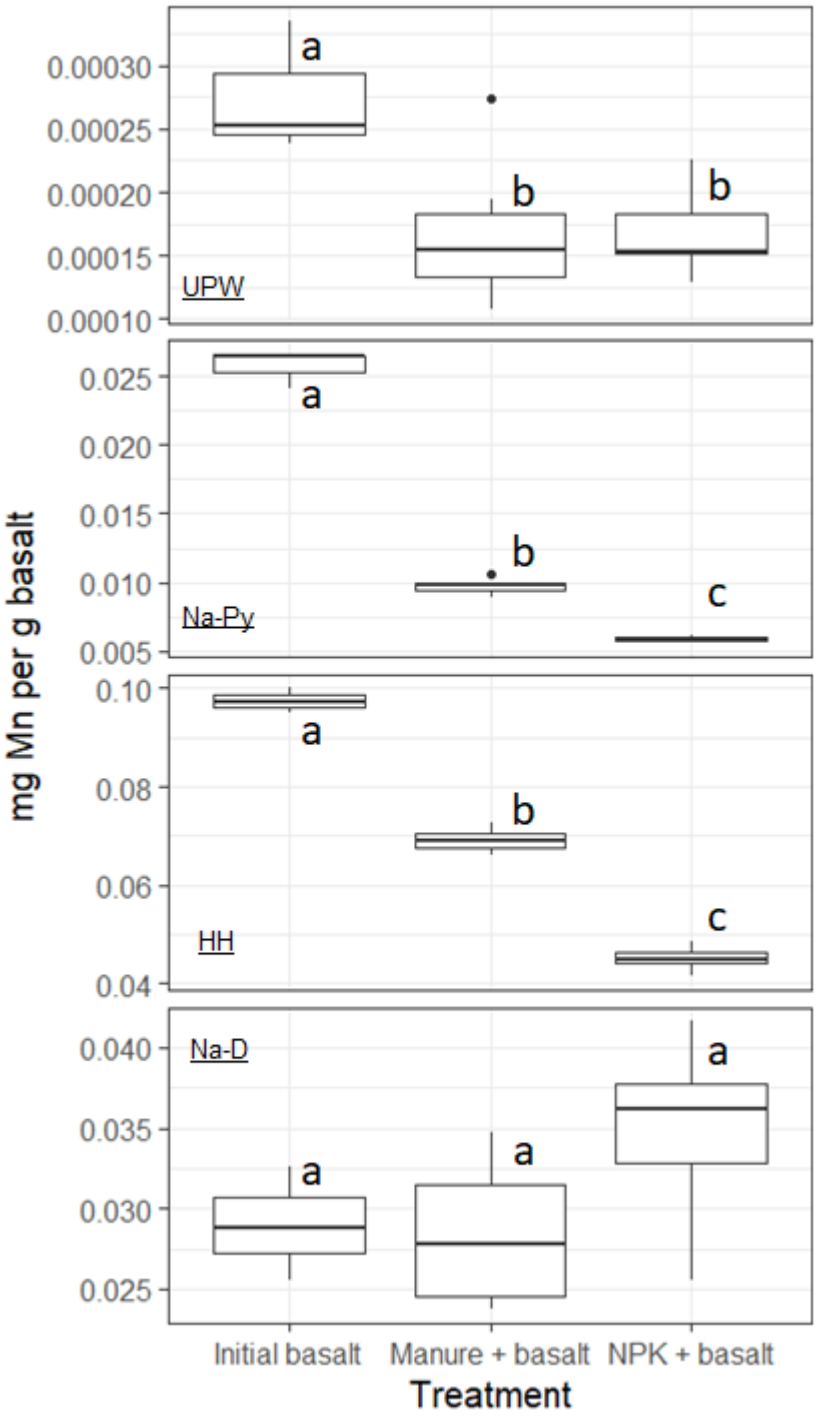

Figure 3.14 – Extractable-Mn fractions for the Initial basalt grains (n = 3) and grains extracted from the Manure + basalt (n = 7) and NPK + basalt (n = 7) fertiliser treatments. Letters are used to differentiate significant differences between different treatments (e.g. a and b are significantly different; a and a are not significantly different.). UPW = Ultra-pure water; Na-Py = Na-pyrophosphate; HH = hydroxylamine hydrochloride; Na-D = Na-dithionite.

3.3.5. TGA-MS analysis

The TGA-MS data are summarised in Table 3.3. Total calcite decreased in both treatments, with more pronounced decreases observed in the NPK + basalt sample where 0.157 wt.% calcite was lost relative the Manure + basalt sample which lost 0.131 wt.% calcite. As only one replicate was carried out from each treatment, no statistical analysis could be conducted.

Table 3.3 – Calcite concentrations in the Initial basalt compared to the NPK + basalt and Manure + basalt samples from Thermogravimetric Analysis with Mass Spectrometry. n = 1 for each sample.

Sample	Total calcite (wt.%)
Initial basalt	0.244
NPK + basalt (C10)	0.087
Manure + basalt (C24)	0.113

3.3.6. SEM imaging

Given the complexity of the basalt grain mixtures, it was not possible to discern changes from the SEM images that occurred as a result of weathering, such as grain rounding or deepening of cracks. Fine particulates (Figure 3.15a, Figure 3.16a and 3.17a) were also observed on several grain edges as well as cracks (Figure 3.15b, Figure 3.16b and 3.17b). Occasionally, fungal hyphae were observed attached to the rock grains. Because no quantitative analysis by counting fungal hyphae from basalt grains was conducted, it is not possible to comment on which fertiliser treatment contained the highest amount of fungal hyphae (Figures 3.16c and 3.17c).

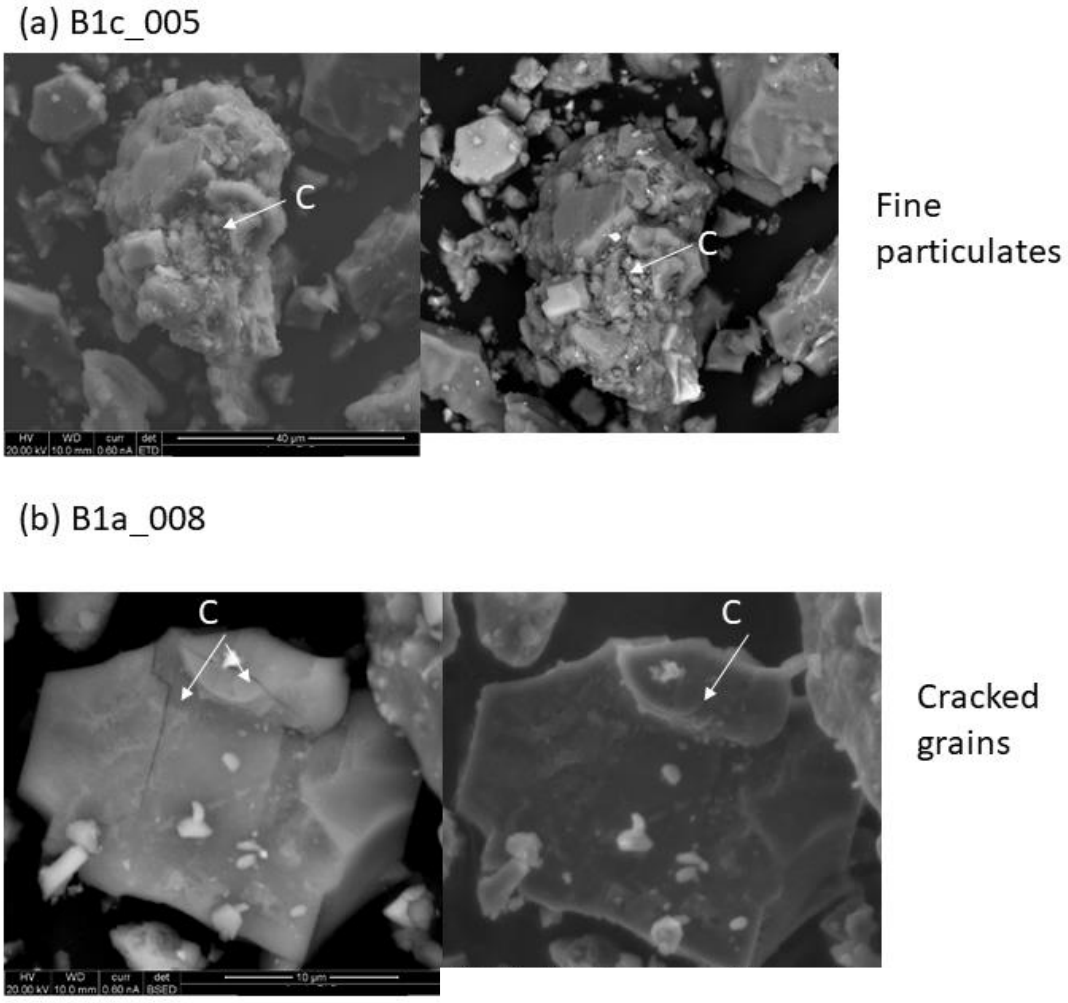

Figure 3.15 – Secondary (right) and backscattered (left) electron photomicrographs of the Initial basalt treatment, showing: (a) fine particulates (F denotes particulates) and (b) cracked grains (C denotes cracks). Secondary and backscatter electron images are shown to make it easier to identify features.

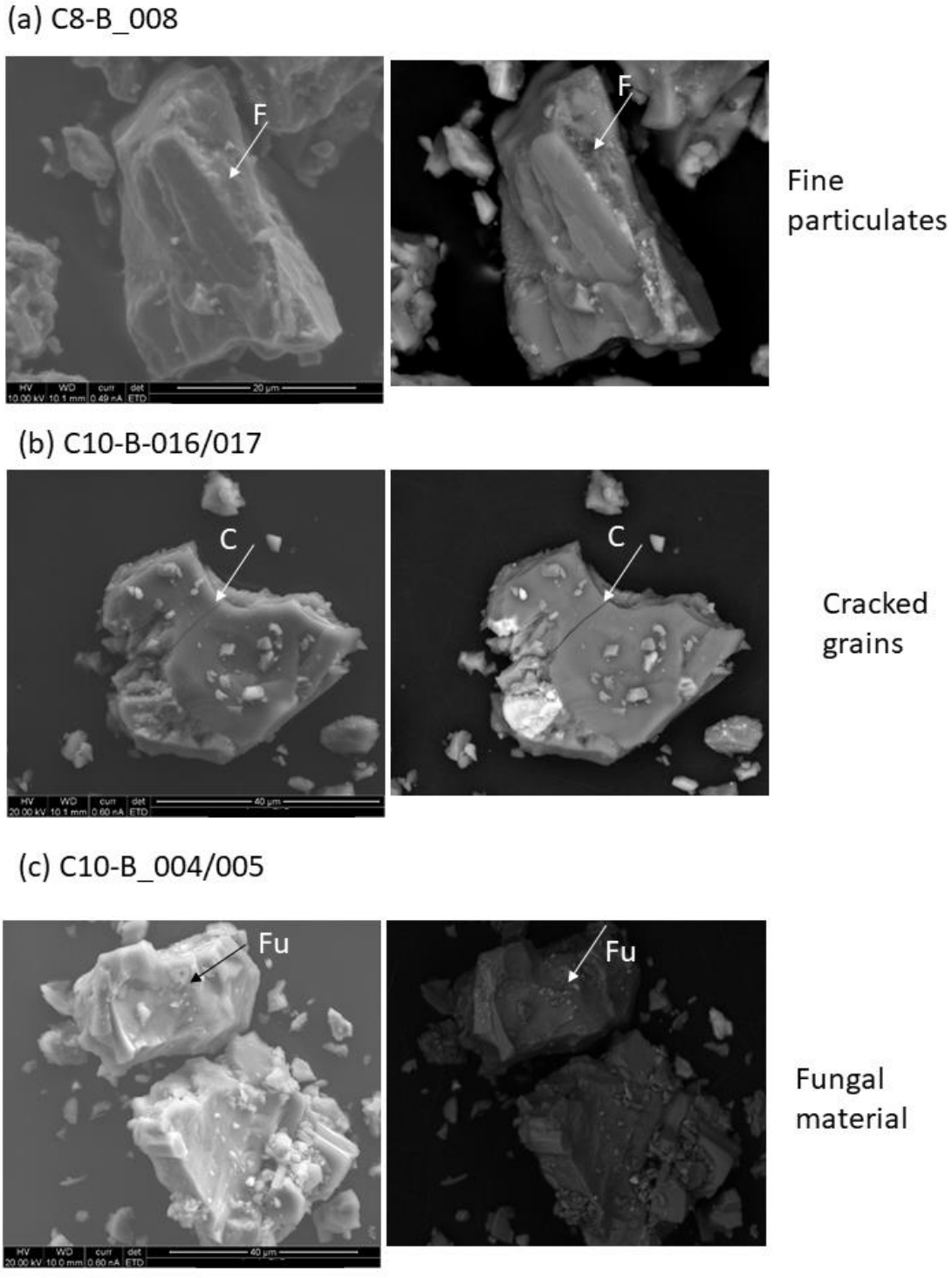

Figure 3.16 – Secondary (right) and backscattered (left) electron photomicrographs of the NPK + basalt treatment, showing: (a) fine particulates (F denotes particulates), (b) cracked grains (C denotes cracks) and (c) fungal material adhered to some mineral (Fu denotes fungal material). Secondary and backscatter electron images are shown to make it easier to identify features.

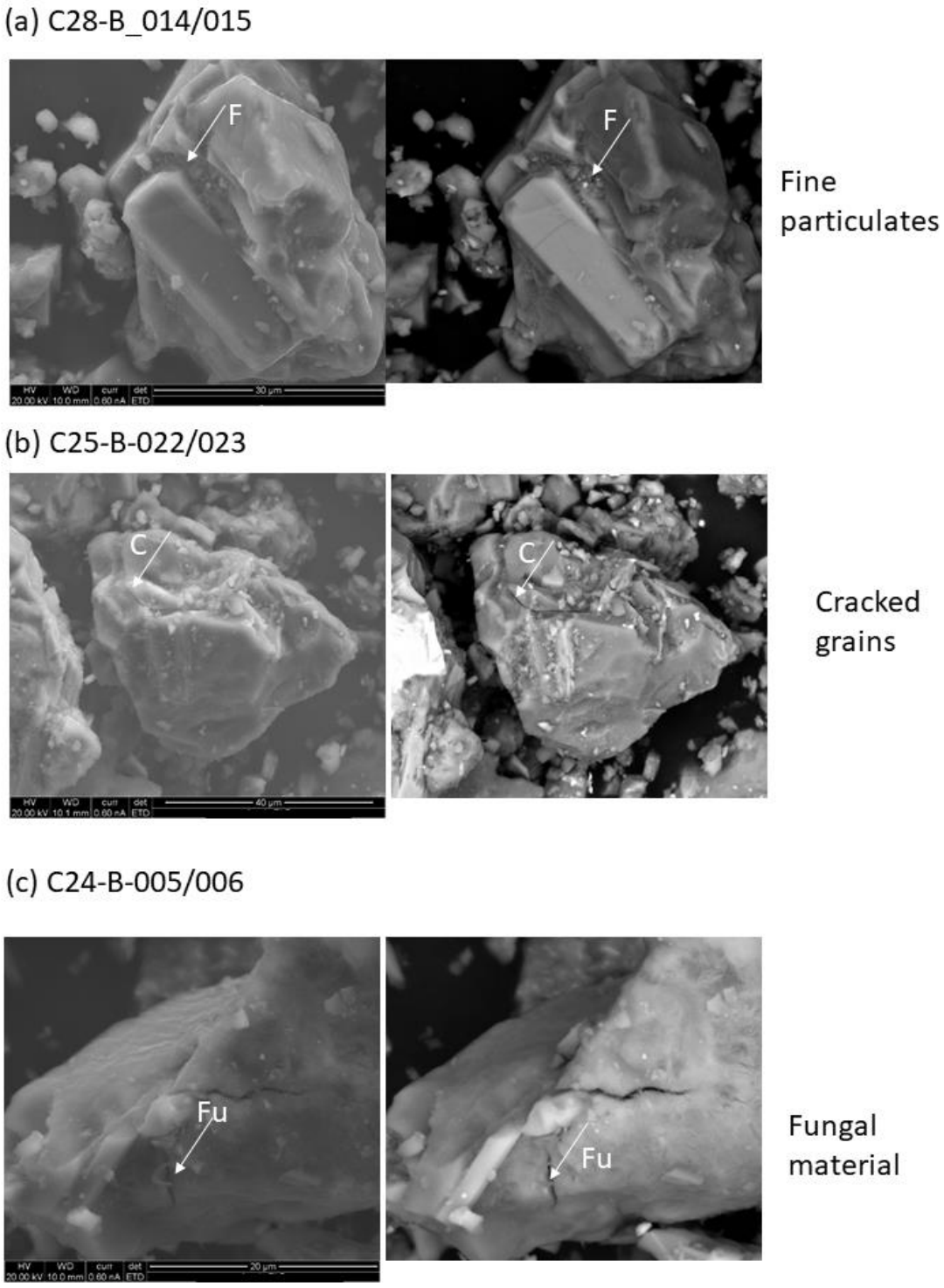

Figure 3.17 – Secondary (right) and backscattered (left) electron photomicrographs of the Manure + basalt treatment, showing: (a) Fine particulates (F denotes particulates), (b) cracked grains (C denotes cracks) and (c) fungal material adhered to a basalt grain superimposed on top of a cracked grain (Fu denotes fungal material). Secondary and backscatter electron images to make it easier to identify features.

3.3.7. Geochemical modelling of the compost extract dissolution experiment

3.3.7.1. Overall comments on compost extract solution chemistry

The solution chemistry of the initial compost extract and the reacted compost extract after one week of weathering is summarised in Table 3.4. Changes in solution pH of 0.3 pH units, from 7.48 to 7.79, and substantial increases in Si, Ca and Mg concentrations were observed (by 17.2-fold, 7.0-fold and 2.7-fold respectively). Al and Fe concentrations remained stable - though this is common for solutions at neutral pHs as under these solution conditions both Fe and Al will be bound to organic material or precipitated out as secondary phases (Pourbaix, 1974; Tipping *et al.*, 2002). Inorganic carbon increased 2.4-fold to a final concentration of 12.12 mg L^{-1}. Trace elements concentrations including Mn, Cu, V, Ni, Ba and Sr increased by up to between 6.46- and 20-fold.

3.3.7.2. Model results

The modelling results showed that given the solution pH and Fe concentrations, amorphous $Fe(OH)_3$ would be saturated and therefore had the potential to precipitate in both the initial compost extract and the solution after 1 week of weathering (Figure 3.18a and b) in spite of low initial Fe concentrations (Table 3.4). However, Al concentrations were not high enough to precipitate $Al(OH)_{3(a)}$ out of the solution in either of the measured solutions. When Al concentrations in the solution after 1 week of weathering were artificially increased to represent the potential Al that may have been released, assuming a stoichiometric release of Si to Al, $Al(OH)_{3(a)}$ is predicted to precipitate (Figure 3.18b).

Given the potential kaolinite contamination (see Section 3.4.1.1.), the SI of kaolinite were also determined. Kaolinite was found to be saturated in both the initial compost extract and the solution after 1 week of weathering (Figure 3.18a and b).

Neither calcium carbonate ($CaCO_3$) or amorphous Si ($SiO_{2(a)}$) were predicted to precipitate in either the initial compost extract, the solution after one week of weathering or the solution after one week of weathering with elevated Al

concentrations; i.e. they would be undersaturated. Additionally, no Mn-bearing minerals were found to have the potential to precipitate out of solution.

Fe and Al activities indicate that amorphous hydroxides $Fe(OH)_3$ and $Al(OH)_4^-$ have the highest activities both the initial compost extract and the solution after one week of weathering (Figure 3.19a and b and 3.20a and b). The Fe-humate activities contributed minimally to the overall activities of both solutions with log activities of *c.* -12 and -13 for the initial and weathered solution respectively. Al-Humate cannot be modelled in PHREEQC at present, and neither can the SI of Al/Fe-Humate precipitants as equilibrium data for these phases are not currently documented in the Amm_T-H.dat database. Determining the potential for co-precipitates to form would be useful in the cross-interpretation of Al and Fe co-precipitates (from the Na-pyrophosphate extractable fractions).

Table 3.4 – The solution chemistry of the initial compost extract and the reacted compost extract after 1 week of weathering from the flask dissolution experiment. For each measurement, n = 3. Data provided by Dr B Sarkar as discussed in Section 3.2.5.

Variable	Flask dissolution experiment	
	Initial Solution	Solution after 1 week of weathering
pH	7.48	7.80
Electrical conductivity (mS m^{-2})	8.73	8.90
M Alkalinity (ppm)	43.39	46.36
Dissolved Inorganic Carbon (mg L^{-1})	5.02	12.12
Dissolved Organic Carbon (mg L^{-1})	10.39	12.17
Elemental Analysis		
Ca (mg L^{-1})	4.69	32.97
Mg (mg L^{-1})	7.17	19.47
Si (mg L^{-1})	0.63	10.87
Sr (mg L^{-1})	0.01	0.20
K (mg L^{-1})	18.4	20.80
Na (mg L^{-1})	2110	2126
Fe (mg L^{-1})	0.074	0.05
Al (mg L^{-1})	0.008	0.006
Li (mg L^{-1})	0.002	0.0053
Ba (mg L^{-1})	0.004	0.058
Cu (mg L^{-1})	0.005	0.0323
Ni (mg L^{-1})	0.002	0.014
Zn (mg L^{-1})	0.011	0.007
P (mg L^{-1})	7.34	5.07
S (mg L^{-1})	8.38	9.323
V (mg L^{-1})	0.002	0.0133
B (mg L^{-1})	0.021	0.04

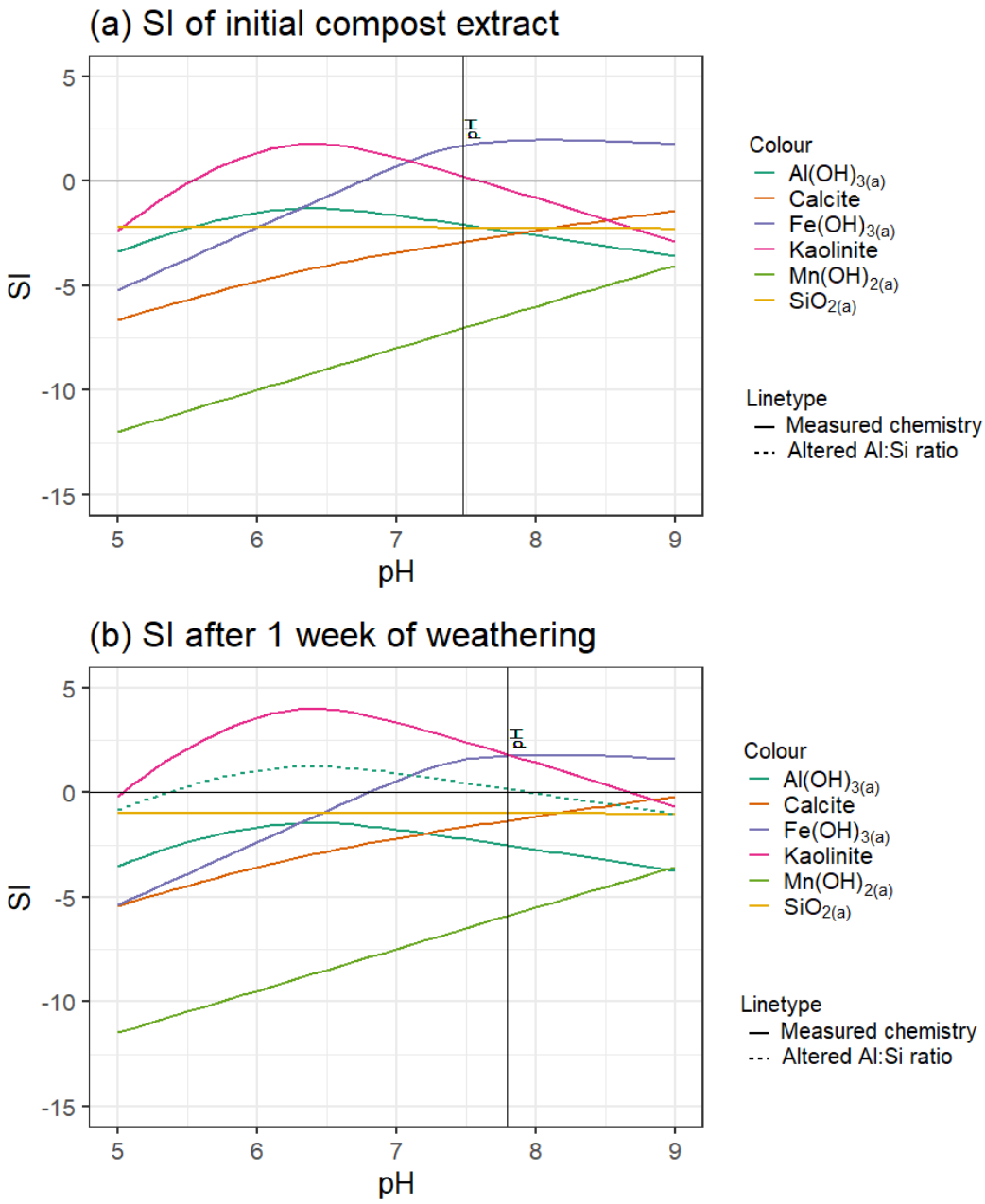

Figure 3.18 – Graph showing Saturation Indices (SI) of several Al, Fe, Si, Ca and Mn phases as a function of pH in (a) the initial compost extract and (b) the solution after 1 week of weathering. Vertical line represents the measured solution pH of each respective solution. Red dashed line in (b) represents the SI of Al $(OH)_{3(a)}$ when the solution Al concentration, [Al], is increased by the following equation: [Al] = [Si] · Initial basalt Al/Si ratio (0.264091). The justification for doing this is provided in Section 3.3.7.2.

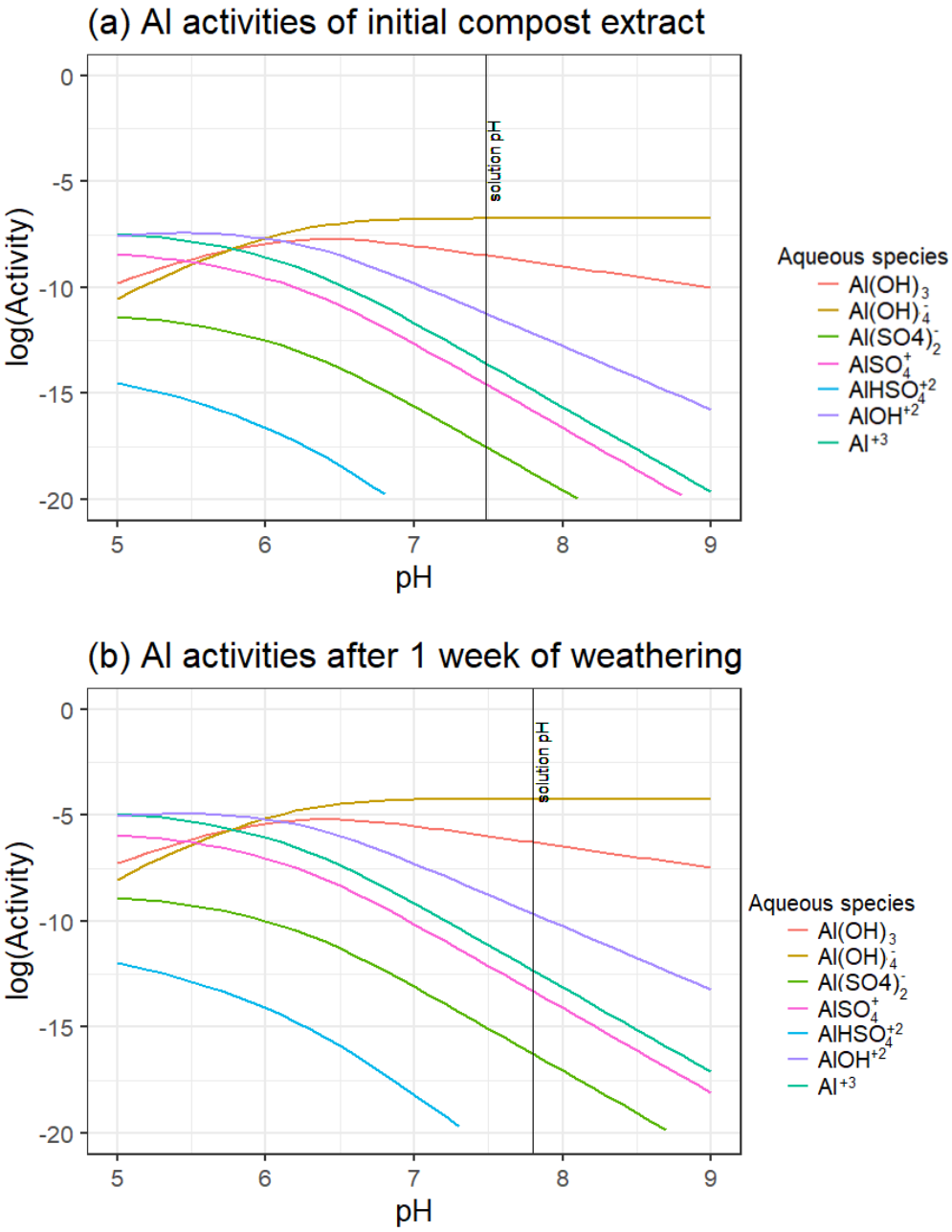

Figure 3.19 – Graph showing Al ion activities as a function of pH in the (a) initial compost extract and (b) solution after 1 week of weathering. Vertical line represents the measured solution pH of each respective solution.

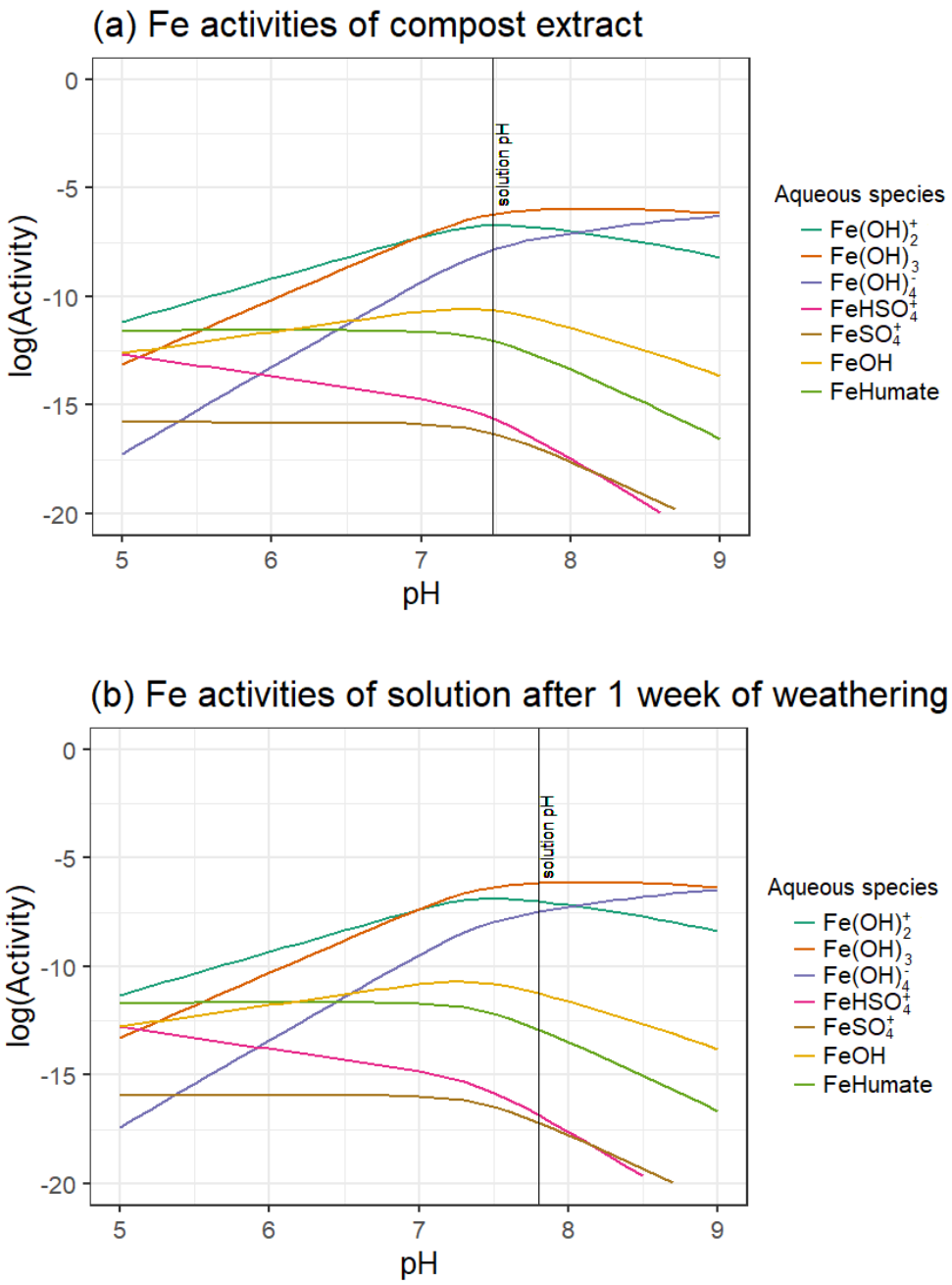

Figure 3.20 – Graph showing Fe ion activities as a function of pH in the (a) initial compost extract and (b) solution after 1 week of weathering. Vertical line represents the measured solution pH of each respective solution.

3.4. Discussion

3.4.1. Evidence of chemical weathering

The whole rock and surface chemistry, from XRF and XPS respectively, both show significant depletions and enrichments of certain elements when comparing the Initial basalt to the two weathered grain treatments (Manure + basalt and NPK + basalt).

3.4.1.1. Potential kaolinite contamination affects chemical data

Al was hypothesised to be depleted relative to Si, in accordance with the generalised description of dissolution reported in Oelkers (2001) which was introduced in Section 3.1. However, the XPS results showed significant increases in the Al/Si ratio from 0.21 to up to 0.32 – an increase of up to 0.11 (calculated from data in Figure 3.2), indicating an enrichment of Al concentrations. An increase in surface Al could have been interpreted as Al secondary phase precipitation which can precipitate from the soil solution onto grain edges (Nugent *et al.*, 1998).

Secondary phase precipitation was ruled out because the DRIFTS data identified kaolinite ($Al_2Si_2O_5(OH)_4$) at an estimated *c.* 1 wt.% in the basalt and quartz mesh bags as well as the bulk soil (Figures 3.11 and 3.12). The rate of kaolinite formation required to form 1 wt.% kaolinite after 3 months of weathering is not consistent with current scientific precedent. The geochemical modelling did show that kaolinite to be saturated and had the potential to precipitate out of solution. However, it is important to note that even over long term timescales, kaolinite is absent from active basaltic soils younger than 400 kyr (Chorover, Amistadi, and Chadwick, 2004) and near-equilibrium laboratory-scale feldspar dissolution experiments identified that little kaolinite (*c.* 0.06 wt.%) would precipitate after 60 days of weathering at 50°C (Zhu *et al.*, 2020). The SI of any given mineral indicates the potential for that mineral to precipitate, rather than explicitly confirming that the mineral is will have precipitated.

The data presented in this chapter along with scientific background suggest that the relatively large proportion of kaolinite that was identified in

weathered samples is likely to have seeped into the quartz and basalt mesh bags as soil material migrated through the column, rather than as a product of basalt weathering. As there was evidence that the kaolinite was skewing the Al, Si and O proportions in these treatments, these elements were removed from both whole rock and surface chemical analysis and the concentrations of other elements were then recalculated as described in Sections 3.2.5 and 3.2.6. Therefore, the chemical data could only be used to detect the preferential leaching of other elements, including alkaline and alkaline earth metals.

3.4.1.2. Whole-rock chemistry

The corrected whole rock chemistry (XRF) showed significant decreases of up to 1.23, 0.16 and 2.51 wt.% in the MgO, K_2O and Na_2O concentrations respectively when samples from both fertiliser regimes were compared to the Initial basalt (Figure 3.8). These results are consistent with the generalised description of dissolution reported in Oelkers (2001) and support Hypothesis (1) which predicted that there would be evidence of elemental release from the basalt grains (e.g. from the decrease in Mg, Ca, Al and Na and relative to Si) in the XPS and XRF data, because the grains will have dissolved in the soil columns. CaO concentrations were also expected to decrease as they are described as behaving similarly to MgO, but instead the CaO concentrations remained stable (Oelkers, 2001). The whole-rock chemistry also showed some chemical differences in the amount of weathering between the two fertiliser regimes. Whole-rock Mn_3O_4 concentrations were significantly more depleted in the NPK + basalt treatment relative to the Manure + basalt treatments, providing some evidence in support of Hypothesis (2). Porewater solution chemistry identified that the NPK + basalt treatment had a lower pH (4.9 compared to 6.5 for NPK + basalt and Manure + basalt respectively) and higher nitrate concentration (up to 1386 compared to 207 mg L^{-1} for the NPK + basalt and Manure + basalt respectively) relative to the Manure + basalt treatment. Both of these observations suggest that the NPK + basalt soil environment is more suitable for chemical weathering.

Results from this chapter differ from the whole-rock chemical analysis dataset documented in Kelland *et al.* (2020) where only MgO concentrations

(out of SiO_2, K_2O, P_2O_5, MgO and SrO) were identified as significantly decreasing when comparing the Initial basalt to the weathered basalt grains. It is likely that the reduced particle size used in the experiment documented in this chapter, with a *c.* 20-fold lower *p*80 (Section 3.2.1.) relative to the particles used in Kelland *et al.* (2020), might have caused this difference in results. While the results from Lewis *et al.* (2021) (Chapter 2) demonstrated that mineralogy is more important than surface area in controlling CDR rate, Lewis *et al.* (2021) did identify an increased weathering rate of up to 3-fold following a 10-fold increase in surface area over 15-year timescales. While experiments ran over a much shorter timescale in this chapter (three months) relative to the geochemical models in Lewis *et al.* (2021) which ran for 15 years, an increase in weathering from increased surface area could have sufficiently lowered the elemental proportions of the weathered basalts relative to the Initial basalt to generate statistically significant losses.

3.4.1.3. Consistencies between whole rock and surface chemistry

Considering consistencies between the whole-rock and surface chemistry, the Na was consistent in trend but surface Na was not significantly different when considering a $p < 0.05$ ($p < 0.059$ for surface Na). Surface K was also more depleted in the Manure + basalt treatment relative to the Initial basalt ($p = 0.059$) and more depleted in the Manure + basalt treatment compared to the NPK + basalt, though these differences were also not significant ($p = 0.178$). This additional depletion in the NPK + basalt compared to the Initial basalt relative to the Manure + basalt compared to the Initial basalt may not be related to the chemical environment; instead it is thought that there could be a biological reason for the additional K depletion. Given that K is released faster in the NPK fertiliser when compared to Manure fertiliser because KCl (the 'K' source from the NPK fertiliser) dissolves rapidly, the sorghum plant and microbes could have been actively mining the basalt grains in the Manure + basalt treatment to obtain additional nutrients. However, this reasoning was not backed up by SEM imaging which showed fungal hyphae adhered grains from both applied treatments and there was no evidence of increased microbial colonisation in the Manure + basalt treatment.

3.4.1.4. Inconsistencies between whole-rock and surface chemistry

There were some inconsistencies between the trends observed in the XPS and XRF datasets for Mg and Ca (Figures 3.4 and 3.9). Focusing on Mg, there was no significant change in surface Mg (from XPS analyses) even though significant decreases in whole-rock MgO (from XRF analyses) were observed. The inconsistency between surface Mg (XPS) and whole-rock MgO (XRF) can likely be attributed to instrumental limitations when the Mg XPS data was collected. No high resolution scans (0.1 eV resolution) were collected because the Experimental Officer who collected the data did not program the instrument to collect HR scans for Mg. Instead, Mg concentrations were collected from cruder survey scans (1 eV resolution). The survey scan collects data at a lower resolution, which makes it harder to observe changes to peak size and position.

With regard to the differences between the CaO and Ca, where whole-rock CaO concentrations remained the same (XRF) but surface Ca concentrations (XPS) significantly decreased in the NPK + basalt treatment relative to the Initial basalt, several explanations for the differences between CaO and Ca were assessed. However, none of these explanations were deemed adequate to explain the differences between the two chemical analysis methods (XRF and XPS). The depletion in surface Ca could have resulted from the leaching of Ca from basaltic minerals, but there is no known reason for the lack of significant decrease in whole rock Ca.

The precipitation of $CaCO_3$ in grain cracks following the release of Ca from chemical weathering reactions was considered as a reason for the discrepancy between the XPS and XRF analyses. Fluid flow would be more restricted inside grain cracks than the fluid flowing over the grain faces. Therefore, the fluid contained within the grain cracks may be able to become saturated with respect to $CaCO_3$. The $CaCO_3$ may become saturated because the solution pH will increase as protons are consumed during weathering reactions, Ca will be released during weathering and solutions already contain dissolved CO_2 (which at high pH will speciate as CO_3^{-2}). All of these factors will contribute to the precipitation of $CaCO_3$. As $CaCO_3$ is forming inside the grain

cracks, the $CaCO_3$ would be measured as whole-rock Ca but would not be measured on the surface. However, there was no evidence from the TGA-MS data to support the hypothesis that any calcite was forming (Table 3.3).

The difference between surface and whole rock Ca and Mg could also be related to issues in sample size between the two methods. Much more sample is required to prepare samples for XRF relative to XPS (0.5 g in XRF rather than < *c.* 0.1 g in the XPS study) which means that the samples used for XRF analysis are more representative of the total sample. XRF sample preparation also creates a flat surface for analysis which is much more suitable for X-ray analysis. Rough surfaces can either over- or under-estimate elemental concentrations.

3.4.1.5. Inability to compare surface chemistry with other studies

While several studies have assessed the depletion of Na, Ca and K in the surface layers of weathered minerals using XPS, no appropriate studies have considered the depletion of appropriate basaltic materials (e.g. White and Hochella (1992) is not appropriate because the concentrations of Ca, Na and Fe were below the detection limit of their study in their reported weathered samples and Mg was not well represented in the samples used in this chapter). Furthermore, it is not easy to compare results from the basalt bags in this study to the results of surface chemistry of relevant minerals after mineral dissolution, because of the skewed Si concentrations observed in this study as a result of the kaolinite contamination (see Section 3.4.1.1.). This is because most studies use ratios to compare various elements to Si (e.g. Ca/Si, Na/Si, Al/Si) (e.g. Feldspars (Nugent *et al.*, 1998; Lee *et al.*, 2008), Olivine (Zakaznova-Herzog *et al.*, 2008; Garcia *et al.*, 2013), Pyroxene (Zakaznova-Herzog *et al.*, 2008; Schott *et al.*, 2012). It would be possible to extract the Ca and Na values from these studies and create a ratio between them. However, studying Ca/Na ratio is not very useful for understanding weathering in the basalt grains because they would both be expected to be preferentially leached.

It was, however, possible to assess the elemental ratios between elements of interest and Si in the Org 8 experimental sample. Here, the Al/Si ratio increases (indicative of secondary precipitation (Nugent *et al.*, 1998)) while the

Ca/Si ratio decreases (indicative of elemental leaching (Oelkers, 2001)). These results do not bear much significance, though, as Al, Si and Ca concentrations in the Org 8 sample were within 2σ of the values determined in the Initial basalt and were therefore not significant. This lack of significance is most likely a result of the 'relatively mild' dissolution conditions that the Org 8 sample was subjected to.

3.4.2. Secondary phase formation

The sequential extractions, DRIFTS, TGA-MS and XRF identified little evidence of secondary phase precipitation. These results generally corroborate well with the geochemical modelling which identified little potential for secondary phase precipitation, with the exception of $Fe(OH)_{3(a)}$ which was saturated in the geochemical models but there was no laboratory-based evidence to support $Fe(OH)_{3(a)}$ precipitation.

3.4.2.1. Potential for Al, Fe and Mn secondary mineral formation

The sequential extractions showed no significant increases in either Al, Fe or Mn precipitation in either the inferred poorly crystalline (i.e. from hydroxylamine hydrochloride extractable) or crystalline (i.e. from Na-dithionite extractable) pools (Figure 3.13). There was no significant difference in extractable Al or Fe in either of those two pools but there was a decrease in Mn associated with the poorly crystalline pool. This result does not corroborate with Hypothesis (3) which predicted that secondary minerals would precipitate.

There is no corroboration between the sequential extraction results and the modelling results which predicted that in the basalt dissolution microenvironment, $Fe(OH)_{3(a)}$ had the potential to precipitate. When the total extracted Al was added to the Al concentrations, $Al(OH)_{3(a)}$ had the potential to precipitate (Figure 3.18). Amorphous $Mn(OH)_2$ was also modelled but was undersaturated at pH < 9 (basalt microenvironment pH < 7.8). Therefore, there is some corroboration between the Mn extracted from the poorly crystalline phase and the geochemical models.

Even though there was no evidence for secondary phase precipitation, the basalt grains were still a sink for Al and Fe. Both Al and Fe associated with OC via complexation reactions or adsorption onto humus (inferred from Na-pyrophosphate extractions) increased significantly relative to the Initial basalt. Additionally, more humus adsorbed/complexed-Al and -Fe was identified in the NPK + basalt treatment relative to the Manure + basalt treatment. In contrast, humus adsorbed/complexed-Mn decreased significantly in the NPK + basalt and Manure + basalt treatments relative to the Initial basalt.

Clearly, the experimental data show that residual OC on basalt grain edges are a sink for Al and Fe. These interactions could not be modelled as the current model does not have the capabilities to capture: (1) the surface complexation of Fe-, Al- or Mn- to humic/fulvic substances or (2) precipitation of metal-humates/fulvates. Instead, the WHAM (Windermere Humic Aqueous Model (Tipping, 1994)) model could be used to model surface complexation (Lofts *et al.*, 2001) and the precipitation of humic substances (Farmer and Lumsdon, 2001).

The results from the Na-pyrophosphate extraction could appear to corroborate with the trends observed in the whole rock chemical data for Fe_2O_3 and Mn_3O_4 which show Fe_2O_3 concentrations significantly increasing while Mn_3O_4 concentrations decrease (Figure 3.8). However, the magnitude by which both Fe_2O_3 and Mn_3O_4 concentrations change could not be explained by the results from the sequential extractions alone. The increase in humus adsorbed/complexed-Fe would account for a gain of *c.* 0.01 wt.% of the total whole rock Fe_2O_3 (which increases by up to 0.71 wt.%) and the humus adsorbed/complexed-Mn would account for a loss of *c.* 0.0006 wt.% of the total elemental loss of whole rock Mn_3O_4 (which decreases by 0.04 wt.%). Instead, it is likely that the increase in Fe_2O_3 concentrations are a result of the 'relative' nature of semi-quantitative XRF which sums up all the measured elements to 100 wt.%. Therefore, the Fe_2O_3 concentrations are 'making up' for the depletion of other elements. It was not possible to compare between the extractable Al and whole-rock Al_2O_3 obtained from the XRF data due to the kaolinite contamination which was discussed in the Section 3.4.1.1.

3.4.2.2. Potential for calcite and $SiO_{2(a)}$ precipitation

In addition to the variety of potential soil Al, Fe and Mn sinks, the weathering of basalt grains in the soil solution may induce $CaCO_3$ precipitation on the basalt grains. It is hypothesised that $CaCO_3$ may precipitate as a result of: (1) increased pH following dissolution reactions which would shift the inorganic C speciation to CO_3^{2+} (Pourbaix, 1974), or (2) increased Ca concentrations which lowers the amount of CO_3^{2+} (and thus the solution pH) required to induce $CaCO_3$ precipitation (Manning, 2001). Upon precipitating, $CaCO_3$ could be an additional CDR pathway (see Section 2.1, also Renforth and Henderson, 2017; Hartmann *et al.*, 2013) which temporarily sequesters inorganic C in soils. Experimentally there is no evidence of calcite precipitation in the basalt bags: TGA-MS data shows decreasing calcite concentrations (i.e. weathering) in the weathered basalt grains from the two fertiliser treatments relative to the Initial basalt (Table 3.3). Modelling results also suggest that calcite precipitation would not occur given the inferred basalt microenvironment. The TGA and geochemical modelling data do not support Hypothesis (4) which predicted that calcite would precipitate on the basalt grains.

It was thought that DRIFTS could be used to identify Al and Ca secondary precipitates to aid the interpretation of XPS and XRF data upon conception of this experiment. However, there was no evidence of imogolite and allophane (amorphous aluminosilicates identified at *c.* 3400 cm^{-1} (Madejová, 2003) nor any carbonate peaks (present at *c.* 2516 and 2600 cm^{-1} (So, Blair, and Masterson, 2020)). It is likely that the calcite, while present as a primary mineral in the basalt grains (as identified using TGA), has concentrations much too low to be identified using DRIFTS.

$SiO_{2(a)}$ is also undersaturated on the models.

3.4.3. OC stabilisation

The sequential extractions showed that basalt grains have the potential to stabilise OC.

3.4.3.1. Potential for OC stabilisation via adsorption

Data from both the sequential extractions and XPS measurements revealed trace amounts of carbon on basalt grains prior to application (i.e. in the Initial basalt treatment). This trace carbon likely percolated through the basalt stockpile while the crushed basalt was stored outside prior to bagging and export. While carbon was identified at the surface of basalt grains by XPS analysis, it is not possible to determine whether the carbon is organic or inorganic in nature using XPS. Additionally, at least part of the surface C would be adventitious C (i.e. atmospheric CO_2 bonding to surface iron oxides (Miller, Biesinger and McIntyre, 2002)) making it difficult to interpret the source and nature of the carbon. The sequential extractions are therefore more reliable for determining OC stabilisation because they only analysed OC, rather than inorganic carbon or total carbon. While the sequential extraction methods are thought to be more precise, they are operationally defined. The limitations of the sequential extractions used in this chapter are summarised in Section 6.6.1.

Only one extractable OC pool increased significantly in the ERW experiment. The OC associated with the poorly crystalline pool, inferred from hydroxylamine hydrochloride extractions, increased by 0.057 and 0.022 mg OC g basalt^{-1} in the Manure + basalt and NPK + basalt treatment respectively relative to the Initial basalt. As there was no evidence of the amount of poorly crystalline Fe or Al increasing like the OC concentrations have, OC is likely to be associated with poorly crystalline Fe and Al via adsorption to charged sites present on SRO phases that have already formed on the basalt grains rather than co-precipitating with Fe and Al. This finding does not support Hypothesis (5) which predicted that OC would increase via co-precipitation with Al and Fe.

The significant increase in OC adsorbed in the Manure + basalt treatment relative to the NPK + basalt treatment supports Hypothesis (6) which stated that more OC would be stabilised in the Manure + basalt treatment relative to the NPK + basalt treatment. However, it is not possible to discern why there was more OC adsorbed to the Manure + basalt treatment based on the data collected in this chapter. There could be two main reasons for the increase, either: (1) by adsorption dynamics and increased OC concentrations in the Manure + basalt

treatment, (2) nature (i.e. size and composition) of the adsorbed OC molecules or (3) a combination of both. With a lack of experimental data, the following two paragraphs elaborate on potential mechanisms.

Considering OC adsorption dynamics, generally a higher concentration of OC in solution will facilitate more adsorption until the particle's surface has exhausted available bonding sites. However, the maximum OC adsorption capacity of soil OC on either fresh or weathered basalt grains has not been previously determined. Previous work has assessed the adsorption potential of Zn^{2+}, Cd^{2+} (Qi *et al.*, 2016) and Pb^{2+} (Ponce-Lira *et al.*, 2017) to weathered basalt. However, this work would not be applicable to this study because: (1) OC may adsorb via different mechanisms and under different conditions to Zn, Cd or Pb and (2) the adsorption capacity of basalt would be related to the mineralogy and particularly the amount of secondary phases which have been shown to differ enormously between basalt deposits (Figure 2.2; Lewis *et al.*, 2021).

Similarly, the composition and size of the OC molecules could also affect the amount of OC adsorbed to a basalt grain. It may only take one charged bonding site on a grain surface, and one charged functional group on the edge of an OC molecule to stabilise OC. Therefore, the stabilisation of one larger OC molecule which inherently would contain a higher proportion of OC, can then stabilise a greater amount of OC than a smaller organic molecule. Similarly, the OC molecule's composition dictates the amount of OC present in a molecule. It is possible that the Manure + basalt treatment contained larger OC molecules in the soil solution than the NPK + basalt, which could have also explained why a higher concentration of OC was adsorbed to grains in the Manure + basalt treatment. There are some methods which measure the size of molecules and the amount of OC present within molecules, though they were not measured in this study. It is not common to determine the size of OC molecules associated with various soil pools, but it has been attempted previously using ultrafiltration techniques (e.g. Xu *et al.*, 2019; Riise *et al.*, 2000). The composition of OC is regularly tested using nuclear magnetic resonance (Chukov, Lodygin, and Abakumov, 2018) or fourier transform ion cyclotron resonance mass spectrometry (FT-ICR-MS) (e.g. Bahureksa *et al.*, 2021).

3.4.3.2. Potential reasons for a lack of OC stabilisation in Na-pyrophosphate pool

While there were significant results in the hydroxylamine hydrochloride extractions, inferred as the SRO phases, there were no significant differences between fertiliser treatments in the UPW- (water extractable, loose/easily removed), Na-pyrophosphate- (humus adsorbed/complexed) or Na-dithionite - (crystalline) extractable pools (Figure 3.13). The UPW-pool was small and no Na-dithionite extractable pool was detected (i.e. results were below the limit of detection). It is typical for the UPW- and Na-dithionite pools to be small (Gabriel, Kellman, and Prest, 2018; Heckman, Lawrence, and Harden, 2018) with the UPW-extractable pool depending on the background solution chemistry, and increases in Na-dithionite depending on the formation of secondary precipitates. However, it may be expected that OC associated with the Na-pyrophosphate pool would increase to mirror the trend of Fe and Al increases observed in the Na-pyrophosphate pool (Figure 3.13, see Section 3.4.2). Potential reasons for this are detailed in the following paragraphs.

Firstly, degradation of the OC associated with the basalt grains may have occurred from poor sample preservation techniques. The samples were oven dried which typically degrades OC within samples to a greater extent than freeze-drying (Mucciarone, 2005; Beriro *et al.*, 2014).

Secondly, there was also a time lag of 14 months and 20 days between when the experiment was active and when the basalt bags were recovered from the columns, which could have degraded labile OC. During this time lag, samples were left in the moist soil, and periodically wetted for a CO_2 respiration experiment that was conducted by Mr M Kelland. However, if sample degradation had a major role in reducing the amount of OC associated with the humus adsorbed/complexed-pool, degradation could not have happened to the Al-OC and Fe-OC bonds. Otherwise, the Fe and Al would not have been extracted by the Na-pyrophosphate, and would instead have been extracted by the UPW-extraction as water soluble ions. There is no evidence in the UPW-extractable pool to suggest that this is the case, but it is worth noting that an extraction for measuring Al and Fe that was previously bound to OC via adsorption or complexation has not been previously tested.

It could be that OC degradation does not explain why OC concentrations remained stable in spite of the increased Al and Fe and that the Al and Fe ions were simply adsorbed to OC present on the grain edges of the Initial basalt grains. From the data collected in this study, it was not possible to determine how many vacant bonds of OC might have been present with respect to elements bonding to them. It was beyond the scope of this study to investigate the potential Al-, Fe- or Mn-OC interactions using geochemical modelling. While the modelling of the adsorption of elements to humus has not been implemented in the model used in this chapter, it is not possible to model the interaction between humus surfaces and Fe and Mn. However, a recent study has defined constants for the adsorption of Al^{3+} to the OC surfaces (Erlandsson *et al.*, 2016).

The decrease in humus adsorbed/complexed Mn-OC may have also influenced the OC dynamics surrounding the basalt grains. It is current scientific thought that Mn-OC complexation bonds are stable under different environmental conditions compared to adsorbed/complexed Al/Fe-OC bonds. Mn-OC complexes are not stable at pH values < 7 and will consequently break down (Duckworth and Sposito, 2005) while Al and Fe complexes are stable at much lower pHs (e.g. Farmer and Lumsdon, 2001). However, the solution pH for the inferred basalt weathering microenvironment ranges from 7.4-7.8; within the range of Mn-OC complexation.

The deviation of the evidenced (i.e. measured) Mn-OC response from the expected Mn-OC response suggests that the basalt microenvironment inferred from the flask dissolution experiment is not representative of the actual basalt weathering environment. Further evidence to support this idea is indicated by the different fertiliser-related responses which showed: (1) significantly more element depletion in Mn_3O_4 in the NPK + basalt treatment relative to the Manure + basalt treatment (Section 3.4.1) and (2) the significantly more humus adsorbed-Al and -Fe associated with OC (Section 3.4.2). Instead, it is likely that porewater chemistry has a larger control on the basalt microenvironment than originally thought. Given that Mn-OC interactions typically occur at a higher solution pH (pH = 7 – 11 (Duckworth and Sposito, 2005)), and that the soil pH conditions observed in the mesocosm experiment's bulk soil are much lower (pH = 5.2; pH

= 5.8 for NPK + basalt and Manure + Basalt respectively), a decrease in humus adsorbed/complexed-Mn could then be expected.

The decrease in Mn may have provided additional charged sites for Fe and Al to bond with OC. However, this does not account for the entire increase in Fe and Al because humus adsorbed/complexed-Mn decreased by up to 0.0082 mmol Mn g basalt^{-1}, while Al and Fe increased by up to 0.12 and 3.18 mmol Al and Fe g basalt^{-1}, respectively. From the data collected in this chapter, it is not possible to determine if when these Mn-OC bonds deteriorated, the OC associated with the Mn would have degraded. If some of the OC associated with the Mn did degrade, then there could have been some new OC stabilised to maintain similar OC concentrations between the Initial basalt and Manure + basalt treatment.

3.4.3.3. Nature of OC

There were differences observed between the different carbon binding environments with respect to the Initial basalt and fertiliser treated samples (Figure 3.5). However, there was very little difference between the ratios of the two fertiliser treated groups (Table 3.2). This could suggest that the types of bonds within the OC molecules associated with the basalt grains were not different. It is likely that the increases in the O=C-O group, which could be interpreted as either an ester or carbonate bond, are more likely to be an ester because $CaCO_3$ concentrations decreased with increased weathering (Table 3.3).

3.5. Conclusion

This chapter aimed to assess evidence of: (1) grain weathering, (2) secondary phase precipitation and (3) OC stabilisation on basalt grains recovered from an ERW experiment. From these three aims, six hypotheses were formulated and the evidence supporting these hypotheses are considered in this section.

From the data collected and analysed in this chapter, there was sufficient evidence to show grain weathering; whole-rock XRF data showed significant depletion of alkali earth and alkali metals (Na, K and Mg) which is consistent with the generalised description of weathering outlined in Oelkers (2001).

Unfortunately, trends regarding the Al and Si concentrations could not be studied because of the kaolinite contamination in the weathered basalt samples skewed the proportions of these elements. Even so, there was evidence for the release of Ca, Mg, K and Na from the chemical data sets, supporting Hypothesis (1).

It was also hypothesised that there would be increased weathering in the NPK + basalt treatment because of the nitric acid released from the NPK fertiliser (Hypothesis (2)). While most elements did not show evidence of increased depletion in the NPK + basalt relative to the Manure + basalt treatment, the trace whole rock Mn_3O_4 concentrations decreased significantly between the two fertiliser regimes. There was, therefore, some evidence to support Hypothesis (2).

There was no statistically significant evidence to support the formation of secondary phases (as either Al or Fe amorphous or crystalline phases) adhered to the edges of the basalt. However, there was statistically significant evidence that the OC already adhered to the grains were a sink for both humus adsorbed/complexed-Al and -Fe. This was not consistent with Hypothesis (3), which predicted that secondary phases would form on basalt grains during weathering. There were also significant increases in humus adsorbed/complexed-Al and -Fe concentrations between both fertiliser treatments relative to the Initial basalt, with more Al and Fe associated with the NPK + basalt treatment relative to the Manure + basalt treatment. Such an increase could be a result of solution pH (lower pH in the NPK + basalt treatment would favour Al-/Fe-OC bonds (e.g. Rasmussen *et al.*, 2018). No calcite precipitation was observed on the edges of the basalt grains, consistent with the geochemical modelling results and did not support Hypothesis (4).

There was evidence of OC stabilisation by amorphous secondary phases via adsorption. There was no evidence of secondary mineral formation, so the additional OC associated with the SRO phases would have been stabilised by SRO phases that were already present in the basalt prior to application to the mesocosm experiment. This result does not support Hypothesis (5) which predicted that any additional OC would be associated with Al-/Fe- via humus interactions rather than by being adsorbed to basalt grains. Increased OC

stabilisation occurred in the Manure + basalt treatment, consistent with Hypothesis (6) and is likely a result of the additional OC available following the amendment of OC rich manure in the Manure + basalt treatment.

In addition, while not confined to any hypothesis, the results from the chemical extractions were not consistent with the results from the geochemical model. The differences observed between the fertiliser treatments indicate the influence of the soil's porewater rather than the microenvironment assumed from the flask dissolution experiment. Furthermore, it was not possible to model: (1) the surface complexation of Fe-, Al- or Mn- to humic/fulvic substances or (2) precipitation of metal-humates which could both be important for interpreting OC stabilisation mechanisms.

Overall, this chapter has demonstrated that over relatively short periods of time (three months), basalt weathering can be measured on basalt grains using bulk chemical analyses (XRF), that trace OC on basalt grain edges can act as a sink for Al and Fe, and that trace amorphous phases generated from basalt alteration (before being amended into soils) could provide additional sites for OC stabilisation. These trends are hypothesised to continue in experiments where basalt is left to weather for year- to decade-scale periods, and in doing so there will be more evidence for secondary phase precipitation.

Several areas for future work have also been highlighted from this chapter including improving geochemical models and running of experiments for longer periods of time. These areas are considered in detail in Chapter 6.

4. Evidence for secondary phase precipitation and OC stabilisation in basalt-amended soils

4.1 Introduction

Chapter 3 introduced the idea that secondary phases can be a sink for basalt weathering products and that these weathering products could be stored on either the basalt grain surfaces and within the soils. The experiment detailed in Chapter 3 refers to two distinct environments: the basalt grains and the bulk soil. While Chapter 3, in part, investigated the precipitation of secondary phases on the surfaces of basalt grains, this chapter focuses on the precipitation of secondary phases in the bulk soil.

The effect of organic carbon (OC) bound to secondary precipitates forming on basalt grains during weathering is unknown but could hinder further basalt dissolution. However, the precipitation of secondary phases in the bulk soil could be more desirable for enhanced rock weathering (ERW). It is known that the direct precipitation of secondary minerals removes elements from the soil solution, thus lowering the saturation state of primary basaltic minerals and subsequently increasing the rate of mineral weathering, in accordance with Eq. 1.3 (Section 1.1.2). Once the minerals have precipitated, the variable charge associated with the secondary precipitates may increase the cation exchange capacity (CEC), increasing the ability for elements and compounds such as OC to be retained in soils.

The retention of OC in soils is important for both soil function and as a carbon sink. The depletion of soil OC can lead to degraded soil quality, reduced biomass productivity, reduced water quality (Lal, 2004): all of which affect global food production. Soil carbon is the largest terrestrial carbon pool (Jobbágy and Jackson, 2000) but can still be increased to store additional OC: Abramoff *et al.* (2021) predicted that the total carbon stock in soils could be increased by 7% via adsorption. If carbon is retained in soils, it is not released into the atmosphere as CO_2. Increasing soil carbon is, like ERW, a carbon dioxide removal (CDR) method termed soil carbon sequestration (SCS) (The Royal Academy of Engineers and The Royal Society, 2018). SCS aims to increase total carbon in soils by reducing losses of CO_2 from respiration and disturbances, mainly through

managerial change (The Royal Academy of Engineers and The Royal Society, 2018). By providing fresh secondary phases, ERW with basalt amendment could increase insoluble precipitated Al and Fe phases which could retain OC (Vicca *et al.*, 2022). However, to date, ERW as a potential SCS pathway has not received any other published attention.

When basalt weathers, Al and Fe are released into the soil solution as weathering products. These Al and Fe ions can be: (1) complexed with OC, (2) precipitated as poorly crystalline short range order (SRO) phases (e.g. amorphous $Al(OH)_3$, ferrihydrite) and (3) precipitated as crystalline oxides (e.g. gibbsite, goethite). OC may precipitate out of solution as a co-precipitate with Al and Fe. OC may also bond with Mn and Ca in soils. While Mn is present only in trace amounts, Mn has been shown to be an important element for biogeochemical cycling in soils (Li *et al.*, 2021). Although poorly studied, several mechanisms of Ca-OC stabilisation have been studied including: (1) bonding with carboxylic groups through ionic bonding, (2) forming cation bridges with Ca^{2+} adsorbed to clays as CEC and (3) adsorption or inclusion of OC on the edges or interior of calcite particles (Rowley, Grand and Verrecchia, 2018).

The mechanism and capacity of OC stabilisation within soils will vary depending on a variety of different environmental factors. When considering climatic (mean annual precipitation, mean annual temperature, potential evapotranspiration/mean evapotranspiration), chemical (pH, exchangeable Ca, SRO (oxalate-extractable) Al and Fe, crystalline (dithionite-extractable) Fe) and physical (clay and silt fractions) properties of over 390,000 soil analyses from the United States of America, SRO-Al, -Fe and exchangeable Ca were more highly correlated with OC than any of the other aforementioned environmental conditions (Rasmussen *et al.*, 2018). The exchangeable Ca and precipitated Al and Fe in a soil will depend on the soil bedrock (Heckman *et al.*, 2013). Therefore, increasing OC stabilisation in a mature soil would be difficult because the pools of Ca, Al and Fe would be well established in such a system without additional input such as rock or organic amendments.

Amending soils with Ca, Al and Fe sources could therefore be an option to increase the potential for OC stabilisation. Basalt is one such Ca, Al and Fe

rich source containing abundant Al (up to 7.00 wt.%, Table 2.6), Fe (up to 8.65 wt.%, Table 2.6 Chapter 2) and Ca (up to 6.72 wt.%, Table 2.6). Statistical modelling developed by Slessarev *et al.* (2022) has shown that increasing primary silicate Al by 1% could increase secondary Al phases by 20-41%. Given a commonly cited application rate of a 50 tonnes basalt ha^{-1} (Renforth, 2012; Beerling *et al.*, 2020; Lewis *et al.*, 2021) to the top 25 cm of soil, the Oregon basalt would add *c.* 0.1% of primary silicate Al to the top soil per application (Table 2.6).

While methods to understand OC stabilisation associated with Al, Fe and Mn are imperfect (Rennert, 2019), they are routinely-used. Unfortunately, there are no such well-established methods for studying Ca and OC interactions in soils (Rowley, Grand and Verrecchia, 2018). The rest of the chapter now focuses exclusively on OC and the types of association with Al, Fe and Mn (with a main focus on Al and Fe).

Knowledge of the different types of OC interaction are important because the different pools of OC (i.e. associated with metals via complexation, SRO, crystalline Al and Fe) have been shown to have different retention times in soils. Radiocarbon analysis of ^{14}C extracted from different soil pools showed that C associated with crystalline Fe were much more stable than C associated with organo-metal complexes (Heckman, Lawrence and Harden, 2018). The stability of organo-mineral phases have also been assessed using desorption experiments which showed that co-precipitated Fe-OC complexes were more stable against biological forces than adsorbed carbon (Wen *et al.*, 2021). While data on the relative stability of different OC pools are scarce, previously published data do illustrate the importance of understanding the distribution of different OC pools for considering the long-term stability of soil organic carbon (SOC).

Arguably the most common way to assess the association of OC with Al and Fe is to use wet chemical extractions. Particular components of a solid phase (e.g. soil) are targeted by the extractant, and the compounds of interest are removed from the solid phase via a chemical reaction (Rennert, 2019). The solutions containing the extracted constituents are then analysed chemically using, for example, ICP-MS, TOC analysis for Al and Fe, and C respectively. The

ease, rapidity and relatively low expense of chemical extraction makes them suitable for analysing large numbers of samples and replicates. An advantage of using chemical extractions is that they are cheap and simple to conduct. However, the interpretation of the extracted fractions is operationally defined, and there may be some crossover in what is extracted in defined extracted pools (Wagai *et al.*, 2013).

There are several common extractants for determining both OC and its associated metals in either the form of organo-metal complexes or associated with and adsorbed to precipitated phases. These extractions include but are not limited to: dithionite-citrate-bicarbonate (for extracting Fe oxides via reductive dissolution (Holmgren, 1967; Pansu and Gautheyrou, 2006)), ammonium oxalate-oxalic acid (for extracting amorphous Fe and Al compounds (Schwertmann, 1964; Pansu and Gautheyrou, 2006)) and Na-pyrophosphate (for extracting organically complexed Al and Fe (McKeague, 1967)).

However, both dithionite-citrate-bicarbonate and ammonium-oxalate-oxalic acid inherently contain OC. While these aforementioned extractions might prove useful in determining Al and Fe associated with different chemical fractions, they cannot be used to quantify the OC associated with them. Several carbon-free analogues for both of these extractions have been developed including: hydroxylamine hydrochloride to replace ammonium-oxalate-oxalic acid (Wang, Schuppli and Ross, 1987) and Na-dithionite with a HCl wash to replace dithionite-citrate-bicarbonate (Wagai and Mayer, 2007).

Li isotopes can also be used to detect the formation of new secondary phases once soils are subjected to new environmental conditions (e.g. solution pH (Li *et al.*, 2021), amount of weathering vs weathering products in solution (Pogge von Strandmann, Kasemann and Wimpenny, 2020)). Li isotopes do not fractionate during basalt weathering (Pistiner and Henderson, 2003), but they do fractionate during the precipitation of secondary phases after mineral dissolution (Pogge von Strandmann, Kasemann and Wimpenny, 2020). During secondary phase precipitation, lighter ^{6}Li is preferentially taken up into secondary phases relative to heavier ^{7}Li. The environment in which primary silicates (both in bulk soil and basaltic minerals) weather and then secondary phases subsequently

precipitate is altered during basalt amendment. It may then be possible to detect the formation of secondary phases after basalt amendment using Li isotope analysis on selected extractable fractions.

There is a recognised potential of deploying ERW globally across national and continental scales (Beerling *et al.*, 2020), which will involve amending soils of a variety of pH values with basalt. Not only will soil pH affect CDR, given the spectrum of abiotic dissolution rates of primary minerals (Palandri and Kharaka, 2004), but the pH will also affect the type of OC stabilisation mechanisms. While Rasmussen *et al.* (2018) concluded that Al, Fe and Ca are the most important variables associated with soil OC, pH was found to be strongly correlated with these three different mechanisms of soil OC stabilisation. Given their data, Rasmussen *et al.* (2018) proposed that interactions via Al- and Fe-organo-metal complexes are the most important mechanism for stabilising OC at acidic pH's (*c.* pH < 5.5), non-crystalline Al- and Fe- secondary phases become more important stabilisation mechanisms at *c.* pH 5.5-6.5, then exchangeable Ca dominates OC stabilisation at *c.* pH > 6.5. Soil pH, therefore, may affect which pools OC is associated with. Stabilisation via Mn complexation has also been shown to occur between pH 7-11 (Duckworth and Sposito, 2005) and the precipitation of amorphous Mn-oxides/hydroxides tends to occur at alkaline pH, depending on the amount of Mn present in solution.

There is a wealth of research being conducted which aims to understand the efficacy of ERW, but no research has yet attempted to estimate the extent of several Al and Fe pools within soils and their association with OC using laboratory techniques from soils which have been trialled for ERW. In this chapter, soils excavated from the short (81 days) Loddington Farm Mesocosm Experiment, as described in Section 3.2.2, were analysed. The experiment consisted of four treatments: NPK, NPK + basalt, Manure and Manure + basalt. By using these four treatments, there can be some assessment on how basalt amendment effects OC dynamics under both conventional (NPK) and organic (manure) fertiliser regimes. Furthermore, manure is not only an organic fertiliser but also one of the carbon inputs recommended for SCS (The Royal Academy of Engineers and The Royal Society, 2018), so in this experimental set-up it is

possible to assess if there are any additive effects of co-amending basalt and manure for ERW and SCS purposes in the context of this experiment. This chapter broadly investigates the following three aims:

Aim 1: to quantify the different Al, Fe, Mn and OC sinks in soils using an adapted sequential extraction procedure from Heckman, Lawrence and Harden (2018) and Gabriel, Kellman and Prest (2018).

Aim 2: to interpret values determined in Aim (1). To accomplish this aim, a variety of measured soil parameters known to be correlated with soil carbon storage and secondary phases (CEC, pH, total C, N and H) as well as porewater modelling were used to contextualise the environment in which Al, Fe, Mn and OC sinks may form. Geochemical models were employed using the soil porewater chemistry from each treatment to determine whether secondary phases had the potential to precipitate.

Aim 3: to briefly assess how basalt amendment affects OC dynamics in soil.

Following a review of the aims of this chapter detailed above, the following four hypotheses were developed:

Hypothesis (1): There will be increases in humus adsorbed/complexed-Al, –Fe and -Mn in basalt-amended relative to fertiliser only treatments because Al, Fe and Mn will be released during basalt weathering. Once released, these elements can then bond with OC via adsorption and complexation reactions (Aim 1).

Hypothesis (2): Building upon Hypothesis (1), not only will there be increased humus adsorbed/complexed-Al and -Fe in basalt-amended treatments relative to fertiliser only treatments, there will also be a greater increase in humus adsorbed/complexed-Al and -Fe in the NPK + basalt relative to the Manure + basalt treatment. This is hypothesised because the pH in the NPK fertiliser regime is likely to be lower and therefore humus adsorbed/complexed-Al and -Fe will be more common. An increase in humus adsorbed/complexed-Mn in the Manure + basalt relative to Manure only treatment is also hypothesised. This is hypothesised because there will be an increased supply of Mn from basalt

weathering and the inherent pH of the Manure fertiliser regime experimental system will be high enough to facilitate these reactions (Aim 1 and 2).

Hypothesis (3): Basalt amendment will increase precipitated Al and Fe concentrations in soils because basalt weathering will release additional Al and Fe that will precipitate in the bulk soils. There will be evidence of secondary phase precipitation from Li-isotope analysis as well as the chemical extractions (Aim 1).

Hypothesis (4): There will be higher concentrations of extractable soil OC in all extractable phases in the Manure relative to the NPK fertiliser regime because manure is an organic rich fertiliser amendment (Aim 3).

4.2. Experimental setup

The soil samples that were collected from the slightly acidic Loddington Farm Mesocosm Experiment came from the same experimental setup described in Section 3.2.2. In this chapter, the bulk soil excavated from the top 12 cm of the column was used in all of the analyses described in Section 4.3. Briefly, four treatments were used: Manure, Manure + basalt, NPK and NPK + basalt. There were seven samples for each treatment.

4.3. Methods

4.3.1. Sample Preparation

All soil samples were sieved to < 2 mm and dried at room temperature.

Additional sampling and preparatory steps were taken for the sequential extractions and elemental analysis. A sub-sample of the soils underwent additional processing. Firstly, roots were removed using forceps as the roots could dissolve in the sequential extractions and also superficially increase OC concentrations. Once roots were removed, *c*. 5 g of each sample was then pulverised in a Fritsch Pulverisette ball mill (Fritsch International, Oberstein, Germany) to obtain powdered particles < 53 µm. Samples were passed through a 53 µm sieve, and remaining particles > 53 µm were further processed in the ball mill until only a small amount of > 53 µm sample remained. This remaining soil was then crushed using an agate pestle and mortar and passed through the 53 µm sieve. The samples were crushed to this size because it was recommended to crush samples to < 50 µm to ensure that elements occluded within soil aggregates were liberated and available to react with the different extractants (Rennert, 2019).

Once the materials were crushed, they were then vortexed using a Medline Scientific Vortex to ensure the powders were well mixed and homogenous before being weighed out for the extractions and elemental analysis.

4.3.2. Sequential extractions

The protocol for the chemical extractions used in this chapter are detailed in Section 3.2.9. Analysis was carried out on all soil samples collected from the top 12 cm of the experimental column (n = 7 per treatment). Chemical extraction data for the Initial Oregon basalt is presented in Chapter 3 (see Section 3.3.4), but is highlighted occasionally in this chapter for comparison purposes.

The only difference between the extractant protocol described in Chapter 3 and the protocol used in this Chapter are that 1 g of soil was used rather than 0.5 or 0.25 g of basalt, as used in Chapter 3. This is because soil samples were more plentiful so more material could be used for the extractions.

4.3.3. Elemental analysis

For each independent sample, two types of elemental analysis samples were produced: (1) < 53 μm, as is, (for total carbon, TC data) and (2) < 53 μm and acid stripped (for OC data). Collecting data from both types of samples allows for the determination of: (1) TC, (2) OC and (3) IC (inorganic carbon, calculated by subtracting TC from OC).

For the elemental analysis, all treatments except the Manure only treatment used 7 replicates. Only 6 replicates were used for the Manure only treatment because only 1 weight (C15) was measured incorrectly and therefore the weight correction that was applied to acid stripped samples was not reliable. Therefore, it was excluded from analysis.

4.3.3.1 Acid-stripping process (for OC analysis)

Prior to acid stripping, 60 mg ± 1 mg were weighed out into 1.5 mL Starstedt centrifuge tubes. During the acid stripping process, 800 μL of 6 M HCl acid was added to each sample in two doses of (1) 700 μL and then, after 30 minutes, (2) a further 100 μL. After each addition of the acid, the samples were stirred using a blunt needle to ensure good contact between the soil particles and the acid solution. Samples were left overnight to allow reactions to occur. After the final 100 μL of 6 M HCl was added to the sample, the presence of effervescence was monitored. For the samples analysed in this chapter, there was

no additional effervescence so no extra acid was added to the samples. After 24 hours, excess acid was evaporated from the samples by placing the centrifuge tubes in a Techne DB 200/3 Dri-Block at 105°C until all the samples were dry. After acid stripping, samples were re-homogenised using a blunt needle.

The samples were re-weighed to account for the added mass of Cl during the HCl dissolution reactions. During the dissolution of calcium carbonate ($CaCO_3$) via HCl acid, CO_2 is outgassed and Ca^{2+} then bonds with Cl^- to form $CaCl_2$ in accordance with Eq. 4.1:

$$CaCO_3 + HCl \rightarrow CaCl_2 + CO_2 + H_2O \quad \text{(Eq. 4.1)}$$

However, the molecular weight of $CaCl_2$ (110.98 g mol^{-1}) is 10.89 g mol^{-1} (+11%) higher than the molecular weight of $CaCO_3$ (100.09 g mol^{-1}) which means that the sample weight increases. The samples were then reweighed to account for these differences.

Three replicates of 'blank tubes' and 'blank tube + acid' were also subjected to the acid stripping process, and weighed after analysis to test if the weight of any of the 1.5 mL centrifuge tubes changed during the acid stripping process. In both samples, the weight decreased by an average of 0.83 mg. This was subtracted from the final mass calculations.

4.3.3.2 Elemental analysis measurement

Elemental Analysis was conducted by Mr J Smith in the Department of Chemistry, at the University of Sheffield. For both types of normal and acid stripped samples, the total C, H, N and S concentrations were measured. Before analysis, 2 mg of each sample were weighed into aluminium tin weighing boats and folded into a package.

All samples were then measured on an Elementar Vario Micro Cube using the Vario software. The furnace temperature was set to 1150°C for the combustion tube and 850°C for reduction. The gas pressure was set to 1200-1250 mbar with a flow rate of 200 ml min^{-1} He and 20-30 ml min^{-1} O_2 (during dosing).

Two blanks and five standards of sulfanilamide were analysed before the run, then every twelve samples, three sulfanilamide samples were analysed. Data from both the blanks and standards were factored into the final calculations.

4.3.4. CEC measurements

The cation exchange capacity of each sample was determined using an ammonium acetate extraction by Mr M Kelland. The air-dried and sieved to 2 mm fraction from both studies were used in CEC measurements. These samples were not crushed further to produce a <53 µm particle size like the samples used for the sequential extractions and elemental analysis were (Sections 4.3.2 and 4.3.3).

Then, 2 g of samples were weighed into 50 mL polypropylene centrifuge tubes and 20 mL of 1 M ammonium acetate (VWR >99% HiPerSolv Chromanorm) was dispensed into each tube. Tubes were then shaken on a Bibby Scientific Stuart Rotator Disk SB3 at an angle of 50° and speed of 20 rpm for 2 hours. Samples were then centrifuged for 10 minutes at 4000 g using a Centrifuge Heraeus Megafuge 40. After centrifugation, samples were passed through a 0.45 µm filter, diluted to a 1:10 ratio of sample:solution and acidified to a concentration of 2% HNO_3^-. Samples were sent off to the University of Nottingham for cation analysis using ICP-MS and analysed in accordance with the protocol noted in Section 3.2.9.2.

The CEC was calculated using Ca, Mg, Na and K data using the following formula (Eq. 4.2):

$$CEC\ (meq\ g^{-1}) = \sum \frac{weight_e(mg)}{equivalent\ weight\ (meq\ g^{-1}) \cdot weight_s\ (g)} \quad \text{(Eq. 4.2)}$$

where the $weight_e$ is the weight of each element of interest, the equivalent weight corresponds to 20.04, 12.15, 23.00 and 39.10 meq g^{-1} for Ca, Mg, Na and K respectively and $weight_s$ is the weight of soil used in each extraction (2 g in this protocol).

4.3.5. Soil pH

Soil pH was measured on the dried and sieved to < 2 mm samples (i.e. the same type of samples used for CEC measurements). 3 g of soil were weighed into a 50 mL centrifuge tube, then 15 mL of 0.01 M of $CaCl_2$ was added to each tube to produce a 1:5 solid:solution ratio. Samples were shaken for 1 hr on a Bibby Scientific Stuart Rotator Disk at a speed of 20 rpm and then left for 30 minutes for particles to settle. The supernatant was then measured. This protocol was taken from Rayment and Higginson (1992).

All pH measurements were conducted on a Jenway 3540 Bench Combined Conductivity/pH meter. Before measurement, the pH metre was calibrated using standards of pH 4, 7 and 10. For each independent sample measurement, the pH probe was left in the solution for 3 minutes to allow the supernatant pH to stabilize and for method consistency between samples.

4.3.6. Equilibrium phase modelling

Geochemical modelling was conducted on porewater solutions to identify the potential for the precipitation of several secondary phases including: $Al(OH)_{3(a)}$, $Fe(OH)_{3(a)}$, calcite ($CaCO_3$), $Mn(OH)_{2(a)}$. This was done by determining the SI of the phase over a range of pH values. The SI for $SiO_{2(a)}$ could not be determined because Si was not measured in the porewater samples.

The porewater solutions that were modelled were collected and analysed by M Kelland (PhD student at the University of Sheffield). Porewaters were sampled using ‘Macro Rhizon’ samplers (Van Walt Ltd, Haslemere, UK) which were emplaced vertically at the top of the column into the amended layer (top 12 cm), 4 cm from the edge of the column. A vacuum was maintained by locking a Henke-Ject 30 mL luer lock syringe without needle (HenkeSassWolf, Tuttlingen, Germany) with custom-made acrylic spacers. The porewater samples used in this chapter were taken on two dates: day 7 and day 70 and represent the first and last sampling points during the experiment. Up to seven independent samples were taken per treatment (i.e. porewater from each column). Several replicates were missing at experiment day 7 (NPK, n = 7; NPK + basalt, n = 6; Manure, n = 4; Manure + basalt, n = 7) due to a lack of porewater sample that could be extracted.

All of the treatments had a full set of replicates (n = 7) for the porewater solution at experiment day 70.

The following datasets were inputted into the model: cations (from ICP-MS results – Al, Ba, Ca, Fe, K, Li, Mg, Mn, Na, Sr, Ti, Zn, S), anions (from ion chromatography – Cl^-, F^-, NO_3^-), organic and inorganic carbon (from dissolved total carbon analysis), and pH (using a pH probe). Si was not analysed for these porewater samples so no Si concentrations could not be inputted into the geochemical model. The mean values, based on the raw values, were computed for each of the parameters in R (R Development Core Team, 2018). These data are presented in Table 4.1.

The porewater concentrations of Al and Fe were all consistently low (< 0.08 mg Al L^{-1} and < 0.14 mg Fe L^{-1} and decreased to < 0.01 at experiment day 70, Table 4.1) due to their insolubility at the solution pH observed in these experiments (pH 4.9-7.6) (Pourbaix, 1974).

However, as Al and Fe are central to this chapter, the presence of these elements in the model was considered important for understanding the potential precipitation of Al and Fe phases. The concentration of these two elements, as well as Mn, were artificially increased using the results from the UPW-extractable pool plus the low values from the porewater extracts. The UPW-pool was selected because it likely represents more closely the porewater that could develop in the soil. Some of the Al that was extracted from this phase may have been retained via adsorption and complexation reactions or by the precipitation of secondary phases. The porewater solutions themselves were too dilute to show any precipitation of Al phases. Considering the sum of all other extractable phases (i.e. the Na-pyrophosphate- and hydroxylamine hydrochloride-extractable phases) would have produced Al and Fe concentrations that would be unrealistically high because they would mostly be comprised of phases that would have developed in the soil over much longer periods of time than this experiment ran for.

However, for use in the modelling work in the future, the author acknowledges that it would be better to take baseline extractions on the initial soil

prior to the experiment. Then, the sum of the changes in Na-pyrophosphate- and hydroxylamine hydrochloride-extractable pools in the experimental samples relative to the initial soil could have been used as an input solution for Al, Fe and Mn instead of the UPW-pool plus porewater Al and Fe used in this chapter.

As the UPW-extraction only occurred at the end of the experiment, there were minimal changes to the Al, Fe and Mn concentrations. This meant that little difference was observed in the saturation indices of both $Al(OH)_{3(a)}$, $Fe(OH)_{3(a)}$ and $Mn(OH)_{2(a)}$ with respect to pH in this modelling experiment. As the Al, Fe and Mn concentrations decreased from experimental day 7 to 70, solutions became slightly less saturated over time.

The input solutions are summarised in Table 4.1 and the model set-up using the TidyPhreeqc package in R is described in detail in Section 3.2.11.

Table 4.1 - Mean values for the porewater chemistry of the four fertiliser treatments at Experiment day 7 and 70. Raw data was provided by Mr M Kelland, and mean values calculated from n number of replicates. Titanium data are considered semi-quantitative because Ti standards were not routinely ran on the instrument used. OC = organic carbon, IC = inorganic carbon. Al and Fe collected from the porewater samples.

Date	**Porewater at Experiment day 7**				**Porewater at Experiment day 70**			
Treatment	Manure (n = 4)	Manure + basalt (n = 7)	NPK (n = 7)	NPK + basalt (n = 6)	Manure (n = 7)	Manure + basalt (n = 7)	NPK (n = 7)	NPK + basalt (n = 7)
pH	6.02	6.06	5.09	4.99	7.61	7.47	6.59	6.52
Al (mg L^{-1})	0.05	0.07	0.05	0.08	0.00	0.01	0.00	0.01
Ba (mg L^{-1})	0.14	0.06	0.27	0.43	0.00	0.00	0.02	0.02
Ca (mg L^{-1})	309.35	235.08	521.37	789.54	9.84	13.86	31.59	51.15
Fe (mg L^{-1})	0.08	0.05	0.02	0.14	0.01	0.03	0.01	0.01
K (mg L^{-1})	39.90	18.77	94.34	113.50	1.30	1.03	6.97	6.51
Li (mg L^{-1})	0.01	0.00	0.02	0.03	0.00	0.00	0.00	0.00
Mg (mg L^{-1})	127.56	201.03	454.64	705.86	3.46	10.23	30.99	36.43
Mn (mg L^{-1})	0.07	0.00	0.19	0.31	0.00	0.00	0.02	0.02
Mo (mg L^{-1})	0.00	0.00	0.00	0.00	0.00	0.00	0.00	0.00
Na (mg L^{-1})	25.03	37.37	283.81	477.37	0.94	1.96	21.75	27.41
Sr (mg L^{-1})	0.77	0.49	1.30	2.12	0.02	0.03	0.08	0.12
Ti (mg L^{-1})	0.03	0.02	0.05	0.07	0.00	0.00	0.00	0.00
Zn (mg L^{-1})	0.03	0.02	0.04	0.04	0.00	0.00	0.00	0.00
Cl (mg L^{-1})	25.03	37.37	283.81	477.37	0.88	2.13	18.72	25.42
S (mg L^{-1})	21.70	23.96	17.95	27.57	1.02	1.75	1.26	1.61
NO_3^- (mg L^{-1})	127.56	201.03	454.64	705.86	3.40	11.77	30.80	38.32
C (IC, mg L^{-1})	1.53	1.88	0.28	0.45	7.45	12.85	1.69	2.35
Humate (OC, mg L^{-1})	11	23.89	14.69	19.18	28.35	19.64	14.20	13.59

4.3.9. Lithium isotope analysis

Lithium isotope analysis was conducted by Dr D Wilson at University College London (UCL). Four extracts from the 0.1 M hydroxylamine hydrochloride extraction were selected for Li-isotope analysis. Each extract represents one of the four bulk soil treatments (NPK only – taken from C5; NPK + basalt – taken from C10; Manure only – taken from C17; Manure + basalt – taken from C24). The following methods are summarised in Wilson *et al.* (2021), but a short description is provided below for reference.

The Li separation followed a standard method of elution in 0.2 M HCl through AG50W X-12 resin, with two column passes through different-sized columns to ensure matrix removal. Isotopic measurements were performed on a Nu Plasma 3 MC-ICP-MS at UCL using a Cetac Aridus 2 desolvation system, 'super-lithium' cones, and standard-sample bracketing with the IRMM-016 Li standard. Samples were measured three times within an analytical session, with each measurement integrating *c.* 50 seconds and renormalizing to the NIST-8454 LSVEC standard. The mean and value of two standard deviations of δ^7Li were reported and used in this thesis. The long-term reproducibility of the instrument is continually assessed using seawater and the USGS standard BCR-2; these values (mean±2 standard deviations) are reported as δ7 Li +31.3 ± 0.6‰ δ^7Li (n = 28) and +2.5 ± 0.3‰ δ^7Li (n = 5) for the seawater and BCR-2 standards respectively (Wilson *et al.*, 2021).

As these were single replicates, it was not possible to conduct any ANOVA analysis on the samples. However, an internally measured standard deviation was used to assess some of the differences between samples.

4.3.10. Additional corrections applied to concentration data to account for low-yielding soil amendments in bulk soil analyses

After assessing results from the soil sequential extractions it was decided that it would be worth investigating whether the application of soil amendments had affected the results of the sequential extractions by diluting soil signals.

The soil studied in this chapter came from the top 12 cm and accounted for 1.98 kg of soil. 91 g of basalt were added to the 1.98 kg of topsoil, which meant

that the concentration of basalt grains in the top 12 cm of soil was 4.74 wt.%. In the manure treatments, 18 g of manure was amended into the 1.98 kg of soil in the top 12 cm which meant that manure comprised 0.91 wt.% of the total soil mass. Neither of these values are insignificant.

The proportions of extractable Al, Fe, Mn and OC from the soils were compared to the extractable fractions of these elements in the basalt grains. No extractions were carried out on the initial manure for comparison. These comparisons showed that the basalt grains yielded relatively low extractable elements compared to the soils (Table C1).

The calculations provided in the previous paragraph shows that a relatively large proportion of basalt has been amended into the soils (4.74 wt.%). Extractions are also usually used to calculated concentrations (i.e. mg element per g bulk soil) but in an amended soil, the mass of soil per unit area increases. As part of this chapter, calculations were undertaken to test whether the low-yielding basalt affected results from the chemical extractions. It was found that the addition of the low yielding basalt grains significantly affected the extractable elements in the soils. The calculations simply accounted for the mass addition of manure and basalt added to the Manure, Manure + basalt and NPK + basalt treatments by the following equation (Eq. 4.3):

$$Conc_{corr} = (Conc_e \cdot \%_{b,m,b+m}) + Conc_e \qquad \text{(Eq. 4.3)}$$

where the $Conc_{corr}$ is the corrected concentration, $Conc_e$ is the extracted mass of element from a chemical extraction (in mg element g soil^{-1}), $\%_{b,m,b+m}$ is the proportion of basalt (b), manure (m) or basalt and manure (b+m) added to the soil. The contribution of the extractable-Al, -Fe, -Mn and -OC were assumed negligible for this study. In case a comparison between the original values ($Conc_e$) and the values which were corrected for the addition of low-yielding results are of interest ($Conc_{corr}$), figures and statistical significance data are provided in Figures C1-4.

The addition of NPK was assumed to have not diluted any of the soil signals. This was assumed because a comparatively small amount of NPK fertiliser was added to the experiment (3.46 g of NPK fertiliser) and because the compounds which comprised the NPK fertiliser (compounds = urea, di-ammonium phosphate

and potassium chloride) are highly soluble. Furthermore, the fertiliser was applied as a powder rather than a pellet which would have dissolved very quickly; the use of a pellet would have slowed the dissolution of the NPK compounds. Some ammonium, K and P may have been retained in the soil via exchange and sorption reactions but in this chapter the NPK fertiliser is assumed to have dissolved very quickly, infiltrating through the column and into the leachate quickly. In assuming this, the NPK fertiliser was unlikely to be retained within the soil and therefore would not have diluted any of the soil chemical signals.

Given the results that these calculations have shown, the effect of basalt and manure amendment on the total OC, IC and H data, as well as CEC, were also considered. It is understood by the author that the application of such corrections are not common practice in soil science. In spite of this the author has decided that, while these dilution calculations are imperfect, these calculations provide a more representative picture of chemical processes occurring within the soil. When the effect of the application of amendments are extrapolated to global scales, area is the easiest parameter to multiply by (i.e. basalt amendment rates and CDR are typically calculated per ha (e.g. Beerling *et al.*, 2020; Kelland *et al.*, 2020)). Therefore, this approach can be justified because the addition of amendments to soil affect the amount of material within a unit area of a soil profile. For convenience, however, the units are still displayed in mg element g $soil^{-1}$.

Unless otherwise stated, the results presented and discussed from this point of the chapter onwards for: the sequential extractions, OC, IC, H and CEC represent corrected data.

4.3.11. Statistical analysis

Statistical analysis of the soils from Loddington Farm were conducted to compare several different effects on the dataset. Firstly, a one-way ANOVA analysis was conducted between each fertiliser regime (NPK and Manure) to determine the individual effect of basalt amendment with each type of fertiliser. Then, a two-way ANOVA was conducted to compare each independent variable (e.g. pH, CEC) with respect to the fertiliser regime and basalt amendment (e.g. fertiliser only and basalt-amended). A post-hoc tukey honestly significant

difference test (Tukey HSD) was used when results were relevant to the aims of the chapter in instances when there were significant differences in the interactions between basalt amendment (e.g. ±basalt) and fertiliser regime to identify which pairs within the ANOVA were significantly different from each other.

4.4. Results

4.4.1. Sequential Extraction Results

The results from the sequential extractions are summarised in Figure 4.1 and 4.2, with probability values presented in the text. Although Na-dithionite extractants were analysed for Al, Fe and OC, when the blanks from each of the extracts were removed from the results, the mean values for these elements in each treatment were consistently negative and were therefore not reported in Figure 4.1.

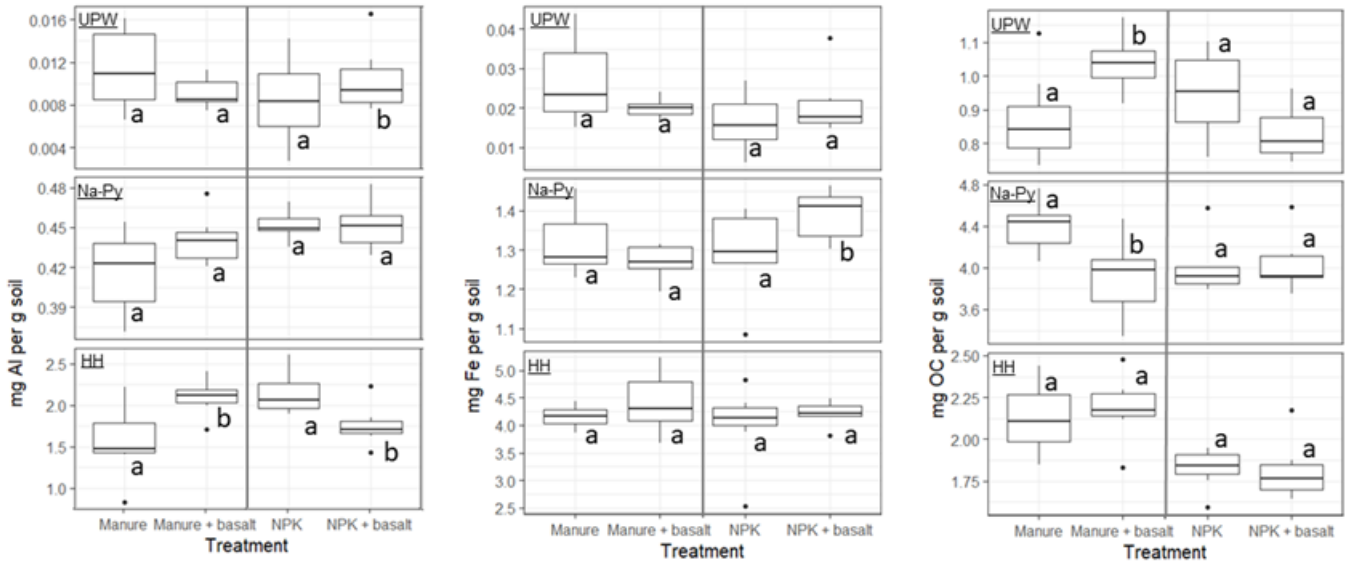

Figure 4.1 – Extractable- Al, -Fe and -OC fractions for the fertiliser only and basalt-amended treatments in the Manure and NPK fertiliser regimes (n = 7 for each treatment). Letters are used to differentiate significant differences between different treatments for each fertiliser regime (e.g. two one-way ANOVAs were conducted – one between NPK and NPK + basalt and one between Manure and Manure + basalt). UPW = ultra-pure water; Na-Py = Na-pyrophosphate; HH = hydroxylamine hydrochloride.

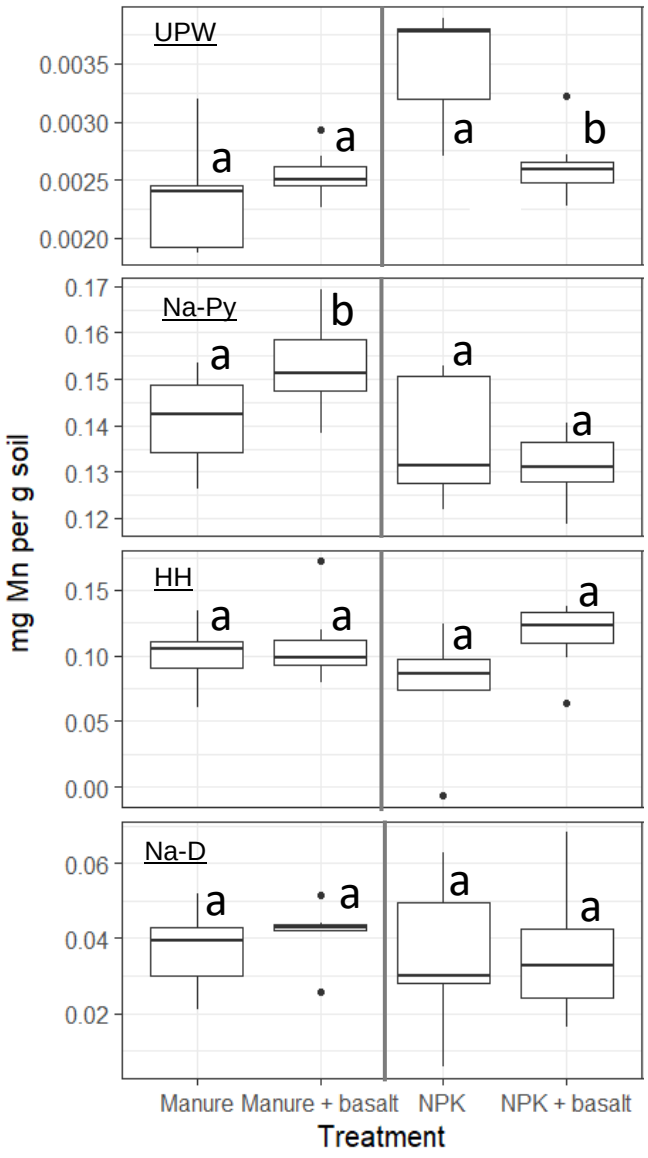

Figure 4.2 – Extractable-Mn fractions for the fertiliser only and basalt-amended treatments in the Manure and NPK fertiliser regimes (n = 7 for each treatment). Letters are used to differentiate significant differences between different treatments for each fertiliser regime (e.g. two one-way ANOVAs were conducted – one between NPK and NPK + basalt and one between Manure and Manure + basalt). UPW = Ultra-pure water; Na-Py = Na-pyrophosphate; HH = hydroxylamine hydrochloride; Na-D = Na-dithionite.

The UPW-extractable phase, referred to as water soluble-, identified OC concentrations between 0.83 and 1.04 mg OC g soil^{-1}, Al concentrations between 0.009 and 0.011 mg Al g soil^{-1}, Fe concentrations between 0.016 and 0.027 mg Fe g soil^{-1} and Mn between 0.0023 and 0.0035 mg Mn g soil^{-1}. Water soluble-OC

increases when basalt is applied in the Manure fertiliser regime (increase of 0.17 mg OC g soil^{-1}, p = 0.017), but there were no significant changes in the NPK fertiliser treatment (p = 0.065). The only significant results from the one-way ANOVA were observed in the water soluble-Mn in the NPK regime where UPW-extractable Mn decreased by 0.0009 mg Mn g soil^{-1} (p = 0.001) in the NPK + basalt treatment relative to the NPK only treatment.

The two-way ANOVA did also reveal a significant difference in water soluble-OC (p = 0.002, Table 4.2) when the interaction between basalt amendment and fertiliser regime was considered. The post-hoc Tukey HSD test revealed that there were two significant pairings between the Manure + basalt and NPK + basalt treatment (p = 0.009) and between the Manure only and NPK only treatment (p = 0.041). While the water soluble-Mn only a trace component, the two-way ANOVA shows that fertiliser regime, basalt amendment type, and the interaction between both variables all significantly effect water soluble-Mn concentrations (Table 4.2). No post-hoc Tukey HSD test was conducted on the interaction between the fertiliser regime and basalt amendment because the prevalence of water soluble-Mn did not fit into any of the hypotheses presented in this chapter.

The humus adsorbed/complexed pool, inferred from the Na-pyrophosphate extractable phases, represents the largest pool of OC by comprising between 3.90 and 4.40 mg OC g soil^{-1}. Despite this, there were no significant differences between the treatments in the NPK regime (p = 0.77) but OC significantly decreased in the Manure + basalt treatment relative to the Manure only treatment (p = 0.011). Neither the NPK or Manure regime saw significant differences in the amount of Fe or Al between the fertiliser only and basalt-amended treatments but there were increases in humus adsorbed/complexed-Al in the Manure + basalt relative to the Manure only treatment (by 0.024 mg Al g soil^{-1}, p = 0.097) and in humus adsorbed/complexed-Fe in the NPK + basalt relative to the NPK only treatment (by 0.09 mg Fe g soil^{-1}, p = 0.081). There was also an increase in the humus adsorbed/complexed-Mn in the Manure + basalt relative to the Manure only treatment (by 0.012, p = 0.050).

There were several interactions between fertiliser regime, basalt amendment and the interaction between both of these, as shown by the two-way ANOVA analysis. Basalt amendment affected the amount of humus adsorbed/extractable-OC ($p = 0.050$) while fertiliser regime affected the amount of Al ($p = 0.007$) and Mn ($p = 0.004$), with increased Mn was observed in the Manure regime and increased Al was observed in the NPK regime. OC, Fe and Mn were shown to be significantly affected by the interactions between fertiliser regime and basalt amendment ($p = 0.021$, 0.032 and 0.031 respectively).

A post-hoc Tukey HSD test revealed that there were no significant differences between any of the treatments in the humus adsorbed/complexed-Fe (i.e. $p > 0.05$ for all treatments). Two significant pairings were identified in the humus adsorbed/complexed-Mn pool, with differences between the NPK + basalt and Manure + basalt treatment ($p = 0.004$) as well as the NPK only and Manure + basalt treatment ($p = 0.048$). For humus adsorbed/complexed-OC, the Tukey HSD test revealed one significant pairing between the Manure only and NPK only treatment ($p = 0.019$).

Table 4.2 – ANOVA summary table considering effects of basalt amendment, fertiliser regime and the interaction between these two variables for all chemical extractions. Grey shaded values highlight relationships with a significance value of $p < 0.05$; values shaded in green highlight relationships with a significance of < 0.10. UPW = Ultra-pure water; Na-Py = Na-pyrophosphate; HH = hydroxylamine hydrochloride; Na-D = Na-dithionite; Total extracted = sum of all extractions for a specific element.

Extraction	Element	Amendment (+/- basalt)	Fertiliser regime	Amendment X fertiliser regime
UPW	OC	0.545	0.126	0.002
	Fe	0.694	0.130	0.065
	Al	0.884	0.477	0.101
	Mn	0.037	0.0002	0.00082
Na-Py	OC	0.050	0.256	0.021
	Fe	0.481	0.123	0.032
	Al	0.148	0.007	0.125
	Mn	0.482	0.004	0.031
HH	OC	0.770	0.00006	0.592
	Fe	0.200	0.352	0.872
	Al	0.520	0.300	0.0005
	Mn	0.064	0.517	0.226
Na-D	OC	NA	NA	NA
	Fe	NA	NA	NA
	Al	NA	NA	NA
	Mn	0.695	0.575	0.637
Total extracted	OC	0.151	0.0002	0.471
	Fe	0.195	0.519	0.815
	Al	0.475	0.239	0.00056
	Mn	0.010	0.029	0.808

The hydroxylamine-hydrochloride-extractable pool is inferred as poorly-crystalline and SRO phases. From this point onwards, the hydroxylamine-hydrochloride-extractable pool is referred to as SRO-(element). There were notable and significant differences in the hydroxylamine-hydrochloride-extractable pool with respect to Al concentrations. When basalt was amended into to the Manure fertiliser regime, extractable SRO-Al concentrations increased by 0.53 mg Al g soil^{-1} ($p = 0.013$), but SRO-Al concentrations decreased by 0.39 mg Al g soil^{-1} when basalt was added to the NPK regime ($p = 0.016$). However, there were no significant differences observed in either the Fe (ranging from 4.02 to

4.49 mg Fe g soil^{-1}, $p < 0.475$) or OC (mean values ranging from 1.81 to 2.19 mg OC g soil^{-1}, $p < 0.839$) between the basalt-amended fertiliser treatments and their fertiliser only counterparts.

The two-way ANOVA identified several interactions between basalt amendment, fertiliser regime and the interaction between both of these. SRO-OC was shown to only be affected by the fertiliser regime with significantly more OC identified in the Manure regime (mean OC = 2.13-2.19 mg OC g soil^{-1}) compared to the NPK regime (mean OC = 1.81-1.83 mg OC g soil^{-1}) ($p < 0.001$, Table 4.2). SRO-Al was shown to be strongly affected by the interaction between basalt amendment and fertiliser regime ($p < 0.001$, Table 4.2). The post-hoc Tukey HSD test revealed that the statistical significance for the post-hoc test was related to the Manure only and Manure + basalt treatments ($p = 0.014$) and the NPK only and Manure only treatments ($p = 0.007$).

No Na-dithionite-extractable Fe, Al, or OC was detected in any of the samples. Trace Na-dithionite-extractable Mn, inferred as crystalline Mn-oxides/hydroxides (Crystalline-Mn), was also detected in all the treatments and accounts for between 0.036 and 0.042 mg Mn g soil^{-1}. However, the differences in these results were not significant in either of the fertiliser regimes when fertiliser only and basalt amended treatments were considered (from one-way ANOVA, $p > 0.964$). The two-way ANOVA could only be considered for the extractable Mn, though there was no evidence for the interactions between basalt amendment, fertiliser regime or the combined effect of both of these variables.

The sum of the extracted Al, Fe, OC and Mn (i.e. UPW- + Na-pyrophosphate- + hydroxylamine-hydrochloride- extractable element for Al, Fe and OC; UPW- + Na-pyrophosphate- + hydroxylamine-hydrochloride- + Na-dithionite- extractable Mn for Mn) were also determined to test if a loss or increase in one extractable pool was quantitatively accounted for by another extractable pool. The results of these sums are summarised in Figure 4.3.

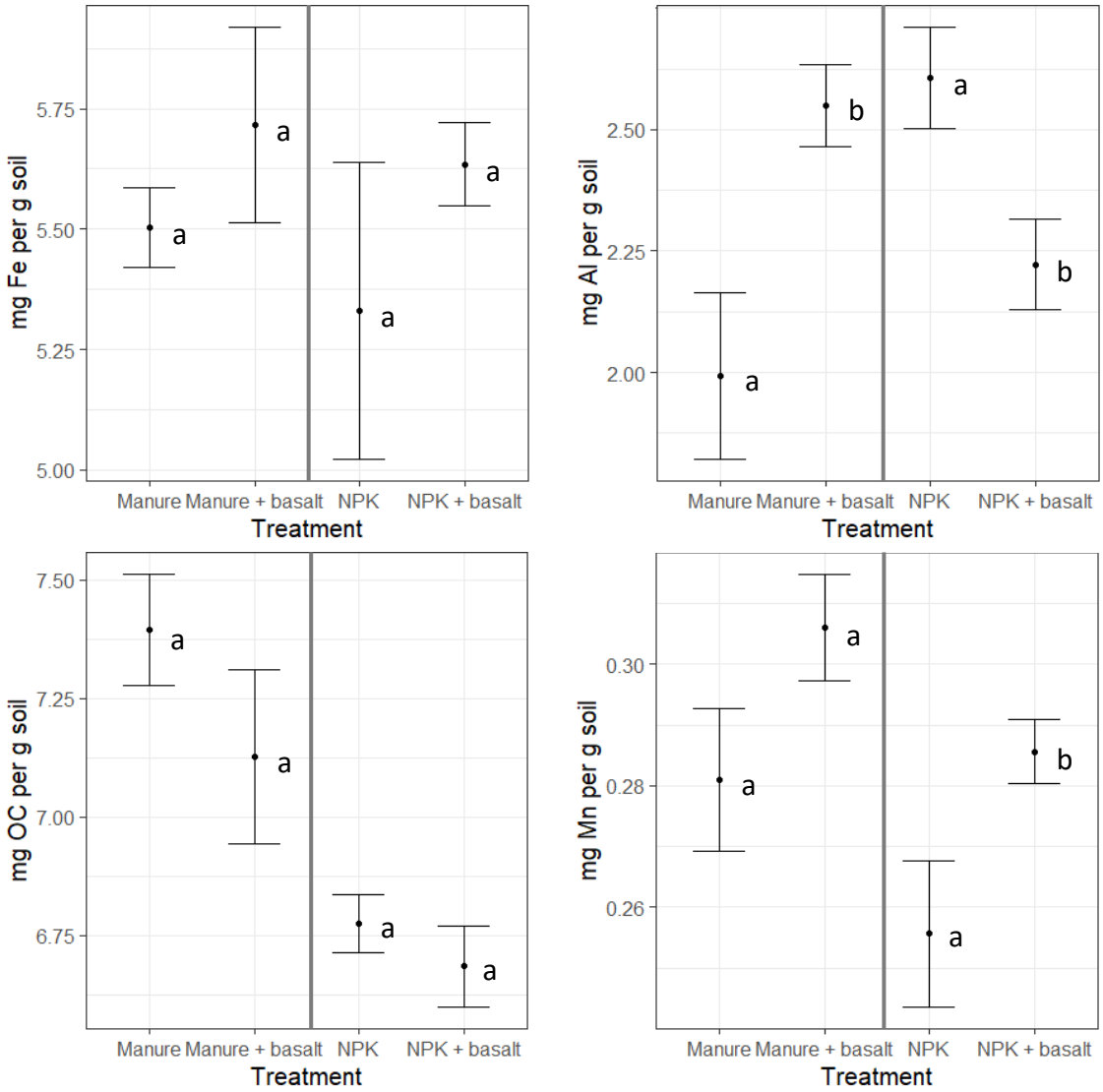

Figure 4.3 – Total extracted Fe, Al, OC and Mn. Values calculated by adding the total UPW-, Na-pyrophosphate and hydroxylamine hydrochloride extractions of each extraction. Letters are used to differentiate significant differences between different treatments for each fertiliser regime (e.g. two one-way ANOVAs were conducted – one between NPK and NPK + basalt and one between Manure and Manure + basalt). n = 7 for all treatments.

The results showed that basalt amendment did not significantly affect the total amount of extracted OC ($p = 0.403$ for NPK: NPK+ basalt; $p = 0.243$ for Manure: Manure + basalt). However, results from the fertiliser regime did significantly influence the amount of total-extractable OC with significantly more OC extracted from the Manure compared to the NPK regime ($p < 0.001$, Table 4.2).

Total extractable Al was significantly affected by the interaction between basalt amendment and fertiliser regime ($p < 0.001$) but was not significantly affected by the basalt amendment ($p = 0.475$) or fertiliser regime ($p = 0.239$) independently. Given that the vast majority of extractable Al was extracted from the hydroxylamine hydrochloride pool (up to *c.* 82 wt.%) the total extractable Al pool mirrors the significant increase in the Manure + basalt relative to the Manure only treatment ($p = 0.013$), and significant decrease observed in the NPK + basalt treatment relative to the NPK only treatment ($p = 0.017$). The results for the post-hoc Tukey HSD test on the total extractable Al were similar to the results of the SRO-Al, with significant differences between the Manure only and Manure + basalt pair ($p = 0.014$) and the Manure only and NPK only pair ($p = 0.006$).

There were no significant differences in the total extracted Fe concentrations between fertiliser only and basalt-amended treatments ($p < 0.361$) nor was there any significant effect of basalt amendment, fertiliser regime or the interaction between basalt amendment and fertiliser regime (Table 4.2).

There was, however, a treatment effect observed in the total Mn calculations. Increased total extractable Mn was observed in the NPK + basalt treatment relative to the NPK only treatment ($p = 0.042$). While basalt amendment did significantly affect the amount of Mn between basalt amended and fertiliser only treatments the NPK regime, total Mn was significantly higher in the Manure fertiliser regime compared to the NPK regime ($p = 0.029$, Table 4.2). Basalt amendment also significantly increased the total extractable Mn relative to fertiliser only treatments ($p = 0.010$, Table 4.2) but the interaction between basalt amendment and fertiliser regime did not significantly affect total Mn ($p = 0.808$).

4.4.2. OC/IC, H, N and S

With the exception of two samples, one in the Manure only and another in the Manure + basalt treatment, N was below the CHNS analyser's limit of detection of 0.3 wt.% N for most samples. No S was identified in any of the 'Total CHNS' samples, but S was detected in most (26 out of 28) of the acid-stripped (OC) samples. The increase in S is likely to have resulted from contamination, possibly from the HCl used in the acid stripping process because S concentrations should have decreased in acid stripped samples as a result of the extra weight added from the conversion of $CaCO_3$ to $CaCl_2$ (see Eq. 4.1). This section therefore only considers OC, IC and H data. The results are summarised in Figure 4.4 and results from the two-way ANOVA are summarised in Table 4.3.

Considering the differences between the two fertiliser regimes, the mean OC values were 2.3 and 2.4 wt.% in the NPK regime and 2.6 and 2.7 wt.% in the Manure regime. The two-way ANOVA revealed significant differences between the four treatments on account of different fertiliser regimes ($p < 0.001$, Table 4.3) and the interactions between basalt amendment and fertiliser regime ($p = 0.043$). The post-hoc Tukey HSD test revealed three statistically significant pairings between the NPK + basalt and Manure + ($p < 0.001$), between the NPK and Manure + basalt ($p = 0.001$) and between the Manure and NPK + Basalt ($p = 0.37$) treatments. The significant increase in mean IC values varied at 0 and 0.1 wt.%, and at 0.48 and 0.51 wt.% for the NPK and Manure fertiliser regimes respectively. The difference between the two fertiliser regimes were determined to be highly significant different ($p < 0.001$, Table 4.3).

Focusing specifically on the Manure regime, the mean OC increased in the Manure + basalt relative to the Manure only treatment, by 0.1 wt.% however this increase was not significant ($p = 0.085$). Meanwhile, in the NPK regime, OC increases in NPK + basalt treatment relative to the NPK only treatment by 0.1 wt.% and this increase was also not significant ($p = 0.33$).

The results from the two-way ANOVA showed that total H values were significantly different between the two fertiliser results ($p < 0.001$) at mean values of 1.2 wt.% for the NPK fertiliser regime and 1.3 wt.% for the Manure fertiliser regime (Figure 4.4). Even though the differences between treatments

were small, basalt amendment did affect H concentrations ($p = 0.002$) but there was no significant influence on the interaction between basalt amendment and fertiliser regime ($p < 0.687$). The pair-wise one-way ANOVA results showed that basalt amendment significantly increased total H concentrations in the NPK + basalt relative to the NPK only treatment ($p = 0.008$). Although a similar increase was observed, there were no significant differences between the Manure and Manure + basalt treatment ($p = 0.089$).

Table 4.3 – ANOVA summary table considering effects of basalt amendment, fertiliser regime and the interaction between the two variables for various measured soil parameters. Grey shaded values highlight relationships with a significance of $p < 0.05$.

Chemical parameter	Amendment (+/- basalt)	Fertiliser regime	Amendment · Fertiliser regime
Organic C	0.429	2.72E-5	0.043
Inorganic C	0.437	0.0001	0.939
Total H	1.68E-6	0.004	0.565
CEC	0.008	2.00E-16	0.045
pH	8.95E-13	0.009	0.387

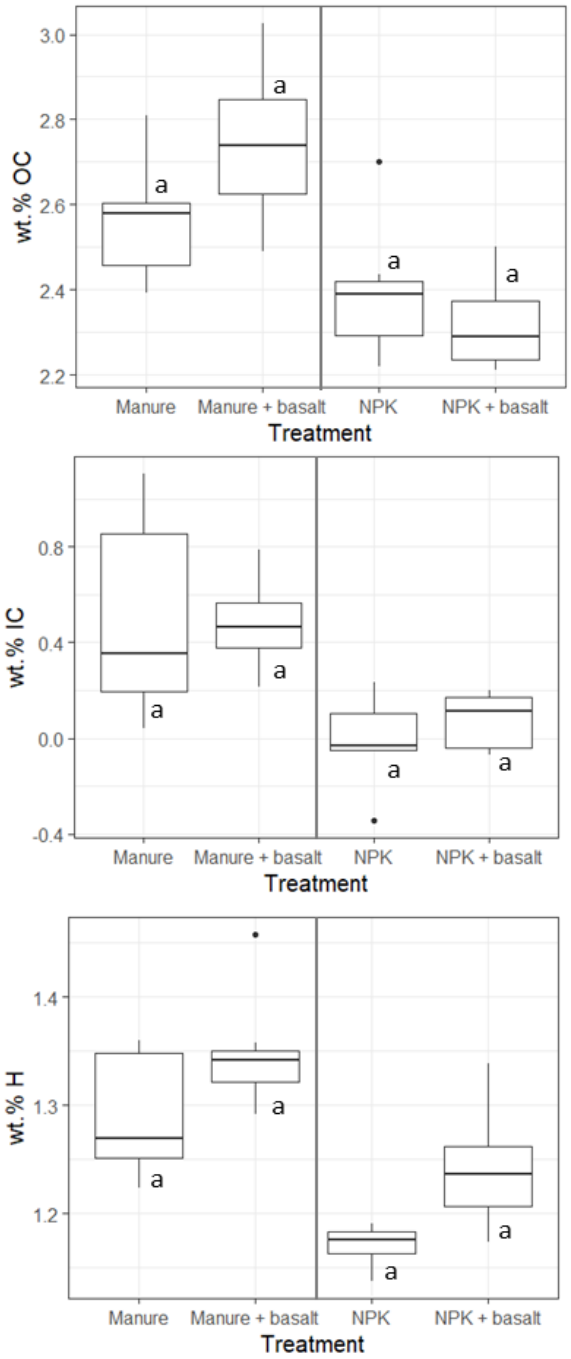

Figure 4.4 – Total OC, IC and H for each treatment. Letters are used to differentiate significant differences between different treatments for each fertiliser regime (e.g. two one-way ANOVAs were conducted – one between NPK and NPK + basalt and one between Manure and Manure + basalt), n = 7 for all treatments with the exception of Manure for which n = 6.

4.4.3. Soil pH and CEC

Mean soil pH values for each fertiliser treatment were 5.7 and 5.9 in the Manure fertiliser treatments and were 5.1 and 5.2 in the NPK fertiliser treatment (Figure 4.5). The two-way ANOVA identified that basalt amendment does significantly increase pH ($p = 0.009$, Table 4.3). However, in each fertiliser regime, the pH values between the fertiliser only and basalt-amended treatments were not shown to be significantly different from each other. For both fertiliser regimes, the significance values were close to the significance threshold of $p = 0.05$ between NPK and NPK + basalt treatments ($p = 0.067$) and between the Manure and Manure + basalt treatments ($p = 0.055$).

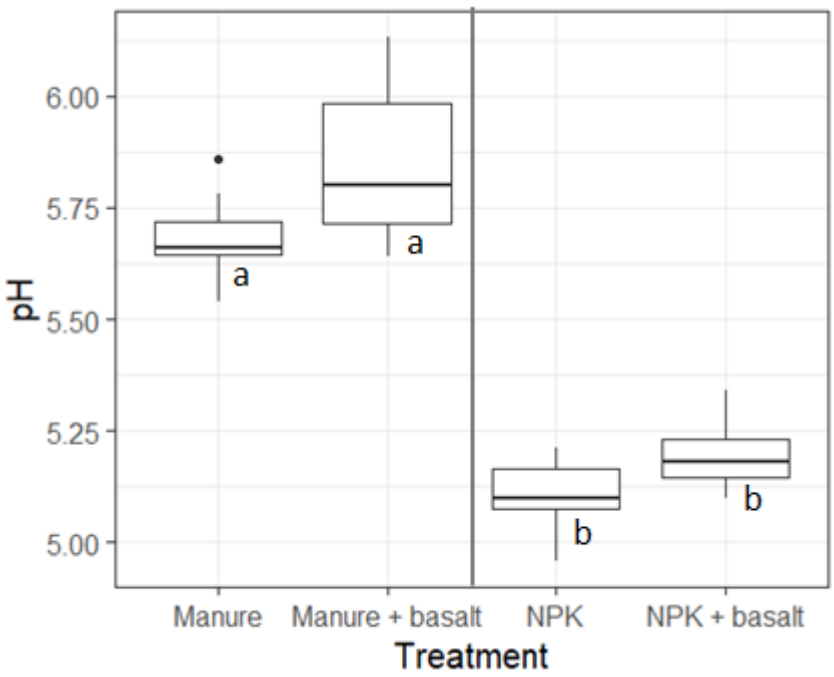

Figure 4.5 – Soil pH. Letters are used to differentiate significant differences between different treatments for each fertiliser regime (e.g. two one-way ANOVAs were conducted – one between NPK and NPK + basalt and one between Manure and Manure + basalt), n = 7 for all treatments.

The mean CEC of the two fertiliser regimes were 0.137 and 0.149 meq g soil^{-1} in the NPK fertiliser regime, and 0.163 and 0.171 meq g soil^{-1} for the Manure fertiliser regime (Figure 4.6). Basalt amendment significantly increased CEC in both of the fertiliser regimes ($p < 0.001$ for both fertiliser treatments).

Fertiliser regime also significantly influenced the CEC values ($p < 0.001$), as well as the basalt amendment ($p = 0.008$) and the interaction between both fertiliser regime and basalt amendment ($p = 0.045$). The post-hoc Tukey HSD test revealed that all of the possible pair combinations were significantly different from each other (< 0.008) with the exception of the Manure only relative to the Manure + basalt treatment ($p = 0.941$).

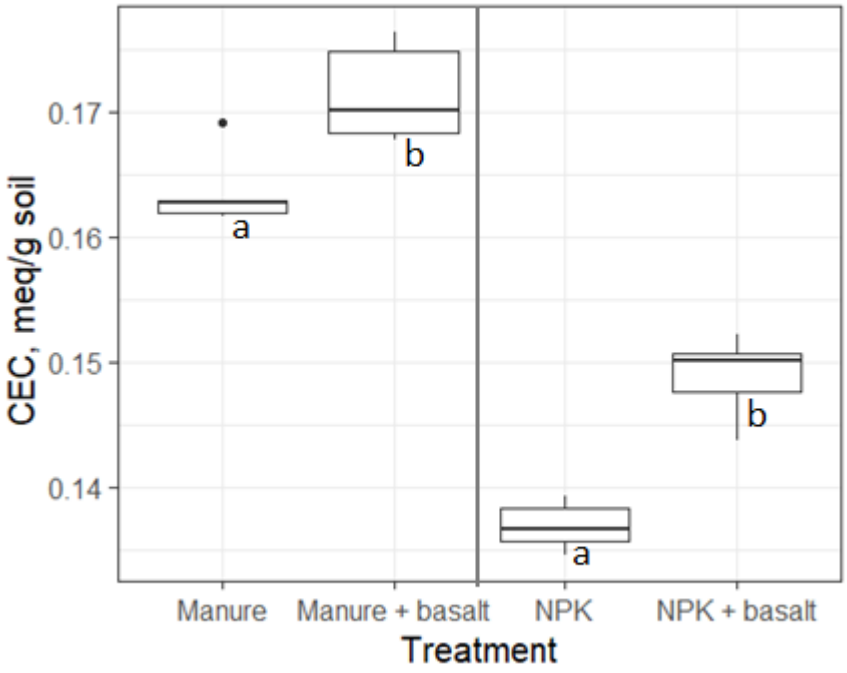

Figure 4.6 – Soil CEC. Letters represent statistically significant groupings between either fertiliser only or basalt-amended treatments (e.g. a and a would indicate a lack of significance from each other, a and b would be statistically significantly from each other).

4.4.4. Lithium isotope data

The Li-isotope data show a similar trend to the SRO-Al data with ^{7}Li concentrations increasing in the Manure + basalt sample relative to the Manure only, and NPK + basalt decreasing compared to the NPK only treatment (Table 4.4). The highest and lowest boundaries for the mean value ± standard deviation meet each other in the Manure compared to Manure + basalt, but cross over between the NPK compared with the NPK + basalt sample. Generally, total Li from the hydroxylamine hydrochloride extraction followed the same trend as ^{7}Li and Al concentrations.

Table 4.4 – ^{7}Li values and total Li, [Li], identified in the hydroxylamine hydrochloride extraction. sd = standard deviation. ^{7}Li values determined at UCL (methods in Section 4.3.9) and [Li] data determined using ICP-MS (methods in Section 3.2.9.2).

Treatment	δ^{7}Li, ‰	2sd, ‰	mean±2SD, ‰	average [Li] ± SE, mg L^{-1}
NPK	3.4	0.4	3.0-3.8	98.22 ± 6.98
NPK + basalt	2.8	0.3	2.5-3.1	74.70 ± 3.04
Manure	2.4	0.2	2.2-2.6	77.02 ± 5.2
Manure + basalt	3.0	0.4	2.6-3.4	81.02 ± 6.95

4.4.5. Porewater modelling

4.4.5.1. Comments on porewater solution measurements

Overall, there were differences in porewater solution chemistry between the porewater samples collected at experiment day 7 and 70 in all treatments, as summarised in Table 4.1. Generally, in each treatment, the alkali and alkaline earth metals (Na, K, Ca and Mg) as well as the sulphate and nitrate concentrations decreased over time. The Al, Fe and Mn concentrations remained constantly low throughout the experiment. The IC values all increase over time, but the magnitude of this increase is larger in Manure relative to the NPK treatments. OC concentrations also become higher in the Manure treatments over time. There are no differences in the NPK + basalt treatment relative to the Manure + basalt treatment.

4.4.5.2. Model results

The geochemical modelling results are summarised in Figure 4.7. As very few differences are observed between each of the four treatments, only the Manure + basalt treatment is shown in the main chapter text. Geochemical modelling of the other treatments soil solutions can be found in Appendix D.

As noted in the first paragraph of this section, however, between the porewater samples at experiment day 7 and 70, there were substantial increases in

pH by up to a mean of 1.69 and 1.56 pH units for the NPK and Manure regimes respectively.

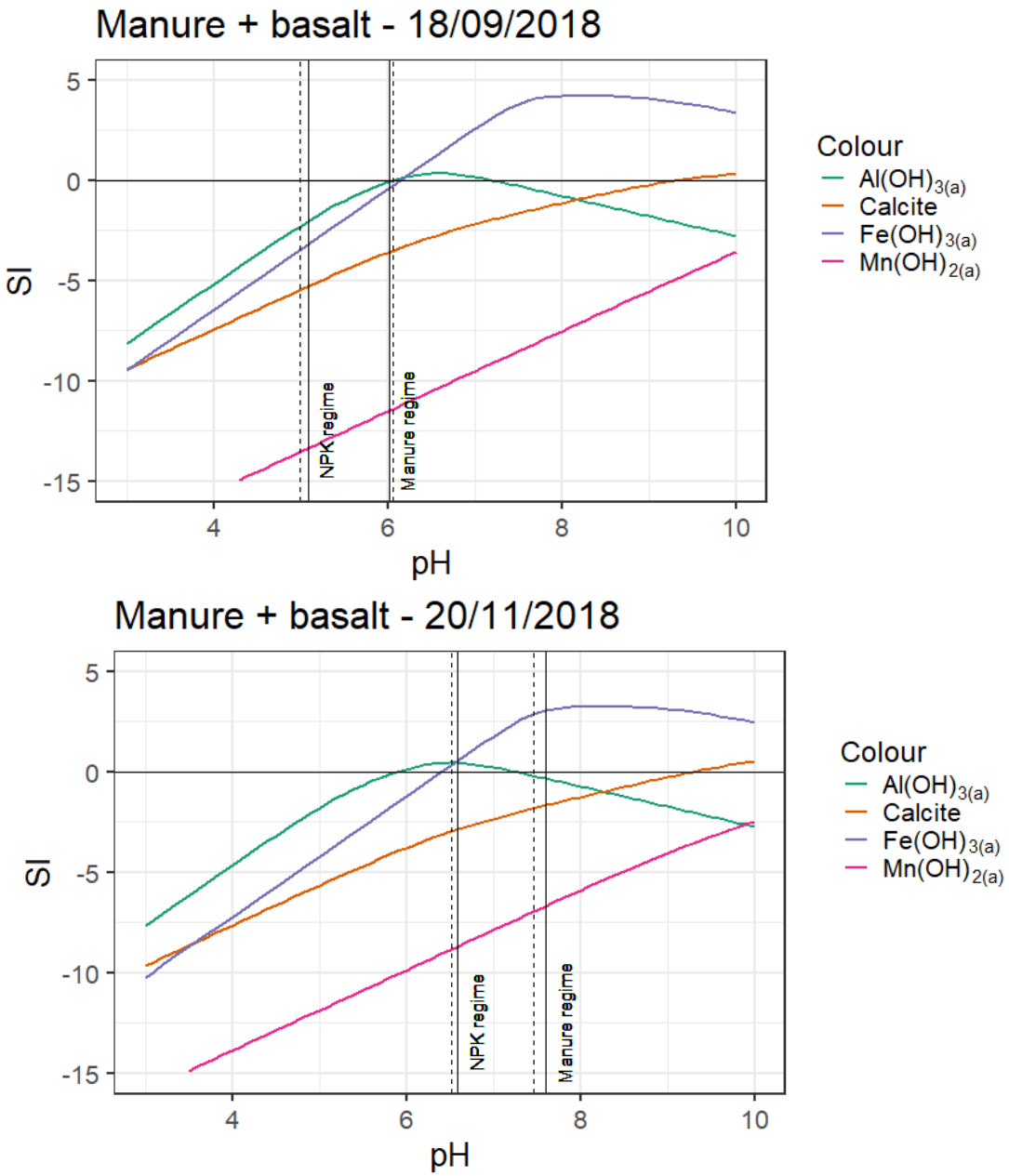

Figure 4.7 – Graph showing Saturation Indices (SI) of several Al, Fe, Si, Ca and Mn phases as a function of pH in the Manure + basalt treatment after experimental day (a) 7 and (b) 70 Vertical line represents the measured porewater pH of each respective solution. Dashed line represents the pH of the basalt-amended treatment and solid line represents the pH of the fertiliser only solution. The results for all other treatments can be found in Appendix D.

In the mean porewater solutions at experiment day 7 for NPK only and NPK + basalt measured pH 5.1 and 4.9 respectively. At these acidic pH values, $Al(OH)_{3(a)}$ is undersaturated and therefore has the potential to dissolve. The porewater after 70 days of weathering increases to 6.6 and 6.5 for the NPK only and NPK + basalt treatments respectively. At experiment day 70, in both NPK treatments, the pH is sufficiently high enough for $Al(OH)_{3(a)}$ to be saturated and therefore has the potential to precipitate out of solution. In the Manure fertiliser regime, the mean porewater solution pH is initially much higher at pH 6.0 and 6.1 for the Manure and Manure + basalt treatments respectively. Here, the opposite trend in $Al(OH)_{3(a)}$ was observed with $Al(OH)_{3(a)}$ being saturated after experimental day 7, but became undersaturated by experiment day 70 when solution pH increased to pH 7.6 and 7.5 for the Manure and Manure + basalt treatments respectively – out of the $Al(OH)_{3(a)}$ range.

Under both fertiliser regimes and both sets of treatments, $Fe(OH)_{3(a)}$ was undersaturated in the porewater after 7 days of weathering. However, $Fe(OH)_{3(a)}$ becomes saturated after 70 days of weathering in both fertiliser regimes. The amorphous Mn-oxide did not become saturated in the conditions used in this model.

Briefly, the precipitation of calcite was also modelled given its potential to stabilise OC via occlusion (Rowley, Grand and Verrecchia, 2018). Generally, the pH threshold for calcite precipitation is slightly higher in the Manure relative to the NPK regime. Calcite becomes saturated at *c.* pH 9.2 in the Manure regime whereas calcite becomes saturated at *c.* pH 9.8-10 in the NPK regime. These pH values are much higher than the pH values observed in the experiments detailed in this chapter.

4.5. Discussion

4.5.1. Humus associated OC and metal interactions

A range of different responses were observed in the humus adsorbed/complexed-Al, -Fe, -Mn and -OC, as inferred from the Na-pyrophosphate extractions (Figures 4.1 and 4.2). There were no significant differences between basalt-amended and fertiliser only treatments for any of the

elements in the NPK fertiliser regime. However, while not significantly different ($p = 0.081$), there was a notable increase in the amount of humus adsorbed/complexed-Fe in the NPK + basalt treatment relative to the NPK only treatment.

Under the Manure fertiliser regime, humus adsorbed/complexed-OC significantly decreased while humus adsorbed/complexed-Mn significantly increased when comparing the Manure + basalt to the Manure only treatment. Additionally, while not significant ($p = 0.097$), there was a notable increase in humus adsorbed/complexed-Al in the Manure + basalt treatment. The interpretation of the humus adsorbed/complexed-Mn is discussed in more detail in Section 4.5.2.

These results only partially support Hypothesis (1), which predicted that there would be increases in the humus adsorbed/complexed-Al, -Fe and -Mn after basalt weathering because of an increased flux of Al and Fe released into soil solutions that could interact with OC molecules via adsorption and complexation. The short duration of the active stage of the experiment (81 days) could have limited the development of the increased humus adsorbed/complexed-Al and -Fe concentrations that were observed in the Manure + basalt and NPK + basalt treatments respectively. If the experiment was conducted for a longer period of time, Al and Fe concentrations could have further accumulated and the increase in these elements could have become significant.

The results also do not support the predictions made for Al and Fe in Hypothesis (2), which predicted that there would be greater increases in the humus adsorbed/complexed-Al and -Fe in the NPK regime relative to the Manure regime on account of more favourable solution conditions for both weathering of basalt grains and for humus adsorption/complexation interactions in the NPK relative to the Manure fertiliser regime. It is therefore unclear why there were significant changes in the Manure fertiliser regime when there were no significant changes in the NPK fertiliser regime when the opposite effects were expected.

There was evidence of increased weathering of Mn-bearing minerals in the NPK + basalt relative to the Manure + basalt treatments from the XRF data,

as detailed in Chapter 3 (Section 3.4.1.2) and given the lower porewater and soil pH observed in the NPK relative to the Manure fertiliser regime, more weathering would be expected in the NPK regime. Fe increased, which could have been an artefact of the semi-quantitative XRF method (as explained in Section 3.4.2.1) and changes in Al could not be used due to kaolinite contamination (as explained in Section 3.4.1.1). With increased weathering, an increase in Al, Fe and Mn could be available to either adsorb or form complexes with humus. The NPK regime would also have a greater potential to stabilise OC through these mechanisms.

The general pH conditions in both the NPK and NPK + basalt treatments are within the pH range that Al- and Fe- complexes have been shown to predominate (e.g. pH < 5.5, (Rasmussen *et al.*, 2018)). Given the pH conditions and the increased flux of Al and Fe released during basalt weathering, an increase in Al and Fe associated with humus adsorption and complexation could be expected. There was no significant increase nor was there any indication that humus adsorbed/complexed-Al would increase in the NPK + basalt relative to the NPK only treatment (i.e. there were no almost significant increases in humus adsorbed/complexed-Al in the NPK + basalt relative to the NPK only treatment ($p = 0.928$) like there had been in the NPK regime for humus adsorbed/complexed-Fe). Instead, weathered Al could have been incorporated into the interlayer of 2:1 layer silicates (Dahlgren and Ugolini, 1989; Takahashi and Dahlgren, 2016). The incorporation of Al into 2:1 layer silicates was not measured in this chapter.

Conversely, in the Manure fertiliser regime, the porewater pH after experiment day 7 was significantly higher than the NPK fertiliser regime (Manure regime pH = 6-6.1, NPK regime pH = 5.0-5.1) and therefore humus adsorption/complexation would be less likely. Instead, at these pH conditions, Al would be more likely to either co-precipitate with OC or to be precipitated as SRO phases. The increases in humus adsorbed/complexed-Al in the Manure + basalt relative to the Manure only treatment could be indicative of an additional microenvironment within the bulk soil that has not been studied in the work presented in this thesis: the rhizosphere. There may be localised areas in soils

within a few millimetres from the plant roots where both organic acids are exuded from the plant roots and associated microorganisms respire CO_2 after metabolising the organic acids. Both the organic acids and increased CO_2 concentrations in the rhizosphere lower the pH. Typically, the rhizosphere is 2 pH units lower than the surrounding soil (Hinsinger *et al.*, 2003) and these lower pHs could facilitate the formation of Al-OC complexes.

It is worth noting that bulk soils behave very differently to the basalt grains which were studied using the same extractions in Chapter 3 (see Sections 3.3.4 and Figures 3.14 and 3.15). Consistently, there were significant increases in Fe and Al associated with humus in the basalt bags but there were no such significant increases in the amount of Al and Fe associated in the bulk soils. This may suggest that the basalt grains may have been a sink for Al and Fe. Even though the presence of relatively low concentrations of Al and Fe on the basalt grains were accounted for in this chapter by increasing the amount of each extractable element from the bulk soils by the amount of either manure or basalt that was amended into the soil (see Section 4.3.10), the increase in Al and Fe in the basalt bags was not sufficiently high to produce significantly higher results in the variable and highly concentrated (in respect to Al and Fe) bulk soil. The OC concentrations remained constant between the fertiliser regimes in both sites.

4.5.3. The precipitation of short range order minerals

The precipitation of SRO phases is inferred from the hydroxylamine hydrochloride extractions. Neither the SRO-Mn or -Fe increased in either treatment, but there were significant differences in the SRO-Al concentrations. Therefore, this section focuses on evidence and interpretation of the precipitation of SRO-Al. Hypothesis (3) predicted that both SRO-Al and -Fe would increase as a result of basalt amendment. Before considering the occurrence of SRO-Al, it is worth noting that Hypothesis (3) was partly disproved because of the lack of SRO-Fe precipitation.

There was a significant increase in extractable SRO-Al in the Manure + basalt relative to the NPK + basalt treatment while there was a significant decrease in SRO-Al in the NPK + basalt relative to the NPK only treatment. This

means that there are mixed results supporting Hypothesis (3) with the results from the Manure fertiliser regime supporting this hypothesis, but the results from the NPK fertiliser regime not supporting this hypothesis. The interaction between basalt amendment (i.e. amended or fertiliser only) and the fertiliser regime was shown to be an important predictor for determining the response of SRO-Al precipitation.

The extractable SRO-Al corroborates with the porewater modelling results presented in this chapter. $Al(OH)_{3(a)}$, inferred as a likely SRO-Al sink, was initially saturated in both Manure + basalt and Manure only treatments at experiment day 7 but did become undersaturated by experiment day 70. The modelling showed that in both of the NPK treatments at experiment day 7, the porewater and soil pH (pH = 4.9-5.2) were undersaturated with respect to $Al(OH)_{3(a)}$. As $Al(OH)_{3(a)}$ is undersaturated it would have, at least at experiment day 7, had the potential to dissolve. Towards the end of the experiment, at experiment day 70 when porewater pH in the NPK regime increased to between pH 6.5-6.6, $Al(OH)_{3(a)}$ was saturated and therefore had the potential to precipitate secondary minerals.

Some thought was given to discern if this increase in pH was the result of chemistry or preferential flow. The development of preferential flow pathways as roots carve out channels or when soil is rapidly dried as roots uptake water have been shown to influence hydrology in mesocosm experiments (Kelland *et al.*, 2020). If preferential flow pathways had formed, they could reduce the residence time of porewater to react with the soil (including basalt grains) and as a result the porewater results could have only been using fresh irrigation solution that the column was irrigated with. However, the increase of soil and porewater pH in the NPK regime to *c.* pH 6.5 was greater than the artificial rainwater water which had been used to irrigate the experiment (at pH 5.4). Therefore, the increase in pH observed in the NPK fertiliser regime after 70 days of the experiment is not the result of a more rapid loss of porewater as preferential flow pathways developed, but is likely to be the result of chemical processes instead.

If the increase in pH was the result of chemical processes, the models suggest that there was an opportunity for $Al(OH)_{3(a)}$ to dissolve before

reprecipitating but there might not have been sufficient opportunity to reprecipitate all the $Al(OH)_{3(a)}$ that was lost. Even if this is true, and there was a dissolution/reprecipitation reaction occurring here, the modelling results still do not explain why $Al(OH)_{3(a)}$ decreased significantly in the NPK + basalt relative to the NPK only treatment because both treatments were similarly initially undersaturated before becoming saturated by the end of the experiment with respect to $Al(OH)_{3(a)}$.

It would have been expected that the NPK + basalt would have had higher concentrations of SRO-Al than NPK only because of an increased supply of Al from basalt weathering. The weathering of the basalt grains has been evidenced from basalt bag analysis in Section 3.3.1. While it was not possible to determine the removal of Al from basalt grains as a result of weathering due to kaolinite contamination in the basalt mesh bags, Al might be released during basalt weathering and is likely to be the reason for the increased Al which was observed in the Manure + basalt treatment relative to the Manure only treatment.

If there is an increased source of Al in the NPK + basalt relative to the NPK treatment and the Al has not precipitated in secondary phases, there must be other sinks of Al in the solutions, soil and plant. Several other solutions, soil and plant sinks for Al, all of which were measured as part of Mr M Kelland's PhD thesis, were used to assess if other elemental sinks had increased which could then account for the decrease of SRO-Al that was reported in this chapter. These potential Al sinks are summarised in Table 4.5. Leachate Al was significantly lower in the NPK + basalt treatment relative to the NPK only treatment, while porewater concentrations were almost significantly higher ($p = 0.058$) in the NPK + basalt relative to the NPK only treatment. The difference in Al concentration in the leachate between the NPK and NPK + basalt (0.005 mg Al L^{-1}) was similar to the difference in Al concentration in the porewater (0.004 mg Al L^{-1}). Considering the other measured soil pools, exchangeable Al (as determined from 0.1 M ammonium acetate extractions) was lower in the NPK + basalt relative to the NPK only treatment. No significant differences were identified in the different plant Al sinks (roots, shoots, and seeds) between the NPK + basalt and NPK only treatments. Even though the results were not significantly different, the amount of

Al in the roots also decreased. While there was a small increase in the amount of Al in the seeds (*c.* 0.02 mg Al in seeds column^{-1}), there was also a large decrease in the amount of Al in the plant shoots (*c.* 0.10 mg Al in shoots column^{-1}) so therefore the total Al sink is lower in the NPK + basalt treatment relative to the NPK only treatment.

Table 4. 5 – Mean measured values for other measured Al sinks ± standard error. Exchangeable Al was determined (using 0.1 M ammonium acetate extraction as described in Section 4.3.2) and root, shoot and seed concentrations were determined via microwave digestion and ICP-MS. Unless otherwise stated, n = 7 for all of the Al sinks and treatments listed in this table.

Sink	**NPK**	**NPK + Basalt**	**Significant? ($p < 0.05$)**	**Trend (NPK + B relative to NPK only)**
Solution				
Leachate at day 70, mg L^{-1}	0.008±0.002	0.003±0.001	Yes – p = 0.038	Significantly lower Al
Porewater at day 70, mg L^{-1}	0.005±0.0004	0.009± 0.002	No – p = 0.058	Almost significant increased Al
Soil				
Exchangeable Al, mg L^{-1}	0.028±0.001	0.024±0.001	No – p = 0.154	Slight decrease
Plant				
Roots, mg Al $column^{-1}$	0.07±0.01	0.06±0.02	No – p = 0.848	No change
Shoots, mg Al $column^{-1}$	0.36±0.09	0.26±0.05	No – p = 0.359	Slight decrease
[1]Seeds, mg Al $column^{-1}$	0.14±0.01	0.16±0.01	No – p = 0.286	Slight increase

[1]n = 6 for NPK only seeds, n = 7 for NPK + basalt seeds

There could be several other sinks for Al that have not been considered within this study. Firstly, this study only used soil from the top 12 cm of the experiment. The Al could have relocated to somewhere in the other 38 cm of the soil column. Secondly, the precipitation of clays such as kaolinite and smectite were not considered in this study, although these could be less likely to form because they typically form on longer time scales than poorly crystalline Al (Chorover, Amistadi and Chadwick, 2004). The abundance of kaolinite could be determined using a 0.5 M NaOH extraction (Hashimoto and Jackson, 2013) and the presence of smectite could be determined using a 0.6 M HCl extraction (Pogge von Strandmann *et al.*, 2019). As mentioned in Section 4.4.1, given the lower pH of the NPK fertiliser regime, it could be useful to test if there were changes in the amount of Al contained within the interlayer of clay species

(Takahashi and Dahlgren, 2016) by subtracting the results from a 0.33 M Na-citrate extraction from the results of a 0.2 M ammonium oxalate extraction (Soon, 1993).

Li isotopes were also used to assess the precipitation of secondary minerals. Unfortunately, the lack of statistical significance in the Li-isotope data makes it difficult to compare the corroboration between the sequential extractions with the Li-isotope data. Only one independent sample was measured for its δ^7Li value per treatment, so it was not possible to conduct an ANOVA on this analysis. The standard deviations, calculated internally in the instrument by measuring the sample three times, shows that these samples are only marginally different from one another.

While the δ^7Li results were not significant, they show a similar pattern to extracted SRO-Al extractions with increased value of δ^7Li in the Manure + basalt relative to the Manure only treatment, and a decrease in the NPK relative to the NPK + basalt treatment. Unfortunately, this is not an indication of secondary phase precipitation. If secondary phases were precipitated, the opposite trend would be expected as lighter ^{6}Li would have been preferentially incorporated into the structure of secondary minerals relative to ^{7}Li (Pogge von Strandmann, Kasemann and Wimpenny, 2020). This would then produce a lower δ^7Li value. The reasons for this trend are not clear, but the interpretation of these results is challenging due to the small number of samples analysed which means that there is a lack of statistical significance. This means that there was no evidence to support the prediction made in Hypothesis (3) which predicted that Li isotope measurement would be able to detect the formation of secondary phases.

These Li isotope analyses provide just a snapshot of Li dynamics in the soil system. Just as it has proven useful to assess a variety of Al sinks in solutions, soil and the plant to interpret the results of Al precipitation in this chapter, it may also prove useful in interpretation to assess a variety of Li sinks. Several other important sinks have been identified for interpreting secondary phase precipitation as a result of silicate weathering including: (1) exchangeable Li, (2) whole-rock Li (i.e. HF digested Li) and (3) porewater (Pogge von Strandmann *et al.*, 2019; Wilson *et al.*, 2021). Determining the Li-isotope

signature of these sinks has been proven to be important for understanding the precipitation of secondary phases as a result of weathering (Pogge von Strandmann *et al.*, 2019; Wilson *et al.*, 2021). In addition to these sinks, it would also be useful in the context of this experiment to determine the Li-isotope signature of the manure, NPK and artificial rain irrigation water.

Comparing the SRO-Al results in the bulk soils to the SRO-Al extracted from the basalt grains, the SRO-Al did behave similarly to the basalt grains (Section 3.4.2.1). Here, while there were no significant changes between the Initial basalt and the basalt grains from the two treatments (NPK + basalt and Manure + basalt), there was a noted increase in the mean Al in the Manure + basalt treatment relative to a decreased mean Al concentration in the NPK + basalt treatment when both treatments are compared to the Initial basalt (Figure 3.13). While there were no significant differences when comparing the fertiliser treated results to the Initial basalt, there were significant differences between the two fertiliser treatments which replicated the trend of SRO-Al observed in this chapter.

4.5.2. Humus adsorbed/complexed-Mn

The increase of humus adsorbed/complexed-Mn supports both Hypothesis (1) and Hypothesis (2).

While the humus adsorbed/complexed-Mn concentrations are 9.4-fold lower than the humus adsorbed/complexed-Fe, the increase of Mn within this pool is still an important finding because Mn is noted to influence OC dynamics in soils (Li *et al.*, 2021). Interactions between Mn and humus typically occur at pH values between 7–11 (Duckworth and Sposito, 2005) which could be possible in the Manure + basalt because the highest porewater pH measured in this treatment was 7.5. Although the pH of the Manure + basalt was not significantly different to the Manure only treatment at pH 7.6, the increase in humus adsorbed/complexed-Mn relative to the Manure only treatment could have been a result of an additional source of Mn from basalt weathering. The release of Mn from the basalt grains is supported by evidence of Mn leaching from basalt grains in Section 3.4.1.2 (also see Figure 3.9).

The pH was similarly high in the basalt grain microenvironment studied in Chapter 3 (pH = 7.8). However, in the basalt grain microenvironment, there was a decrease in humus adsorbed/complexed-Mn extracted from basalt retrieved from the Manure + basalt treatment. Therefore, the increase in bulk soil humus adsorbed/complexed-Mn could be the result of another soil microenvironment: the manure. The properties of manure are not well characterised. Even though manure is widely applied to fields, very few studies have characterised the properties of manure prior to application to experiments and studies have instead focused on the effect of manure applications on the bulk soils (e.g. Vanden Nest *et al.*, 2016). Cattle manure, which was used in this experiment, has been reported to have a relatively high pH (*c.*7.86 (Huang *et al.*, 2017)). While, to the author's knowledge, no studies have tested the CEC of cattle manure prior to application to a field, numerous studies show increased CEC with manure amendment (e.g. Schjønning, Christensen and Carstensen, 1994; Gao and Chang, 1996). It is likely that properties of cattle manure will differ from one study to another, so it might be difficult to compare between different studies if these properties have not been characterised amongst contrasting studies. Instead the properties of manure used in individual studies (including this chapter) should be determined independently.

The increase in CEC in soils amended with manure is attributed to increased surface area from OC functional groups which metals can then bond with (Department of Primary Industries, 1993). This is supported by results reported in this chapter where the CEC increases significantly in the Manure relative to the NPK fertiliser regime. While typical extractions for CEC (i.e. ammonium acetate) do not typically target Al- and Fe-OC complexes, the CEC does indicate potential sites of charge present in a soil. The CEC of the basalt used in this study is unknown, but when Korchagin, Caner and Bortoluzzi (2019) assessed the CEC of highly weathered basaltic quarry fines, they found that the CEC of the samples used in their study were relatively high (at up to 0.6 meq g^{-1}). However, basalt is unlikely to provide many OC functional groups for Mn to bond with because basalt is a silicate rock with a low OC content. The increase in Mn weathering from the basalt grains coupled with the high pH and higher number of charged sites in the manure could have led to a significant increase in the humus adsorbed/complexed-Mn in the Manure + basalt relative to the Manure

treatment. Therefore, manure amendment appears to be responsible for increases in humus adsorbed/complexed-Mn.

4.5.4. Stabilisation of OC to SRO phases

The OC associated with SRO phases also increased in the Manure relative to the NPK fertiliser regime. However, there were no significant differences in each of the fertiliser regimes between the fertiliser only and basalt-amended treatment. These results directly support Hypothesis (4) which predicted that OC would increase in the Manure relative to the NPK regime.

Given that there were no significant changes to the amount of SRO-OC between basalt-amended and fertiliser only treatments despite there being significant changes in the amount of SRO-Al, this suggests that the increase in OC was the result of an increased OC source rather than adsorption of OC to fresh surfaces generated by the neoprecipitation of SRO-Al phases. This result is consistent with the increased porewater OC concentrations which are up to 2.1 times higher in the Manure relative to the NPK fertiliser regimes (Table 4.1). Additionally, this comparison between SRO-Al and SRO-OC suggests that the OC was adsorbed rather than co-precipitated with Al because otherwise there would have been significant increases in both SRO-Al and -OC, but there were only significant increases in SRO-Al.

The same relationship between SRO-Al and SRO-OC was also observed in the basalt grains, where more SRO-OC was extracted in the Manure + basalt relative to the NPK + basalt treatment (see Section 3.13, also Section 3.4.3.1.). The results from both bulk soils and basalt grains directly corroborate with the findings of Abramoff *et al.* (2021). In Abramoff *et al.* (2021), through a set of adsorption experiments, it was found that soils can typically stabilise more OC than they currently do via adsorption mechanisms, if OC is added to the soil solution. OC could be added to the soil solution via the addition of an organic soil amendment like manure.

4.5.5. Potential for $CaCO_3$ precipitation

There was no detectable IC in the NPK, and only trace IC (<0.06 wt.% IC) carbonate identified in the NPK + basalt treatment. These results are on a similar magnitude to the results reported in Kelland *et al.* (2020) who detected *c.* 0.09-0.2 wt.% IC. However, non-negligible IC was identified in the Manure and Manure + basalt treatments (0.45-0.51 wt.% IC) which equates to 3.75-4.25 wt.% $CaCO_3$. This equates to more than double the carbonate identified in Kelland *et al.* (2020) (1.66 wt.% $CaCO_3$).

Coulometric analysis on the same samples was organised by Mr M Kelland and conducted at the University of Southampton. These analyses were consistently below the limit of detection (LOD) (LOD < 2.33 wt.% $CaCO_3$), and thus consistently lower than the amount of carbonate identified in this study. Generally, evidence from this project does not support the precipitation of $CaCO_3$ under the environmental conditions in the Loddington Farm Mesocosm experiment. Calcite was never saturated in the porewater modelling that was conducted in this chapter (Figure 4.7) nor was it saturated in the modelled basalt microenvironment (detailed in Section 3.3.7). There was also no evidence of calcite precipitation on the basalt grains themselves from TGA (Section 3.3.5).

Some of the increase in IC in the manure fertiliser regime could have originated from the inherent carbonate in manure; manure has been shown to comprise between 1-4 wt.% carbonate (Eghball, 1999). However, considering that manure comprises up to 0.91 wt.% of the amended soil, and manure could contain between 1 and 4 wt.% $CaCO_3$, the maximum amount of manure that could be present would be on the magnitude of an increase of up to 0.03 wt.%. This is an order of magnitude lower than the carbonate measured from the IC analysis. It is therefore thought that the reason for the increased IC in the Manure treatments is related to the imprecise nature of the acid stripping process.

4.5.6. Potential synergy between ERW and soil carbon sequestration

It was possible to assess additive effects between manure and basalt application to an agricultural soil given that manure and basalt were

simultaneously applied in the Manure + basalt treatment and that there is a Manure only fertiliser treatment.

Unsurprisingly the application of manure, an OC rich soil amendment that is frequently applied to land as a soil management and SCS strategy (The Royal Academy of Engineers and The Royal Society, 2018), significantly increased the SOC content. This is consistent with literature (e.g. Shi *et al.*, 2016) and consistent with expectations that adding a material with high concentrations of carbon (total C = 46.5 ±0.03 wt.% - this study) at 0.91 wt.% will increase SOC. Manure also increased the total extractable OC in the Manure relative to the NPK fertiliser regime. Much of this increase was attributed to the SRO-OC pool which could be considered to be the most stable element bound-OC identified in this study (Heckman, Lawrence and Harden, 2018).

Overall, there was no evidence to suggest that basalt amendment affected SOC concentrations during the 81-day duration of the experiment. There were no significant differences in the total OC (Figure 4.4) not were there any significant differences in the amount of total extractable OC from the sum of the sequential extractions between the Manure + basalt and Manure only treatment.

While there was no significant increase in OC as a result of basalt amendment, there was also no significant decrease which means that under the conditions used in this experiment and after a three-month duration, that basalt amendment did not negatively affect OC in soils. This finding suggests that, at least on short term time scales, there is not a negative feedback whereby basalt amendment reduces the SOC concentrations and therefore could impact global carbon cycling and thus CO_2 fluxes.

It was noted in the previous section that the lack of statistical difference in SRO-OC compared with the significant increase in SRO-Al indicated that the soils used in this experiment might not have been saturated with respect to the amount of OC. This means that given the soil properties, the soil has a potential to stabilise more OC than it currently does. However, it is hypothesised that with continued manure amendment, it might be possible to utilise the fresh SRO-Al precipitated out of solution for stabilising OC. Already, after 81 days of

weathering, the precipitation of SRO-Al has increased by 0.53 mg Al g soil^{-1}. While this appears to be a minimal amount, when these results are scaled up to the amount of material present in the bulk soil across one hectare (e.g. multiplying 0.53 mg g soil^{-1} by the amount of soil in the top 12 cm of one ha of soil), SRO-Al could increase by 2313 kg per ha^{-1}. This means that basalt amendment could create a large amount of OC to be stabilised in the future. To the author's knowledge, there have been no flask-based experiments to estimate the amount of OC adsorbed to SRO minerals that could be used to estimate the amount of OC that could be stabilised in this way.

Even though there was no evidence to suggest that basalt amendment changed the amount of OC associated with the chemical extractions, there is some evidence to suggest that basalt amendment affects OC dynamics in soils. Significantly more UPW-OC and significantly less humus adsorbed/complexed-OC was observed when comparing the Manure + basalt to the Manure only treatments. Some consideration of the UPW-pool is warranted. Frequently, UPW extractions are used to remove any loosely attached material from the grains which could skew the results from the previous extractions. The occurrence of the other elements of interest in this study (Al, Fe and Mn) in the UPW-pool should be approached with caution as the extraction could dissolve soil and basalt grains and skew results. This is not the case for OC because OC is not a key component of basalt and therefore the UPW-extraction would represent loose/fine OC particles within the soil samples.

While the extraction represents loosely bound OC particles, the size of these particles will be relatively small. No filtering took place before OC analysis to prevent OC contamination from the syringe filters (see Section 3.2.9.2). However, the size of OC molecules present in the extract could be estimated using Stokes Law (Stokes, 1851). Given the density of the heavy fraction OC (1.37 cm g^{-1} (Hassink, Whitmore and Kubát, 1997)), density and viscosity of water (0.997 cm g^{-1} and 0.001 Pa s^{-1}), the centrifugation force (13,000 g) and the distance between the uppermost boundary of the 30 mL of fluid and top of the settled soil pellet at the bottom of the centrifuge tube (*c.* 6.2 cm), the centrifugation process would have settled out OC particles greater than 0.15 μm

in size. In summary, the supernatant that was measured in the water soluble-pool would have included OC molecules less than 0.15 μm.

The OC particles analysed are small and the origin of such particles are unknown. It is also beyond the scope of this study to interpret this pool in great detail. However, it seems likely that, at least in the initial stages of basalt amendment, there is an initial breakdown of humus adsorbed/complexed-OC during basalt amendment. This could be due to changes in solution chemistry as a result of basalt weathering. It could be that the UPW-extractable OC that was extracted from the OC pool was simply free within the soil. The structure and size of the OC molecules is unknown and it could be the case that the OC was 'free' (i.e. not occluded) as fine particulates in the soil if the OC extracted in the UPW-extractable phase is relatively stable in soils. It could also be that the OC could be less stable (i.e. more palatable to microbes) within the soils but was physically protected by occlusion within soil aggregates (Blanco-Canqui and Lal, 2004). Any OC within soil aggregates greater than 53 μm in size would have been liberated by the crushing of soils to less than 53 μm prior to the sequential extractions (see Section 4.3.1). This means that (some of) the UPW-pool could have been composed of the particles making up aggregates, though this is purely speculative.

The degree of protection within the UPW-OC pool is unknown, but if the OC was not contained within aggregates, it could be assumed that the UPW-OC pool would be less stable than humus adsorbed/complexed-OC (Heckman, Lawrence and Harden, 2018). The assessment of the stability of the different OC pools (using i.e. radiocarbon dating) and the effects of basalt-amendment on the formation of soil aggregates were both beyond the scope of this study.

4.6. Conclusion

This chapter aimed to: (1) quantify possible Al, Fe, Mn and OC sinks in soils, (2) interpret results in the context of commonly measured soil parameters, and (3) consider if ERW can positively influence SCS techniques. From these three aims, four hypotheses were predicted and the evidence for/against these hypotheses are discussed below.

Hypothesis (1) predicted that humus adsorbed/complexed-Al, -Fe and -Mn would increase in the basalt-amended relative to fertiliser only treatments. There is some evidence to support this hypothesis in the Manure fertiliser regime, where humus adsorbed/complexed-Mn increased in the Manure + basalt relative to Manure only treatment. There were no significant differences observed between basalt-amended and fertiliser only treatments in the NPK fertiliser regime in relation to humus adsorbed/complexed elements. However, while not significant, there were notable increases in humus adsorbed/complexed-Al and humus adsorbed/complexed-Fe in the Manure + basalt and NPK + basalt treatments, respectively, relative to their fertiliser only counterparts. It is thought that if the experiment had continued for a longer period of time, higher concentrations of humus adsorbed/complexed-Al and -Fe would have been observed in the basalt-amended treatments as there would be an increased availability of Fe and Al for these interactions to occur.

Hypothesis (2) built upon Hypothesis (1) and predicted that, not only would there be increased humus adsorbed/complexed-Al and -Fe in basalt-amended treatments but that there would also be a greater increase in humus adsorbed/complexed-Al and -Fe in the NPK + basalt relative to the Manure + basalt treatment. This hypothesis was disproved because both fertiliser regimes behaved differently with respect to the adsorption of these elements to humus or the complexation of these elements with OC. There was an increase in humus adsorbed/complexed-Mn in the Manure + basalt relative to the Manure only treatment and this increase was attributed to the increased Mn supply from basalt weathering bonding with OC functional groups within the Manure microenvironment.

Hypothesis (3) predicted that both SRO-Al and -Fe would have increased as a result of basalt amendment and that Li isotope measurements would support this finding. The summary of Hypothesis (3) is split into two parts. Firstly, considering the SRO-Al phase, a highly significant fertiliser regime effect was observed. The hypothesis was supported in the Manure fertiliser regime because there was an increase in SRO-Al following basalt amendment but this hypothesis was not supported in the NPK fertiliser regime because there was a decrease in

SRO-Al following basalt amendment. Based on the data presented in this thesis, only speculative reasons could be provided for the decrease in SRO-Al in the NPK fertiliser regime in this chapter including the intercalation of Al into clay minerals or the transport of Al into other soil depths that were not measured in this chapter. Secondly, hypothesis (3) was also partly disproven because of the lack of SRO-Fe precipitation in both fertiliser regimes and the fact that Li isotope measurements were inconclusive.

Hypothesis (4) predicted that there would be significant increases in OC concentrations in the Manure relative to the NPK regime. This hypothesis was consistently supported by the evidence provided in this chapter with both total soil OC and total extracted OC being higher in the Manure relative to the NPK regime. The adsorbed OC is of particular interest, because once adsorbed, OC is shown to be more stable than 'free' total OC due to its protection via mineral bonding. This may therefore help increase OC in soils and thus aid SCS efforts.

The chapter also aimed to assess the potential for synergy between SCS and ERW. Based on the results from this experiment, there was no evidence to suggest that basalt amendment affects the total SOC content in soils. There could be evidence that the soils were undersaturated with respect to adsorbed OC which is why there were significant increases in the amount of OC. However, basalt amendment co-deployed with manure has been shown to increase the production of SRO-phases. If the amount of SRO generated contains sites of charge which are not occupied, these sites will be available to stabilise OC.

Overall, this chapter has demonstrated that over relatively short periods of time (81 days), basalt weathering can affect secondary phase precipitation in soils and that soils may act as a sink for Al, Fe and Mn. It is expected that the trends observed in this chapter will grow stronger when basalt is left to weather for substantially longer timescales. With increased secondary phase formation, it is likely that there will be increased OC stabilisation and that ERW is likely to work additively with SCS. Longer ERW studies are required to test that this assumption is true.

5. Assessing secondary mineral precipitation at the field-scale

5.1. Introduction

The responses of various Al, Fe, Mn and OC sinks in soils after basalt amendment for enhanced rock weathering (ERW) were introduced in Chapter 4, which analysed various sinks of these elements in the bulk soils of the Loddington Farm Mesocosm Experiment. This chapter investigates the response of the same sinks in a bulk soils from an ERW field demonstrator. As such, the background for this chapter is almost identical to the background of Chapter 4 just instead of analysing samples from the Loddington Farm Mesocosm Experiment, this chapter analyses samples from a field site setup on alkaline soils: the Flitcham Farm Field Demonstrator. Even though this chapter and Chapter 4 investigate similar processes, the two chapters were split (1) for reader clarity by keeping the chapters reasonably short and self-contained, and (2) because the Loddington Farm Mesocosm Experiment and the Flitcham Farm Field Demonstrator are two very different experiments.

The two datasets originate from two very different soil types (Loddington Farm (LF) Mesocosm Experiment used a mildly acidic clay loam whereas the Flitcham Farm (FF) Field Demonstrator takes place on a mildly alkaline sandy soil (see Section 5.2.1). The two experiments also used different basalts (the Oregon basalt was used in LF (see Section 3.2.2) vs Middleton basalt used at FF (see Section 5.2.2)) and had two different cropping regimes (sorghum vs peas and sugar beet followed by barley). The difference in soil pH may change the dominant mechanism for OC stabilisation (Rasmussen *et al.*, 2018) and may also change the speciation of Al, Fe and Mn in solution as well as the potential for these elements to precipitate (Pourbaix, 1974). The different basalts are also comprised of different mineralogies and will be interacting with soil solutions of a different chemistry. Both mineralogy and solution chemistry will affect the amount of weathering that could occur. The amount of weathering then affects the supply of Al, Fe and Mn in the soil solutions, subsequently affecting the potential for these elements to interact with OC or for the precipitation of secondary phases to occur. Although it is beyond the scope of this chapter and thesis to assess the effects of different types of basalt and crop type on Al, Fe, Mn

and OC sinks in ERW experiments, different crops may also change soil conditions thus affecting weathering rates. For all of the above differences and reasons, the direct comparisons between these two field experiments is difficult and it therefore felt sensible to split the findings from both experiments into two chapters.

As it was stated in the General Introduction (Section 1.2.4), there is a need to understand the processes that occur as result of basalt amendment for ERW at the field scale because it is conceptualised that ERW will be deployed at a large scale over fields and will not deployed in mesocosm experiments. This thesis aimed to identify different sinks for Al, Fe and Mn and their association with OC over a range of scales including: (1) the grain scale (Chapter 3), (2) the bulk soil from a controlled mesocosm-scale ERW experiment (Chapter 4) and finally (3) the bulk soil from a field scale experiment (this Chapter). At the Loddington Farm Mesocosm Experiment, there has been evidence of OC stabilisation via adsorption onto SRO-phases in both soils and on basalt grain surfaces (see Section 4.4.1 and 4.5.4 for soils and Section 3.3.4 and 3.4.2 for basalt grains) and different responses to the amount of SRO-Al phases under two fertiliser treatments (see Section 4.4.1 and 4.5.2).

Using the same methods that were used in Chapter 4 (i.e. sequential extractions to determine Al, Fe, Mn and OC sinks in soils, total OC/IC/H, CEC and pH), the sinks for Al, Fe and Mn and the subsequent interaction of these elements with OC were studied in this chapter. However, given the alkaline nature of the soils studied in this chapter, OC stabilisation is more likely to be mediated through interactions with Ca because Rasmussen *et al.* (2018) found that Ca-OC interactions dominate at pH values > 6.5. There are several mechanisms of Ca-mediated OC stabilisation with the Ca^{2+} ion including: ligand exchange (Mikutta *et al.*, 2014), chelation (Ahmed and Holmström, 2014) and cation bridging (Iskrenova-Tchoukova, Kalinichev and Kirkpatrick, 2010)). OC can also be stabilised by $CaCO_3$ via (1) mineral occlusion (where $CaCO_3$ physically protected OC), (2) inclusion (whereby the OC is enveloped within the $CaCO_3$ mineral assemblage) and (3) adsorption of OC to carbonate surfaces.

There are no routine methods to study the mechanisms for the stabilisation of OC via Ca interactions (Rowley, Grand and Verrecchia, 2018). In addition, one of the known methods for measuring the relative abundance of Ca with OC in different OC density fractions (e.g. Rowley *et al.*, 2021) was not attempted in this study. However, as OC stabilisation may be mediated by $CaCO_3$, it might be possible to infer OC stabilisation via $CaCO_3$ precipitation by analysing changes in inorganic carbon (IC) between Control and Basalt-amended treatments.

The chapter therefore aims to assess evidence for changes in Al, Fe, Mn, Ca and OC in an ERW field demonstrator which was set up on alkaline soil. The field demonstrator is described in detail in Section 5.2.1., but for context to the aims provided below, the field demonstrator consists of two field sites on similar soil conditions with two different crop histories. The key aims of this chapter are the same as Chapter 4 but include one additional aim related to Ca-mediated OC stabilisation. The aims for the chapter are:

Aim 1: to quantify the different Al, Fe, Mn and OC sinks in soils using an adapted sequential extraction procedure from Heckman, Lawrence and Harden (2018) and Gabriel, Kellman and Prest (2018) (same as Chapter 4).

Aim 2: to interpret values determined in Aim (1). To accomplish this aim, a variety of measured soil parameters known to be correlated with soil carbon storage and secondary phases (CEC, pH, total C, N and H) as well as porewater modelling were used to contextualise the environment in which Al, Fe, Mn and OC sinks may form. Geochemical models were employed using the soil porewater chemistry from each treatment to determine whether secondary phases had the potential to precipitate (same as Chapter 4).

Aim 3: to briefly assess how basalt amendment affects OC dynamics in soil (same as Chapter 4).

Aim 4: to briefly assess whether basalt amendment has the potential to increase OC stabilisation by assessing changes to IC concentrations between Control and Basalt-amended plots.

From these four aims, the four hypotheses were developed:

Hypothesis (1): There will not be any significant changes to humus adsorbed/complexed-Fe, -Al or -OC because typically adsorption and complexation interactions between these elements typically occur at lower pH conditions (pH < 5.5) than to the pH conditions observed at the Flitcham Farm Field Demonstrator (pH > 7). Additionally, humus adsorbed/complexed-Mn will increase in this chapter because Mn-OC complexation reactions typically take place under higher pH values (between pH 7 and 11) (Aim 1, 2 and 3).

Hypothesis (2): There will be evidence for SRO-Fe, -Al and -Mn precipitation in Basalt-amended relative to Control plots because there should be an increase in available Al and Fe in the soil solution for these phases to precipitate as a result of basalt weathering and the pH observed at this field demonstrator. There will also be increased SRO-OC in the Basalt-amended relative to the Control plot (Aim 1 and 2).

Hypothesis (3): There will be evidence for increased calcite in Basalt-amended relative to Control plots because there will be an increased source of Ca from basalt weathering and soil pH (pH > 6.5) will high enough to facilitate Ca-mediated OC interactions. This could be inferred as an increased potential to stabilise OC (Aim 2 and 4).

Hypothesis (4): There will be no significant differences between the amount of Al, Fe, Mn and OC extracted from the sequential extractions between the two field sites because the two sites are characterised as ‘the same soil type’ in accordance with soil maps (Aim 2).

5.2. Fieldsite characterisation

5.2.1. Field site history

Samples were collected from the Flitcham Farm Field Demonstrator, located *c.* 14 km north-east of Flitcham, Norfolk (Figure 5.1). This field demonstrator was set up as part of the Leverhulme Grant (RC-2015-029) by a group of academics from both the University of Sheffield and the University of Southampton. The author of this thesis did not help with the set-up or maintenance of the Flitcham Farm Field Demonstrator. The demonstrator consists of two separate field sites named: (1) Bottom Brek and (2) Longspring Head. Each site contains two 0.5 ha plots, a Control plot (i.e. grown as it is) and a Basalt-amended plot (i.e. amended with 40 t ha^{-1} yr^{-1} of the Middleton basalt). More information on the basalt applied to this field trial can be found in Section 5.2.2.).

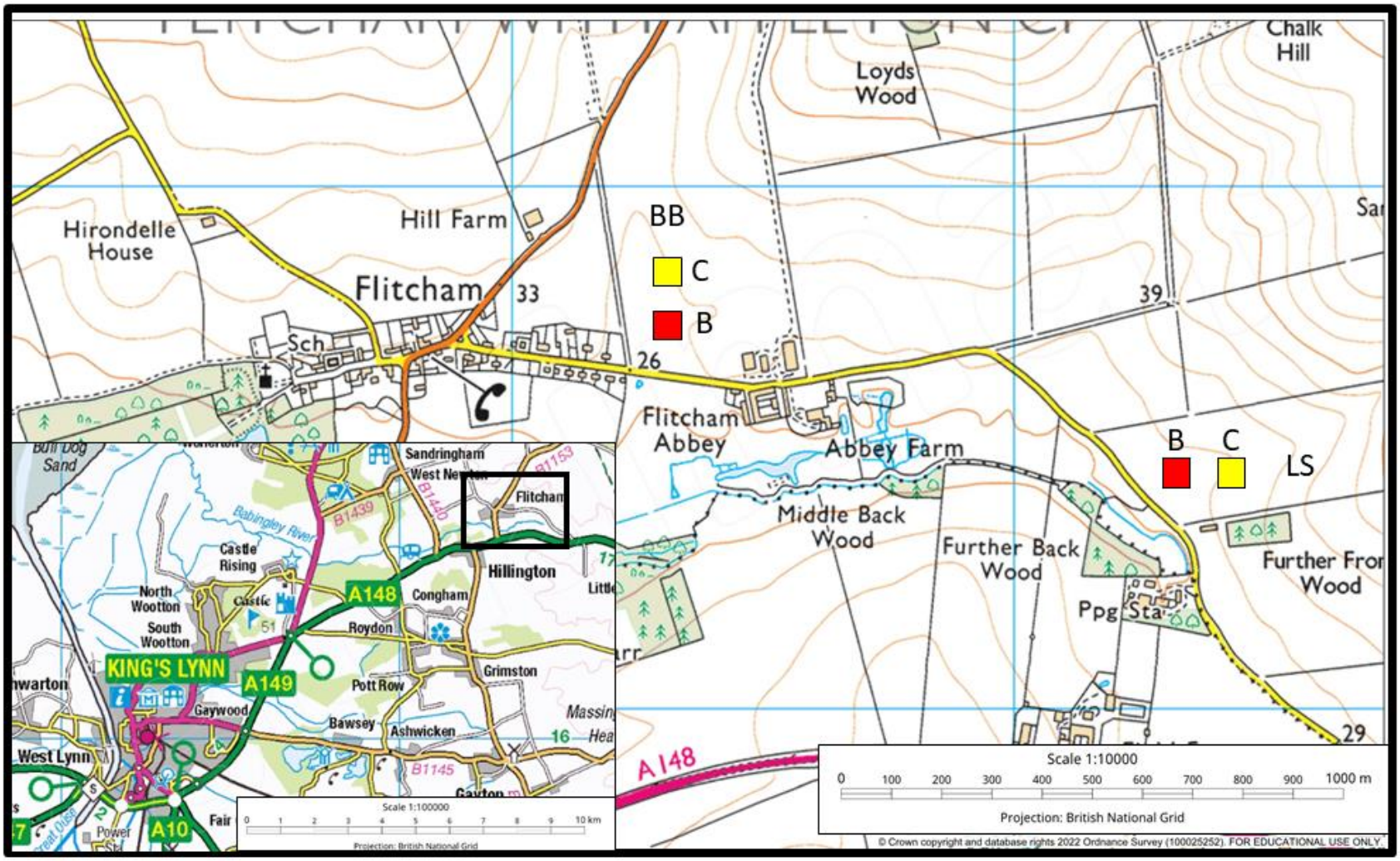

Figure 5.1 – Map showing location of the Flitcham Farm Field Demonstrator. Inset map shows the broader area that the field demonstrator is placed. Yellow and red boxes represent Control and basalt-amended treatments respectively. BB – Bottom Brek, LS – Longspring Head; C – Control; B – Basalt-amended. Maps produced using Digimap Roam.

No analysis had previously been completed independently by the author or any of the collaborators who had set up the field site before the basalt was applied. However, soil maps identify the plots as a Leptosol (World Reference Base, from BGS UK soil observatory (Lawley, Emmett and Robinson, 2014) and is more specifically defined as belonging to the 'Newmarket 2' series soil (Farewell *et al.*, 2011; Cranfield University, 2022). This type of soil is a well-drained, coarse, alkaline soil which forms on calcareous bedrock and contains coarse to very-coarse gravel-sized chunks of chert.

During the two years that basalt had been applied to the fields, two crops were grown. At Longspring Head, sugar beet was grown in 2019 followed spring barley in 2020, whereas Bottom Brek grew peas in 2019 followed by winter barley in 2020.

From 2019-2020, the mean soil temperature varied between 4 and 20°C, with mean temperatures in July 2020 at 18°C (Met Office, 2021 - Figure 5.2a). Total monthly rainfall varied between 11 mm $month^{-1}$ and 215 mm $month^{-1}$, though rainfall was significantly reduced from March-May 2020 compared to March-May 2019 - with rainfall at 375.8 mm yr^{-1} and 300.2 mm yr^{-1} (Met Office, 2021 - Figure 5.2b).

Up until the sampling time (July 2020), the site had had two applications of the Middleton basalt, firstly in February 2019 and March 2019 for Bottom Brek and Longspring Head respectively and secondly in September 2019 and February 2020 (again, for Bottom Brek and Longspring Head sites respectively). At the field site, the basalt was spread onto the soil using a tractor and conventional lime spreader and then ploughed into soil to a depth of *c.* 20 cm.

5.2.2. Applied basalt characteristics

The 'Middleton basalt' was applied to the Flitcham Farm Field Demonstrator. This basalt has not been previously described in this thesis but has been used in simulations to predict the potential of ERW in the UK (Kantzas *et al.*, 2022). The basalt was characterised by the author. As with the Cragmill basalt, the Middleton basalt is sourced from part of the Whin Sill formation and is mined by CEMEX UK at their Forcegarth Quarry (Durham, DL12 0EP).

Both mineralogy, particle size and BET specific surface area (SSA) were determined using the methods described in Section 2.1, Section 2.3 and Section 2.4 respectively. The mineralogy is summarised in Figure 5.3a. The mineralogy is similar to the Cragmill basalt and is composed of a similar proportion of plagioclase and augite, but has slightly increased chlorite-smectite, phlogopite and ilmenite and reduced sanidine and quartz. The Middleton basalt also has a slightly higher *p*80 - at 1519 μm compared to the Cragmill which had a *p*80 of 1138 μm (see Figure 2.3). The BET SSA for the Middleton basalt, as sourced from the quarry and applied to the field demonstrator, was determined to be 0.80 ± 0.03 m^2 g $basalt^{-1}$.

In this chapter the sequential extraction, as described in Section 5.3.2 was also conducted on the Middleton basalt before it was applied to the field sites. The results from these extractions are referred to throughout the chapter as the 'Initial Middleton basalt' from this point onwards.

5.2.3. Field sampling

The soil sampling took place in Summer 2020 (14th-15th July 2020). Six independent samples were collected from each of the four plots. The independent sample comprised soil which was excavated from the top 20 cm using an auger, which drilled down to *c.* 20 cm.

After excavation, the samples were placed on a blue tarpaulin before being tipped into the polyethylene sample bag. The blue tarpaulin was changed between plots but was shaken between the independent samples of each plot. A large weight of sample was extracted from the soil using the auger (*c.* 2 kg) and given the dry conditions during field sampling, only a small number of remnant soil particulates were identified on the tarpaulin. For the types of analysis that were being conducted in this chapter, (i.e. no trace metal or microbiological data collection), this method was considered acceptable for sampling these soils.

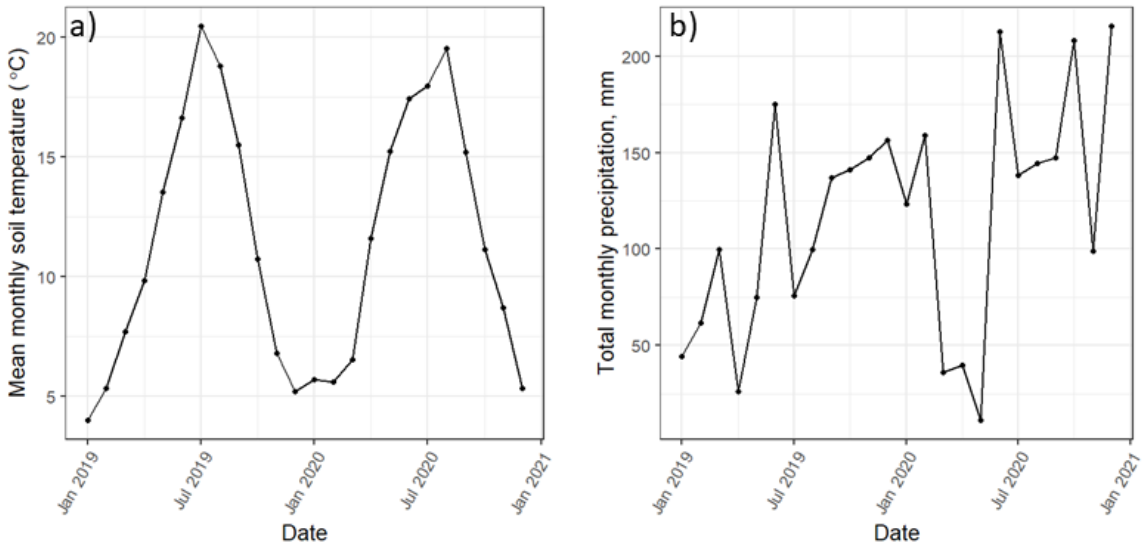

Figure 5.2 – (a) mean monthly soil temperature and (b) total monthly precipitation of the area surrounding the field site. Data was obtained from Met office (2021) using data from the Marham Met Office weather station (*c.* 17 km from Flitcham, as the crow flies).

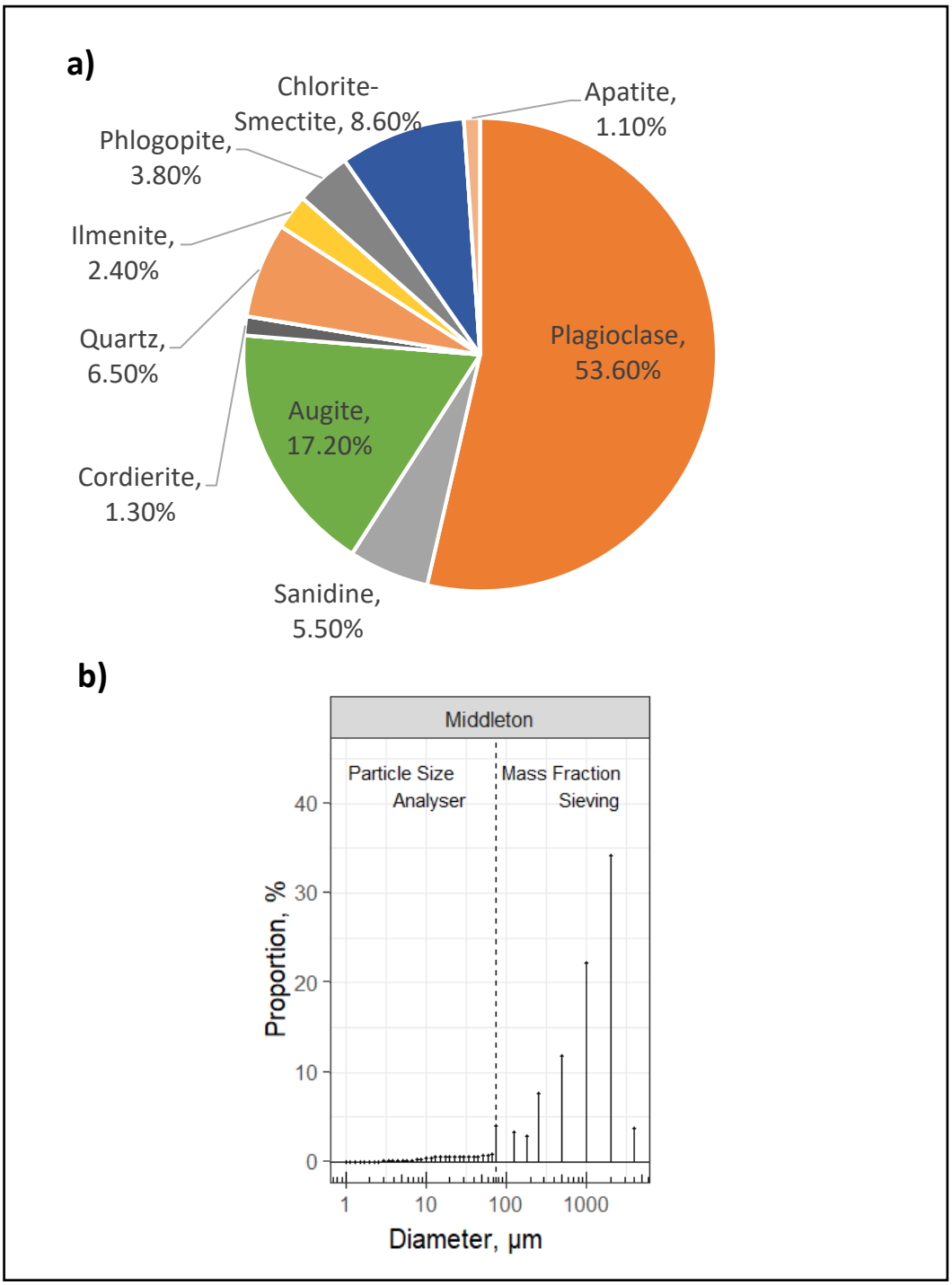

Figure 5.3 – (a) Middleton basalt mineralogy and (b) particle size distribution.

5.3 Methods

5.3.1 Sample Preparation

The soil samples from the Flitcham Farm Field Demonstrator were prepared to the same protocol as the Loddington Farm Mesocosm Experiment, as described in Section 4.2.1.

In addition to the soil collected from the field sites, the Initial Middleton basalt was also crushed to < 53 μm using a pestle and mortar to ensure that any occluded Fe (i.e. buried within the basalt grains) would also be extracted. This was done because any of the Initial Middleton basalt that had weathered within the bulk soil would have also been crushed to < 53 μm in accordance with the protocol in Section 4.2.1.

5.3.2. Sequential extractions

The sequential extractions were carried out to the same protocol as the soils from the Loddington Farm Mesocosm Experiment, as detailed in Section 4.3.2. Due to the unexplained differences in 8 out of 12 of the hydroxylamine hydrochloride extractions at the Longspring Head site in the ICP-MS dataset (i.e. Al, Fe and Mn), these results were not considered valid and were therefore discounted from this thesis.

5.3.3 Elemental Analysis

The elemental analysis was carried out using the same methodology as at the Loddington Farm Mesocosm Experiment, as detailed in Section 4.3.3. There are only slight changes to the acid stripping process, which are detailed in Section 5.3.3.1.

5.3.3.1 Acid stripping (for organic carbon analysis)

The methodology for preparing the soils for acid stripping was the same as the methods used for the preparation of the Loddington Farm Mesocosm Experiment soils. However, instead of using 60 mg ± 1 mg of soil, 40 mg ± 1 mg of soil was used in the acid stripping process. A lower sample weight was used for the Flitcham Farm soils because these soils contained a high carbonate

content. Soils with a higher carbonate concentration will require more acid to dissolve the carbonate, however, adding more acid to the 1.5 mL centrifuge tubes could cause them to overflow.

Given the carbonate-bearing nature of the Flitcham Farm Field Demonstrator soils, most of these samples required more acid than the 800 μL added to the Loddington Farm Mesocosm Experiment soils (see Section 4.3.3.1) to fully react with all of the calcium carbonate. The additional acid was added in small increments until the visible effervescence from $CaCO_3$ dissolution had stopped.

5.3.4. CEC measurements

The CEC measurements were conducted following a different protocol to the protocol detailed in Section 4.2.6 because the researcher who conducted the analysis in this chapter, Dr D Epihov, used a different protocol. A 1M ammonium acetate extractant, adjusted to pH 8.5 to prevent solubilisation of $CaCO_3$, was prepared to extract exchangeable cations. For the extraction, 2 g of soil was mixed with 20 mL of solution, shaken for 1 hr at 220 rpm, then centrifuged for 5 minutes at a force of 4700 g. After centrifugation, the supernatant was filtered through a 0.45 μm syringe filter and then acidified with 2% HNO_3 and sent for ICP-MS analysis). The CEC was then calculated from the ICP-MS data using Eq. 4.2.

5.3.5. Soil pH

The soil pH was determined using the same method as the Loddington Farm Mesocosm Experiment, as detailed in Section 4.3.5.

5.3.6. Equilibrium phase modelling

The geochemical modelling was conducted on soil solutions to identify the potential for the precipitation of several secondary phases ($Al(OH)_{3(a)}$, $Fe(OH)_{3(a)}$, $Mn(OH)_{2(a)}$ $SiO2_{(a)}$, calcite ($CaCO_3$).

Soil solutions were collected and analysed by Dr G Andrews (former postdoc at the University of Southampton). The aqueous solution used in the

geochemical modelling is best described as leachate as it was collected at the interface of the chalk bedrock and the soil profile. At the point of the chalk bedrock, it was assumed that this water would drain off down the slightly-sloped profile into the river at the bottom of the basin. The leachate samples were collected from SIC20 porewater samplers (LABCELL LTD., Alton, UK) emplaced at 1 m depth with up to 4 samples per plot per two-weekly time points.

Once collected, the solution was analysed for cation concentration (from ICP-MS results – Ca, Fe, K, Mg, Na, Si) and Nitrogen-species (from Ion Chromatography – modelled as NO_3^-). Inorganic carbon was calculated by charge balancing with major cations. The solution pH was not measured but was calculated using PHREEQC based on all other input parameters as well as inputting the measured soil pH value (for soil pH values used see Section 5.4.3). The input solutions are summarised in Table 5.1.

The chemical data for the Flitcham Farm samples were then grouped into seasons (Spring: March-May, Summer: June-August, Autumn: September-November, Winter: December-February). Samples were collected between Spring 2019 and Winter 2020. From the eight seasons of solution that were collected, the number of replicates per each sampling regime varied per time point due to leachate availability. Sometimes the weather was too dry to have generated enough water to produce a leachate sample to be measured. The number of replicates that were used varied between 2 and 20 per season per plot (see Table E1) because seasonal changes to hydrology limited the volume of water that could be collected. The two time points with the greatest difference in Ca concentration were selected and used in the model. The Ca concentration data had the greatest deviation was observed between Spring 2020 and Autumn 2020 (see Figure E1). The porewater data from Spring 2020 and Autumn 2020 were selected for the geochemical model. In the absence of data at the Longspring Head site in Spring 2020, only solution data from Autumn 2020 was used to model potential secondary phase precipitation at the Longspring Head site.

Al, Fe and Mn were not detected during ICP-OES analysis. Similar to the Loddington Farm Mesocosm Experiment, Al, Fe and Mn concentrations were

added to the model artificially using the data from the UPW-extract. The rationale for using this is described in Section 4.3.6. However, as there was no Al, Fe or Mn detected from ICP-OES analysis, no additional Al, Fe and Mn from the leachate was included in addition to the UPW-extracts.

Table 5.1 – Mean values for the porewater chemistry of the six solutions used in the geochemical models. Raw data collected by Dr G Andrews, and mean values calculated from n number of replicates. IC = inorganic carbon. BB = Bottom Brek, LS = Longspring Head, -C = Control, -B = Basalt-amended. pH was calculated from PHREEQC.

	Spring 2020		Autumn 2020			
Treatment	BB-B (n = 4)	BB-C (n = 5)	BB-B (n = 15)	BB-C (n = 6)	LS-B (n = 18)	LS-C (n = 17)
Leachate chemistry						
pH	8.463	8.488	8.645	8.472	8.562	8.612
Element chemistry, mmol L^{-1}						
N	3.754	3.598	9.843	18.069	15.862	24.718
Na	1.103	0.822	0.878	0.860	0.946	1.042
Ca	1.120	1.428	3.510	4.043	3.593	5.019
Mg	0.129	0.137	0.161	0.195	0.127	0.178
K	0.061	0.090	0.068	0.110	0.113	0.165
Si	0.068	0.059	0.062	0.061	0.057	0.061
IC	2.066	2.322	3.566	2.642	2.903	3.402
Al, Fe and Mn extract data, mg L^{-1}						
Al	0.088	0.087	0.088	0.087	0.120	0.112
Fe	0.080	0.057	0.080	0.057	0.104	0.077
Mn	0.011	0.010	0.011	0.010	0.015	0.012

5.3.7. Additional corrections applied to concentration data to account for the dilution of concentrations from low-yielding soil amendments

Similar to the Loddington Farm Mesocosm Experiment, calculations were implemented to account for the addition of basalt in the basalt-amended treatments at the Flitcham Farm Field Demonstrator (see Section 4.3.10). The calculation of the proportion of basalt per unit weight of soil was calculated using the Loddington Farm Mesocosm Experiment parameters. By doing this, the author means that the weight of basalt added to the Basalt-amended plots (40 t ha^{-1} would equate to 0.0726 kg of basalt) was divided by the weight of soil that would be found in the top 20 cm of soil from the Loddington Farm Mesocosm

Experiment (3.308 kg). This meant that the basalt accounted for 4.38 wt.% of the soil that was used in the extractions.

The sequential extraction, total OC, IC and H and CEC results were all corrected by accounting for this extra 4.38 wt.% basalt to the method described in Eq. 4.3.

5.3.8. Statistical analysis

Statistical analysis of the soil was conducted using the same protocol as used in Chapter 4 (Section 4.3.11). Firstly, a one-way ANOVA analysis was used to determine the individual effect of basalt amendment at each site (e.g. Bottom Brek and Longspring Head). Then, a two-way ANOVA was conducted to compare each independent variable (e.g. pH, CEC) with respect to basalt amendment (e.g. ±basalt), field site and the interaction between these two variables. A post-hoc tukey honestly significant difference test (Tukey HSD) was used when results were relevant to the aims of the chapter in instances when there were significant differences in the interactions between basalt amendment and field site to identify which pairs within the ANOVA were significantly different from each other.

5.4 Results

5.4.1. Sequential Chemical Extractions

5.4.1.1. Soils

The results for the sequential extractions on the soils collected from the Flitcham Farm Field Demonstrator are summarised in Figures 5.4 and 5.5. The results from the one-way ANOVA are populated throughout and the results from the two-way ANOVA are summarised in Table 5.2.

The UPW-extractable-OC concentrations, inferred as water soluble-OC, varied between 0.58 and 0.64 mg OC g soil^{-1}, though there were no significant differences between Basalt-amended and Control plots at either site ($p < 0.780$). The results of the two-way ANOVA also identified no significant differences in water soluble-OC as a function of basalt-amendment, field site and the interaction between both of these variables (Table 5.2).

Water soluble-Fe ranged between 0.002 and 0.03 mg Fe g soil^{-1}, and water soluble-Al varied between 0.002 and 0.003 mg Al g soil^{-1}. There was a significant difference in water soluble-Fe between the Basalt-amended and Control plots at Bottom Brek ($p = 0.049$), but there was no significant difference in water soluble-Fe at Longspring Head ($p = 0.121$). There were no significant differences in water soluble-Al at either field site ($p < 0.762$). There were significant differences in the water soluble-Al concentrations between the two field sites ($p = 0.0005$, Table 5.2) but there were no significant differences in water soluble-Fe ($p = 0.102$, Table 5.2). Trace Mn varied between 0.0003 and 0.0005 mg Mn g soil^{-1}. The two-way ANOVA also identified a significant difference between the amount of water soluble-Mn between the two field sites, with significantly more water-soluble Mn identified at the Longspring Head relative to the Bottom Brek site ($p = 0.004$, Table 5.2).

The Na-pyrophosphate extractable pool, inferred as the humus adsorbed/complexed pool, represented the largest pool of OC with mean OC concentrations of 1.61 and 2.24 mg OC g soil^{-1} at the Longspring Head site and 2.51 and 2.68 mg OC g soil^{-1} at the Bottom Brek site. Humus adsorbed/complexed-OC significantly increased by 0.63 mg OC g soil^{-1} ($p = 0.012$) at the Longspring Head site. However, there were no significant changes in humus adsorbed/complexed-Fe, -Al or -Mn between the Control and Basalt-amended plot at the Longspring Head site. While there were no significant differences in humus adsorbed/complexed-OC at the Bottom Brek site ($p = 0.648$), there were significant increases in the humus adsorbed/complexed-Fe in the Basalt-amended plot which increased by 0.026 mg Fe g soil^{-1} ($p = 0.027$) relative to the Control plot. There were no significant differences in the humus-adsorbed/complexed-Al and -Mn between the Basalt-amended and Control plots at the Bottom Brek site ($p = 0.28$ for Al, $p = 0.21$ for Mn).

The hydroxylamine hydrochloride extraction was used to infer the precipitation of short-range order (SRO) phases. As stated in the sequential extraction method section for this chapter (Section 5.3.2.), the data for SRO-Al, -Fe, and -Mn at the Longspring Head site were discounted due to experimental errors. The two-way ANOVA could therefore only be conducted on the SRO-OC

dataset. Therefore, focusing on SRO-OC, the amount of SRO-OC was almost significantly different between the two field sites ($p = 0.051$, Table 5.2) with higher SRO-OC observed at the Bottom Brek site.

Specifically, at the Bottom Brek site, there were significant differences between the Basalt-amended and Control plots in SRO-Fe and SRO-Mn concentrations ($p = 0.025$ for Fe; $p = 0.045$ for Mn) with SRO-Fe significantly increasing and SRO-Mn significantly decreasing. There were no significant increases in SRO-OC between Basalt-amended and Control plots at the Bottom Brek site ($p = 0.964$), but SRO-OC significantly increased at the Longspring Head site ($p = 0.041$) increasing by 0.37 mg OC g soil^{-1}.

Some crystalline-Al, -Fe and -Mn, as inferred from the Na-dithionite extraction, was extracted at both field sites with mean crystalline-Al varying between 0.15 and 0.44 mg Al g soil^{-1}, Fe between 0.16 and 0.38 mg Fe g soil^{-1}, and Mn between 0.035 and 0.063 mg Mn g soil^{-1}. There were no significant differences between the Basalt-amended and Control plots at either of the two field sites ($p < 0.628$ for Al, $p < 0.580$ for Fe, $p < 0.738$ for Mn). The two-way ANOVA revealed that there was consistently higher crystalline-Al, -Fe, and -Mn at the Longspring Head relative to Bottom Brek site ($p < 0.001$ for Al; $p = 0.008$ for Fe; $p < 0.001$ for Mn; Table 5.2.). There was no OC associated with the crystalline phases at either of the field sites at the Flitcham Farm Field Demonstrator.

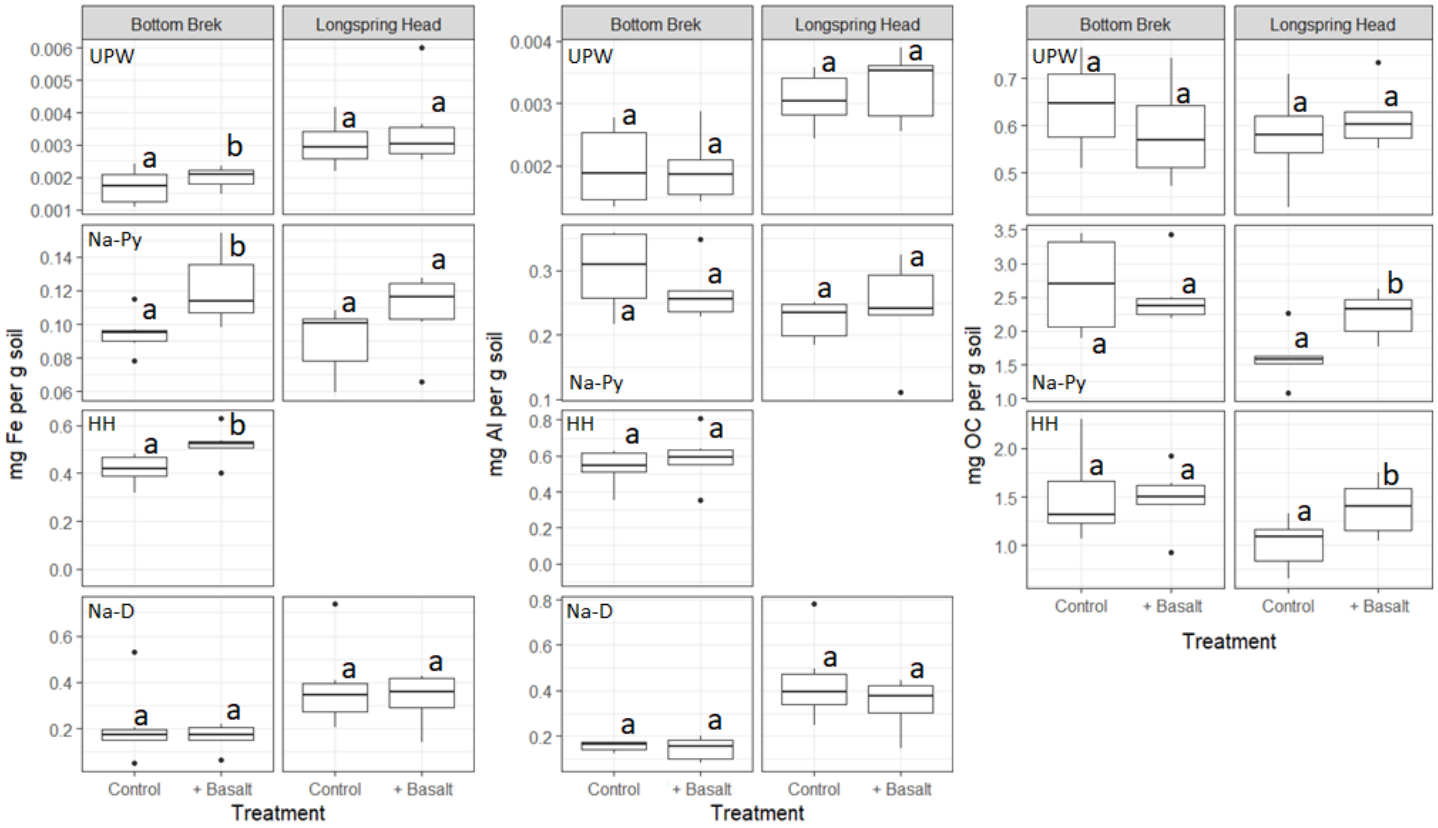

Figure 5.4 – Extractable- Al, -Fe and -OC fractions for the Control and Basalt-amended treatments at the Bottom Brek and Longspring Head sites (n = 6 for each treatment). Letters are used to differentiate significant differences between Control and Basalt-amended treatments at each site (e.g. a and b are significantly different; a and a are not significantly different). Mean Na-dithionite-extractable OC values were below detection limit. UPW = ultra-pure water; Na-Py = Na-pyrophosphate; HH = hydroxylamine hydrochloride; Na-D = Na-dithionite.

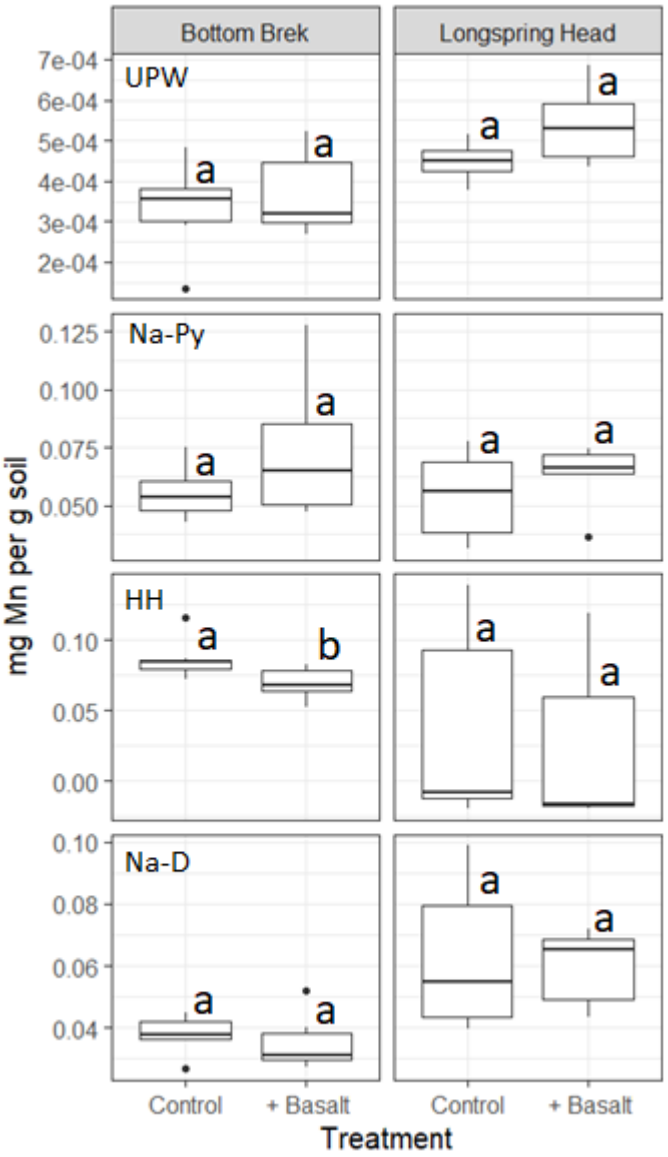

Figure 5.5 – Extractable-Mn fractions at the Bottom Brek and Longspring Head sites (n = 6 for each treatment). Basalt-amended treatments at each site (e.g. a and b are significantly different; a and a are not significantly different). UPW = Ultra-pure water; Na-Py = Na-pyrophosphate; HH = hydroxylamine hydrochloride; Na-D = Na-dithionite.

Table 5.2 – ANOVA summary table considering effects of basalt amendment, field site and the interaction between these two variables for all chemical extractions. Grey shaded values highlight relationships with a significance value of $p < 0.05$; values shaded in green highlight relationships with a significance of < 0.10. UPW = Ultra-pure water; Na-Py = Na-pyrophosphate; HH = hydroxylamine hydrochloride; Na-D = Na-dithionite; Total extracted = sum of all extractions for a specific element.

Extraction	Element	Amendment (+/- basalt)	Site (BB or LS)	Amendment X fertiliser regime
UPW	OC	0.593	0.104	0.539
	Fe	0.409	0.102	0.897
	Al	0.754	0.00045	0.69669
	Mn	0.191	0.03370	0.637
Na-pyrophosphate	OC	0.380	0.004	0.062
	Fe	0.012	0.315	0.613
	Al	0.710	0.401	0.245
	Mn	0.120	0.499	0.583
Hydroxylamine hydrochloride	OC	0.291	0.049	0.181
	Fe	NA	NA	NA
	Al	NA	NA	NA
	Mn	NA	NA	NA
Na-dithionite	OC	NA	NA	NA
	Fe	0.396	0.008	0.977
	Al	0.255	0.00004	0.367
	Mn	0.670	0.0006	0.986

5.4.1.2. Initial Middleton basalt

The sequential extractions were also carried out on the Initial Middleton basalt with the results summarised in Table 5.3. In the Fe, Al and Mn extractable pools, the SRO pool was the largest: yielding 0.63 mg Al g basalt^{-1}, 2.26 mg Fe g basalt^{-1} and 0.015 mg Mn g basalt^{-1}. Trace amounts of humus absorbed/complexed-Fe, -Al and -Mn were also identified (0.11 mg Al g basalt^{-1}, 0.16 mg Fe g basalt^{-1} and 0.007 mg Mn g basalt^{-1}). The crystalline pool was highly variable, with very high standard errors. OC was only identified in the water-soluble pool, where 0.002 mg OC g basalt^{-1} was extracted. OC was below the limit of detection for all other OC pools.

Table 5.3 – Extractable Al, Fe, organic carbon (OC) and Mn from the Initial Middleton basalt. Error bars represent standard error, n = 3. BDL = below detection limit.

	Element (mg Al/ Fe/C/Mn g basalt^{-1})			
Extraction	Al	Fe	OC	Mn
Water soluble (UPW)	0.003 ± 0.0008	0.004 ± 0.002	0.002 ± 0.0005	0.00007 ± 0.00001
Humus adsorbed/complexed (Na-Pyrophosphate)	0.11 ± 0.002	0.16 ± 0.003	BDL	0.007 ± 0.0003
SRO (Hydroxylamine hydrochloride)	0.63 ± 0.02	2.26 ± 0.10	BDL	0.015 ± 0.001
Crystalline (Na-Dithionite)	0.002 ± 0.12	0.46 ± 0.34	BDL	0.009 ± 0.002

5.4.2 Total OC/IC, H, N and S

The OC, IC and total H data are summarised in Figure 5.6. Both total N and S data were below the limit of detection for all of the samples measured in the Flitcham Farm soils, and the S identified in the acid stripped sampling is attributed to contamination as explained in Section 4.4.2. Therefore, only OC, IC and total H data are presented in this chapter. Similar to the sequential extractions the statistical data from one-way ANOVAs, comparing the effect of basalt amendment are populated throughout the text. The results from the two-way ANOVA which compared the effect of basalt amendment, the field site and the interactions between basalt amendment and field site together are summarised in Table 5.4.

The mean OC concentrations varied between 1.51-1.67 wt.% and 2.20-2.21 wt.% at the Longspring Head and Bottom Brek sites, respectively. Mean IC ranged from 0.93-1.00 wt.% and 1.41-2.36 wt.% for the Longspring Head and Bottom Brek, respectively. There were no significant differences between the Control and Basalt-amended plots ($p < 0.954$ for OC; $p < 0.910$ for IC) at both field sites.

The two-way ANOVA showed that there was significantly more OC observed at the Bottom Brek site ($p = 0.050$, Table 5.4) and that, when considering a p-value of < 0.05, there was also almost significantly more IC at the Bottom Brek relative to the Longspring Head site ($p = 0.078$, Table 5.4).

The mean total H content varied between 0.56-0.68 wt.% and 0.54-0.58 wt.% for the Bottom Brek and Longspring Head sites, respectively. Significant differences were observed between the Control and Basalt-amended plots at the Longspring Head site, with mean total H decreasing by 0.04 wt.% ($p = 0.008$) in the Basalt-amended relative to the Control plot. An almost significant decrease in mean total H, with mean total H decreasing by 0.11 wt.% in the Basalt-amended relative to the Control plot, was observed at the Bottom Brek site ($p = 0.094$). The two way ANOVA revealed that there was significantly less total H at the Longspring Head relative to Bottom Brek site ($p = 0.003$, Table 5.4) and there was an interaction between the basalt amendment and field site ($p = 0.005$, Table 5.4). The tukey HSD test revealed that only one significant pairing: the pairing between the Longspring Head Control and Bottom Brek Control ($p < 0.001$).

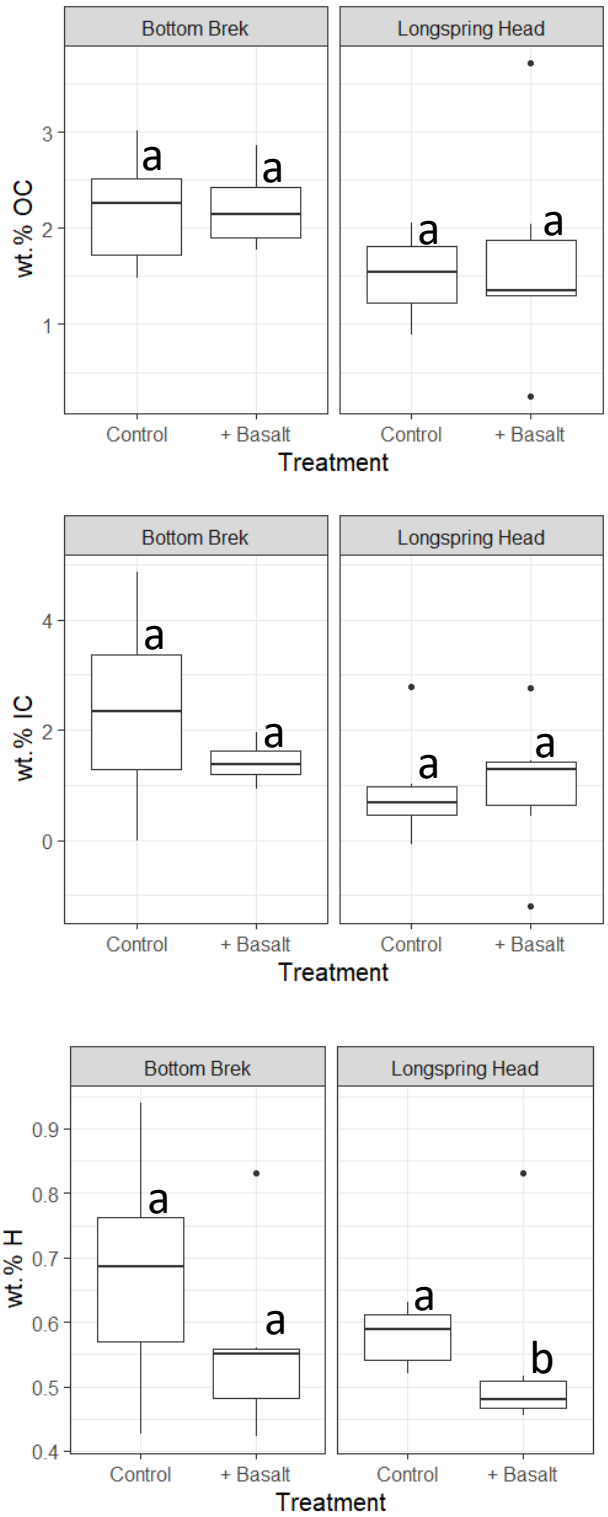

Figure 5. 6 – Total OC, IC and H for each treatment. Letters represent statistically significant groupings from the one-way ANOVA between either Control and Basalt-amended treatments (e.g. a and a would not be significantly different from each other, a and b would be statistically significantly from each other), n = 6 for all treatments.

Table 5.4 – ANOVA summary table considering effects of basalt amendment, field site and the interaction between the two variables for various measured soil parameters. Grey shaded values highlight relationships with significance of $p < 0.05$ and green shaded values highlight almost significant values.

Chemical parameter	Amendment (+/- basalt)	Field Site	Amendment · Fertiliser regime
Organic C	0.768	0.050	0.813
Inorganic C	0.391	0.078	0.314
Total H	0.918	0.003	0.005
CEC	0.277	0.002	0.007
pH	0.311	0.698	0.148

5.4.3. Soil pH and CEC

The mean soil pH at both the Control and Basalt-amended plot at Bottom Brek field site were measured as pH 7.4 and at pH 7.3 and 7.5 at the Longspring Head site (Figure 5.7). Basalt amendment did not significantly alter soil pH at both sites when comparing Control and Basalt-amended plots ($p < 0.688$). Neither basalt amendment, field site or the interaction between basalt amendment and field site had a significant effect on soil pH (Table 5.4).

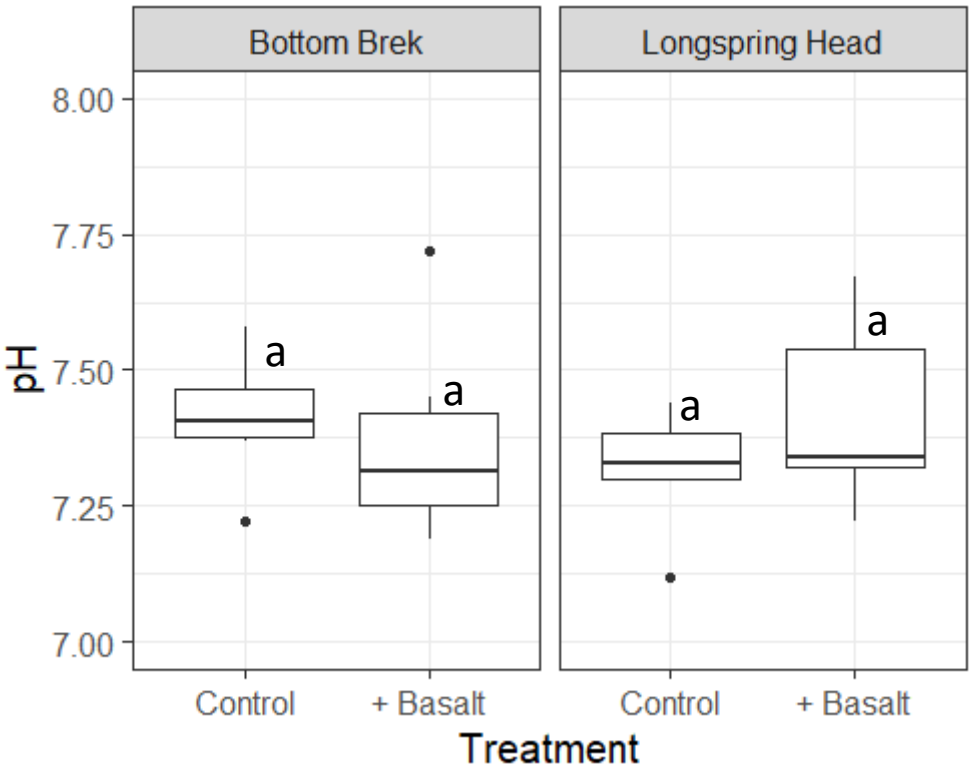

Figure 5. 7 – Soil pH. Letters represent statistically significant groupings between either control and basalt-amended treatments (e.g. a and a would indicate a lack of significance from each other, a and b would be statistically significantly from each other) from the one-way ANOVA, n = 6 for all treatments.

The mean CEC between each plot varied between 0.058-0.064 meq g soil^{-1} (Figure 5.7). Even with the CEC was corrected for two applications of the Initial Middleton basalt (see Section 5.3.7), the CEC is still significantly lower in the Basalt-amended plot relative to the Control plot at Longspring Head ($p = 0.0141$). While the mean CEC increased by 0.002 meq g soil^{-1} after basalt was amended at Bottom Brek, this increase was not significant ($p = 0.175$). The decrease of 0.003 meq g soil^{-1} observed in the Basalt-amended relative to the Control plot at Longspring Head was significant ($p = 0.014$).

The two-way ANOVA showed that there was a significantly higher CEC at Bottom Brek relative to Longspring Head ($p = 0.002$) and that there was a significant interaction between the field sites and basalt amendment ($p = 0.007$). The tukey HSD test revealed two significant pairing: one between the Longspring Head basalt-amended plot and the Bottom Brek basalt-amended plot ($p < 0.001$),

and the other between the Longspring Head Control to the Longspring Head basalt-amended treatment (p = 0.048).

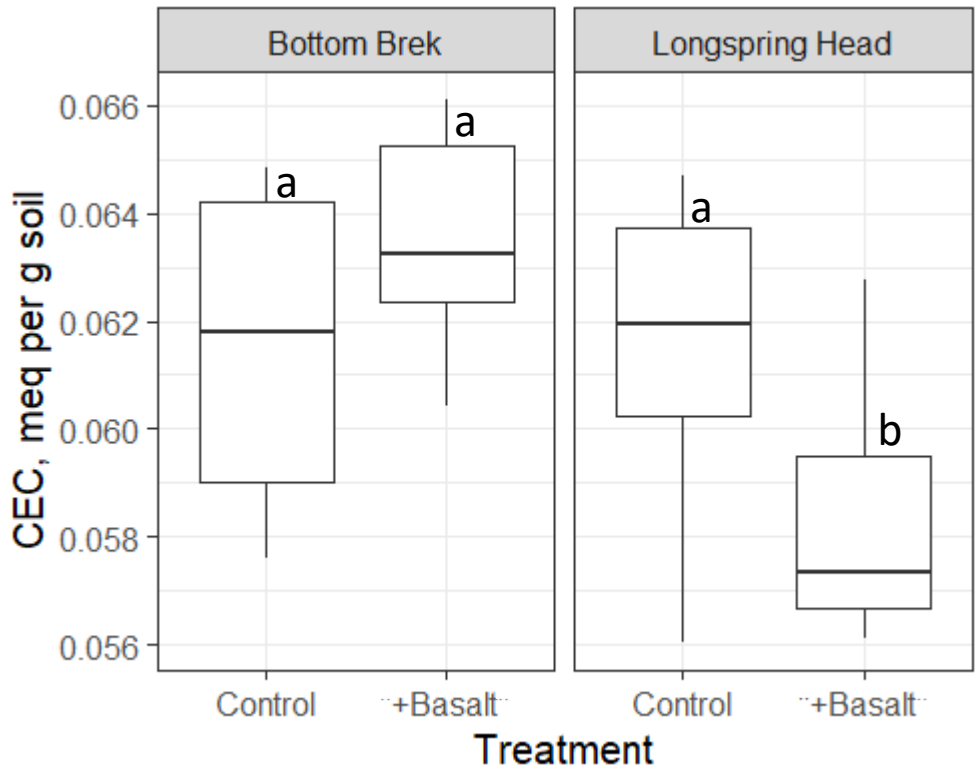

Figure 5.8 – Soil CEC. Letters represent statistically significant groupings between either fertiliser only or basalt-amended treatments (e.g. a and a would indicate a lack of significance from each other, a and b would be statistically significantly from each other). n = 6 for the Bottom Brek-Control, n = 8 for Bottom Brek – Basalt-amended, n = 10 for Longspring Head – basalt amended, n = 8 for Longspring Head – Control.

5.4.4. Equilibrium modelling

Given the large number of graphs that the porewater modelling generates and the fact that all of the results were very similar to each other, only the porewater modelling results from Bottom Brek in Spring 2020 are shown in Figure 5.9. The rest of the porewater modelling data can be found in Figures E2 and E3.

As stated in the methods for equilibrium modelling (Section 5.3.6.), Al, Mn and Fe concentrations were fixed to the values determined from the UPW-

extract as neither Al, Fe or Mn was not detected via ICP-OES data. The soil solutions from all treatments in both spring and summer 2020 were saturated with respect to $Fe(OH)_{3(a)}$, and thus this phase has the potential to precipitate out of the leachate solutions. $Al(OH)_{3(a)}$ was consistently undersaturated in the geochemical model. While there were variations in Ca between the Spring and Autumn 2020 samples (Figure E1), $CaCO_3$ remained saturated at both sites in both Spring and Autumn 2020 (Figures 5.9 and E2). $SiO_{2(a)}$ and $Mn(OH)_{2(a)}$ were consistently undersaturated at the Si and Mn concentrations, and across the pH range that was modelled during this modelling exercise.

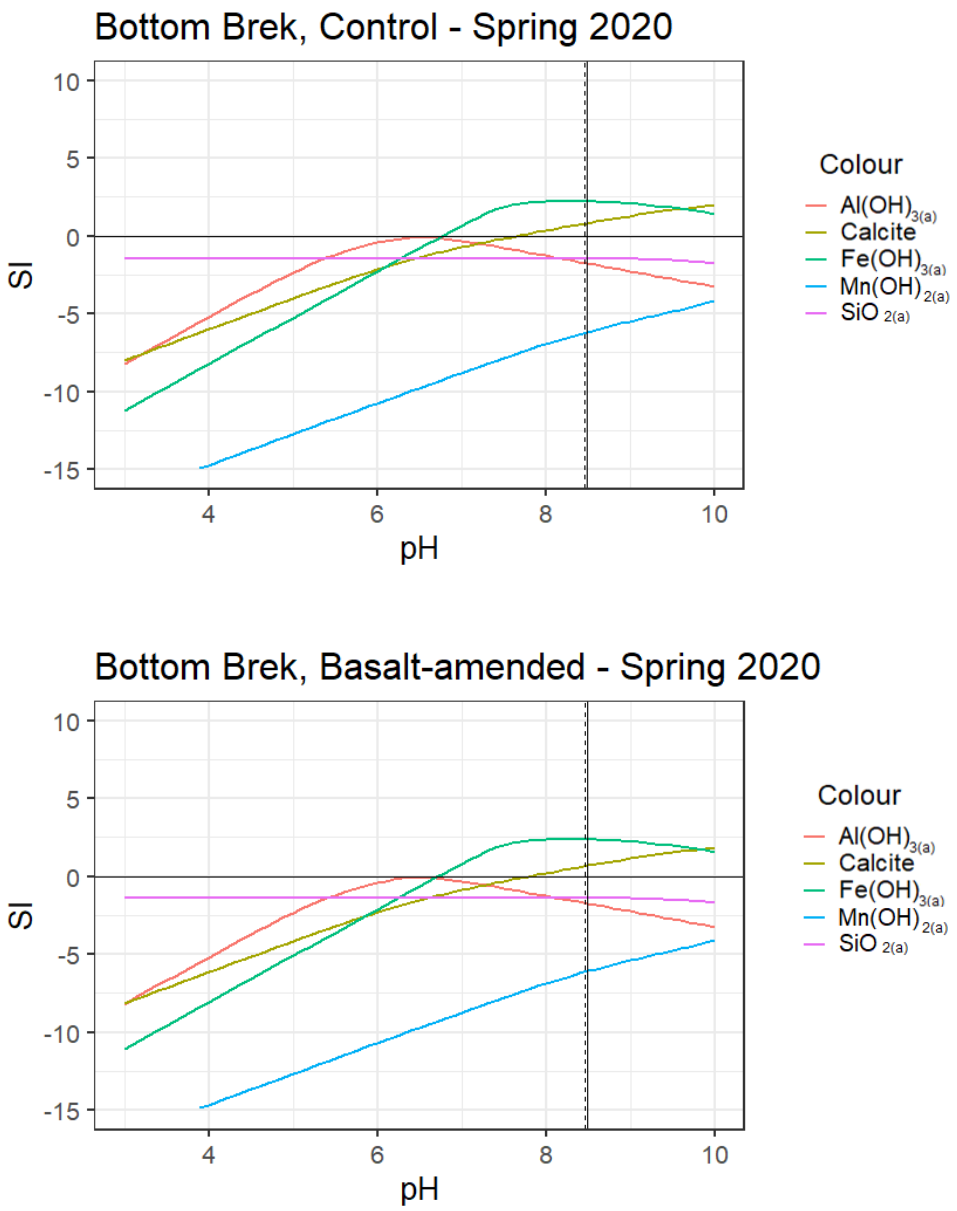

Figure 5.9 – Graph showing Saturation Indices (SI) of several Al, Fe, Mn, Ca and Si phases as a function of pH at both the Control and Basalt-amended plots at the Bottom Brek site at the Flitcham Farm Field Demonstrator. Vertical line represents the measured porewater pH of each respective solution. Dashed line represents the pH of the Basalt-amended treatment and solid line represents the pH of the Control treatment solution. The results for all other treatments can be found in Appendix E, Figure E2 and E3.

5.5. Discussion

5.5.1. Humus adsorbed/complexed OC and metal interactions

There were two significant results observed from the Na-pyrophosphate extractions, which are inferred as representing the humus adsorbed/complexed pool. These significant results were: (1) an increase in Fe in the Basalt-amended relative to the Control plot at the Bottom Brek site and (2) an increase in OC in the Basalt-amended relative to the Control plot at the Longspring Head site. The fact that these two significant results were observed disproves Hypothesis (1) which stated that changes to the proportions of humus adsorbed/complexed-Al, -Fe and -OC would not be observed because the soil pH would be too low to facilitate such interactions, but that there would be an increase in humus-adsorbed/complexed-Mn in Basalt-amended relative to Control treatments. This hypothesis was formulated because Fe/Al-OC complexes form at a low pH (dominant at pH < 5.5, (e.g. Rasmussen *et al.*, 2018)) whereas an alkaline soil pH (pH 7.3-7.6) was observed in the Flitcham Farm Field Demonstrator samples used in this chapter. Mn-OC interactions favour a higher soil pH (pH 7-11 (Duckworth and Sposito, 2005)), and given a fresh source of Mn, it is hypothesised that humus adsorbed/complexed-Mn will increase.

One reason for this increase in humus adsorbed/complexed-Fe in the Basalt-amended treatment relative to the Control treatment could be attributed to a soil microenvironment: the rhizosphere. The increases in the humus adsorbed/complexed-Al and Fe in the Loddington Farm Mesocosm Experiment (see Section 4.5.1) were also attributed to rhizosphere processes. In Section 4.5.1 it was suggested that the lower pH surrounding a root could facilitate adsorption and complexation reactions and that basalt weathering would provide additional Al and Fe to be used in these reactions. While there were no changes to Al, the increase in humus adsorbed/complexed-Fe is only observed in the Bottom Brek site. Therefore, if the increase in humus adsorbed/complexed-Fe was only explained by the presence of the rhizosphere microenvironment, there would have also been a significant increase in humus adsorbed/complexed-Fe at the Longspring Head site too. Similarly, the presence of the rhizosphere interactions alone could not have explained why there was a significant increase in humus

adsorbed/complexed-OC in the Basalt-amended relative to the Control plot at the Longspring Head site when there were no significant changes to humus adsorbed/complexed-OC at the Bottom Brek site.

The second part of this hypothesis, stating that humus adsorbed/complexed-Mn will increase, was also disproven because there were no significant increases in this extracted pool at either the Bottom Brek or Longspring Head site. The reason for this is unknown.

The differences in the significant results between the humus adsorbed/complexed-OC and -Fe between the two field sites could be caused by other variables which were not considered in this chapter including crop type. The effect of crop type on the measured Al, Fe, Mn and OC sinks studied in this chapter was beyond the scope of this study.

There could have been some increase in the total amount of humus adsorbed/complexed-Fe from the basalt itself. The Initial Middleton basalt contained slightly higher concentrations of humus adsorbed/complexed-Fe (0.16 ± 0.003 mg Fe g basalt^{-1}, Table 5.3) to the amount of humus adsorbed/complexed-Fe identified in the soils (mean values of between 0.09 and 0.12 mg Fe g soil^{-1}). This was not the case in the Loddington Farm Mesocosm Experiment because the pool of humus adsorbed/complexed-Fe was *c.* 10-fold higher (Table C1) in soil samples compared to the 'Initial basalt' (i.e. the Oregon basalt from the Loddington Farm Mesocosm Experiment (see Chapter 3 and Section 3.2.2)). After two applications of the Initial Middleton basalt at 40 t ha^{-1} to the Bottom Brek site, the soil would be composed of *c.* 4.38 wt.% Initial Middleton basalt (see Section 5.3.7 for details of how this was calculated). This amount of the Initial Middleton basalt would increase the humus adsorbed/complexed-Fe concentrations by 0.0069 mg Fe g soil^{-1}. Therefore, the amendment of the Initial Middleton basalt into soils could not sufficiently explain the increase of 0.026 mg Fe g soil^{-1} observed in the Basalt-amended relative to the Control plot at the Bottom Brek site. The Na-pyrophosphate-extraction did not extract detectable OC from the Initial Middleton basalt (Table 5.3) so the increase in humus adsorbed/complexed-OC observed at the Longspring Head site could not have originated from the amendment of the basalt grains into the soil.

5.5.2. Short range order precipitation and carbon stabilisation

Hypothesis (2) stated that there would be evidence of increased SRO-Al, -Fe and -Mn, and associated OC (SRO-OC) in Basalt-amended relative to Control plots. There was some evidence to suggest that SRO-Fe increased at the Bottom Brek site and SRO-OC increased at the Longspring Head site, both increasing in Basalt-amended relative to Control plots. Considering the results presented in Section 5.4, both of these findings support Hypothesis (2).

However, the increase in SRO-Fe could have resulted from the amendment of the Initial Middleton basalt itself. The Initial Middleton basalt was found to be composed of high concentrations of SRO-Fe (2.26 ± 0.1 mg Fe g basalt^{-1}, Table 5.3) relative to the soils which had mean SRO-Fe concentrations of 0.41 and 0.52 mg Fe g soil^{-1}. With the Basalt-amended soil comprising 4.38 wt.% basalt (see Section 5.3.7), 0.1 mg Fe g soil^{-1} of the measured bulk soil SRO-Fe would have originated from the inherent characteristic of the basalt. An increase of 0.1 mg Fe g soil^{-1} is comparable to the increase in SRO-Fe identified in the Basalt-amended plot relative to the Control plot at the Bottom Brek site. This finding therefore suggests that the increase in SRO-Fe at the Bottom Brek site might be an artefact of basalt amendment and may not have originated from the precipitation of new SRO-Fe phases. Therefore, as there is not likely to be any newly precipitated SRO-Fe in the Basalt-amended relative to Control plot at Bottom Brek, there is no evidence to support Hypothesis (2). However, the increase in SRO-OC in the Basalt-amended relative to the Control plot at the Longspring Head site still supports Hypothesis (2) because no SRO-OC was detected in the Initial Middleton basalt sample was zero (Table 5.3).

The increase in SRO-OC at the Longspring Head is the only significant result that supports basalt amendment increasing OC stabilisation in this thesis. As the results from the SRO-Al, Fe and Mn from the Longspring Head site were discarded from this chapter, the associated type for OC (i.e. adsorbed to surfaces or co-precipitated with Al, Fe or Mn) is unknown. It is also uncertain why there was a significant increase in SRO-OC at the Longspring Head site and why there was no significant difference observed at the Bottom Brek site, but it could be due to differences in unmeasured/unconsidered variables between the two sites.

The increase in SRO-OC was also not correlated with an increase in CEC (which can be correlated with increased OC (e.g. Rasmussen *et al.*, 2018)). Instead, CEC significantly decreased in the Basalt-amended relative to Control treatment at Longspring Head (Figure 5.8).

It was also hypothesised in Hypothesis (2) that SRO-Mn would not be significantly different between the Basalt-amended plot relative to the Control plot because soil pH would not be high enough to facilitate SRO-Mn precipitation. The geochemical models of the inferred basalt grain microenvironment presented in Chapter 3 (Section 3.3.7) predicted that amorphous Mn-oxides would precipitate at pH > 9 and the geochemical models in this chapter also showed $Mn(OH)_{2(a)}$ to be consistently undersaturated under all pH conditions. There was, however, a significant decrease in SRO-Mn at the Bottom Brek site. The reason for this decrease is unknown because the pH between the Basalt-amended and Control plots were not significantly different from each other and the source of Mn in solution should be higher as a result of basalt weathering and should therefore increase the potential for SRO-Mn precipitation. With regards to SRO-Mn, Hypothesis (2) was therefore disproven.

There was no significant difference in the amount of SRO-Al between Basalt-amended and Control plots at either of the two sites at the Flitcham Farm Field Demonstrator. This result does corroborate with geochemical modelling from this chapter which found $Al(OH)_{3(a)}$ to be consistently undersaturated.

5.5.3. Potential for OC stabilisation via Ca interactions

Data from Rasmussen *et al.* (2018) suggest that the interactions between OC and Ca dominate as an OC stabilisation method at soil pH > 6.5 (Rasmussen *et al.*, 2018). The pH values observed in this study vary between 7.3-7.6 for soil pH and between 8.1-8.3 for solution pH (as calculated by PHREEQC, see Section 5.3.6) are consistently > 6.5. As mentioned in the introduction, there are no routine methods to study the stabilisation of OC via Ca interactions (Rowley, Grand and Verrecchia, 2018). However, given that OC can be occluded within $CaCO_3$ precipitants (Rowley, Grand and Verrecchia, 2018), the occurrence of

$CaCO_3$ is discussed below. Hypothesis (3) stated that there would be increased in IC which could be inferred as potentially increasing OC in soils.

The possible stabilisation of OC via occlusion within calcite was inferred from IC data. While considerable IC was identified (0.93 - 2.36 wt.% IC, equating to 7.75-19.66 wt.% $CaCO_3$), there were no significant differences in the amount of $CaCO_3$ precipitated between Basalt-amended and Control plots at either of the field sites ($p < 0.910$). Generally, there was high variability in IC within each of the plots at each field site. The high variability may be expected because usually calcite precipitates heterogeneously in small pockets where solution conditions (i.e. the required amount of Ca^{2+} and CO_3^{2-}) permit carbonate precipitation. As a result of this increased variability, it was not possible to comment on whether basalt amendment had increased the amount of carbonate that would have precipitated in soils. Changes in IC might not have been detected because the method used to determine changes in IC used in this chapter are relatively imprecise (i.e. acid stripping with combustion). Changes in IC might be detected by using more precise methods including: coulometry, ^{13}C isotopes (Walthert *et al.*, 2010) or TGA (Kemp *et al.*, in press). The modelled SI also showed the precipitation of $CaCO_3$ to be consistent between field plots, so the IC data does corroborate with geochemical modelling.

As there were no significant differences in IC between Control and Basalt-amended plots, there is no evidence to suggest that Basalt-amendment can facilitate Ca-mediated OC stabilisation via the occlusion of OC in calcite. Therefore, there was no data to support Hypothesis (3).

5.5.4. Comparisons between sites

Hypothesis (4) predicted that there would be no significant differences between the amount of Al, Fe, Mn and OC extracted from the sequential extractions from the two field sites because the two sites are characterised as the same soil type. However, this hypothesis was disproved because 7 out of 12 of the extractable pools that yielded positive values/were not discarded from this study (Al, Fe, Mn and OC concentrations from UPW, Na-pyrophosphate, hydroxylamine hydrochloride and Na-dithionite extractions) showed significant

differences when the Bottom Brek and Longspring Head sites were compared to each other (Table 5.2). Similarly, there were significant differences between the Bottom Brek and Longspring Head site for CEC, OC and Total H data.

The reasons for the site differences are unknown, but it is likely that unmeasured variables could account for these differences such as: different crops being planted and subtle changes to hydrology. This finding highlights the potential variability between individual field sites on similar soil conditions. As a result, the data highlight the need for thorough site characterisations to interpret data and predict responses to Al, Fe, Mn and OC sinks within soils.

5.6. Conclusion

This chapter aimed to: (1) quantify possible Al, Fe, Mn and OC sinks in soils with and without basalt amendment, (2) interpret the results from Aim (1) in the context of commonly measured soil parameters, (3) consider if basalt amendment increased OC in soils and (4) to briefly infer whether basalt amendment has the potential to increase OC stabilisation via Ca-mediated interactions. From these aims, four hypotheses were formulated and the evidence which either supports or disproves these hypotheses are discussed below.

Hypothesis (1) was comprised of two parts relating to the humus adsorbed/complexed pool. Firstly, the hypothesis predicted that there would not be any change to humus adsorbed/complexed-Fe, Al or OC because typically adsorption and complexation interactions between these elements and OC pool typically take place under lower pH conditions (pH < 5.5) than to the pH conditions observed in this chapter (pH > 7). Secondly, Hypothesis (1) also predicted that adsorbed/complexed-Mn would increase in this chapter because Mn-OC complexation reactions typically take place under higher pHs conditions (pH values between 7 and 11). Both parts of this hypothesis were disproven because there was evidence for increased humus adsorbed/complexed-Fe and -OC in Basalt-amended relative to Control plots at the Bottom Brek and the Longspring Head field sites respectively; there were also no significant changes to humus adsorbed/complexed-Mn. The presence of a rhizosphere microenvironment was thought to have generated the lower pH conditions

necessary to facilitate the adsorption and complexation reactions between Fe and OC. Variables outside of this study, such as crop type, are likely to have influenced the relative changes to Al, Fe, Mn and OC sinks both between Basalt-amended and Control plots and also between field sites.

Hypothesis (2) was split into two parts. The first part of Hypothesis (2) predicted that there would be evidence for SRO-Al, -Fe and -Mn precipitation in Basalt-amended relative to Control plots because of the pH conditions measured at both sites at the Flitcham Farm Field Demonstrator (pH > 7) would have been high enough to facilitate some SRO precipitation. This part of Hypothesis (2) was disproven because there was no significant difference in the amount of SRO-Al at either site and while there was a significant increase in SRO-Fe at the Bottom Brek site, this increase could be attributed to the high concentration of SRO-Fe measured in the Initial Middleton basalt. SRO-Mn concentrations decreased in the Basalt-amended relative to the Control plot at the Bottom Brek site but the reasons for this decrease could not be discerned in this study.

The second part of Hypothesis (2) predicted that there would be evidence for OC stabilisation in the Basalt-amended relative to the Control plot. There was evidence of increased SRO-OC in Basalt-amended plots at the Longspring Head site, providing evidence to support this part of Hypothesis (2) and provides the only significant result in support of basalt amendment increasing OC stabilisation in this thesis. However, the increase in SRO-OC was limited to the Longspring Head site; no significant differences in the SRO-OC were observed at the Bottom Brek site.

Hypothesis (3) predicted that there would be evidence for increased $CaCO_3$ which could be inferred as providing potential for OC stabilisation via occlusion. The hypothesis was formulated because Ca-interactions are thought to be the dominant OC stabilisation mechanism in soils with a pH > 6.5. There were no significant differences in $CaCO_3$ between the Basalt-amended and Control plots at either the Bottom Brek or Longspring Head sites. Therefore, there was no data to support Hypothesis (3).

Hypothesis (4) predicted that the amounts of Al, Fe, Mn and OC within the water soluble-, humus adsorbed/complexed-, poorly crystalline- and crystalline-pools would not be significantly different between the two field sites. Both components of this hypothesis were disproven because most (7 out of 12) of the variables measured after the sequential extractions were significantly different between field sites. Some of these differences could be the result of an unknown experimental error (i.e. 8 out of 12 of the hydroxylamine hydrochloride extractions at Longspring Head were consistently low in ICP-MS measurements for Al, Fe and Mn). As a result, however, Hypothesis (4) was disproven. This finding highlights the importance of site-specific characterisation for understanding Al, Fe, Mn and OC sinks in soils. Only two sites were studied in this chapter and field sites can be highly variable. If more sites were studied, it may be possible to infer trends in Al, Fe, Mn and OC sinks in alkaline soils.

Overall, this chapter has demonstrated that basalt amendment can increase OC stabilised via association with humus/complexation and association with SRO phases in alkaline soils but the reason for this interaction is unknown. Furthermore, there were some changes observed in the Fe and Mn sinks within the soils, but again the reasons for these increases could not be discerned from the data collected in this chapter. The chapter also highlighted the variability between field sites on soils classified as being ‘the same type’, highlighting the importance of conducting field trials on a variety of test plots to further understand how basalt amendment affects Al, Fe, Mn, OC (and to a lesser extent, Ca) pools within alkaline soils. From the data collected in this chapter, it was not possible to determine a conceptual model on how basalt amendment has altered the measured proportions in an alkaline field trial.

6. General discussion

6.1. Introduction

The overall aim of this thesis was to explore basalt weathering, subsequent secondary mineral precipitation and organic carbon (OC) stabilisation when basalt is amended into a soil system. Four broad research questions were set out in the General Introduction (Section 1.3):

1. How do the mineralogical and specific surface area (SSA) characteristics affect carbon dioxide removal (CDR) potential of basaltic quarry fines?
2. How do basalt grains weather in soil solutions?
3. Does OC associated Al, Fe and Mn, and secondary precipitants of Al, Fe and Mn increase in soils and on grains following basalt amendment?
4. Is there evidence for increased OC stabilisation following basalt amendment?

Firstly, this chapter summarises how each of these questions have been addressed in this thesis. Then, this chapter summarises some of the overall limitations of the work presented in this thesis and provides some suggested areas for future work.

6.2. How do the mineralogical and SSA characteristics affect CDR potential of basaltic quarry fines?

Chapter 2 addressed the heterogeneity in mineralogy and SSA characteristics across a range of commercially available basaltic quarry fines. To the author's knowledge, a thorough characterisation of a range of commercially produced basaltic quarry fines, followed by the computation of CDR via geochemical modelling has not been previously conducted prior to the writing of this thesis. The basaltic quarry fines were studied using range of solid-phase characterisation techniques including: XRD, SEM-EDS, HF digest with ICP-OES, sieving and laser particle size analysis, and BET N_2 adsorption (for SSA determination). Then, these measured characteristics were inputted into a published geochemical model which simulated basalt grain dissolution in a soil solution. While the consideration of basalt for CDR and agricultural potential has been considered previously, often published datasets of basalt properties are

incomplete and focus on a limited number of parameters including: rock chemistry (Renforth, 2012), mineralogy (Dalmora *et al.*, 2020a),SSA (Rigopoulos *et al.*, 2016; Dalmora *et al.*, 2020a) or elemental release (Dalmora *et al.*, 2020b). To the author's knowledge, no study has provided quantitative mineralogy of quarry fines before. This chapter is therefore novel because a number of chemical and physical properties were reported, so that the modelled CDR potential could then be compared to the different measured properties including: fast weathering minerals, chemical composition (via R_{CO_2}) and SSA.

The results identified a range of CDR values between the six basaltic quarry fines studied for this chapter, with CDR ranging from 1.4 to 8.5 t CO_2 ha^{-1} after 15 years of weathering following a single baseline application rate of 50 t ha^{-1} of crushed basalt. This range of CDR was a result of a broad range of mineralogy and SSAs which were identified in the characterisation analysis. The proportion of faster weathering minerals (e.g. olivine, pyroxene, basaltic glass and in the case of the metabasalt studied – ferroactinolite) varied by 7.4-fold (11.6-86.1 wt.%). The BET SSA of the basaltic quarry fines also varied by one order of magnitude with values ranging between 1-14 m^2 g^{-1} basalt.

Significant proportions of minerals that will not contribute to CDR were also identified in this chapter. Mg-rich clay minerals comprised significant proportions of several of the basaltic quarry fines (up to 10.4 wt.%) which, while contributing to elemental Mg concentrations (and therefore R_{CO_2} values, see Eq. 2.4), will not contribute to cation release because clay minerals weather relatively slowly compared to primary Mg-rich silicates. Furthermore, significant proportions of quartz were identified in some of the basaltic quarry fines and comprised up to 19.1 wt.% of their composition. Quartz (SiO_2) does not contribute any cations for CDR removal.

A major finding from this chapter revealed that, given the modelled parameters used in this thesis, mineralogy was more important than SSA for predicting potential CDR. Modelled CDR did not increase proportionally to the inputted SSA. Instead, CDR increased by up to a factor of *c.* 2 despite a factor of 10 increase in SSA. This finding is important as it suggests that sourcing basaltic quarry fines from quarries with higher proportions of fast weathering minerals

may be more beneficial than sourcing basaltic quarry fines with smaller particle sizes (and thus potentially larger SSAs). This could therefore reduce the carbon cost of ERW as rock crushing is considered the most energy intensive step of the ERW technology (e.g. Moosdorf *et al.*, 2014). However, SSA is still important to maximise CDR and ideally basaltic quarry fines composed of a fast weathering material that is pre-processed by quarries to produce as fine a particle size as possible should be sourced.

It is difficult to compare the CDR potential computed in this chapter with the CDR potential calculated by other workers because previous workers have used different model parameters (e.g. Kelland *et al.* (2020) used a different solution pH and amount of amended material) or have only used one basalt in their simulations. However, Beerling *et al.* (2020) used two 'generic' basalt mineralogies in their simulations to predict ERW potential and identified a *c.* 2.4-fold difference between a faster weathering alkaline basalt and the slower weathering tholeiitic basalt. A 7.2-fold difference between the basalts after 15 years of weathering was identified in Chapter 2 (Table 2.5). Both the results from Beerling *et al.* (2020) and from this thesis corroborate with each other and further demonstrate the key importance of determining mineralogical characterisation prior to the field application of basaltic quarry fines.

6.3. How do basalt grains weather in soil solutions?

Part of Chapter 3 aimed to assess how basalt grains weathered within the soil environment. The results from this chapter also have implications for Chapter 2 which considered the weathering of basaltic quarry fines using geochemical models.

Two data sets were used to assess the weathering of the basalt grains in soils from the Loddington Farm Mesocosm Experiment: XRF and XPS. There was evidence from the whole rock XRF data which showed significant depletion of several alkali earth and alkali metals (Na, K and Mg) which supports the generalised description of weathering outlined in Oelkers (2001). This description of weathering predicts the release of elements from a mineral structure in the following order: Na and K, Ca, Mg, Al and Si. Additionally, evidence for the

preferential release of Ca from basalt grains was identified in XPS analysis. Previous experiments have identified the depletion of Mg in basalt grains following application of basalt in an ERW experiment (Kelland *et al.*, 2020). The dataset presented in this thesis, however, also identified significant decreases in Na and K after weathering which had not been previously observed by Kelland *et al.* (2020). The additional depletion of Na and K, when comparing results from between this thesis and Kelland *et al.* (2020), was most likely the result of a finer particle size used in the experiment studied in this thesis (see Section 3.3.1 for differences in how the basalt used in this thesis was treated when compared to the basalt applied in Kelland *et al.* (2020)). There was no evidence to suggest Fe and Al were depleted from the basalt grains: Fe showed relative increases while Al concentrations could not be measured due to the kaolinite contamination (as outlined in Section 3.4.1.1.)

The evidenced depletion of Na and K does not corroborate well with the data from Chapter 2 which show that Na and K bearing minerals (which are typically slower weathering) do not weather until the faster weathering minerals (typically containing Ca and Mg) have been depleted (Figure 2.7). This is likely to have been observed because Na and K are preferentially removed from mineral structures before the final breaking of silicate bonds occurs (i.e. dissolution is non-stoichiometric). However, stoichiometric dissolution is modelled in the RTM used in Chapter 2, whereas in nature, dissolution is non-stoichiometric and Na and K would be released into solution via preferential leaching (Nugent *et al.*, 1998).

Preferential leaching of alkaline and alkaline earth cations could have some interesting implications for ERW because CDR does not require the final breaking of the strong Si-O bonds. Ca, Mg, Na and K ions can be released from the rock via proton exchange reactions (Oelkers, 2001). If the protons by which these exchange reactions are occurring originate from the dissociation of a carbonic acid molecule (H_2CO_3), bicarbonate can be charge balanced in solution by cations released via preferential leaching. A similar principle has been previously considered in the context of Mg being leached from ultramafic rocks and then binding with carbonate as a CDR strategy (Styles *et al.*, 2014).

It was not possible within this study to investigate changes of Al and Si from either the XPS or XRF data due to the kaolinite contamination identified from DRIFTS analysis. If changes to these elements were measured, it would have been useful for comparison with other studies mentioned in Section 3.4.1.5 which have compared the relative change of alkaline and alkaline earth elements from the basalt grain surface to Al and Si using ratios.

6.4. Does OC associated and secondary precipitants of Al, Fe and Mn increase in soils and on grains following basalt amendment?

Various sinks for Al, Fe and Mn were investigated in Chapters 3, 4 and 5. Three main sinks were considered: elements associated with humus, poorly crystalline (short range order - SRO) phases and crystalline oxide minerals. The section is divided into two subsections to discuss the results from the: (1) 81-day Loddington Farm Mesocosm Experiment and (2) 1.5 year Flitcham Farm Field Demonstrator. The two experiments are discussed separately as both of these experiments were very different and almost incomparable to each other (see Section 5.1 for details).

6.4.1. Loddington Farm Mesocosm Experiment

The study of the Loddington Farm Mesocosm Experiment was split into two soil environments: the bulk soil and the basalt grains. The bulk soil was studied in Chapter 4 and the basalt grains were studied in Chapter 3. A comparison of data from these two chapters shows that the Al, Fe and Mn behave differently in bulk soils compared to the basalt grain microenvironment.

While there were no significant differences in the humus adsorbed/complexed-Al and -Fe in the bulk soils, there were significant increases observed between the unweathered (Initial basalt) and weathered (from NPK + basalt and Manure + basalt treatments) basalt grains. There were also significant differences between the basalt grains emplaced in the two fertiliser regimes: both humus adsorbed/complexed-Al and -Fe were consistently higher in the NPK + basalt relative to the Manure + basalt treatment. A lower pH and a potentially higher availability of Al and Fe in the soil solution from increased basalt weathering in the NPK + basalt relative to the Manure + basalt treatment was

suggested as a reason for this difference. Al- and Fe- humus associations have been shown to favour lower pH solutions (e.g. Rasmussen *et al.*, 2018) and the porewater solution pH was shown to be lower in the NPK + basalt relative to the Manure + basalt treatment. The lower porewater pH of the NPK + basalt treatment is preferable for Al and Fe to be weathered into the soil solutions and therefore more Al and Fe would be available to for adsorption and complexation reactions. It was not possible to definitively consider the origin of the Al and Fe in this study. However, given that the humus adsorbed/complexed-Al and -Fe did not significantly change in the bulk soil (see Figure 4.1, presented and discussed in Sections 4.4.1 and 4.5.1) but did significantly increase in the basalt grains (see Figure 3.13, presented and discussed in Sections 3.3.4 and 3.4.2), it is postulated that trace humus surrounding the basalt grains could have been immediate sinks for Al and Fe that was released from the basalt via adsorption and complexation reactions. Given the size of the bulk soil pool (1.98 kg) relative to the size of the amended basalt pool (0.091 kg), it would be harder to detect a small change to the bulk soil. Changes would be easier to detect in the basalt pool because comparisons are made before and after weathering and in this respect, there is no pool size; there is only basalt before and basalt after weathering. Therefore, relative 'pool size' could be one reason why no significant changes were observed in the bulk soil pool but why there were significant changes observed in the basalt pool.

Soil porewater pH is likely to have affected the amounts of Mn associated with the basalt grain and bulk soil pools. When Mn soil pools were considered, there was only a significant increase in humus adsorbed/complexed Mn in the Manure + basalt treatment relative to the Manure only treatment. Conversely, humus adsorbed/complexed-Mn significantly decreased in the weathered basalt grains when compared to the Initial basalt, with a greater loss of humus adsorbed/complexed-Mn in the NPK + basalt relative to the Manure + basalt grains. One potential explanation for the increase in Mn in soils compared to the loss of Mn from the basalt grains was that the manure provided an alkaline microenvironment with a high CEC in the soils within the soil (Gao and Chang, 1996; Shi *et al.*, 2016). The association of Mn with OC favours higher pH environments (pH 7-11 (Duckworth and Sposito, 2005)) and the higher CEC from

OC functional groups in the manure provides sites for Mn-OC bonding to occur. The manure microenvironment could have hosted additional Mn that was released into the soil solution as a result of basalt grain weathering via OC at higher pH.

The abundance of Al within SRO minerals changed in the bulk soils as a result of basalt amendment. Basalt applied to the NPK fertiliser regime led to a significant decrease in the amount of SRO-Al while basalt applied to the Manure fertiliser regime significantly increased the amount of SRO-Al measured in the soils. The increase of SRO-Al was thought to have occurred as a result of higher Al concentrations in the porewater as a result of basalt weathering. The porewater pHs of the Manure fertiliser regime were within the range that amorphous $Al(OH)_3$ could precipitate out of the soil solution. However, at the time of writing this thesis, no definitive reason for the decrease of SRO-Al in the NPK + basalt relative to the NPK only treatment could be provided but some speculative reasons were considered in Section 4.5.3. These speculative reasons include: the transfer of Al to other sinks within the experimental system, the transfer of Al into unmeasured parts of the soil (i.e. only 12 cm out of 38 cm depth of soil was analysed in this thesis) and the intercalation of Al within clay mineral structures. There was no evidence for SRO-Fe or -Mn concentrations changing in either fertiliser regime as a result of basalt amendment.

No crystalline Al or Fe oxides were detected in the Loddington Farm Mesocosm Experiments, nor was there any additional precipitation of crystalline Al, Fe and Mn oxides on the basalt grains from either the NPK + basalt or Manure + basalt treatment.

Overall, the Loddington Farm Mesocosm Experiment has shown that the type of fertiliser used (i.e. conventional vs organic fertiliser) does significantly affect both (1) the amount of Al, Fe and Mn in a soil and (2) how these elements will be retained in soils (i.e. associated with OC or precipitated as SRO phases). The experiment also demonstrated that the basalt grains themselves might be a sink for Al, Fe and Mn that has most likely been released from the basalt.

6.4.2. Flitcham Farm Field Demonstrator

Chapter 5 considered the various Al-, Fe- and Mn-sinks within field sites at the Flitcham Farm Field Demonstrator.

Some significant trends in measured Al-, Fe- and Mn- sinks were identified at the Flitcham Farm Field Demonstrator. However, these trends were different to the trends that were identified at the Loddington Farm Mesocosm Experiment. This could be because both experiments had different soil pHs; the Flitcham Farm Field Demonstrator was a clay poor, alkaline soil while the Loddington Farm Mesocosm Experiment was mildly acidic and clay rich. Different soil pH values have been shown to strongly affect the precipitation of SRO minerals (Pourbaix, 1974) and the association of Al, Fe and Mn with humus (Rasmussen *et al.*, 2018; H. Li *et al.*, 2021). It is therefore not surprising that there were different trends in Al, Fe and Mn sinks observed at both field sites.

The chemical extractions used to quantify Al, Fe and Mn sinks identified two significant results at the Flitcham Farm Field Demonstrator: (1) Increased humus adsorbed/complexed-Fe and (2) decreased SRO-Mn, with both of these results occurring in the Basalt-amended relative to the Control plot at the Bottom Brek site. No significant trends in Al, Fe or Mn were observed at the Longspring Head site.

It was surprising that there were increases in humus adsorbed/complexed-Fe at the Bottom Brek site because humus adsorbed/complexed-Fe is more commonly associated with acidic soils (pH < 5.5, (Rasmussen *et al.*, 2018)). These complexes are interpreted as forming in the rhizosphere microenvironment which would be more acidic than the bulk soil pH measured at the field site.

The reason for the decrease in SRO-Mn in the Basalt-amended plot relative to the Control plot at the Bottom Brek site is unknown because the pH between the Basalt amended and Control plots were not significantly different from each other.

Overall, there were fewer significant results at the Flitcham Farm Field Demonstrator (2 results) when compared with the Loddington Farm Mesocosm

Experiment (5 results). One reason for this could be the suitability of these extractions on an alkaline soil; these extractions yield data for Al, Fe and Mn but Ca is likely to be a more important element for the Flitcham Farm Field Demonstrator soils (Rasmussen *et al.*, 2018; Rowley, Grand and Verrecchia, 2018).

Another reason for the fewer significant results could be because the Flitcham Farm Field Demonstrator was less controlled than the Loddington Farm Mesocosm Experiment. The soil at the Flitcham Farm Field Demonstrator was very heterogeneous with localised pockets of carbonate and coarse chert pieces compared to the Loddington Farm Mesocosm Experiment which was homogeneous in nature because the soil was sieved through a 2 mm sieve during the set-up of the experiment. Furthermore, the application of basalt was less controlled at the Flitcham Farm Field Demonstrator relative to the Loddington Farm Mesocosm Experiment. At the Flitcham Farm Field Demonstrator, the basalt application process was less precise (mechanical spreading and ploughing of basalt into soils) compared to the Loddington Farm Mesocosm Experiment which carefully mixed the basalt into the soil by hand to produce a homogenous soil-basalt mixture.

Mixed results were identified at the Flitcham Farm Field Demonstrator, but there was an indication that basalt amendment increased humus adsorbed/complexed-Fe and that basalt amendment increased the amount of OC that was associated with SRO-Al/Fe/Mn in an alkaline soil. It is likely that Ca stabilisation mechanisms may have played an important role in OC stabilisation at the Flitcham Farm Field Demonstrator, but the use of methods for determining Ca-OC interactions was beyond the scope of this chapter. Reasons for differences between the two field sites at the Flitcham Farm Field Demonstrator was also unknown, but could potentially be explained by differences in hydrology and cropping regime.

6.5. Is there evidence for OC stabilisation in bulk soils following basalt amendment?

OC was studied using the sequential extractions that were used to study Al-, Fe- and Mn- sinks in soils and on basalt grains, and therefore evidence for

potential OC stabilisation was discussed in Chapters 3, 4 and 5. This section predominately focuses on OC stabilisation from the Loddington Farm Mesocosm Experiment (Chapters 3 and 4) because there was very little evidence of OC stabilisation at the Flitcham Farm Field Demonstrator as a result of basalt amendment (Chapter 5).

In the Loddington Farm Mesocosm Experiment, basalt grains did show evidence of OC stabilisation via adsorption to SRO phases with more OC identified in the Manure + basalt treatment relative to the NPK + basalt treatment. The bulk soils responded similarly, with more SRO-OC identified in the Manure and Manure + basalt treatments relative to the NPK and NPK + basalt treatments. To the author's knowledge, hydroxylamine hydrochloride extractions (used in this thesis to extract SRO-Al, -Fe, -Mn and associated OC) have not been previously used to compare the differences of SRO phase and associated OC stabilisation in manure and/or basalt-amended treatments within an experiment. However, the increased SRO-OC that was observed in the Manure fertiliser regime is consistent with previously published work which documents manure concentrations increasing OC content in soils (e.g. Li *et al.*, 2020).

Even though manure affected SRO-OC, the data from this thesis suggest that basalt amendment did not affect the extent of OC stabilisation; there were no differences between fertiliser only and fertiliser + basalt treatments in both the NPK and Manure regime. However, a change in SRO-OC could have been undetectable because of large quantities of background SRO-OC present in the bulk soil prior to basalt amendment. This suggests that application of organic amendment was the driving force for OC adsorption to secondary phases. Given that OC adsorbed to secondary phases is considered relatively stable as it is less available to be consumed by microbes, the increase in adsorbed OC in the Manure regime could be interpreted as an increase in OC stabilisation.

The results, in part, suggest that the Loddington Farm Mesocosm Experiment soil is undersaturated with adsorbed OC and that adsorbed OC in soils could be increased with organic amendments (e.g. in the form of manure). This is evidenced because there were significant differences in SRO-OC between the two fertiliser regimes despite overall insignificant changes to SRO-Al

between fertiliser regimes (see Section 4.5.4 and Table 4.2). This finding would be consistent with predictions made in Abramoff *et al.* (2021) who identified that globally, soils have the potential to increase their OC content by up to 7%. If it is true that OC was stabilised by vacant charged sites on pre-existing SRO-Al, -Fe and -Mn phases, over time the sites on these pre-existing SRO-Al, -Fe and -Mn will become filled. Once the vacant, charged sites on these pre-existing phases are filled, the sites of charge on the neoformed SRO-Al, -Fe and -Mn may help stabilise more OC than was possible before basalt was amended into the soils.

The effect that basalt amendment had on the overall distribution of OC in manure-amended soils was also noteworthy. There was a significant decrease in the amount of humus adsorbed/complexed-OC in the Manure + basalt relative to the Manure only treatment but this was matched by a significant increase in water soluble-OC and a (non-significant) increase in the SRO-OC pool. The effects of these changes on ERW as the effect of soil OC on weathering is unknown but should be investigated further (see Section 4.5.4). However, humus adsorbed/complexed-OC is likely to be more stable than water-soluble OC in the soil system (Heckman, Lawrence and Harden, 2018) because water-soluble-OC, by definition, can be flushed out of the soil.

Briefly, there was evidence of increased OC stabilised at the Flitcham Farm Field Demonstrator. Both the humus adsorbed/complexed-OC and SRO-OC pool significantly increased at the Longspring Head site as a result of basalt amendment. It was not possible to discern reasons for why these increases were only observed at the Longspring Head (and not at the Bottom Brek site) and by what mechanisms this stabilisation occurred.

6.6. Experimental limitations

6.6.1. Limitations of the sequential extraction procedure used to determine Al, Fe, Mn and OC sinks (Chapter 3, 4 and 5)

Given that data from the sequential extractions form an important part of three chapters, the author decided it would be best to provide a summary of the limitations of the sequential extraction procedure in the General Discussion rather

than in each chapter individually. This section is referenced in each chapter where data from the sequential extractions were used.

The procedure used for the sequential extractions are reported in Chapter 3 and 4 (Sections 3.2.9 and 4.3.2 respectively). This procedure was based on a set of sequential chemical extractions that were developed to quantify the water soluble-, humus adsorbed/complexed-, poorly crystalline (SRO)- and crystalline-pools of Al, Fe, Mn and OC in soils. The method was first developed by Heckman, Lawrence and Harden (2018) and adapted by Gabriel, Kellman and Prest (2018) though the individual extraction procedures were established longer ago. A standard protocol was followed throughout this thesis so therefore the data presented in this thesis are internally consistent with each other. However, there are several limitations to the protocol used in this thesis and several adaptations of this method that could be tested in the future.

In themselves, sequential chemical extractions are limited because they are, by nature, 'operationally defined'. For example, by using a Na-pyrophosphate extraction it is inferred in this thesis and by previous studies (Heckman, Lawrence and Harden, 2018) that humus adsorbed/complexed-Al, Fe, Mn and OC will be extracted and measured. There is often the possibility for other sources of elements that are measured (in this study: Al, Fe, Mn and OC) will also be extracted in addition to the phase that is inferred. Considering Na-pyrophosphate, in addition to releasing humus adsorbed/complexed-Fe, Al and Mn, the extraction may also release some SRO-Al and potentially disperse ferrihydrite and goethite colloids into solution (Wagai *et al.*, 2013).

There are some changes that could be made to the chemical background of the sequential extractions used in this study. Firstly, the Na-pyrophosphate solution is often conducted at pH 10 but the protocols published in Heckman, Lawrence and Harden (2018) and Gabriel, Kellman and Prest (2018) do not refer to a pH correction. The original hydroxylamine hydrochloride extraction was carried out at much lower solid:solution ratios (e.g. 1:40 used in this study, but 1:250 used in the original extraction (Ross, Wang and Schuppli, 1985)). While the Na-dithionite extractions were not important for the work presented in this

thesis because none of the results from Na-dithionite extracts were significant, it is worth noting that there were some differences observed between the method published in Heckman, Lawrence and Harden (2018) the original method published in Wagai and Mayer (2007). The former used 0.5 M Na-dithionite compared to 0.049 M Na-dithionite. There are likely to be other limitations regarding the chemical background of the extractions, which could be investigated further. However, based on the three points mentioned in this paragraph, the author believes it would be worthwhile to assess the sensitivity of these changes to the results presented in this chapter by: (1) testing the effect of altering the pH of the Na-pyrophosphate to pH 10 on the results presented in this thesis (i.e. completing Na-pyrophosphate extractions at pH on a subset of samples used in this thesis), (2) testing the extractability of all the hydroxylamine hydrochloride extraction at different solid:solution ratios and (3) testing the Na-dithionite extraction at the lower extractant concentration (0.049 M rather than 0.5 M).

There were also a number of limitations to the practicalities of the procedure. In this study, effort was made to avoid disturbing the pellet that settled after centrifugation by leaving a proportion of the remnant supernatant in the centrifuge tube and oven drying the sample until a moist soil/basalt sample was left at the bottom in the pellet. Then, the potential increase in concentrations of elements as a result of the evaporation was subtracted retrospectively (as described in Section 3.2.9.1). This method could be improved by leaving a smaller proportion of the supernatant in the bottom of the centrifuge tube, as the interference with the concentrated remnant supernatant with the next chemical extraction was unknown. It may also have been better to have conducted the experiment in glass centrifuge tubes to avoid the potential abrasion of the polypropylene centrifuge tube which could have artificially increased OC concentrations.

6.6.2. Kaolinite contamination in basalt-filled mesh bags (Chapter 3)

Kaolinite contamination was identified in the basalt mesh bags. The discovery of kaolinite contamination (Section 3.4.1.1) made it impossible to interpret Si and Al data from XRF and XPS analyses. Both Si and Al are

frequently used in calculations to compare the extent of alteration after rocks are weathered (e.g. weathering indices (Price and Velbel, 2003); ratio comparisons (e.g. Lee *et al.*, 2008)). If the DRIFTS data were not collected, the trends observed in the Si and Al XRF and XPS data may have been used as evidence of potential weathering. The kaolinite contamination was therefore an important discovery for future researchers using mesh bags to study rock grain weathering in soils.

In the context of this experiment, it would be quite difficult to avoid contamination because the soil did contain significant proportions of kaolinite and because the mesh size (35 μm) would allow for kaolinite crystals (typically < 2 μm) to filtrate into the basalt sample. Finer mesh could have been used to limit contamination from soil particles but still allow fluid flow through. While nylon mesh can be purchased to sizes as low as 0.2 μm, it is unknown if/how quickly the mesh pores of mesh of this size might become clogged with soil material. The basalt grains could also be ultrasonically cleaned, though this procedure may also remove any new precipitates or any alteration rims that had formed during the experiment. Some testing could be conducted to assess if the ultrasonic cleaning and/or other methods of removing substrate contamination would be sufficient and what effects such procedures would have on the methods used in this thesis to characterise basalt grain transformation.

6.6.3. Lack of manure characterisation (Chapter 3 and 4)

In the Loddington Farm Mesocosm Experiment, basalt was identified as a microenvironment where unique processes that differed from processes occurring in the bulk soil were investigated. However, the manure could have also been a unique microenvironment but very few characteristics of the manure were measured. Several of the untested characteristics of the manure (e.g. sequential extraction data on Al, Fe and Mn) could have been particularly useful for the interpretation of bulk soil data in Chapter 4.

6.6.4. Soil conditions mismatch between grain mesocosm and field demonstrator-scale (Chapter 4 and 5)

This thesis attempted to progressively investigate secondary mineral and OC stabilisation from grain- to mesocosm- through to field demonstrator- scale.

The field demonstrator had different soil characteristics, cropping regime and basalt when compared to the experimental setup used in the grain- and mesocosm-scale studies. It was therefore difficult to compare the field-scale data and interpretations to the grain- and mesocosm-scale data.

6.6.5. Reaction time limitations (Chapter 3, 4 and 5)

It was hypothesised that at the grain- (Chapter 3), mesocosm – (Chapter 4) and field- (Chapter 5) scale, there would be evidence for the precipitation of secondary phases and that humus would provide a sink for the additional Al, Fe and Mn that would be released during basalt weathering. The hypotheses were developed based on evidence from: (1) short term flask experiments (e.g. Goût *et al.*, 2021), (2) long-term field observations over a basaltic soil chronosequence (Chorover, Amistadi and Chadwick, 2004) and (3) general observations of basaltic soil development (Heckman *et al.*, 2018). Overall, from the experiments conducted in this thesis, evidence for increases in Al, Fe and Mn sinks as a result of basalt amendment are limited.

There was some evidence for secondary phase precipitation in the Manure + basalt relative to the Manure only treatment in the Loddington Farm Mesocosm Experiments. However, it is likely that the duration that the experiments used in this thesis ran for was too short to identify strong evidence for secondary phase precipitation. It was thought that measurable concentrations of secondary phases would have been observed in the experiments ran in this thesis because basaltic quarry fines (i.e. crushed rock) would have a higher surface area than basaltic bedrock. During the weathering of crushed rock in soils, there would be a larger surface area for dissolution reactions to occur which would have increased basalt weathering and provided a higher concentration of elements for secondary phase precipitation to occur. The precipitation of secondary phases in soil systems amended with crushed rock might still occur on faster time scales than observed in Chorover *et al.* (2004). However, the precipitation of secondary phases did not occur on the timescales used in this thesis which were 81 days (for the Loddington Farm Mesocosm Experiment – Chapter 3 and 4) and 1.5 years (for the Flitcham Farm Field Demonstrator – Chapter 5). These short durations are just a fraction of time compared with 100-kyr time scales studied in Chorover *et al.* (2004), and as basalt weathers on decadal time scales, a stronger evidence base

for these processes occurring could be formed. However, this does not invalidate the use of ERW as a CDR strategy because ERW is predicted to be successful on decadal time scales (Kantzas *et al.*, 2022).

6.6.6. Limitations in accounting for low-yielding soil amendments (basalt and manure) in bulk soil analysis (Chapter 4 and 5)

While there was some attempt to account for the additional weight of either manure or basalt applied to fields and the dilution of these materials, the method used in this thesis could be improved. In this thesis, the values taken from extractions and analyses were multiplied by the proportion of an amendment that was added to the soils, assuming that the value from the measurement of interest of the amendment (e.g. SRO-Al, CEC) is much lower than the value taken from the soil. This was not the case for the total OC concentration of manure in the Loddington Farm Mesocosm Experiment or the SRO-Fe in the Initial Middleton basalt at the Flitcham Farm Field Demonstrator. The measurement of both parameters identified substantially higher concentrations than the measured bulk soil concentrations. Therefore, the concentrations were artificially increased when in reality, the values for the bulk soil would have inherently been lower concentrations of than the values measured for the basalt grains/manure.

Therefore, future attempts to account for the increased weight added to the soil as basalt amendments should subtract the measured value for the variable of interest of the soil amendment from the bulk soil measurement after it has been corrected for the weight of soil amendment added.

For example, Eq. 4.3:

$$Conc_{corr} = (Conc_e \cdot \%_{b,m,b+m}) + Conc_e \text{ (Eq. 4.3)}$$

Should be modified to Eq. 6.1:

$$Conc_{corr} = (Conc_e \cdot \%_{b,m,b+m}) + Conc_e - (Conc_{am} \cdot \%_{b,m,b+m}) \text{ (Eq. 6.1)}$$

Where the $Conc_{corr}$ is the corrected concentration, $Conc_e$ is the measured value from the bulk soil, $Conc_{am}$ is the measured value from the soil amendment and $\%_{b,m,b+m}$ is the proportion of basalt (b), manure (m) or basalt and manure (b+m) added to the soil.

It would have been better to calculate the corrected values using Eq. 6.1, however, they were not calculated in this way because of time constraints. The limitations of the method used (i.e. Eq. 4.3) which are stated in this section were not thought of when the calculations were implemented. It was only after the increased SRO-Fe in the Middleton basalt were identified to be substantially larger than the bulk soil SRO-Fe that this limitation was made known. At this point, the author ran out of time to redo these calculations for Chapter 4, and decided to keep the method consistent with Chapter 4 for Chapter 5.

6.7. Further work

There are several avenues of further work that could be explored as a result of this thesis and some of the key areas of interest are detailed in the sub-sections below.

6.7.1. Comparative dissolution rate experiments (Chapter 2)

The geochemical modelling presented in Chapter 2 allowed for like-for-like comparisons in CDR potential between a range of commercially available basaltic quarry fine materials. An important conclusion from Chapter 2 was that mineralogy was a more important characteristic than surface area when basalt grain weathering is simulated in an agricultural soil model. These modelled comparisons are useful, but experimental data should be collected to determine if the conclusions from the geochemical model are upheld in an experimental system or whether they are an artefact of the geochemical model.

Such experimental data could be collected through a range of experimental set-ups such as the far-from-equilibrium batch experiments described in Section 3.2.4 or flow-through reactors where the solution is changed periodically via inflow of fresh reactant solution and outflow of reacted solution to prevent the effects of mineral saturation (SR term, as described in Eq. 1.3). Flow-through reactors are likely to be more effective as the basalt would be exposed to fresh solution, like basalt would be once amended into a soil.

6.7.2. Geochemical modelling – adding Al, Fe and Mn sinks to weathering models (Chapter 3, 4 and 5)

One major limitation in Chapter 3, 4 and 5 was the inability to model (1) the adsorption of Al and Fe ions onto already-present OC surfaces and (2) the co-precipitation of organo-metal phases. This has made it difficult to corroborate modelling results with experimental data (e.g. sequential extractions). These processes can be modelled using the WHAM geochemical modelling software (Tipping, 1994). While it would be a complex and potentially time consuming task to feed the results from WHAM OC model into a PHREEQC weathering model, running some simulations independently in WHAM could prove useful for understanding Al, Fe and OC interactions.

6.7.3. Understanding OC adsorption dynamics of basalt grains and bulk soils (Chapter 3 and 4)

As discussed in Section 4.3.3.1., the maximum potential OC adsorption of basalt grains are not currently known. Evidence from this thesis suggests that determining the maximum potential OC adsorption would be useful to assess the maximum capacity for OC adsorption to soils and basalt grains.

The maximum capacity of OC adsorption in soils could be determined using a similar methodology to Feng *et al.* (2014) who tested how much OC could be adsorbed to soils in a set of adsorption experiments using high concentrations of OC (up to 600 mg OC L^{-1}).The adsorption of OC to basalt grains could be determined by weathering basalt grains in the laboratory in an artificial porewater solution and then using these basalt grains in a set of adsorption experiments. In the case of both soil and basalt grains, these adsorption experiments could use a variety of OC concentrations and controlled pHs to determine how much OC can be adsorbed to basalt grains under a variety of pH conditions.

6.7.4. Effects of OC adsorbed grains on basalt dissolution (Chapter 2 and 3)

There is strong evidence to suggest that basalt grains do interact with OC in soil solutions through the hydroxylamine hydrochloride extractions, most likely via adsorption. Previous work in this area has shown that mineral dissolution is not affected by adhering secondary precipitants (Hodson, 2003; Stockmann *et al.*, 2011) because the precipitates are typically porous. However, the adsorption of OC could infill the porosity of these precipitates, making it harder for the soil solution to interact with the surface of the basalt grains which could then inhibit further basalt grain dissolution.

To test this, allophane and imogolite could be synthesised in a laboratory (e.g. using methods outlined and/or cited within Du *et al.* (2017)) and adsorbed onto basalt grains to produce SRO-coated basalt grains. Then, a subset of the SRO-coated grains could be placed in a porewater solution containing realistic levels of OC to test how much OC could adsorb onto the coated SRO-phases. The grains could then be placed within a dissolution experiment, like the experiments described in Section 6.7.1, to test whether OC adsorption to secondary precipitates on the surface of grains effects the dissolution of the primary silicate minerals contained within the basalt.

6.7.5. Ca as an OC stabilisation mechanism (Chapter 3 and 5)

A major limitation of Chapter 3 and 5 was the lack of data that was collected for interpreting Ca-mediated OC stabilisation. The sequential chemical extraction procedure that were used in this thesis is not reliable for extracting Ca from the same phases that Al and Fe were extracted from. At pH values greater than 6.5, such as the potential solution surrounding the basalt grains studied in Chapter 3 and the soil pH measured at the Flitcham Farm Field Demonstrator (Chapter 5), the dominant mechanism for OC stabilisation switches from Al and Fe to Ca-mediated OC stabilisation mechanisms (Rasmussen *et al.*, 2018). Some inference for potential OC stabilisation by two of these mechanisms described in Rowley *et al.* (2018) were inferred in Chapter 5 including: (1) occlusion and cementation of OC within $CaCO_3$ precipitation in aggregates and (2) sorption of OC via cation bridging with Ca ions. It would be worthwhile to study the

interactions between Ca and OC in future, building upon the methods set out Rowley *et al.* (2021).

6.7.6. Running experiments for a longer time (Chapter 3, 4 and 5)

There are several long term (e.g. 10 yr) ERW field demonstrators which have been set up and are in the process of completion under the supervision of the Leverhulme Trust Research Centre Award (RC-2015-029). Sinks for Al, Fe, Mn and OC should be investigated at various time points at these field demonstrator experiments.

6.8. Conclusion

In short, the main conclusions of this thesis are:

- The CDR potential of commercially available basaltic quarry fines can vary considerably as a result of (1) their inherent mineralogical properties and (2) SSA.
- Mineralogy and SSA both affect CDR potential of basalts used for ERW. However, models used in this thesis suggest that CDR potential is more strongly influenced by mineralogy rather than SSA.
- Alkali and alkaline earth elements will be preferentially leached from basalt grains when weathering in a soil solution. This leaching is not currently represented in RTM used in Chapter 2.
- The small amounts of humus associated with basalt grains could act as a sink for Al and Fe that has most likely weathered from the basalt grains themselves. However, the adsorption of Al and Fe to humus in both the basalt and bulk soil environment is not currently represented in geochemical models.
- OC will adsorb to existing SRO phases present in cracks/on the surface of basalt grains and the bulk soil. The application of organic fertiliser like manure will increase the amount of OC adsorbed to these SRO phases.
- The use of different fertiliser treatments with and without basalt amendment affects the abundance of Al-bearing SRO minerals in soils. This could have implications on future OC storage within soils. On short-

term timescales, the results of this thesis suggest that a manure fertiliser will generate more SRO minerals which could then provide more sites for OC to be stabilised.

- At the field scale in alkaline soils, there was some evidence to suggest increased humus adsorbed/complexed-Fe and -OC, as well as increased SRO-OC after basalt amendment. However, the reasons for these increases could not be discerned.

The application of this research is very new, so there are several important research avenues that could be followed in the future. Running experiments for longer periods of time will be important as this will allow more time for weathering reactions, weathering product soil sinks (e.g. Al, Fe, Mn pools in soils) and potential OC stabilisation to occur.

References

Abramoff, R. Z. *et al.* (2021) 'How much carbon can be added to soil by sorption?', *Biogeochemistry*, 152(2), pp. 127–142. doi: 10.1007/s10533-021-00759-x.

Agricultural and Horticultural Development Board (AHDB) (2020) *GB Fertiliser Price Market Update May 2020*. Available at: https://projectblue.blob.core.windows.net/media/Default/Market Intelligence/GB Fertiliser Price Series - bi-monthly report - May 2020.pdf.

Ahmed, E. and Holmström, S. J. M. (2014) 'Siderophores in environmental research: roles and applications', *Microbial Biotechnology*, 7(3), pp. 196–208. doi: https://doi.org/10.1111/1751-7915.12117.

Allen, C. C. *et al.* (1981) 'Altered basaltic glass: A terrestrial analog to the soil of Mars', *Icarus*, 45(2), pp. 347–369. doi: https://doi.org/10.1016/0019-1035(81)90040-3.

Amann, T. and Hartmann, J. (2019) 'Ideas and perspectives: Synergies from co-deployment of negative emission technologies', *Biogeosciences*, 16(15), pp. 2949–2960. doi: 10.5194/bg-16-2949-2019.

Amiotte Suchet, P., Probst, J.-L. and Ludwig, W. (2003) 'Worldwide distribution of continental rock lithology: Implications for the atmospheric/soil CO2 uptake by continental weathering and alkalinity river transport to the oceans', *Global Biogeochemical Cycles*, 17(2). doi: https://doi.org/10.1029/2002GB001891.

Amundson, R. *et al.* (2015) 'Soil and human security in the 21st century', *Science*. doi: 10.1126/science.1261071.

Anda, M., Shamshuddin, J. and Fauziah, C. I. (2013) 'Increasing negative charge and nutrient contents of a highly weathered soil using basalt and rice husk to promote cocoa growth under field conditions', *Soil and Tillage Research*, 132, pp. 1–11. doi: 10.1016/J.STILL.2013.04.005.

Anthony, J. W. *et al.* (1995) *Handbook of mineralogy (Volume II- Silica, Silicates. Part 1 and 2)*. Mineral Data publishing. Available at: http://www.handbookofmineralogy.org/search.html?p=all.

Appelo, C. A. J. and Postma, D. (2004) *Geochemistry, groundwater and pollution*. CRC press.

Aradóttir, E. S. P., Sonnenthal, E. L. and Jónsson, H. (2012) 'Development and evaluation of a thermodynamic dataset for phases of interest in CO2 mineral sequestration in basaltic rocks', *Chemical Geology*, 304–305, pp. 26–38. doi: 10.1016/J.CHEMGEO.2012.01.031.

Bahureksa, W. *et al.* (2021) 'Soil Organic Matter Characterization by Fourier Transform Ion Cyclotron Resonance Mass Spectrometry (FTICR MS): A Critical Review of Sample Preparation, Analysis, and Data Interpretation', *Environmental Science & Technology*, 55(14), pp. 9637–9656. doi: 10.1021/acs.est.1c01135.

Banwart, S. A., Berg, A. and Beerling, D. J. (2009) 'Process-based modeling of silicate mineral weathering responses to increasing atmospheric CO2 and climate change', *Global Biogeochemical Cycles*, 23(4). doi:

https://doi.org/10.1029/2008GB003243.

Bas, M. J. L. E. *et al.* (1986) 'A Chemical Classification of Volcanic Rocks Based on the Total Alkali-Silica Diagram', *Journal of Petrology*, 27(3), pp. 745–750. Available at: http://dx.doi.org/10.1093/petrology/27.3.745.

Beerling, D. J. *et al.* (2018) 'Farming with crops and rocks to address global climate, food and soil security', *Nature Plants*, 4(3), pp. 138–147. doi: 10.1038/s41477-018-0108-y.

Beerling, D. J. *et al.* (2020) 'Potential for large-scale CO2 removal via enhanced rock weathering with croplands', *Nature*, 583(7815), pp. 242–248. doi: 10.1038/s41586-020-2448-9.

Beriro, D. J. *et al.* (2014) 'Effects of drying and comminution type on the quantification of Polycyclic Aromatic Hydrocarbons (PAH) in a homogenised gasworks soil and the implications for human health risk assessment', *Chemosphere*, 111, pp. 396–404. doi: https://doi.org/10.1016/j.chemosphere.2014.03.077.

Blanc-Betes, E. *et al.* (2021) 'In silico assessment of the potential of basalt amendments to reduce N2O emissions from bioenergy crops', *GCB Bioenergy*, 13(1), pp. 224–241. doi: https://doi.org/10.1111/gcbb.12757.

Blanc, P. *et al.* (2012) 'Thermoddem: A geochemical database focused on low temperature water/rock interactions and waste materials', *Applied Geochemistry*, 27(10), pp. 2107–2116.

Blanco-Canqui, H. and Lal, R. (2004) 'Mechanisms of Carbon Sequestration in Soil Aggregates', *Critical Reviews in Plant Sciences*, 23(6), pp. 481–504. doi: 10.1080/07352680490886842.

Brantley, S. L. and Mellott, N. P. (2000) 'Surface area and porosity of primary silicate minerals', *American Mineralogist*, 85(11–12), pp. 1767–1783. doi: 10.2138/am-2000-11-1220.

Brantley, S. L., White, A. F. and Hosdson, M. E. (1999) 'Surface area of Primary Silicate Minerals', in Jamtveit, B. and Meakin, P. (eds) *Growth, dissolution and pattern formation in geosystems*. Springer, pp. 291 – 326. doi: https://doi.org/10.1007/978-94-015-9179-9_14.

Brunauer, S., Emmett, P. H. and Teller, E. (1938) 'Adsorption of Gases in Multimolecular Layers', *Journal of the American Chemical Society*, 60(2), pp. 309–319. doi: 10.1021/ja01269a023.

Bryan, S. E. *et al.* (2010) 'The largest volcanic eruptions on Earth', *Earth-Science Reviews*, 102(3), pp. 207–229. doi: https://doi.org/10.1016/j.earscirev.2010.07.001.

Chen, H. *et al.* (2017) 'Mechanisms of soil humic acid adsorption onto montmorillonite and kaolinite', *Journal of Colloid and Interface Science*, 504, pp. 457–467. doi: 10.1016/J.JCIS.2017.05.078.

Chorover, J., Amistadi, M. K. and Chadwick, O. A. (2004) 'Surface charge evolution of mineral-organic complexes during pedogenesis in Hawaiian basalt', *Geochimica et Cosmochimica Acta*, 68(23), pp. 4859–4876. doi:

10.1016/J.GCA.2004.06.005.

Chukov, S. N., Lodygin, E. D. and Abakumov, E. V (2018) ‘Application of 13C NMR Spectroscopy to the Study of Soil Organic Matter: A Review of Publications’, *Eurasian Soil Science*, 51(8), pp. 889–900. doi: 10.1134/S1064229318080021.

Ciceri, D., Manning, D. A. C. and Allanore, A. (2015) ‘Historical and technical developments of potassium resources’, *Science of The Total Environment*, 502, pp. 590–601. doi: https://doi.org/10.1016/j.scitotenv.2014.09.013.

Cordell, D. and White, S. (2014) ‘Life’s Bottleneck: Sustaining the World’s Phosphorus for a Food Secure Future’, *Annual Review of Environment and Resources*, 39(1), pp. 161–188. doi: 10.1146/annurev-environ-010213-113300.

D’Hotman, D. and De Villers, O. (1961) ‘Soil rejuvenation with crushed basalt in Mauritius.’, *International Sugar Journal*, 63, pp. 363–364.

Dahlgren, R. A. and Ugolini, F. C. (1989) ‘Formation and stability of imogolite in a tephritic Spodosol, Cascade Range, Washington, U.S.A.’, *Geochimica et Cosmochimica Acta*, 53(8), pp. 1897–1904. doi: https://doi.org/10.1016/0016-7037(89)90311-6.

Dalmora, A. C. *et al.* (2020a) ‘Application of andesite rock as a clean source of fertilizer for eucalyptus crop: Evidence of sustainability’, *Journal of Cleaner Production*, 256, p. 120432. doi: https://doi.org/10.1016/j.jclepro.2020.120432.

Dalmora, A. C. *et al.* (2020b) ‘Understanding the mobility of potential nutrients in rock mining by-products: An opportunity for more sustainable agriculture and mining’, *Science of The Total Environment*, 710, p. 136240. doi: https://doi.org/10.1016/j.scitotenv.2019.136240.

Declercq, J. and Oelkers, E. H. (2014) ‘CarbFix Report 4 PHREEQC mineral dissolution kinetics database 5’.

DEFRA (2020) *The British Survey of Fertiliser Practice Fertiliser use on Farm crops for crop year 2019*. London. Available at: https://assets.publishing.service.gov.uk/government/uploads/system/uploads/attachment_data/file/872453/fertiliseruse-report2018-13mar20.pdf.

Dogan, A. U. *et al.* (2006) ‘Baseline studies of the clay minerals society source clays: Specific surface area by the Brunauer Emmett Teller (BET) method’, *Clays and Clay Minerals*, 54(1), pp. 62–66. doi: 10.1346/CCMN.2006.0540108.

Dontsova, K. *et al.* (2009) ‘Solid phase evolution in the Biosphere 2 hillslope experiment as predicted by modeling of hydrologic and geochemical fluxes’, *Hydrology and Earth System Sciences*, 13(12), pp. 2273–2286. doi: 10.5194/hess-13-2273-2009.

Dontsova, K. *et al.* (2014) ‘Impact of organic carbon on weathering and chemical denudation of granular basalt’, *Geochimica et Cosmochimica Acta*, 139, pp. 508–526. doi: 10.1016/J.GCA.2014.05.010.

Du, P. *et al.* (2017) ‘Insights into the formation mechanism of imogolite from a full-range observation of its sol-gel growth’, *Applied Clay Science*, 150, pp. 115–124. doi: https://doi.org/10.1016/j.clay.2017.09.021.

Duckworth, O. W. and Sposito, G. (2005) 'Siderophore−Manganese(III) Interactions. I. Air-Oxidation of Manganese(II) Promoted by Desferrioxamine B', *Environmental Science & Technology*, 39(16), pp. 6037–6044. doi: 10.1021/es050275k.

Dunnington, D. (2020) 'Tidyphreeqc: Tidy geochemical modeling using PHREEQC.' Available at: https://github.com/paleolimbot/tidyphreeqc.

Eghball, B. (1999) 'Liming effects of beef cattle feedlot manure or compost', *Communications in Soil Science and Plant Analysis*, 30(19–20), pp. 2563–2570. doi: 10.1080/00103629909370396.

Elser, J. and Bennett, E. (2011) 'A broken biogeochemical cycle', *Nature*, 478(7367), pp. 29–31. doi: 10.1038/478029a.

Epihov, D. Z. *et al.* (2021) 'Legume–microbiome interactions unlock mineral nutrients in regrowing tropical forests', *Proceedings of the National Academy of Sciences*, 118(11), p. e2022241118. doi: 10.1073/pnas.2022241118.

Erlandsson, M. *et al.* (2016) 'Spatial and temporal variations of base cation release from chemical weathering on a hillslope scale', *Chemical Geology*, 441, pp. 1–13. doi: https://doi.org/10.1016/j.chemgeo.2016.08.008.

Eusterhues, K., Rumpel, C. and Kögel-Knabner, I. (2005) 'Stabilization of soil organic matter isolated via oxidative degradation', *Organic Geochemistry*, 36(11), pp. 1567–1575. doi: 10.1016/J.ORGGEOCHEM.2005.06.010.

Fairley, N. *et al.* (2021) 'Systematic and collaborative approach to problem solving using X-ray photoelectron spectroscopy', *Applied Surface Science Advances*, 5, p. 100112. doi: https://doi.org/10.1016/j.apsadv.2021.100112.

Fakhraei, H. and Driscoll, C. T. (2015) 'Proton and Aluminum Binding Properties of Organic Acids in Surface Waters of the Northeastern U.S.', *Environmental Science & Technology*, 49(5), pp. 2939–2947. doi: 10.1021/es504024u.

Farewell, T. S. *et al.* (2011) 'Use and applications of the Soilscapes datasets'. Cranfield University.

Farmer, V. C. and Lumsdon, D. G. (2001) 'Interactions of fulvic acid with aluminium and a proto-imogolite sol: the contribution of E-horizon eluates to podzolization', *European Journal of Soil Science*, 52(2), pp. 177–188. doi: https://doi.org/10.1046/j.1365-2389.2001.00377.x.

Feng, W. *et al.* (2014) 'Soil organic matter stability in organo-mineral complexes as a function of increasing C loading', *Soil Biology and Biochemistry*, 69, pp. 398–405. doi: https://doi.org/10.1016/j.soilbio.2013.11.024.

Flaathen, T. K., Gislason, S. R. and Oelkers, E. H. (2010) 'The effect of aqueous sulphate on basaltic glass dissolution rates', *Chemical Geology*, 277(3–4), pp. 345–354.

Fuss, S. *et al.* (2018) 'Negative emissions—Part 2: Costs, potentials and side effects', *Environmental Research Letters*, 13(6), p. 63002. doi: 10.1088/1748-9326/aabf9f.

Fyfe, W. S., Turner, F. J. and Verhoogen, J. (1959) *Fyfe, William S. Metamorphic reactions and metamorphic facies. Vol. 73.* Baltimore: The Geological Society of America.

Gabriel, C. E., Kellman, L. and Prest, D. (2018) 'Examining mineral-associated soil organic matter pools through depth in harvested forest soil profiles', *PLOS ONE*, 13(11), p. e0206847. Available at: https://doi.org/10.1371/journal.pone.0206847.

Gao, G. and Chang, C. (1996) 'Changes in CEC and particle size distribution of soils associated with long-term annual applications of cattle feedlot manure', *Soil Science*, 161(2).

Garcia, B. *et al.* (2013) 'An experimental model approach of biologically-assisted silicate dissolution with olivine and Escherichia coli – Impact on chemical weathering of mafic rocks and atmospheric CO_2 drawdown', *Applied Geochemistry*, 31, pp. 216–227. doi: https://doi.org/10.1016/j.apgeochem.2013.01.007.

Geddes, J. (2006) *Quantification of swelling clays in mineral mixtures and rocks using infrared spectroscopy.* Sheffield Hallam University. Available at: http://shura.shu.ac.uk/19682/.

GERM (2000) *The Geochemical Earth Reference Model*. Available at: http://earthref.org/agenda.htm.

Gillman, G. P., Burkett, D. C. and Coventry, R. J. (2002) 'Amending highly weathered soils with finely ground basalt rock', *Applied Geochemistry*, 17(8), pp. 987–1001. doi: 10.1016/S0883-2927(02)00078-1.

Goldich, S. S. (1938) 'A Study in Rock-Weathering', *The Journal of Geology*, 46(1), pp. 17–58. doi: 10.1086/624619.

Goût, T. L. *et al.* (2021) 'Temperature dependent lithium isotope fractionation during glass dissolution', *Geochimica et Cosmochimica Acta*, 313, pp. 133–154. doi: https://doi.org/10.1016/j.gca.2021.09.005.

Grosvenor, A. P. *et al.* (2004) 'Investigation of multiplet splitting of Fe 2p XPS spectra and bonding in iron compounds', *Surface and Interface Analysis*, 36(12), pp. 1564–1574. doi: https://doi.org/10.1002/sia.1984.

Haque, F. *et al.* (2019) 'Co-Benefits of Wollastonite Weathering in Agriculture: CO_2 Sequestration and Promoted Plant Growth', *ACS Omega*, 4(1), pp. 1425–1433. doi: 10.1021/acsomega.8b02477.

Hartmann, J. *et al.* (2013) 'Enhanced chemical weathering as a geoengineering strategy to reduce atmospheric carbon dioxide, a nutrient source and to mitigate ocean acidification', *Reviews of Geophysics*, 51(2012), pp. 113–149. doi: 10.1002/rog.20004.

Hashimoto, I. and Jackson, M. L. (2013) 'Rapid dissolution of allophane and kaolinite-halloysite after dehydration', in INGERSON, E. B. T.-C. and C. M. (ed.). Pergamon, pp. 102–113. doi: https://doi.org/10.1016/B978-0-08-009235-5.50008-5.

Hassink, J., Whitmore, A. P. and Kubát, J. (1997) 'Size and density fractionation

of soil organic matter and the physical capacity of soils to protect organic matter', *European Journal of Agronomy*, 7(1), pp. 189–199. doi: https://doi.org/10.1016/S1161-0301(97)00045-2.

Heckman, K. *et al.* (2013) 'Sorptive fractionation of organic matter and formation of organo-hydroxy-aluminum complexes during litter biodegradation in the presence of gibbsite', *Geochimica et Cosmochimica Acta*, 121, pp. 667–683. doi: https://doi.org/10.1016/j.gca.2013.07.043.

Heckman, K. *et al.* (2018) 'Variation in the Molecular Structure and Radiocarbon Abundance of Mineral-Associated Organic Matter across a Lithosequence of Forest Soils', *Soil Systems*. doi: 10.3390/soilsystems2020036.

Heckman, K., Lawrence, C. R. and Harden, J. W. (2018) 'A sequential selective dissolution method to quantify storage and stability of organic carbon associated with Al and Fe hydroxide phases', *Geoderma*, 312, pp. 24–35. doi: 10.1016/J.GEODERMA.2017.09.043.

Hellenbrandt, M. (2004) 'The Inorganic Crystal Structure Database (ICSD)—Present and Future', *Crystallography Reviews*, 10(1), pp. 17–22. doi: 10.1080/08893110410001664882.

Hillier, S. (1999) 'Use of an air brush to spray dry samples for X-ray powder diffraction', *Clay Minerals*. 2018/07/09, 34(1), pp. 127–135. doi: DOI: 10.1180/000985599545984.

Hinsinger, P. *et al.* (2003) 'Origins of root-mediated pH changes in the rhizosphere and their responses to environmental constraints: A review', *Plant and Soil*, 248(1), pp. 43–59. doi: 10.1023/A:1022371130939.

Hodson, M. E. (1998) 'Micropore surface area variation with grain size in unweathered alkali feldspars: implications for surface roughness and dissolution studies', *Geochimica et Cosmochimica Acta*, 62(21–22), pp. 3429–3435. doi: 10.1016/S0016-7037(98)00244-0.

Hodson, M. E. (2003) 'The influence of Fe-rich coatings on the dissolution of anorthite at pH 2.6', *Geochimica et Cosmochimica Acta*, 67(18), pp. 3355–3363. doi: https://doi.org/10.1016/S0016-7037(02)01370-4.

Hodson, M. E., Lee, M. R. and Parsons, I. (1997) 'Origins of the surface roughness of unweathered alkali feldspar grains', *Geochimica et Cosmochimica Acta*, 61(18), pp. 3885–3896. doi: 10.1016/S0016-7037(97)00197-X.

Holmgren, G. G. S. (1967) 'A Rapid Citrate-Dithionite Extractable Iron Procedure', *Soil Science Society of America Journal*, 31(2), pp. 210–211. doi: https://doi.org/10.2136/sssaj1967.03615995003100020020x.

Huang, J. *et al.* (2017) 'Chemical structures and characteristics of animal manures and composts during composting and assessment of maturity indices', *PloS one*, 12(6), pp. e0178110–e0178110. doi: 10.1371/journal.pone.0178110.

Huang, P. M. *et al.* (2002) 'Aluminum Hydroxides', *Soil Mineralogy with Environmental Applications*. (SSSA Book Series), pp. 261–289. doi: https://doi.org/10.2136/sssabookser7.c8.

IBM Corp (2020) 'IBM SPSS Statistics for Windows, Version 27.0.' Armonk,

NY: IBM Corp.

Inorganic Crystal Structure Database (ICSD) (2019) ‘ICSD’. FIZ Karlsruhe. Available at: http://www.fiz-karlsruhe.de/icsd.html or http://icsdweb.fiz-karlsruhe.de.

International Centre for Diffraction Data (ICDD) (2019) ‘PDF-4+ 2019 (database)’. Newtown Square, PA: International Centre for Diffraction Data.

IPCC (2018) *Summary for Policymakers of IPCC Special Report on Global Warming of 1.5°C approved by governments.* Incheon.

IPCC (2021) *Climate Change 2021: The Physical Science Basis. Contribution of Working Group 1 to the Sixth Assessment Report of the Intergovernmental Panel on Climate Change*. Edited by V. Masson-Delmotte et al. Cambridge University Press.

Iskrenova-Tchoukova, E., Kalinichev, A. G. and Kirkpatrick, R. J. (2010) ‘Metal Cation Complexation with Natural Organic Matter in Aqueous Solutions: Molecular Dynamics Simulations and Potentials of Mean Force’, *Langmuir*, 26(20), pp. 15909–15919. doi: 10.1021/la102535n.

Jagadamma, S. *et al.* (2014) ‘Sorption of organic carbon compounds to the fine fraction of surface and subsurface soils’, *Geoderma*, 213, pp. 79–86. doi: 10.1016/J.GEODERMA.2013.07.030.

Jobbágy, E. G. and Jackson, R. B. (2000) ‘The vertical distribution of soil organic carbon and its relation to climate and vegetation.’, *Ecological Applications*, 10(2), pp. 423–436. doi: https://doi.org/10.1890/1051-0761(2000)010[0423:TVDOSO]2.0.CO;2.

Kaiser, K. and Zech, W. (2000) ‘Dissolved organic matter sorption by mineral constituents of subsoil clay fractions’, *Journal of Plant Nutrition and Soil Science*, 163(5), pp. 531–535. doi: 10.1002/1522-2624(200010)163:5<531::AID-JPLN531>3.0.CO;2-N.

Kantola, I. *et al.* (2017) ‘Potential of global croplands and bioenergy crops for climate change mitigation through deployment for enhanced weathering’, *Biology Letters*, 13(4). doi: https://doi.org/10.1098/rsbl.2016.0714.

Kantzas, E. P. *et al.* (2022) ‘Substantial carbon drawdown potential from enhanced rock weathering in the United Kingdom’, *Nature Geoscience*. doi: 10.1038/s41561-022-00925-2.

Kelland, M. E. *et al.* (2020) ‘Increased yield and CO_2 sequestration potential with the C4 cereal Sorghum bicolor cultivated in basaltic rock dust-amended agricultural soil’, *Global Change Biology*, n/a(n/a). doi: 10.1111/gcb.15089.

Kemp, S. J., Ellis, M. A., *et al.* (2016a) ‘Palaeoclimatic implications of high-resolution clay mineral assemblages preceding and across the onset of the Palaeocene–Eocene Thermal Maximum, North Sea Basin’, *Clay Minerals*, 51(5), pp. 793–813. doi: 10.1180/claymin.2016.051.5.08.

Kemp, S. J., Smith, F. W., *et al.* (2016b) ‘An Improved Approach to Characterize

Potash-Bearing Evaporite Deposits, Evidenced in North Yorkshire, United Kingdom', *Economic Geology*, 111(3), pp. 719–742. doi: 10.2113/econgeo.111.3.719.

Kemp, S. J., Lewis, A. L. and Rushton, J. C. (in press) 'Detection and Quantification of Low Levels of Carbonate Mineral Species Using Thermogravimetric-Mass Spectrometry to Validate CO_2 Drawdown Via Enhanced Rock Weathering', *Applied Geochemistry*.

Kirstein, L. A., Davies, G. R. and Heeremans, M. (2006) 'The petrogenesis of Carboniferous–Permian dyke and sill intrusions across northern Europe', *Contributions to Mineralogy and Petrology*, 152(6), pp. 721–742. doi: 10.1007/s00410-006-0129-9.

Kleber, M. *et al.* (2005) 'Poorly crystalline mineral phases protect organic matter in acid subsoil horizons', *European Journal of Soil Science*, 56(6), pp. 717–725. doi: 10.1111/j.1365-2389.2005.00706.x.

Kloprogge, J. T. *et al.* (2006) 'XPS study of the major minerals in bauxite: Gibbsite, bayerite and (pseudo-)boehmite', *Journal of Colloid and Interface Science*, 296(2), pp. 572–576. doi: https://doi.org/10.1016/j.jcis.2005.09.054.

Köhler, P. *et al.* (2013) 'Geoengineering impact of open ocean dissolution of olivine on atmospheric CO_2, surface ocean pH and marine biology', *Environmental Research Letters*, 8(1), p. 14009. doi: 10.1088/1748-9326/8/1/014009.

Köhler, P., Hartmann, J. and Wolf-Gladrow, D. A. (2010) 'Geoengineering potential of artificially enhanced silicate weathering of olivine', *Proceedings of the National Academy of Sciences*, 107(47), pp. 20228 LP – 20233. doi: 10.1073/pnas.1000545107.

Korchagin, J., Caner, L. and Bortoluzzi, E. C. (2019) 'Variability of amethyst mining waste: A mineralogical and geochemical approach to evaluate the potential use in agriculture', *Journal of Cleaner Production*, 210, pp. 749–758. doi: https://doi.org/10.1016/j.jclepro.2018.11.039.

Kristmannsdottir, H. (1979) 'Alteration of Basaltic Rocks by Hydrothermal-Activity at 100-300°C', in Mortland, M. M. and Farmer, V. C. B. T.-D. in S. (eds) *International Clay Conference 1978*. Elsevier, pp. 359–367. doi: https://doi.org/10.1016/S0070-4571(08)70732-5.

Lackner, K. S. *et al.* (1995) 'Carbon dioxide disposal in carbonate minerals', *Energy*, 20(11), pp. 1153–1170. doi: 10.1016/0360-5442(95)00071-N.

Lal, R. (2004) 'Soil Carbon Sequestration Impacts on Global Climate Change and Food Security', *Science*, 304(5677), pp. 1623 LP – 1627. Available at: http://science.sciencemag.org/content/304/5677/1623.abstract.

Lawley, R., Emmett, B. A. and Robinson, D. A. (2014) 'Soil observatory lets researchers dig deep', *Nature*, 509(7501), p. 427. doi: 10.1038/509427b.

Lee, M. R. *et al.* (2008) 'The composition and crystallinity of the near-surface regions of weathered alkali feldspars', *Geochimica et Cosmochimica Acta*, 72(20), pp. 4962–4975. doi: https://doi.org/10.1016/j.gca.2008.08.001.

Lee, M. R. and Parsons, I. (1995) 'Microtextural controls of weathering of perthitic alkali feldspars', *Geochimica et Cosmochimica Acta*, 59(21), pp. 4465–4488. doi: 10.1016/0016-7037(95)00255-X.

Le Maitre, R.W.,Streckeisen, A., Zanettin, B., Le Bas, M.J, Bonin, B., Bateman, P., Bellieni, G., Dudek, A., Efremova, S., Keller, J., Lamere, J., Sabine, P.A., Schmid, R., Sorensen, H. and Woolley, A.R. 2002 Igneous Rocks: A Classification and Glossary of Terms, Recommendations of the International Union of Geological Sciences, Subcommission of the Systematics of Igneous Rocks. Cambridge University Press. ISBN 0-521-66215-X

Lewis, A. L. *et al.* (2021) 'Effects of mineralogy, chemistry and physical properties of basalts on carbon capture potential and plant-nutrient element release via enhanced weathering', *Applied Geochemistry*, 132, p. 105023. doi: https://doi.org/10.1016/j.apgeochem.2021.105023.

Li, H. *et al.* (2021) 'A Critical Review on the Multiple Roles of Manganese in Stabilizing and Destabilizing Soil Organic Matter', *Environmental Science & Technology*, 55(18), pp. 12136–12152. doi: 10.1021/acs.est.1c00299.

Li, T. *et al.* (2020) 'Contrasting impacts of manure and inorganic fertilizer applications for nine years on soil organic carbon and its labile fractions in bulk soil and soil aggregates', *CATENA*, 194, p. 104739. doi: https://doi.org/10.1016/j.catena.2020.104739.

Li, W. *et al.* (2021) 'Lithium and potassium isotope fractionation during silicate rock dissolution: An experimental approach', *Chemical Geology*, 568, p. 120142. doi: https://doi.org/10.1016/j.chemgeo.2021.120142.

Lofts, S. *et al.* (2001) 'Modelling pH buffering and aluminium solubility in European forest soils', *European Journal of Soil Science*, 52(2), pp. 189–204. doi: https://doi.org/10.1046/j.1365-2389.2001.00358.x.

De Lucia, M. and Kühn, M. (2013) 'Coupling R and PHREEQC: Efficient Programming of Geochemical Models', *Energy Procedia*, 40, pp. 464–471. doi: https://doi.org/10.1016/j.egypro.2013.08.053.

Madejová, J. (2003) 'FTIR techniques in clay mineral studies', *Vibrational Spectroscopy*, 31(1), pp. 1–10. doi: https://doi.org/10.1016/S0924-2031(02)00065-6.

Manning, D. A. C. (2001) 'Calcite precipitation in landfills: an essential product of waste stabilization', *Mineralogical Magazine*, p. 603. doi: 10.1180/002646101317018424.

Matter, J. M. *et al.* (2016) 'Rapid carbon mineralization for permanent disposal of anthropogenic carbon dioxide emissions', *Science*, 352(6291), pp. 1312–1314. doi: 10.1126/science.aad8132.

Mayes, W. M., Aumônier, J. and Jarvis, A. P. (2009) 'Preliminary evaluation of a constructed wetland for treating extremely alkaline (pH 12) steel slag drainage', *Water Science and Technology*, 59(11), pp. 2253 LP – 2263. Available at: http://wst.iwaponline.com/content/59/11/2253.abstract.

McKeague, J. A. (1967) 'An evaluation of 0.1 M pyrophosphate and

pyrophosphate-dithionite in comparison with oxalate as extractants of the accumulation products in podzols and some other soils', *Canadian Journal of Soil Science*, 47(2), pp. 95–99. doi: 10.4141/cjss67-017.

Mercure, J.-F. *et al.* (2018) 'Macroeconomic impact of stranded fossil fuel assets', *Nature Climate Change*, 8(7), pp. 588–593. doi: 10.1038/s41558-018-0182-1.

Met office (2021) *Met Office Integrated Data Archive System (MIDAS) Land and Marine Surface Stations Data (1853-current)*. NCAS British Atmospheric Data Centre, date of citation. Available at: http://catalogue.ceda.ac.uk/uuid/220a65615218d5c9cc9e4785a3234bd0.

Mikutta, R. *et al.* (2006) 'Stabilization of Soil Organic Matter: Association with Minerals or Chemical Recalcitrance?', *Biogeochemistry*, 77(1), pp. 25–56. doi: 10.1007/s10533-005-0712-6.

Mikutta, R. *et al.* (2014) 'Properties and reactivity of Fe-organic matter associations formed by coprecipitation versus adsorption: Clues from arsenate batch adsorption', *Geochimica et Cosmochimica Acta*, 144, pp. 258–276. doi: https://doi.org/10.1016/j.gca.2014.08.026.

Miller, D. J., Biesinger, M. C. and McIntyre, N. S. (2002) 'Interactions of CO2 and CO at fractional atmosphere pressures with iron and iron oxide surfaces: one possible mechanism for surface contamination?', *Surface and Interface Analysis*, 33(4), pp. 299–305. doi: https://doi.org/10.1002/sia.1188.

Mindat (2022) *Definition of essential mineral*. Available at: https://www.mindat.org/glossary/essential_mineral (Accessed: 17 May 2022).

Minx, J. C. *et al.* (2018) 'Negative emissions—Part 1: Research landscape and synthesis', *Environmental Research Letters*, 13(6), p. 63001. doi: 10.1088/1748-9326/aabf9b.

Moore, D. M. and Reynolds, R. C. (1997) *X-Ray Diffraction and the Identification and Analysis of Clay Minerals*. Second. New York: OXFORD UNIVERSITY PRESS.

Moosdorf, N., Renforth, P. and Hartmann, J. (2014) 'Carbon Dioxide Efficiency of Terrestrial Enhanced Weathering', *Environmental Science & Technology*, 48(9), pp. 4809–4816. doi: 10.1021/es4052022.

Moreno-Pérez, E. *et al.* (2018) 'Chemical and Mineralogical Characterization of Recycled Aggregates from Construction and Demolition Waste from Mexico City', *Minerals* . doi: 10.3390/min8060237.

Mucciarone, D. (2005) *Internal Laboratory Report on Freeze Drying vs Oven Drying Sediments at 40°C*. Available at: https://osf.io/x7vyt/.

Muir, I. J. *et al.* (1990) 'A SIMS and XPS study of dissolving plagioclase', *Geochimica et Cosmochimica Acta*, 54(8), pp. 2247–2256. doi: https://doi.org/10.1016/0016-7037(90)90049-Q.

Nan, W. *et al.* (2016) 'The factors related to carbon dioxide effluxes and production in the soil profiles of rain-fed maize fields', *Agriculture, Ecosystems & Environment*, 216, pp. 177–187. doi:

https://doi.org/10.1016/j.agee.2015.09.032.

Neal, C. (2002) ‘Calcite saturation in eastern UK rivers’, *Science of The Total Environment*, 282–283, pp. 311–326. doi: https://doi.org/10.1016/S0048-9697(01)00921-4.

Nemet, G. F. *et al.* (2018) ‘Negative emissions—Part 3: Innovation and upscaling’, *Environmental Research Letters*, 13(6), p. 63003. doi: 10.1088/1748-9326/aabff4.

Vanden Nest, T. *et al.* (2016) ‘The long term use of farmyard manure and compost: Effects on P availability, orthophosphate sorption strength and P leaching’, *Agriculture, Ecosystems & Environment*, 216, pp. 23–33. doi: https://doi.org/10.1016/j.agee.2015.09.009.

Ng, H. C. P. *et al.* (1999) ‘Nutrient requirements and sustainability in mature oil palms - an assessment.’, *Planter*, 75(880), pp. 331–345.

Ni, M. and Ratner, B. D. (2008) ‘Differentiating calcium carbonate polymorphs by surface analysis techniques—an XPS and TOF-SIMS study’, *Surface and Interface Analysis*, 40(10), pp. 1356–1361. doi: https://doi.org/10.1002/sia.2904.

Nugent, M. A. *et al.* (1998) ‘The influence of natural mineral coatings on feldspar weathering’, *Nature*, 395(6702), pp. 588–591. doi: 10.1038/26951.

O’Connor, J. *et al.* (2021) ‘Production, characterisation, utilisation, and beneficial soil application of steel slag: A review’, *Journal of Hazardous Materials*, 419, p. 126478. doi: https://doi.org/10.1016/j.jhazmat.2021.126478.

Oades, J. M. (1988) ‘The retention of organic matter in soils’, *Biogeochemistry*, 5(1), pp. 35–70. doi: 10.1007/BF02180317.

Oelkers, E. H. (2001) ‘General kinetic description of multioxide silicate mineral and glass dissolution’, *Geochimica et Cosmochimica Acta*, 65(21), pp. 3703–3719. doi: 10.1016/S0016-7037(01)00710-4.

Oelkers, E. H. and Gislason, S. R. (2001) ‘The mechanism, rates and consequences of basaltic glass dissolution: I. An experimental study of the dissolution rates of basaltic glass as a function of aqueous Al, Si and oxalic acid concentration at 25°C and pH = 3 and 11’, *Geochimica et Cosmochimica Acta*, 65(21), pp. 3671–3681. doi: 10.1016/S0016-7037(01)00664-0.

Palandri, J. L. and Kharaka, Y. K. (2004) *A compilation of rate parameters of water-mineral interaction kinetics for application to geochemical modeling*, *USGS Open File Report*. doi: 10.1098/rspb.2004.2754.

Pansu, M. and Gautheyrou, J. (eds) (2006) ‘Mineralogical Separation by Selective Dissolution BT - Handbook of Soil Analysis: Mineralogical, Organic and Inorganic Methods’, in. Berlin, Heidelberg: Springer Berlin Heidelberg, pp. 167–219. doi: 10.1007/978-3-540-31211-6_6.

Parkhurst, D. L. and Appelo, C. A. J. (2013) *Description of input and examples for PHREEQC version 3: a computer program for speciation, batch-reaction, one-dimensional transport, and inverse geochemical calculations*. US Geological Survey.

Parry, S. A. *et al.* (2015) ‘The surface area and reactivity of granitic soils: I. Dissolution rates of primary minerals as a function of depth and age deduced from field observations’, *Geoderma*, 237–238, pp. 21–35. doi: https://doi.org/10.1016/j.geoderma.2014.08.004.

Pistiner, J. S. and Henderson, G. M. (2003) ‘Lithium-isotope fractionation during continental weathering processes’, *Earth and Planetary Science Letters*, 214(1), pp. 327–339. doi: https://doi.org/10.1016/S0012-821X(03)00348-0.

Poblador, S. *et al.* (2022) ‘Enhanced weathering in acid and alkaline agricultural soils: greenhouse gas emissions and soil bacterial communities implications’, in *EGU General Assembly 2022, Vienna, Austria, 23–27 May 2022*. doi: EGU22-13396.

Pogge von Strandmann, P. A. E. *et al.* (2019) ‘Experimental determination of Li isotope behaviour during basalt weathering’, *Chemical Geology*, 517, pp. 34–43. doi: https://doi.org/10.1016/j.chemgeo.2019.04.020.

Pogge von Strandmann, P. A. E., Kasemann, S. A. and Wimpenny, J. B. (2020) ‘Lithium and Lithium Isotopes in Earth’s Surface Cycles’, *Elements*, 16(4), pp. 253–258. doi: 10.2138/gselements.16.4.253.

Pohlmann, M. *et al.* (2016) ‘Pore water chemistry reveals gradients in mineral transformation across a model basaltic hillslope’, *Geochemistry, Geophysics, Geosystems*, 17(6), pp. 2054–2069. doi: 10.1002/2016GC006270.

Ponce-Lira, B. *et al.* (2017) ‘Lead removal from aqueous solution by basaltic scoria: adsorption equilibrium and kinetics’, *International Journal of Environmental Science and Technology*, 14(6), pp. 1181–1196. doi: 10.1007/s13762-016-1234-6.

Pourbaix, M. (1974) *Atlas of Electrochemical Equilibria in Aqueous solutions*.

Power, I. M. *et al.* (2014) ‘Strategizing Carbon-Neutral Mines: A Case for Pilot Projects’, *Minerals* . doi: 10.3390/min4020399.

Pratt, C. *et al.* (2020) ‘Geo-Agriculture: Reviewing Opportunities through Which the Geosphere Can Help Address Emerging Crop Production Challenges’, *Agronomy* . doi: 10.3390/agronomy10070971.

Price, J. R. and Velbel, M. A. (2003) ‘Chemical weathering indices applied to weathering profiles developed on heterogeneous felsic metamorphic parent rocks’, *Chemical Geology*, 202(3), pp. 397–416. doi: https://doi.org/10.1016/j.chemgeo.2002.11.001.

Department of Primary Industries (1993) *Cation Exchange Capacity*. Available at: https://www.dpi.nsw.gov.au/agriculture/soils/guides/soil-nutrients-and-fertilisers/cec#:~:text=You can improve CEC in,the CEC of your soil.

Proctor, D. M. *et al.* (2000) ‘Physical and Chemical Characterization of Blast Furnace, Basic Oxygen Furnace and Electric Arc Furnace Steel Industry Slags’, *Environmental Science and Technology*, 34(8), pp. 1576–1582. doi: 10.1021/es9906002.

Qi, S. *et al.* (2016) ‘Investigation of Zn^{2+} and Cd^{2+} Adsorption Performance by Different Weathering Basalts’, *Water, Air, & Soil Pollution*, 227(4), p. 126. doi:

10.1007/s11270-016-2800-8.

Quinn, R. (2020) ‘DTN Retail Fertilizer Trends’, *DTN Progressive Farmer*.

Quirk, J. *et al.* (2012) ‘Evolution of trees and mycorrhizal fungi intensifies silicate mineral weathering’, *Biology Letters*, 8(6), pp. 1006–1011. doi: 10.1098/rsbl.2012.0503.

R Development Core Team (2018) ‘A Language and Environment for Statistical Computing’, *R Foundation for Statistical Computing*. Vienna: R Foundation for Statistical Computing, p. https://www.R-project.org. Available at: http://www.r-project.org.

Ramos, C. G. *et al.* (2019) ‘Evaluation of Soil Re-mineralizer from By-Product of Volcanic Rock Mining: Experimental Proof Using Black Oats and Maize Crops’, *Natural Resources Research*. doi: 10.1007/s11053-019-09529-x.

Rasmussen, C. *et al.* (2018) ‘Beyond clay: towards an improved set of variables for predicting soil organic matter content’, *Biogeochemistry*, 137(3), pp. 297–306. doi: 10.1007/s10533-018-0424-3.

Rayment, G. E. and Higginson, F. R. (1992) *Australian laboratory handbook of soil and water chemical methods*. Inkata Press.

Renforth, P. *et al.* (2011) ‘Silicate Production and Availability for Mineral Carbonation’, *Environmental Science & Technology*, 45(6), pp. 2035–2041. doi: 10.1021/es103241w.

Renforth, P. (2012) ‘The potential of enhanced weathering in the UK’, *International Journal of Greenhouse Gas Control*, 10, pp. 229–243. doi: 10.1016/J.IJGGC.2012.06.011.

Renforth, P. and Henderson, G. (2017) ‘Assessing ocean alkalinity for carbon sequestration’, *Reviews of Geophysics*, 55(3), pp. 636–674. doi: 10.1002/2016RG000533.

Renforth, P., Pogge von Strandmann, P. A. E. and Henderson, G. M. (2015) ‘The dissolution of olivine added to soil: Implications for enhanced weathering’, *Applied Geochemistry*, 61, pp. 109–118. doi: https://doi.org/10.1016/j.apgeochem.2015.05.016.

Rennert, T. (2019) ‘Wet-chemical extractions to characterise pedogenic Al and Fe species – a critical review’, *Soil Research*, 57(1), pp. 1–16. Available at: https://doi.org/10.1071/SR18299.

Rigopoulos, I. *et al.* (2016) ‘On the potential use of quarry waste material for CO2 sequestration’, *Journal of CO2 Utilization*, 16, pp. 361–370. doi: 10.1016/J.JCOU.2016.09.005.

Riise, G. *et al.* (2000) ‘Mobility of different size fractions of organic carbon, Al, Fe, Mn and Si in podzols’, *Geoderma*, 94(2), pp. 237–247. doi: https://doi.org/10.1016/S0016-7061(99)00044-0.

Robertson, S. (1999) *BSG Rock Classification Scheme Volume 2 Classification of metamorphic rocks*.

Rockström, J. *et al.* (2017) ‘A roadmap for rapid decarbonization’, *Science*, 355(6331), pp. 1269 LP – 1271. doi: 10.1126/science.aah3443.

Ross, G. J., Wang, C. and Schuppli, P. A. (1985) ‘Hydroxylamine and Ammonium Oxalate Solutions as Extractants for Iron and Aluminum from Soils’, *Soil Science Society of America Journal*, 49(3), pp. 783–785. doi: https://doi.org/10.2136/sssaj1985.03615995004900030051x.

Ross, P.-S. *et al.* (2005) ‘Mafic volcaniclastic deposits in flood basalt provinces: A review’, *Journal of Volcanology and Geothermal Research*, 145(3), pp. 281–314. doi: https://doi.org/10.1016/j.jvolgeores.2005.02.003.

Rowley, M. C. *et al.* (2021) ‘Evidence linking calcium to increased organo-mineral association in soils’, *Biogeochemistry*, 153(3), pp. 223–241. doi: 10.1007/s10533-021-00779-7.

Rowley, M. C., Grand, S. and Verrecchia, É. P. (2018) ‘Calcium-mediated stabilisation of soil organic carbon’, *Biogeochemistry*, 137(1), pp. 27–49. doi: 10.1007/s10533-017-0410-1.

Sabine, P. A., Morey, J. E. and Shergold, F. A. (1954) ‘The correlation of the mechanical properties and petrography of a series of quartz-dolerite roadstones’, *Journal of Applied Chemistry*, 4(3), pp. 131–137. doi: 10.1002/jctb.5010040307.

Sakizci, M. (2016) ‘Investigation of thermal and structural properties of natural and ion-exchanged analcime’, *Anadolu University Journal Of Science And Technology A - Applied Sciences and Engineering*, 17(AFG5 SPECIAL ISSUE), pp. 724–724. doi: 10.18038/aubtda.266863.

Sarbas, B. (2008) ‘The GEOROC database as part of a growing geoinformatics network’, in *Geoinformatics 2008—Data to Knowledge*. USGS, pp. 42–43. Available at: http://georoc.mpch-mainz.gwdg.de/georoc/Start.asp.

Sarkar, B. *et al.* (2018) ‘Clay Minerals—Organic Matter Interactions in Relation to Carbon Stabilization in Soils’, *The Future of Soil Carbon*, pp. 71–86. doi: 10.1016/B978-0-12-811687-6.00003-1.

Schjønning, P., Christensen, B. T. and Carstensen, B. (1994) ‘Physical and chemical properties of a sandy loam receiving animal manure, mineral fertilizer or no fertilizer for 90 years’, *European Journal of Soil Science*, 45(3), pp. 257–268. doi: https://doi.org/10.1111/j.1365-2389.1994.tb00508.x.

Schott, J. *et al.* (2012) ‘Formation, growth and transformation of leached layers during silicate minerals dissolution: The example of wollastonite’, *Geochimica et Cosmochimica Acta*, 98, pp. 259–281. doi: https://doi.org/10.1016/j.gca.2012.09.030.

Schott, J. and Berner, R. A. (1985) ‘Dissolution Mechanisms of Pyroxenes and Olivines During Weathering BT - The Chemistry of Weathering’, in Drever, J. I. (ed.). Dordrecht: Springer Netherlands, pp. 35–53. doi: 10.1007/978-94-009-5333-8_3.

Schuiling, R. D. and de Boer, P. L. (2013) ‘Six commercially viable ways to remove CO2 from the atmosphere and/or reduce CO2 emissions’, *Environmental Sciences Europe*, 25(1), p. 35. doi: 10.1186/2190-4715-25-35.

Schuiling, R. D. and Krijgsman, P. (2006) 'Enhanced Weathering: An Effective and Cheap Tool to Sequester Co2', *Climatic Change*, 74(1), pp. 349–354. doi: 10.1007/s10584-005-3485-y.

Schwertmann, U. (1964) 'Differenzierung der Eisenoxide des Bodens durch Extraktion mit Ammoniumoxalat-Lösung', *Zeitschrift für Pflanzenernährunge*, 105, pp. 194–202.

Seifritz, W. (1990) 'CO2 disposal by means of silicates', *Nature*, 345(6275), pp. 486–486. doi: 10.1038/345486b0.

Shi, Y. *et al.* (2016) 'The Effects of Long-term Fertiliser Applications on Soil Organic Carbon and Hydraulic Properties of a Loess Soil in China', *Land Degradation & Development*, 27(1), pp. 60–67. doi: https://doi.org/10.1002/ldr.2391.

Singh, M. *et al.* (2017) 'Relationship between soil clay mineralogy and carbon protection capacity as influenced by temperature and moisture', *Soil Biology and Biochemistry*, 109, pp. 95–106. doi: 10.1016/J.SOILBIO.2017.02.003.

Skiba, U. *et al.* (2020) 'Oil palm plantations are large sources of nitrous oxide, but where are the data to quantify the impact on global warming?', *Current Opinion in Environmental Sustainability*, 47, pp. 81–88. doi: https://doi.org/10.1016/j.cosust.2020.08.019.

Slessarev, E. W. *et al.* (2022) 'Rock weathering controls the potential for soil carbon storage at a continental scale', *Biogeochemistry*, 157(1), pp. 1–13. doi: 10.1007/s10533-021-00859-8.

Smith, G. A. and Hayman, G. A. (1987) *Geologic map of the Eagle Butte and Gateway quadrangles, Jefferson and Wasco Counties, Oregon, State of Oregon, Department of Geology and Mineral Industries.*

So, R. T., Blair, N. E. and Masterson, A. L. (2020) 'Carbonate mineral identification and quantification in sediment matrices using diffuse reflectance infrared Fourier transform spectroscopy ', *Environmental Chemistry Letters*, 18(5), pp. 1725–1730. doi: 10.1007/s10311-020-01027-4.

Soon, Y. K. (1993) 'Fractionation of extractable aluminum in acid soils: A review and a proposed procedure', *Communications in Soil Science and Plant Analysis*, 24(13–14), pp. 1683–1708. doi: 10.1080/00103629309368908.

Stephenson, P. J. *et al.* (2007) 'Temporal development of the Atherton Basalt Province, north Queensland AU - Whitehead, P. W.', *Australian Journal of Earth Sciences*, 54(5), pp. 691–709. doi: 10.1080/08120090701305236.

Stockmann, G. J. *et al.* (2011) 'Do carbonate precipitates affect dissolution kinetics? 1: Basaltic glass', *Chemical Geology*, 284(3–4), pp. 306–316. doi: 10.1016/J.CHEMGEO.2011.03.010.

Stockmann, G. J. *et al.* (2013) 'Do carbonate precipitates affect dissolution kinetics?: 2: Diopside', *Chemical Geology*, 337–338, pp. 56–66. doi: https://doi.org/10.1016/j.chemgeo.2012.11.014.

Stockmann, G. J. *et al.* (2014) 'The role of silicate surfaces on calcite precipitation kinetics', *Geochimica et Cosmochimica Acta*, 135, pp. 231–250. doi:

https://doi.org/10.1016/j.gca.2014.03.015.

Stokes, G. G. (1851) ‘On the effect of internal friction of fluids on the motion of pendulums’, *Transactions of the Cambridge Philosophical Society.*, 9(2), pp. 8–106.

Streckeisen, A. (1974) ‘Classification and nomenclature of plutonic rocks recommendations of the IUGS subcommission on the systematics of Igneous Rocks’, *Geologische Rundschau*, 63(2), pp. 773–786. doi: 10.1007/BF01820841.

Strefler, J. *et al.* (2018) ‘Potential and costs of carbon dioxide removal by enhanced weathering of rocks’, *Environmental Research Letters*, 13(3), p. 34010. doi: 10.1088/1748-9326/aaa9c4.

Styles, M. T. *et al.* (2014) ‘The variation in composition of ultramafic rocks and the effect on their suitability for carbon dioxide sequestration by mineralization following acid leaching’, *Greenhouse Gases: Science and Technology*, 4(4), pp. 440–451. doi: https://doi.org/10.1002/ghg.1405.

Tahir, S., Musta, B. and Rahim, I. R. (2010) ‘Geological heritage features of Tawau volcanic sequence, Sabah’, *Bulletin of the Geological Society of Malaysia*, 56, pp. 79–85.

Takahashi, T. and Dahlgren, R. A. (2016) ‘Nature, properties and function of aluminum–humus complexes in volcanic soils’, *Geoderma*, 263, pp. 110–121. doi: 10.1016/J.GEODERMA.2015.08.032.

Tamrat, W. Z. *et al.* (2019) ‘Soil organo-mineral associations formed by co-precipitation of Fe, Si and Al in presence of organic ligands’, *Geochimica et Cosmochimica Acta*, 260, pp. 15–28. doi: 10.1016/J.GCA.2019.05.043.

Taylor, L. L. *et al.* (2016) ‘Enhanced weathering strategies for stabilizing climate and averting ocean acidification’, *Nature Climate Change*, 6, p. 402. Available at: https://doi.org/10.1038/nclimate2882.

Taylor, L. L. *et al.* (2021) ‘Increased carbon capture by a silicate-treated forested watershed affected by acid deposition’, *Biogeosciences*, 18(1), pp. 169–188. doi: 10.5194/bg-18-169-2021.

The Royal Academy of Engineers and The Royal Society (2018) *Greenhouse Gas Removal*. Available at: https://royalsociety.org/~/media/policy/projects/greenhouse-gas-removal/royal-society-greenhouse-gas-removal-report-2018.pdf.

Tipping, E. (1994) ‘WHAMC—A chemical equilibrium model and computer code for waters, sediments, and soils incorporating a discrete site/electrostatic model of ion-binding by humic substances’, *Computers & Geosciences*, 20(6), pp. 973–1023. doi: https://doi.org/10.1016/0098-3004(94)90038-8.

Tipping, E. *et al.* (2002) ‘Al(III) and Fe(III) binding by humic substances in freshwaters, and implications for trace metal speciation’, *Geochimica et Cosmochimica Acta*, 66(18), pp. 3211–3224. doi: https://doi.org/10.1016/S0016-7037(02)00930-4.

Tole, M. P. *et al.* (1986) ‘The kinetics of dissolution of nepheline (NaAlSiO4)’, *Geochimica et Cosmochimica Acta*, 50(3), pp. 379–392. doi: 10.1016/0016-

7037(86)90191-2.

Toplak, M. *et al.* (2021) ‘Quasar: Easy Machine Learning for Biospectroscopy’, *Cells* . doi: 10.3390/cells10092300.

Cranfield University (2022) *The Soils Guide*. Available at: www.landis.org.uk.

USDA (2019) *Fertiliser Use and Price*. Available at: https://www.ers.usda.gov/data-products/fertilizer-use-and-price/.

USGS (2019) *Catoctin Formation - Metabasalt*. Available at: https://mrdata.usgs.gov/geology/state/sgmc-unit.php?unit=VACAZc%3B0 (Accessed: 13 October 2019).

Vicca, S. *et al.* (2022) ‘Is the climate change mitigation effect of enhanced silicate weathering governed by biological processes?’, *Global Change Biology*, 28(3), pp. 711–726. doi: https://doi.org/10.1111/gcb.15993.

Vingiani, S. *et al.* (2010) ‘Weathering of basaltic pebbles in a red soil from Sardinia: A microsite approach for the identification of secondary mineral phases’, *CATENA*, 83(2), pp. 96–106. doi: https://doi.org/10.1016/j.catena.2010.07.001.

Wagai, R. *et al.* (2013) ‘Association of organic matter with iron and aluminum across a range of soils determined via selective dissolution techniques coupled with dissolved nitrogen analysis’, *Biogeochemistry*, 112(1), pp. 95–109. doi: 10.1007/s10533-011-9652-5.

Wagai, R. and Mayer, L. M. (2007) ‘Sorptive stabilization of organic matter in soils by hydrous iron oxides’, *Geochimica et Cosmochimica Acta*, 71(1), pp. 25–35. doi: 10.1016/J.GCA.2006.08.047.

Walthert, L. *et al.* (2010) ‘Determination of organic and inorganic carbon, δ13C, and nitrogen in soils containing carbonates after acid fumigation with HCl’, *Journal of Plant Nutrition and Soil Science*, 173(2), pp. 207–216. doi: https://doi.org/10.1002/jpln.200900158.

Wang, C., Schuppli, P. A. and Ross, G. J. (1987) ‘A comparison of hydroxylamine and ammonium oxalate solutions as extractants for Al, Fe and Si from Spodosols and Spodosol-like soils in Canada’, *Geoderma*, 40(3), pp. 345–355. doi: https://doi.org/10.1016/0016-7061(87)90043-7.

Webmineral (2019) *Chemical Composition*. Available at: http://webmineral.com/chemical.shtml#.XwReFyhKg2w (Accessed: 13 October 2019).

Wen, Y.-L. *et al.* (2021) ‘Organic amendments stimulate co-precipitation of ferrihydrite and dissolved organic matter in soils’, *Geoderma*, 402, p. 115352. doi: https://doi.org/10.1016/j.geoderma.2021.115352.

White, A. F. (2003) ‘5.05 - Natural Weathering Rates of Silicate Minerals’, in Holland, H. D. and Turekian, K. K. B. T.-T. on G. (eds). Oxford: Pergamon, pp. 133–168. doi: https://doi.org/10.1016/B0-08-043751-6/05076-3.

White, A. F. and Hochella, M. F. (1992) ‘Surface chemistry associated with the cooling and subaerial weathering of recent basalt flows’, *Geochimica et*

Cosmochimica Acta, 56(10), pp. 3711–3721. doi: https://doi.org/10.1016/0016-7037(92)90164-E.

Wilson, D. J. *et al.* (2021) 'Seasonal variability in silicate weathering signatures recorded by Li isotopes in cave drip-waters', *Geochimica et Cosmochimica Acta*, 312, pp. 194–216. doi: https://doi.org/10.1016/j.gca.2021.07.006.

Wilson, M. (1989) *Igneous Petrogenesis*. Edited by M. Wilson. Dordrecht: Springer Netherlands. doi: 10.1007/978-1-4020-6788-4.

Woittiez, L. S. *et al.* (2018) 'Nutritional imbalance in smallholder oil palm plantations in Indonesia', *Nutrient Cycling in Agroecosystems*, 111(1), pp. 73–86. doi: 10.1007/s10705-018-9919-5.

Wolff-Boenisch, D. *et al.* (2004) 'The dissolution rates of natural glasses as a function of their composition at pH 4 and 10.6, and temperatures from 25 to 74°C', *Geochimica et Cosmochimica Acta*, 68(23), pp. 4843–4858. doi: https://doi.org/10.1016/j.gca.2004.05.027.

Wolff-Boenisch, D., Gislason, S. R. and Oelkers, E. H. (2006) 'The effect of crystallinity on dissolution rates and CO2 consumption capacity of silicates', *Geochimica et Cosmochimica Acta*, 70(4), pp. 858–870. doi: 10.1016/J.GCA.2005.10.016.

Xu, H. *et al.* (2019) 'Molecular weight-dependent adsorption fractionation of natural organic matter on ferrihydrite colloids in aquatic environment', *Chemical Engineering Journal*, 363, pp. 356–364. doi: https://doi.org/10.1016/j.cej.2019.01.154.

Zakaznova-Herzog, V. P. *et al.* (2008) 'Characterization of leached layers on olivine and pyroxenes using high-resolution XPS and density functional calculations', *Geochimica et Cosmochimica Acta*, 72(1), pp. 69–86. doi: https://doi.org/10.1016/j.gca.2007.09.031.

Zhu, C. *et al.* (2020) 'Decoupling feldspar dissolution and precipitation rates at near-equilibrium with Si isotope tracers: Implications for modeling silicate weathering', *Geochimica et Cosmochimica Acta*, 271, pp. 132–153. doi: https://doi.org/10.1016/j.gca.2019.12.024.

Appendices

APPENDIX A – supplementary information for Chapter 2

This appendix consists of the supplementary Information from Lewis *et al.* (2021).

Tables:

Table A1 – Initial pore water solution used in the RTM. Solution taken from Kelland *et al.* (2020)

Parameter	Value
pH	6.6
Al (µM L^{-1})	1.83
Ba (µM L^{-1})	5.47
Ca (µM L^{-1})	803.46
Fe (µM L^{-1})	4.83
K (µM L^{-1})	20.12
Li (µM L^{-1})	0.34
Mg (µM L^{-1})	61.36
Mn (µM L^{-1})	0.03
Na (µM L^{-1})	180.10
Si (µM L^{-1})	55.34
Sr (µM L^{-1})	0.98
Ti (µM L^{-1})	0.11
Zn (µM L^{-1})	2.31
F (µM L^{-1})	58.44
Cl (µM L^{-1})	163.45
NO_2^- (µM L^{-1})	12.61
SO_4^{2-} (µM L^{-1})	50.78
NO_3^- (µM L^{-1})	451.46
C (µM L^{-1})	1158.50

Table A2- Average mineral composition (normalised to standard oxygen and solid solution contents) for different phases as determined by SEM-EDS and concentration of mineral present in rock powder expressed as wt.% and determined by XRD. (This table has been split into 3 separate tables due to the size of the tables.

Mineral		Basalt					
Mineral Group	Mineral	Cragmill Formula	n	wt. %	Hillhouse Formula	n	wt. %
Feldspars/ feldspathoid	Plagioclase	$(Na_{0.47}Ca_{0.52})Al_{1.42}Si_{2.53}O_8$	25	47.3	$(Ca_{0.56}Na_{0.44})Al_{1.56}Si_{2.44}O_8$	46	34.6
	Sanidine	$(Na_{0.35}K_{0.65})Al_{0.98}Si_{3.02}O_8$	6	11.4			
	Orthoclase						
	Leucite						
Pyroxenes	Augite	$(Ca_{0.62}Na_{0.01}Fe_{0.37})(Mg_{0.93}Ti_{0.3}Fe_{0.4})(Al_{0.05}Si_{0.95})_2O_8$	14	16.3	$(Na_{0.02}Ca_{0.73}Fe_{0.25})(Mg_{0.83}Ti_{0.04}Fe_{0.02})(Al_{0.10}Si_{0.90})_2O_6$	23	32.7
	Diopside						
Ultramafic minerals	Forsterite				$Mg_{1.28}Fe_{0.72}SiO_4$	17	14.7
	Cordierite	$(Mg,Fe)_2Al_4Si_5O_{18}$[1]	--	0.4			
	Spinel				$(Mg_{0.23}Al_{0.57}Ti_{0.14})(Cr_{0.67}Fe_{1.44})O_4$	4	4.5
Metamorphic minerals	Ferro-actinolite						
	Epidote						
	Chlorite						
Quartz	Quartz	SiO_2 (Trace Sn)	8	6.9			
Glass	Basaltic glass	$Na_{0.08}Ca_{0.263}Mg_{0.281}Fe_{0.188}Al_{0.358}SiO_{3.32}$[2]	--	2.6			
Fe-oxides	Ilmenite	$(Fe_{0.47}Ti_{0.52}Mn_{0.1})O_3$	7	1.7	$(Fe_{1.42}Ti_{0.55}Mn_{0.03})O_3$ (Trace V)	9	0.6
	Magnetite						
Ti-Silicate	Titanite						
Zeolite	Analcime				$Na_{0.94}K_{0.02}Ca_{0.04}AlSi_2O_6$	7	7.1
	Epistilbite						
Mica	Phlogopite	$KMg_3(AlSi_3O_{10})(OH)_2$[1]	--	1.1			
	Biotite				$K(Mg,Fe)_3(AlSi_3O_{10})(OH)_2$[1]	--	0.4
Secondary Alteration	Chlorite-Smectite	$(Mg_{0.41}Fe_{0.55}Ca_{0.04})Al(Al_{0.26}Si_{3.74})O_{10}(OH)_8$	42	10.4	$(Mg_{0.52}Fe_{0.32}K_{0.03}Na_{0.27}Ca_{0.1})Al(Si_{3.58}Al_{0.42})O_{10}(OH)_8$	52	5.2
	Mont-morillonite						
Phosphates	Apatite	$Ca_5(PO_4)_3(F,Cl,OH)$	11	0.8	$Ca_5(PO_4)_3(F,Cl,OH)$	6	0.1
Carbonates	Calcite	$CaCO_3$[1]	--	1.3	$CaCO_3$[1]	--	0.2

[1]Not identified through SEM-EDS but measured through XRD.

[2]Formula provided from Oelkers and Gislason (2001)

Mineral		Basalt					
Mineral Group	Mineral	Oregon Formula	n	wt. %	Tichum Formula	n	wt.%
Feldspars/ feldspathoid	Plagioclase	$(Ca_{0.39}Na_{0.56}K_{0.06})Al_{1.3}Si_{2.6}O_8$	15	35.1	$(Ca_{0.35}Na_{0.50}K_{0.14})Al_{1.37}Si_{2.62}O_8$	6	10.9
	Sanidine	$(K_{0.41}Na_{0.56}Ca_{0.03})Al_{1.03}Si_{2.97}O_8$	3	23.0			
	Orthoclase				$(Na_{0.35}K_{0.65})Al_{0.98}Si_{3.02}O_8$[1]	- -	2.4
	Leucite				$(Na_{0.45}K_{0.42}Ca_{0.03})(Al_{0.9}Si_{2.06})O_6$	3	13.4
Pyroxenes	Augite				$(Ca_{0.041}Na_{0.951})(Mg_{0.325}Fe_{0.139}Al_{0.473}Ti_{0.083})(Al_{0.275}Si_{1.75})O_6$	14	42.3
	Diopside	$CaMg_{0.7}Al_{0.6}Si_{1.7}O_6$	14	10.6			
Ultramafic minerals	Olivine	$Fe_{0.96}Mg_{1.04}SiO_4$	14	1.0	$(Mg_{1.27}Fe_{0.69}Ca_{0.02}Mn_{0.01})SiO_4$	6	19.4
	Cordierite						
	Spinel						
Metamorphic minerals	Ferro-actinolite						
	Epidote						
	Chlorite						
Quartz	Quartz	SiO_2[1]	--	0.4			
Glass	Basaltic glass	$Na_{0.13}Ca_{0.08}Mg_{0.05}K_{0.10}Fe_{0.12}Al_{0.26}SiO_{2.86}$	13	24.9	$Mg_{0.05}Ca_{0.02}Fe_{0.05}Al_{0.67}SiO_{3.14}$	2	2.6
Fe-oxides	Ilmenite	$Fe_{1.4}Ti_{0.6}O_3$	2	0.6	$Fe_{0.43}Ti_{1.57}O_3$	7	1.9
	Magnetite						
Ti-Silicate	Titanite						
Zeolite	Analcime				$(K_{0.071}Na_{0.929})AlSi_2O_6 \cdot H_2O$	9	5.8
	Epistilbite						
Mica	Phlogopite						
	Biotite						
Secondary Alteration	Chlorite-Smectite						
	Mont-morillonite	$(Na,Ca)_{0.33}(Al,Mg)_2(Si_4O_{10})(OH)_2 \cdot nH_2O$[1]	--	1.2 %			
Phosphates	Apatite	$Ca_5(PO_4)_3(F,Cl,OH)$	3	2.8 %	$Ca_5(PO_4)_3(F,Cl,OH)$	3	2.0%
Carbonates	Calcite						

[1]Not identified through SEM-EDS but measured through XRD.

[2]Formula provided from Oelkers and Gislason (2001)

Mineral							
Mineral Group	Mineral	Tawau Formula	n	wt. %	Blueridge Formula	n	wt. %
Feldspars/ feldspathoid	Plagioclase	$(Ca_{0.64}Na_{0.36})Al_{1.62}Si_{2.38}O_8$	7	44.6	$NaAlSi_3O_8$	9	19.6
	Sanidine	$(K_{0.59}Na_{0.41})Al_{1.03}Si_{2.97}O_8$	4	13.3			
	Orthoclase						
	Leucite						
Pyroxenes	Augite						
	Diopside	$(Ca_{0.86}Fe_{0.14})(Mg_{0.82}Ti_{0.02}Fe_{0.11}Al_{0.06})(Si_{1.84}Al_{0.16})O_6$	4	12.4			
Ultramafic minerals	Olivine						
	Cordierite						
	Spinel						
Metamorphic minerals	Ferro-actinolite				$Ca_2(Mg_{0.75}Fe_{0.25})_5Si_{8.5}O_{22}(OH)_2$	7	11.6
	Epidote				$Ca_2(Al_{2.53}Fe_{1.09})SiO_4(SiO_7)O(OH)$	12	25.6
	Chlorite				$(Mg_{0.63}Fe_{0.37})_5Al(Si_3Al_{1.2})O_{10}(OH)_8$	5	36.3
Quartz	Quartz	SiO_2	4	19.1	SiO_2	2	5.2
Glass	Basaltic glass						
Fe-oxides	Ilmenite						
	Magnetite	Fe_3O_4 (trace V, Ti)	5	2.0			
Ti-Silicate	Titanite				$CaTiSiO_5$	8	1.7
Zeolite	Analcime						
	Epistilbite	$CaAl_2Si_6O_{16}·5H_2O$	- -	1.0			
Mica	Phlogopite						
	Biotite	$K(Mg,Fe)_3(AlSi_3O_{10})(OH)_2$	- -	0.6			
Secondary Alteration	Chlorite-Smectite						
	Mont-morillonite	$Ca_{0.3}(Mg_{1.74}Fe_{1.25})_3(Al_{0.9}Si_{3.1})_4O_{10}(OH)_2·4H_2O$	1 1	5.8			
Phosphates	Apatite	$Ca_5(PO_4)_3(F,Cl,OH)$	1	0.4			
Carbonates	Calcite	$CaCO_3$[1]	- -	0.8			

[1]Not identified through SEM-EDS but measured through XRD.

[2]Formula provided from Oelkers and Gislason (2001)

Table A3 – P_2O_5 and K_2O fertiliser application for tillage crops in the UK. Fertiliser data from DEFRA (2020) (Table GB1.1), using Average Application Rates.

Crop	P_2O_5, kg ha^{-1}	P, kg ha^{-1}	K_2O, kg ha^{-1}	K, kg ha^{-1}
Spring Wheat	34	14.9	44	36.4
Winter Wheat	57	24.9	67	55.4
Spring Barley	48	21.0	61	50.4
Winter Barley	53	23.1	68	56.2
Oats	48	21.0	68	56.2
Rye	41	17.9	72	59.5
Sugar Beet	47	20.5	88	72.7
Winter Oil Seed Rape	57	24.9	61	50.4
Linseed	56	24.5	58	47.9
Forage Maize	56	24.5	70	57.9
Root Crops for Feedstock	60	26.2	75	62.0

Table A4 – Estimated mass of P_2O_5 reserves found from eight major Large Igneous Provinces. Volume and Area data taken from Ross et al (2005) and Taylor et al (2015) (Supplementary Table S9). P_2O_5 data taken from the GEOROC database (Sarbas, 2008).

Locality	**Area, $x10^6$ km^2**	**Volume, $x10^6$ km^2**	**Mass, tonnes**	**P_2O_5, %**	**Count, P_2O_5 analyses**	**Estimated P_2O_5, tonnes**
Central Atlantic Magmatic Province - CAMP	11	2.5	2.5E+15	0.25	68	6.25E+12
Deccan Traps	0.8	1.5	1.5E+15	0.26	214	3.84E+12
Emeishan Traps	0.25	0.25	2.5E+14	0.36	68	8.99E+11
Ethiopian Plateau	0.6	0.35	3.5E+14	0.46	57	1.60E+12
Karoo And Ferrar Provinces	2.15	0.3	3E+14	0.22	162	6.64E+11
North Atlantic Igneous Province (NAIP)	1.3	6.6	6.6E+15	0.22	177	1.43E+13
Siberian Traps[a]	1.5,3.9	1.1	1.1E+15	0.38	58	4.21E+12
Yemen Plateau	0.6	0.35	3.5E+14	0.45	3	1.55E+12
TOTAL	**16.7**	**12.95**	**1.3E+16**	**--**	**807**	**3.3E+13**

[a]Taken from Ross *et al.* (2005)

Supplementary Information – Figures:

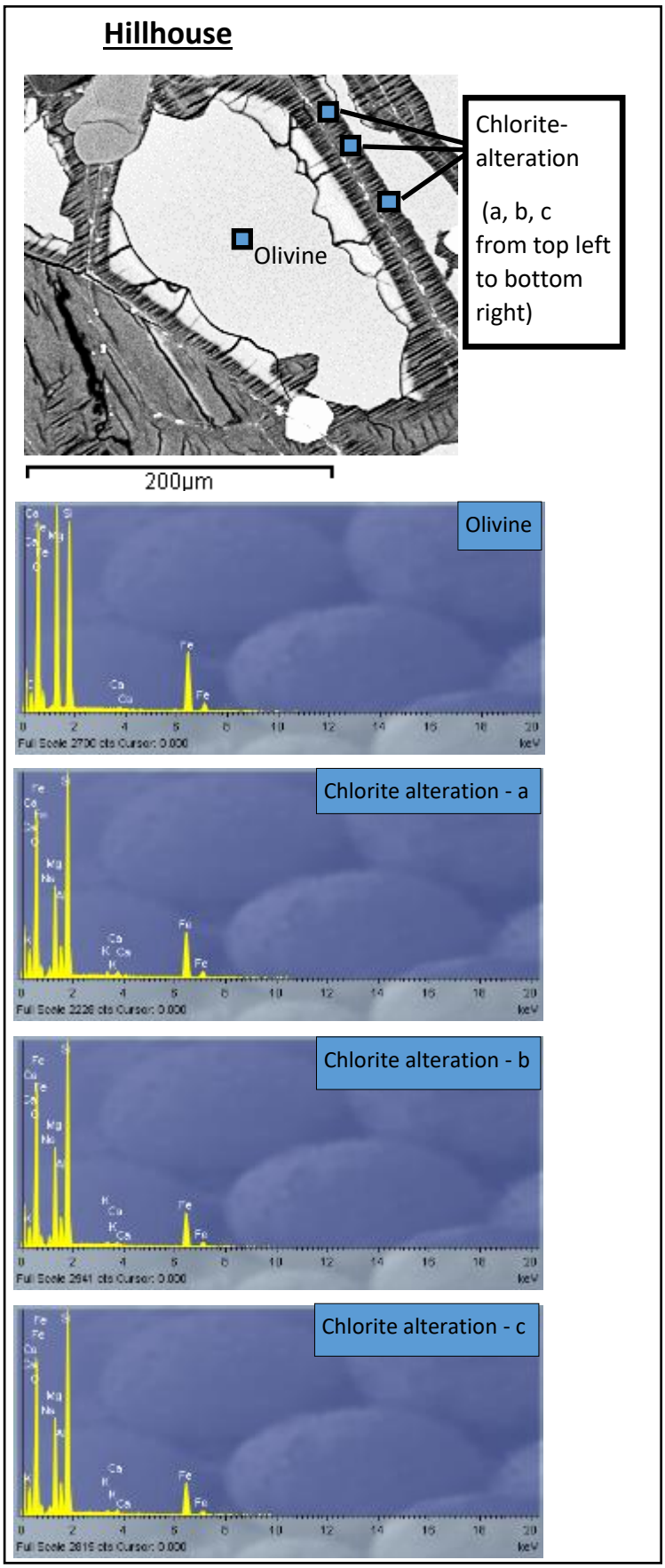

Figure A1 - SEM backscattered electron image of altered olivine in the Hillhouse basalt, showing locations of points where SEM-EDS spectra were taken (top left) with respective spectra in image.

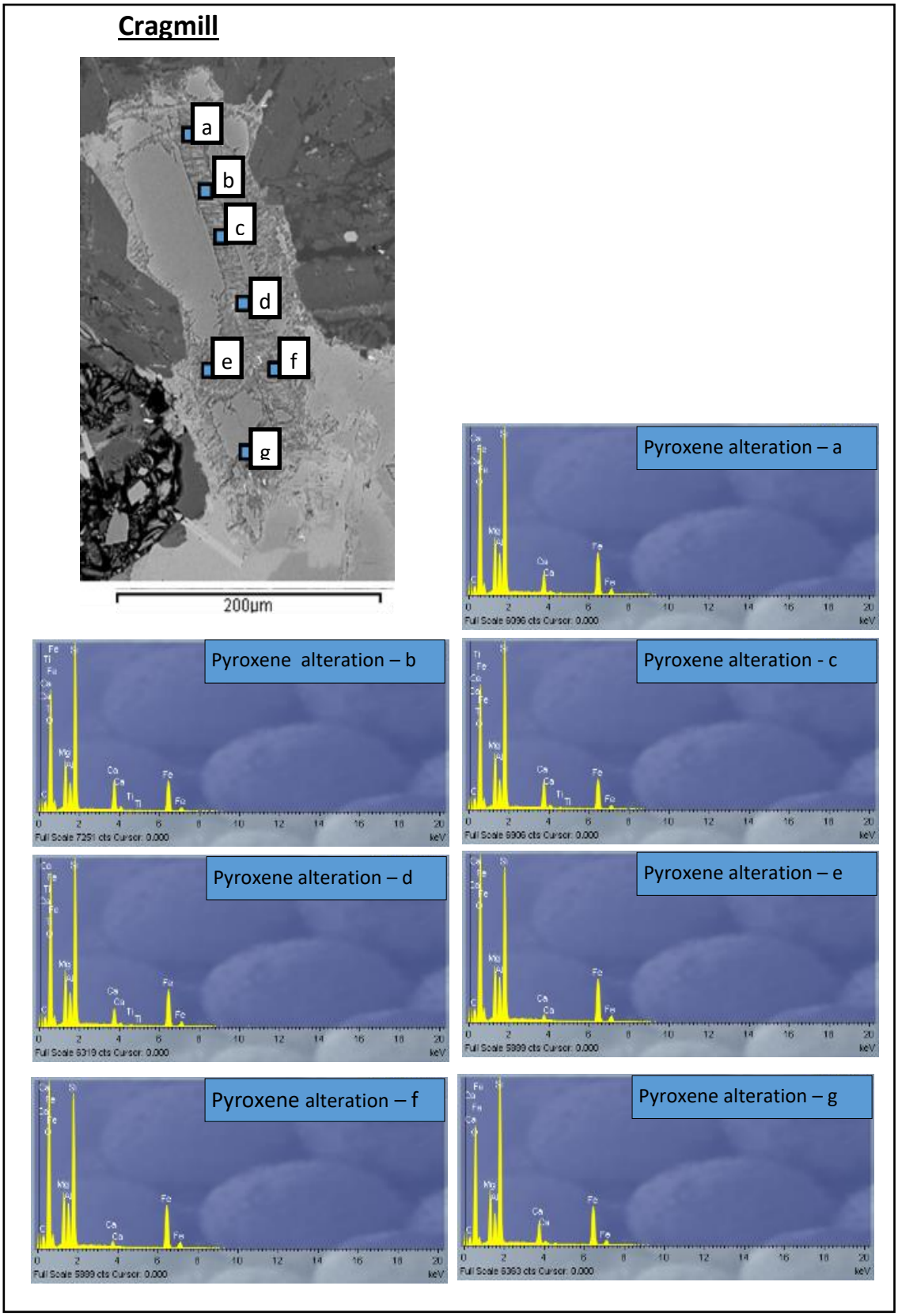

Figure A2- SEM backscattered electron image of altered pyroxene in the Cragmill basalt showing locations of points where SEM-EDS spectra were taken (top left) with respective spectra in image.

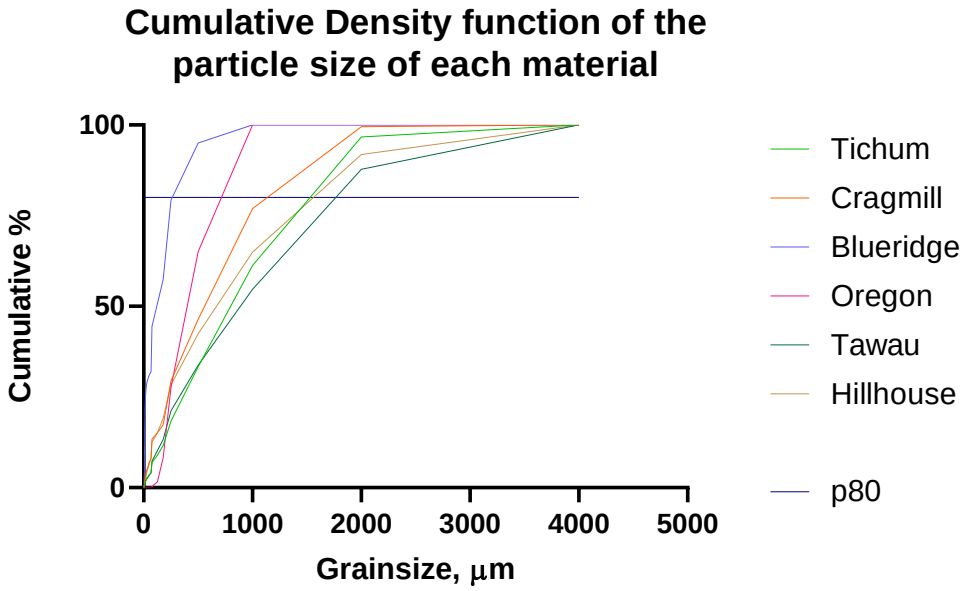

Figure A3 – Cumulative particle size distributions for each of the basalts used in this study.

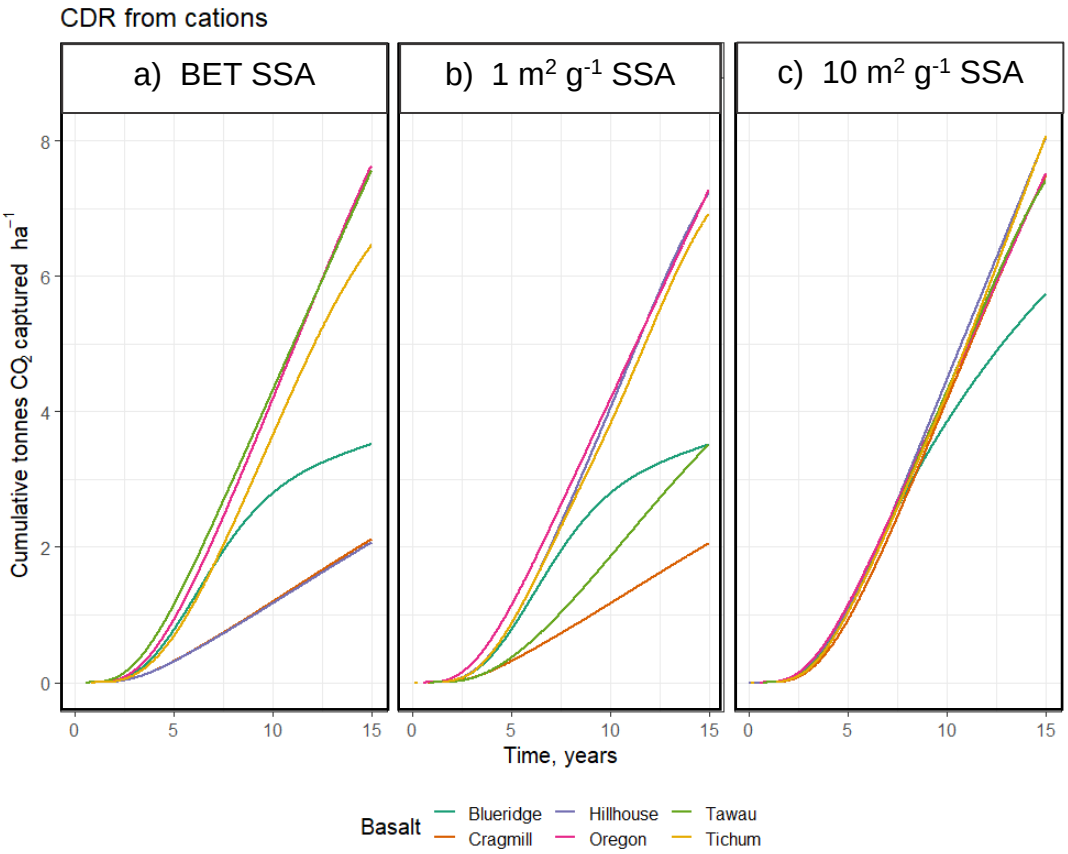

Figure A4 – Cumulative carbon dioxide removal (CDR) after weathering each material using gibbsite as a sink for Al over a fifteen-year period under (a) measured specific surface area (SSA) (from BET analyses), (b) a standardised SSA of 1 m^2 g^{-1} and (c) a standardised SSA of 10 m^2 g^{-1}.

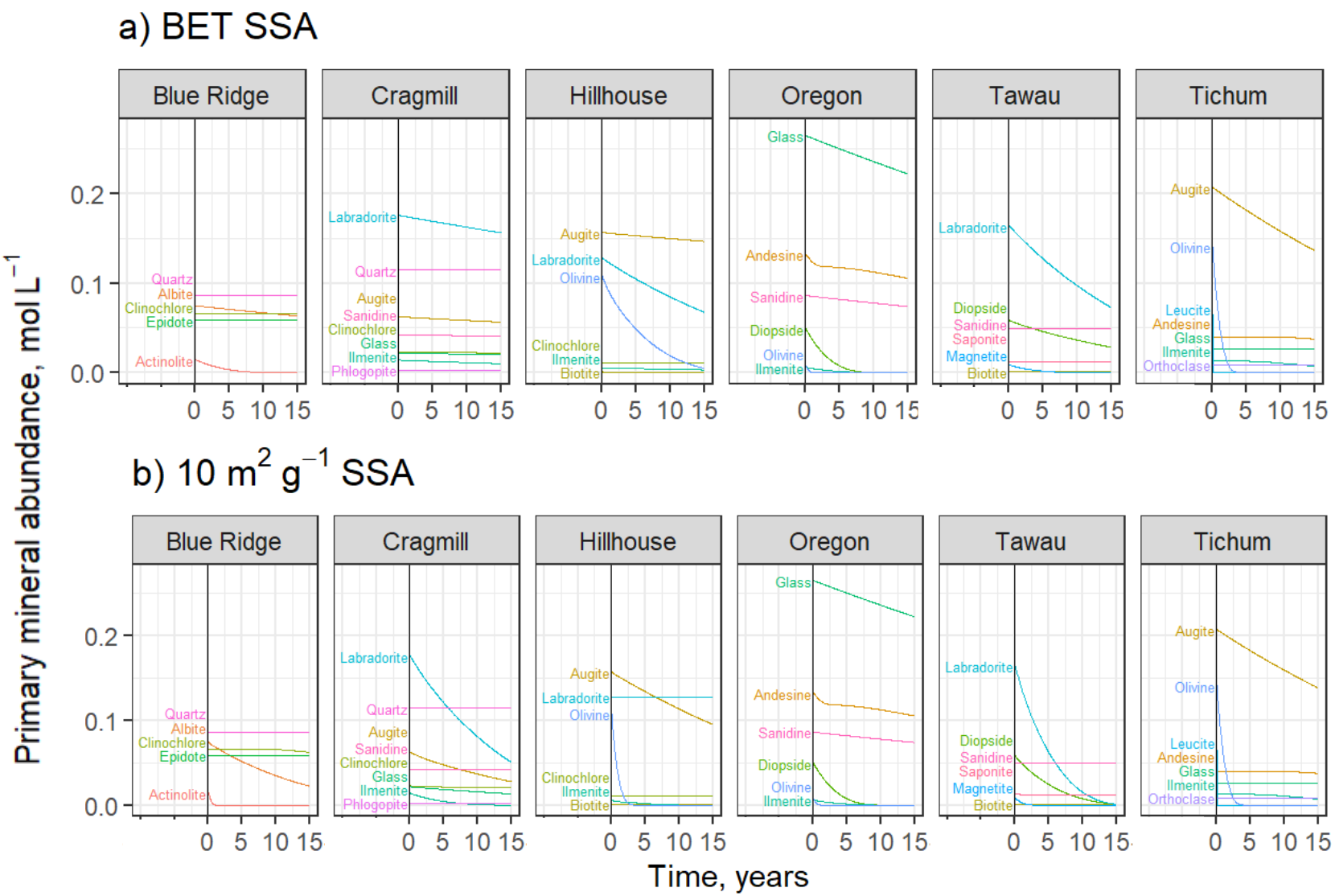
a) BET SSA
b) 10 m^2 g^{-1} SSA
Blue Ridge
Cragmill
Hillhouse
Oregon
Tawau
Tichum
Primary mineral abundance, mol L^{-1}
Time, years
0.0
0.1
0.2
0 5 10 15
Quartz
Albite
Clinochlore
Epidote
Actinolite
Labradorite
Augite
Sanidine
Glass
Ilmenite
Phlogopite
Olivine
Biotite
Andesine
Diopside
Saponite
Magnetite
Leucite
Orthoclase

← (over page) Figure A5 – Modelled mineral concentration of the basalts over time using the (a) measured BET specific surface area (SSA) regime and (b) 10 m^2g^{-1} SSA. The y axis shows the moles of each mineral phase per unit volume of reacting solution in the soil cells containing basalt with the initial value calculated from XRD analysis. These models use gibbsite as the Al-sink.

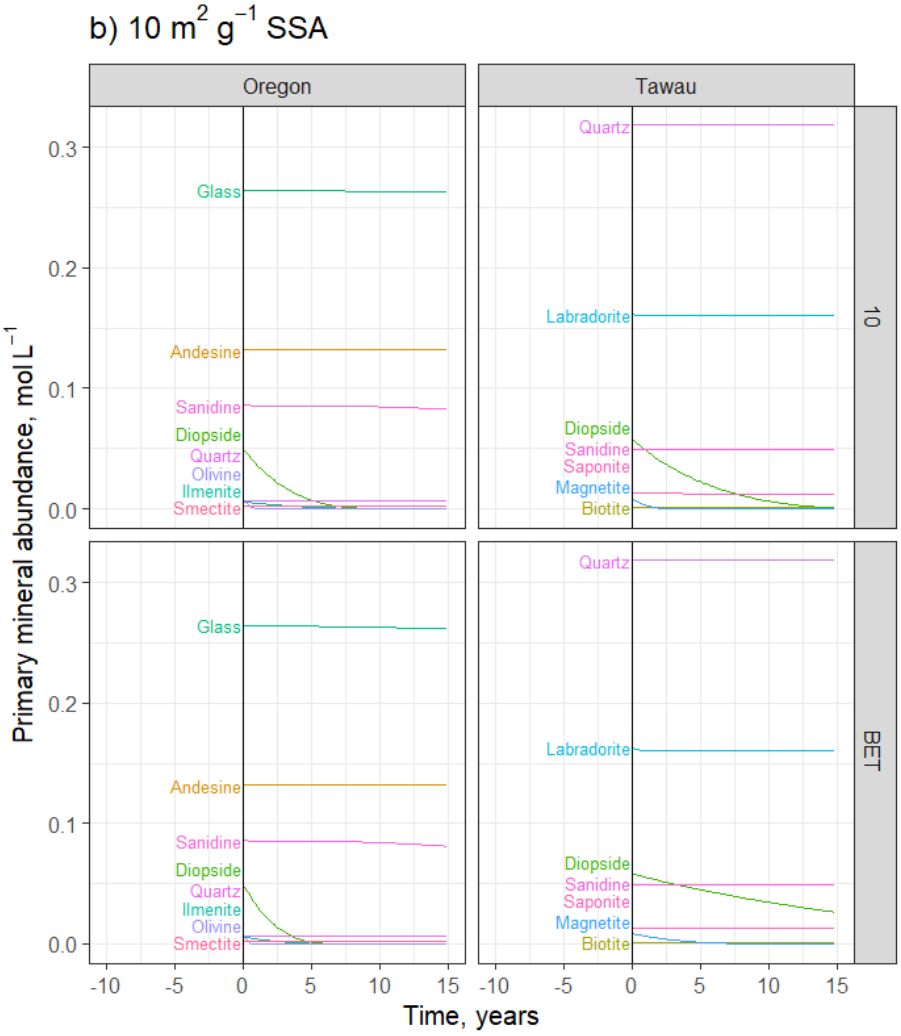

Figure A6 - Modelled mineral concentration of the Oregon and Tawau basalt over time using the BET specific surface area (SSA) regime (a) and the 10 m^2g^{-1} SSA regime (b), shown in concentration of mineral phases in the Oregon basalt in solution. Mineral concentration is shown as the concentration of each mineral phase in contact with the reacting solution in the cells containing basalt, with the initial concentration calculated from XRD analyses.

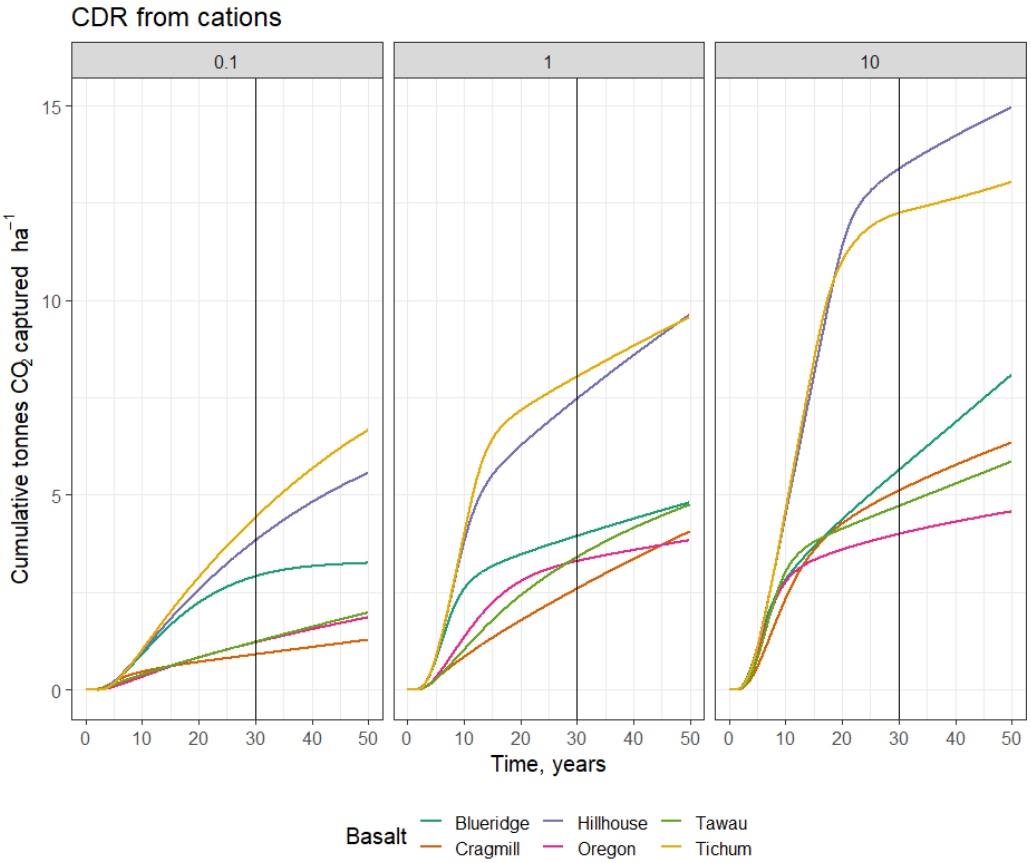

Figure A7 - Results from 50-year Reactive Transport Model (RTM) simulations at each specific surface area (0.1, 1 and 10 m^2 g^{-1}) used in regression studies. Solid black line is drawn at 30 years, at which point data for the regression (Figure A8, Eq. 2.4) were derived.

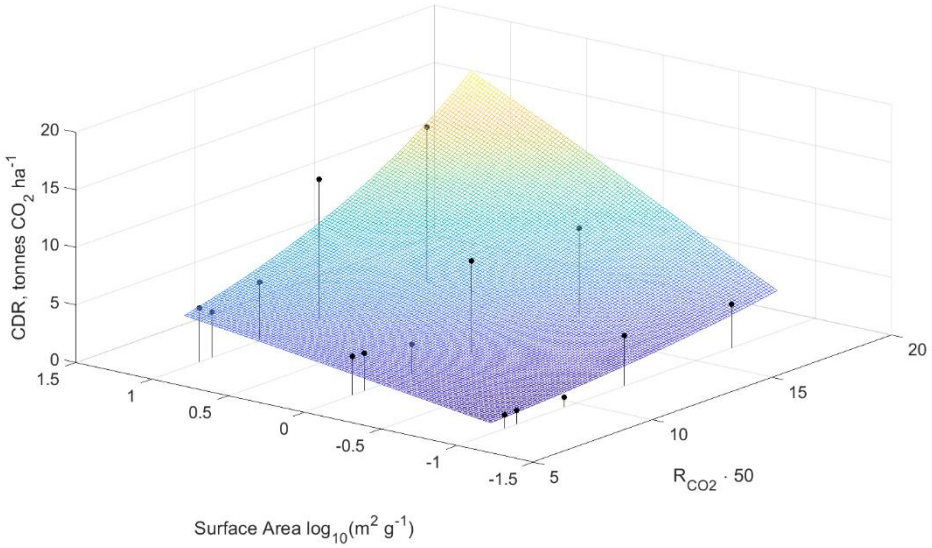

Figure A8 - Surface showing the fit of the basaltic rock powder after 30 years of weathering as a function of a range of specific surface areas (SSA, from 0.01 m^2g^{-1} to 10 m^2g^{-1}) and R_{CO_2}, in accordance with Eq. 2.4: $\text{CDR potential} = \exp(4.4 + 0.7 \cdot log_{10}(SSA) - \frac{9.5}{\sqrt{R_{CO_2} \cdot 50}})$ Equation from this fitting was used to scale up the cumulative CDR potential of basalt from Large Igneous Provinces after 30 years (Figure 2.8).

APPENDIX B – TidyPhreeqc code used to generate SI and activities graphs.

IMPORTANT NOTE - to make this code work, you will need to ensure that the start of every line which is only an explanation is 'commented' by placing a '#' in front of that line, if one is not already there.

This code was slightly modified from the example provided in Dunning (2021). Further details of how to run this code can be found at https://dewey.dunnington.ca/post/2018/pourbaix-ish-diagrams-using-phreeqc-and-r/

Information on the code, in case it is of interest to further update the model, can be found at: https://github.com/paleolimbot/tidyphreeqc

The purpose of this code was to investigate any changes to the saturation indices (SI)of important secondary phases that might be expected to precipitate following basalt amendment and the activities of Fe and Al species in aqueous solution at a range of pH values. In this thesis, solutions with differing elemental compositions before and after weathering were inputted into the model to test if basalt weathering in a flask dissolution experiment and from soil porewater solutions had the potential to precipitate.

This appendix provides the code that was used to generate Figures: 3.18, 3.19, 3.20, 4.7 and 5.7

########## THE CODE

Firstly, import the relevant packages. You may need to install these if you haven't already installed them. The first library is used for viewing and 'manipulating' data into suitable formats and for generating the final plots.

```
library(tidyverse)
```

The second package is the package for implementing PHREEQC in the R language and has been used to complete the calculations required to generate the predominance diagrams.

The set of code installs the relevant package

```
# install.packages("devtools") ### you may need to install 'devtools' which aids package development, including allowing you to install custom-made packages from GitHub

#devtools::install_github("paleolimbot/tidyphreeqc") ### this line of code installs the package that Dunning (2021) made which allows PHREEQC to be implemented in R
```

Note: after installing these two packages, you can ‘comment’ with a # at the start to avoid reinstalling the packages again.

Once these packages are installed, you can then load the 'tidyphreeqc' library.

```
library(tidyphreeqc)
```

The use of the Amm_T-H.dat database was chosen for: (1) corroboration with the Reactive Transport Model used in Chapter 2 and (2) for its ability to model the activity of dissolved organic carbon as humate and fulvate species.

The following two lines of code allow you to load and change the database.

my_custom_db <- readLines("C:\\PHREEQC\\database\\Amm_T-H.DAT") ### THIS FILE PATH MAY NEED UPDATING TO YOUR OWN DATABASE LINK

phr_use_db(my_custom_db)

Mn(OH)2(am) was added from the LLNL.DAT database and was appended onto the Amm_T-H.dat database.

If you need to append the Mn(OH)2(am) to a database, you can do by adding this lines of code to your database file:

##Mn(OH)2 +2.0000 H+ = + 1.0000 Mn++ + 2.0000 H2O

##log_k 15.3102

##delta_h -23.210553 kcal

NOTE: LLNL documents -97.1779 kJ/mole, then converted to -23.210553 kcal/mole, for consistence within the Amm_T-H.dat database.

Next, it is time to load the data. This is the dissolution data provided by Dr B Sarkar that was used in Chapter 3 for generating figures 3.18, 3.19 and 3.20.

The data in this table corresponds to Table 3.4. NOTE - FILEPATH WILL NEED UPDATING

Data <-
read.csv("C:\\Users\\amy\\Downloads\\BinoyDissolutionData_Oct2021.csv") ## this loads the data

glimpse(Data) ## this function allows you to take a look at the layout of the data.

in this file, there are two solution chemistries, on two different rows.

#####

This segment of code generates SI diagrams, as a function of pH.

To generate the SI diagrams, it is nessecary to select each solution individually.

i = 1 # this selects the initial compost extract, from row 1. The solution after 1 week of weathering can be selected by defining i as 2 (e.g. i = 2)

The next part of the code determines the saturation indices of a variety of minerals at measured solution parameters, as a function of pH.

Each component of the 'Data' are selected by choosing the Dataframe (Data), the columns are selected by the column name placed after the $ (e.g. Data$Al selects the column containing Al from the Data dataframe) and the row is selected by referencing [x] (e.g. $Al[i] selects the relevant row from the Al column)

The units are also defined within this piece of code. You can change the units according to 'SOLUTION' in the PHREEQC manual.

```
Binoy.Initial <- phr_run(
 phr_solution_list(pe = 4,
                   units = 'mg/L',
                   Al =       Data$Al[i],
                   Ba =       Data$Ba[i],
                   Ca =       Data$Ca[i],
                   Fe =       Data$Fe[i],
                   K  =       Data$K[i],
                   Li =       Data$Li[i],
                   Mg = Data$Mg[i],
                   Mn = Data$Mn[i],
                   Na =       Data$Na[i],
                   Si =       Data$Si[i],
                   Sr =       Data$Sr[i],
                  # Ti=       Data$Ti.Semi.quant[i], ### Ti was not included in this simulation due to the semi-quantitative nature of its analysis. It was also not considered an important element.
                   Zn =       Data$Zn[i],
                   S  =       Data$S[i],
                   C  =       Data$TIC[i],
                   Humate = Data$TOC[i], ### Total Organic Carbon was added as humate. Results did not differ greatly when fulvate was used to represent TOC.
                   Cu =       Data$Cu[i],
                   Ni =       Data$Ni[i],
                   V  =       Data$V[i],
                   B  =       Data$B[i],
                   P  = Data$P[i],
                   temp = 21, ## Temperature was set to 21 as this was the temperature that the flask experiment was exposed to.  This can be modified.
                   pH = seq(5, 9, by = 0.1)), ## pH was set as a range, so that the SI as a function of pH could be determined. pH 5 - 9 was chosen as the range because this was the expected minimum and maximum range for the flask dissolution experiment.
  phr_selected_output( ### This line of code selects the relevant minerals to export to the selected output file.
    saturation_indices = c(
      "Calcite",
      "SiO2(a)",
      "Al(OH)3(a)",
      "Fe(OH)3(a)",
      "Kaolinite",
      "Mn(OH)2(am)"
    ),
    temp = TRUE)) %>%
### The following code organises the selected output into a tibble which is then used to generate the plot.
  as_tibble() %>%
```

```
  select(pH, temp = `temp(C)`, starts_with("si_")) %>%
  gather(key = "species", value = "saturation_index", -pH, -temp)

### The next part of the code generates the plot of SI as a function of pH
ggplot(Binoy.Initial, aes(pH, saturation_index, col = species)) + ## This line selects the relevant data needed to generate the graphs. aes is defined as aes('x-axis', 'y-axis', col = 'variable to be coloured')
  ggtitle('(a) SI of initial compost extract') + # write a title.
  geom_line(size =0.75) + theme_bw(base_size = 20) + ylab('SI') +
  geom_vline(xintercept =  Data$pH[1]) + ### This line adds the pH of the solution in question to a graph.
  ### This block of code is used to label the pH line.
  geom_text(label="pH",
            x=Data$pH[1]+0.05,
            y=0.5,
            label.padding = unit(0.55, "lines"), # Rectangle size around label
            label.size = 0.75, angle= 90, color = 'black') +
  geom_hline(yintercept = 0) + ## This creates a y = 0 line, to aid readability of the graph.
  ylim(-15,2) + ## This defines the graphs limit
  scale_color_brewer(palette = "Dark2") ## selects a more readable colour scheme.

### The graph can then be saved. There may be some editing to do in an image software to neaten up the legend, as was done in this thesis to improve readability.

#####
#### This segment of code was used to determine the activity of relevant Fe species:
## Much of this code has the same explanation as the previous block of code.

i = 1 ### reference the initial compost extract, as in previous example
Binoy.Initial <- phr_run(
  phr_solution_list(pe = 4,
                    units = 'mg/L',
                    Al=       Data$Al[i],
                    Ba=       Data$Ba[i],
                    Ca=       Data$Ca[i],
                    Fe=       Data$Fe[i],
                    K=        Data$K[i],
                    Li=       Data$Li[i],
                    Mg=       Data$Mg[i],
                    Mn=       Data$Mn[i],
                    Na=       Data$Na[i],
                    Si=       Data$Si[i],
                    Sr=       Data$Sr[i],
                    # Ti=     Data$Ti.Semi.quant[i],
                    Zn=       Data$Zn[i],
                    S =       Data$S[i],
```

```
                C =         Data$TIC[i],
                Humate = Data$TOC[i],
                Cu=         Data$Cu[i],
                Ni=         Data$Ni[i],
                V=          Data$V[i],
                B=          Data$B[i],
                P = Data$P[i],
                temp = 21,
                pH = seq(5, 9, by = 0.1)),
  phr_selected_output(
    activities = c("Fe(OH)2+",
                "Fe(OH)3",
                "Fe(OH)4-",
                "FeOH+2",
                "FeSO4+",
                "FeHSO4+",
                'FeHumate'),
    temp = TRUE)) %>%
  as_tibble() %>%
  select(pH, temp = `temp(C)`, starts_with("la_")) %>%
  gather(key = "species", value = "activity", -pH, -temp)
ggplot(Binoy.Initial, aes(pH, activity, col = species)) +
  geom_line(size = 1) + theme_bw(base_size = 20) + ylab('log(Activity)') +
ylim(-20,0) +
  geom_vline(xintercept =  Data$pH[1]) +
  ggtitle('(a) Fe activities of compost extract') +
  geom_text(label=" solution pH",
          x=Data$pH[1]+0.05,
          y=-4,
          label.padding = unit(0.55, "lines"), # Rectangle size around label
          label.size = 0.75, angle= 90, color = 'black') +
  scale_color_brewer(palette = "Dark2")

#####
#### This segment of code was used to determine the activity of relevant Al
species:
## Much of this code has the same explanation as the previous block of code.
i = 1

Binoy.Initial <- phr_run(
  phr_solution_list(pe = 4,
                units = 'mg/L',
                Al=         Data$Al[i], # Al that is thought to be released per moles of
Si - then divided by 2.
                Ba=         Data$Ba[i],
                Ca=         Data$Ca[i],
                Fe=         Data$Fe[i],
                K=          Data$K[i],
                Li=         Data$Li[i],
                Mg=         Data$Mg[i],
```

```
                Mn=       Data$Mn[i],
                Na=       Data$Na[i],
                Si=       Data$Si[i],
                Sr=       Data$Sr[i],
                # Ti=     Data$Ti.Semi.quant[i],
                Zn=       Data$Zn[i],
                S =       Data$S[i],
                C =       Data$TIC[i],
                Humate = Data$TOC[i],
                Cu=       Data$Cu[i],
                Ni=       Data$Ni[i],
                V=        Data$V[i],
                B=        Data$B[i],
                temp = 21,
                pH = seq(5, 9, by = 0.1)),
  phr_selected_output(
    activities = c("Al(OH)3",
                   "Al(OH)4-",
                   "AlOH+2",
                   "Al+3",
                   "AlSO4+",
                   "Al(SO4)2-",
                   "AlHSO4+2"),
    temp = TRUE)) %>%
  as_tibble() %>%
  select(pH, temp = `temp(C)`, starts_with("la_")) %>%
  gather(key = "species", value = "log_activity", -pH, -temp) %>%
  mutate(activity =  log_activity)

ggplot(Binoy.Initial, aes(pH, activity, col = species, lty = factor(temp))) +
  geom_line(size = 1) + theme_bw(base_size = 20) + ylab('log(Activity)') +
ylim(-20,0) +
  geom_vline(xintercept =  Data$pH[1]) +
  ggtitle('(a) Al activities of initial compost extract') +
  geom_text(label="solution pH",
            x=Data$pH[1]+0.05,
            y=-4,
            label.padding = unit(0.55, "lines"), # Rectangle size around label
            label.size = 0.75, angle= 90, color = 'black') +
  scale_color_brewer(palette = "Dark2")
```

APPENDIX C – Additional corrections applied to concentration data to account for low-yielding soil amendments in bulk soil analyses

This Appendix compares the original values ($Conc_e$) taken from the sequential chemical extractions and the values which corrected for the addition of low-yielding results ($Conc_{corr}$) using Eq. 4.3:

$$Conc_{corr} = (Conc_e \cdot \%_{b,m,b+m}) + Conc_e \text{ (Eq. 4.3)}$$

Where the $Conc_{corr}$ is the corrected concentration, $Conc_e$ is the extracted mass of element from a chemical extraction (in mg element g soil^{-1}), $\%_{b,m,b+m}$ is the proportion of basalt (b), manure (m) or basalt and manure (b+m) added to the soil.

Table C1 - The following table illustrates the mean values for Al, Fe, Mn and OC for the basalt grains compared with the mean values of these elements for the soils analysed in Chapter 4.

		Bulk soil	Initial basalt	Bulk soil	Initial basalt	Bulk soil	Initial basalt	Bulk soil	Initial basalt
Extractant	Treatment	Fe, mg Fe g soil^{-1}	Fe, mg Fe g basalt^{-1}	Al, mg Al g soil^{-1}	Al, mg Al g basalt^{-1}	OC, mg OC g soil^{-1}	OC, mg OC g basalt^{-1}	Mn, mg Mn g soil^{-1}	Mn, mg Mn g basalt^{-1}
Hydroxylamine hydrochloride	Manure	4.16	1.97	1.57	0.35	2.13	0.06	0.10	0.002
	Manure + basalt	4.43		2.10		2.19		0.11	
	NPK	4.02		2.15		1.83		0.08	
	NPK + basalt	4.23		1.76		1.81		0.12	
Na-dithionite	Manure	Na	0.811	Na	0.08	Na	Na	0.04	0.0007
	Manure + basalt	Na		Na		Na		0.04	
	NPK	Na		Na		Na		0.04	
	NPK + basalt	Na		Na		Na		0.04	
Na-pyrophosphate	Manure	1.32	0.13	0.42	0.09	4.40	0.29	0.14	0.0006
	Manure + basalt	1.27		0.44		3.90		0.15	
	NPK	1.30		0.45		4.00		0.14	
	NPK + basalt	1.39		0.45		4.04		0.13	
UHP	Manure	0.03	0.004	0.01	0.0003	0.87	0.35	0.002	2.17E-06
	Manure + basalt	0.02		0.01		1.04		0.003	
	NPK	0.02		0.01		0.95		0.004	
	NPK + basalt	0.02		0.01		0.83		0.003	

On the following graphs, letters are used to differentiate significant differences ($p < 0.05$) between the two treatments (i.e. fertiliser only or Basalt-amended) within each fertiliser regime (NPK or Manure), as results from computed one-way ANOVAs. a and b are significantly different; a and a are not significantly different). 'na' is used to state that statistical analysis was considered invalid because of negative values. The red boxes around the different components of the graph represent results which have changed in significance, noted by a change of lettering.

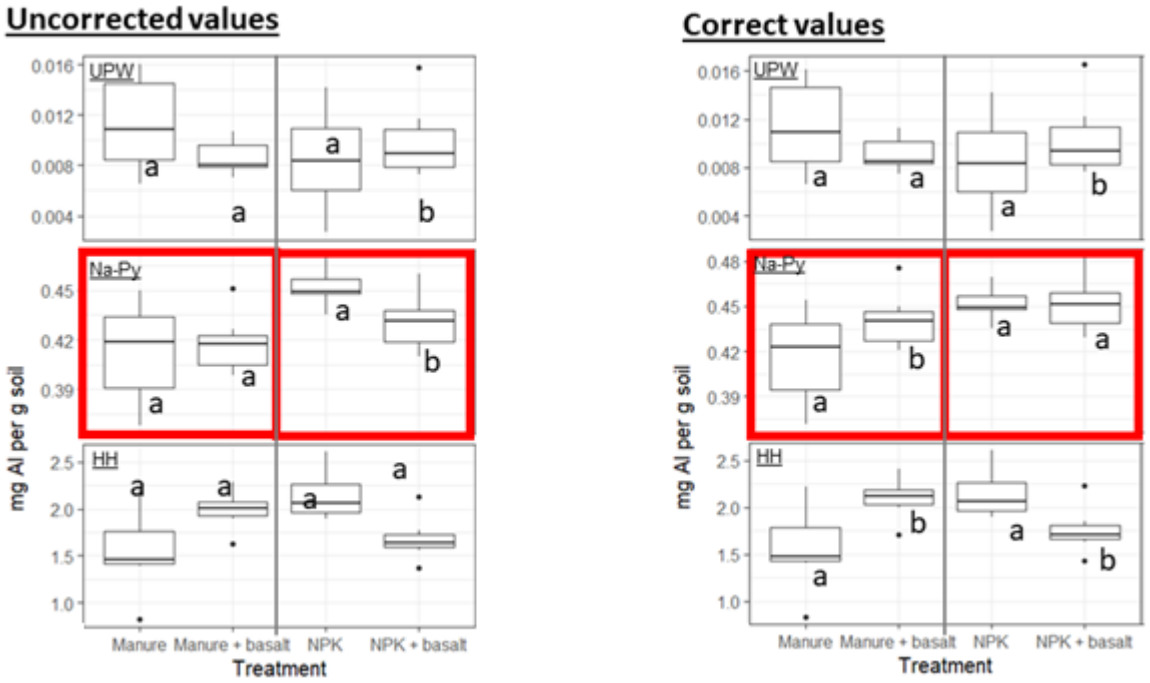

Figure C1 - Differences between uncorrected and corrected values for extractable-Al.

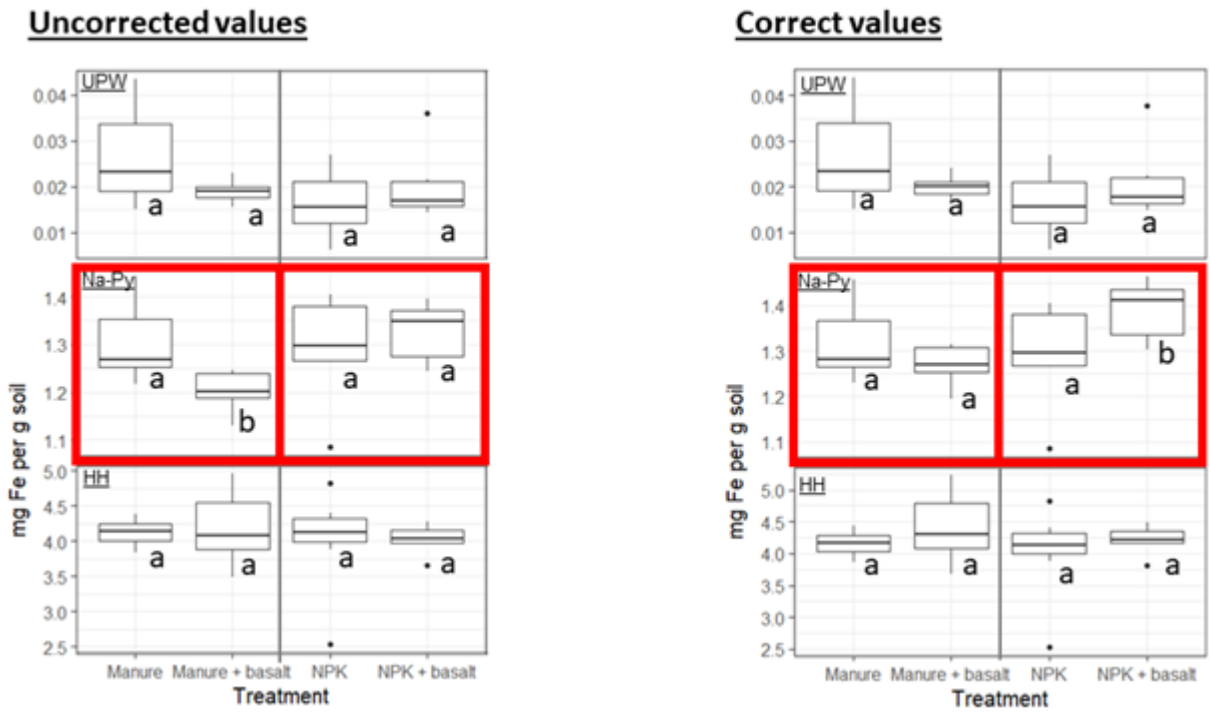

Figure C2 - Differences between uncorrected and corrected values for extractable-Fe.

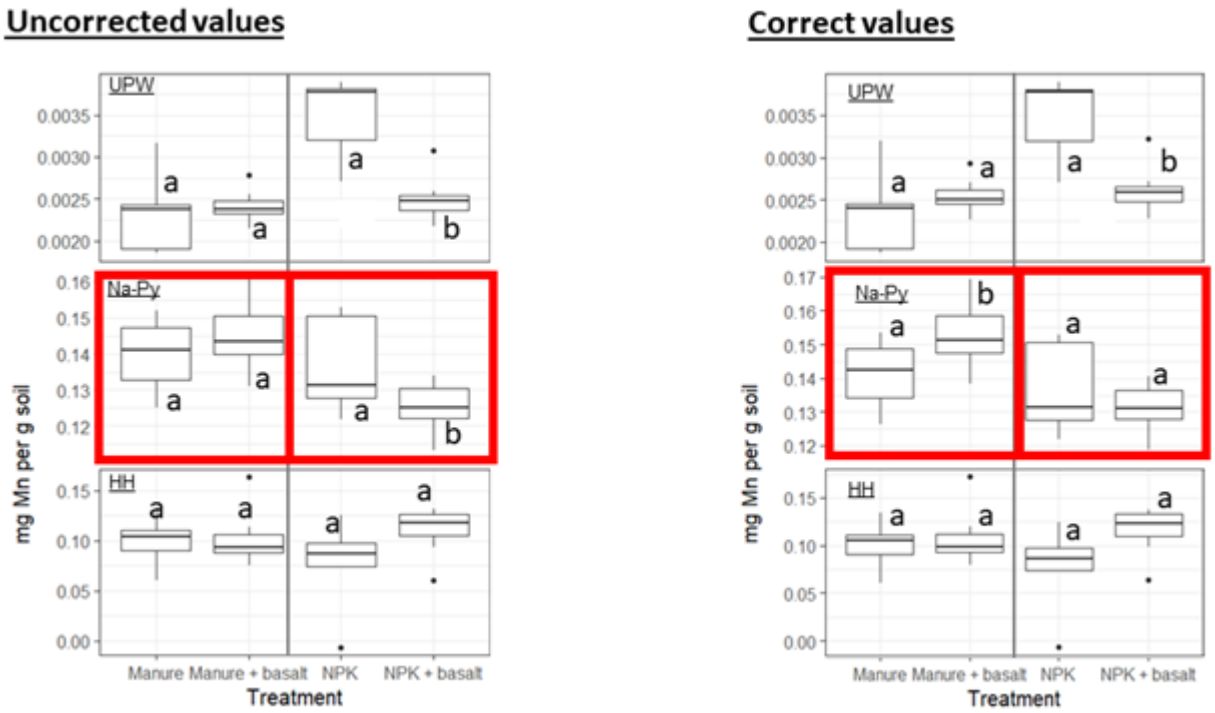

Figure C3 - Differences between uncorrected and corrected values for extractable-Mn.

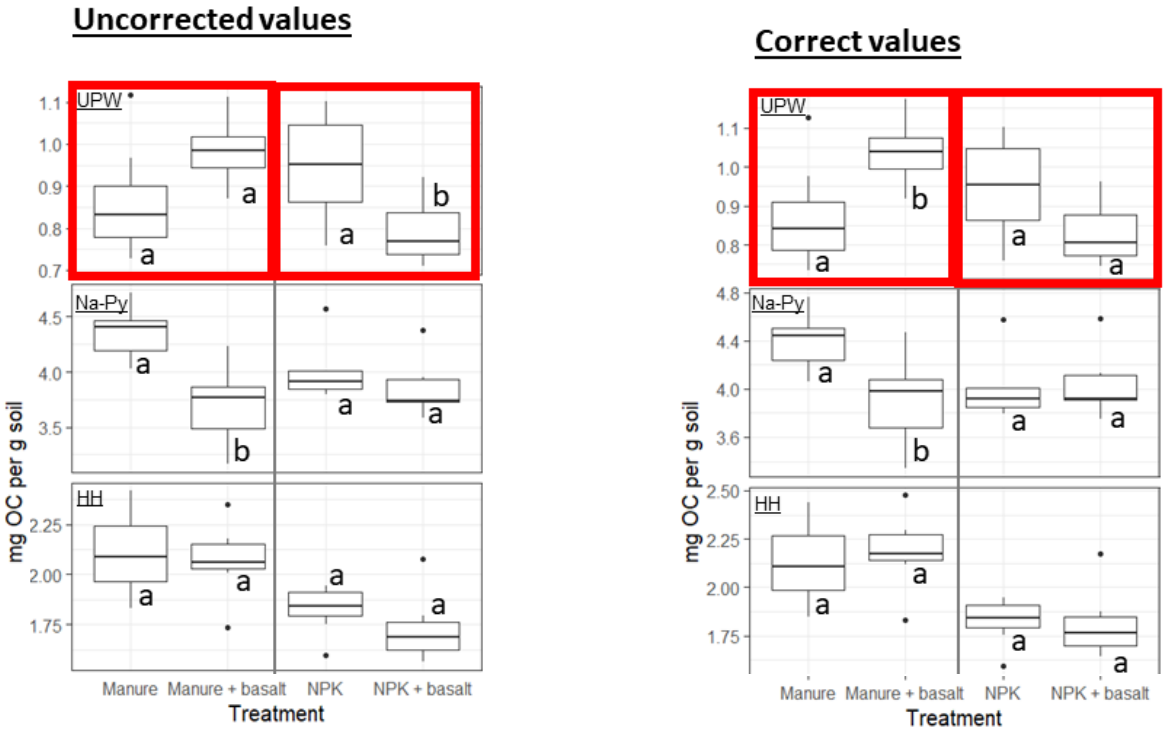

Figure C4 - Differences between uncorrected and corrected values in extractable organic carbon (OC)

APPENDIX D – Supplementary graphs from equilibrium models for Chapter 4

This appendix consists of the equilibrium model runs for the Manure only, NPK only and NPK + basalt treatment from Chapter 4 (see Section 4.4.5.2 for results and 4.3.6 for methodology). The results from the Manure + basalt treatment are presented in Section 4.4.5.2. These figures were not presented in Chapter 4 because they were similar to the Manure + basalt treatment, but they are presented here for completeness of data.

Figure D1 – Graph showing Saturation Indices (SI) of several Al, Fe, Si, Ca and Mn phases as a function of pH in the Manure only treatment after experimental day (a) 7 and (b) 70. Vertical line represents the measured porewater pH of each respective solution. Dashed line represents the pH of the

basalt-amended treatment and solid line represents the pH of the fertiliser only solution.

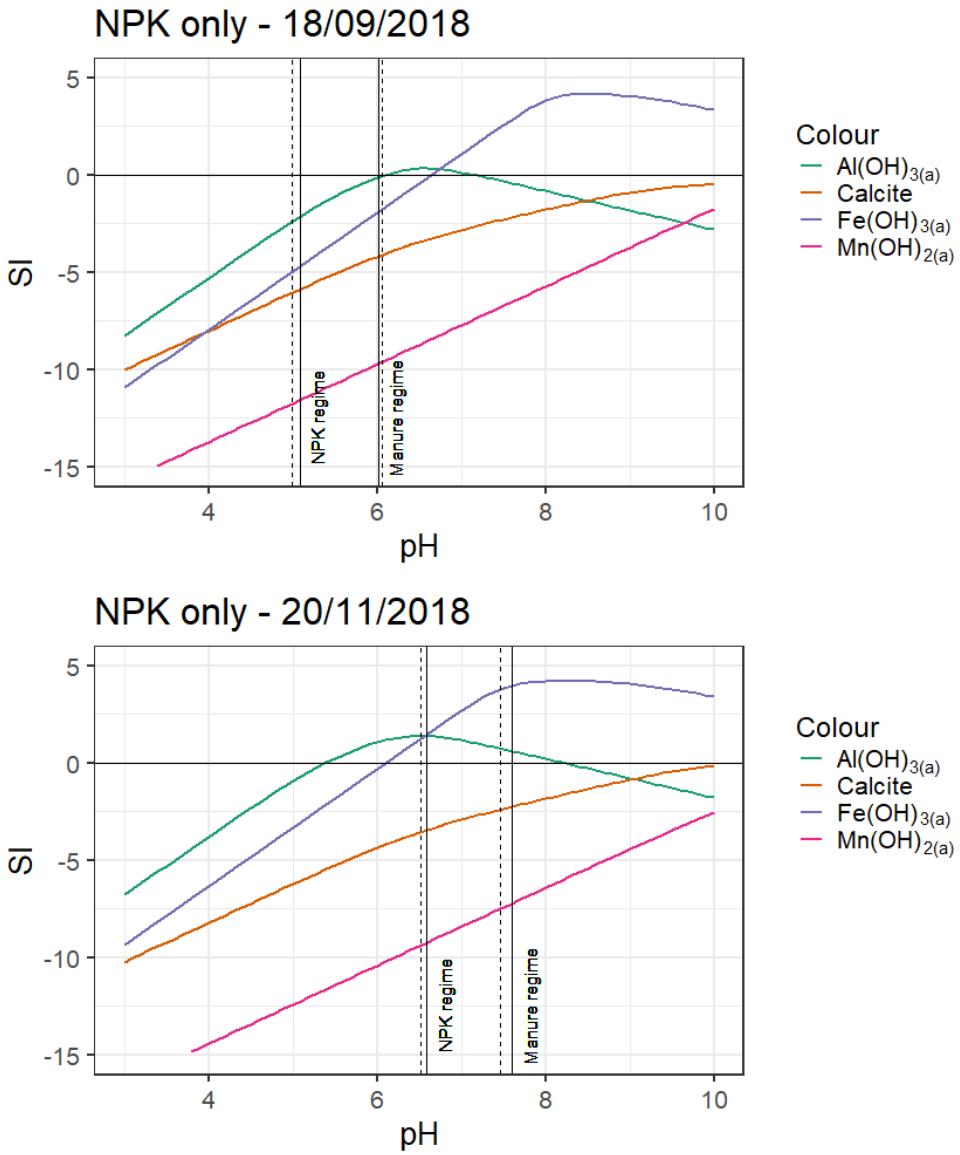

Figure D2 – Graph showing Saturation Indices (SI) of several Al, Fe, Si, Ca and Mn phases as a function of pH in the NPK only treatment after experimental day (a) 7 and (b) 70. Vertical line represents the measured porewater pH of each respective solution. Dashed line represents the pH of the basalt-amended treatment and solid line represents the pH of the fertiliser only solution.

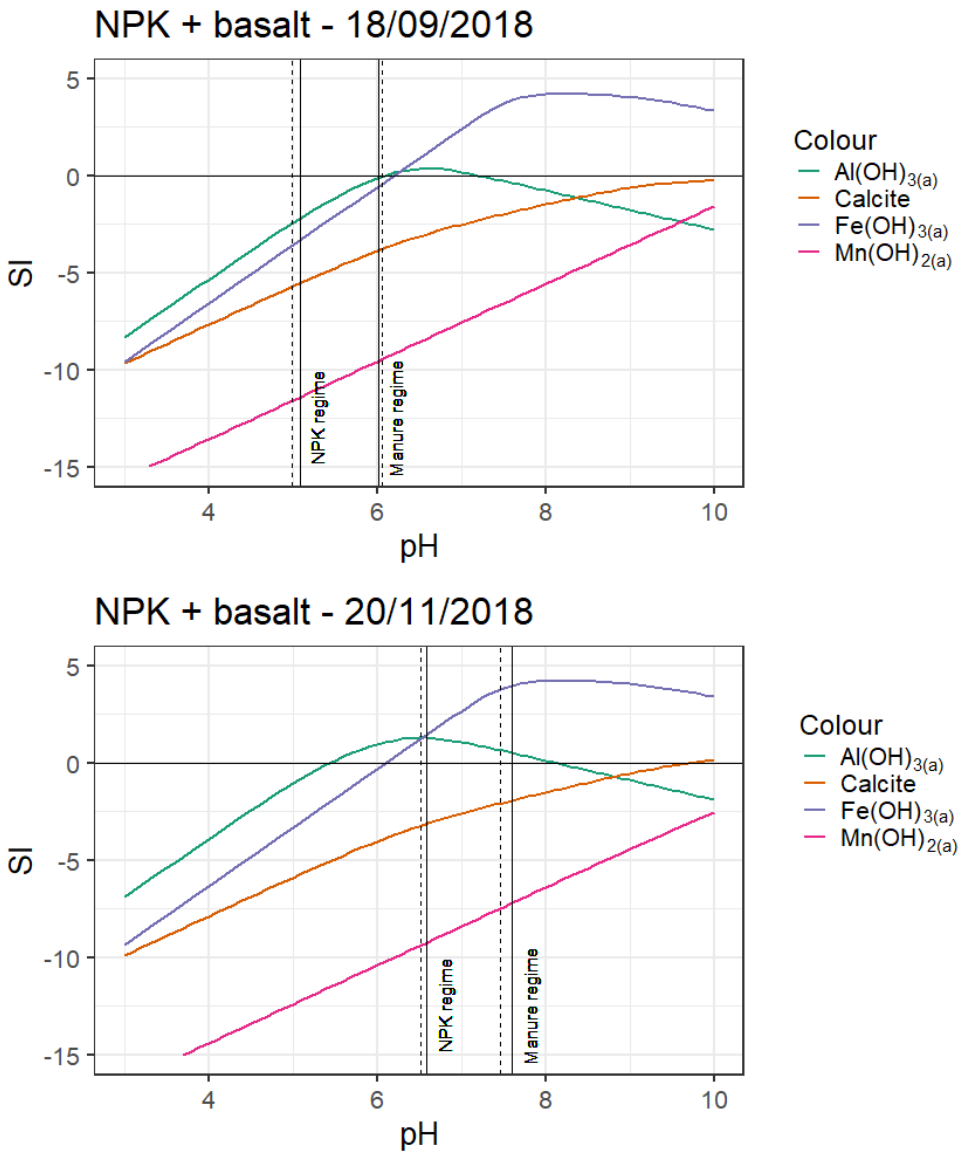

Figure D3 – Graph showing Saturation Indices (SI) of several Al, Fe, Si, Ca and Mn phases as a function of pH in the NPK + basalt treatment after experimental day (a) 7 and (b) 70. Vertical line represents the measured porewater pH of each respective solution. Dashed line represents the pH of the basalt-amended treatment and solid line represents the pH of the fertiliser only solution.

APPENDIX E - Supplementary graphs from equilibrium models for Chapter 5

This appendix consists of: (1) measured leachate chemistry from the Flitcham Farm Field Demonstrator which was used to decide which seasons to conduct the equilibrium modelling of (Figure E1 and Table E2 and (2) additional runs of the equilibrium model that were not featured in the main text of Chapter 5 (Figures E2 and E3) which were not presented in Chapter 5 because they were similar to the results from the Bottom Brek Spring data, but they are presented here for completeness of data.

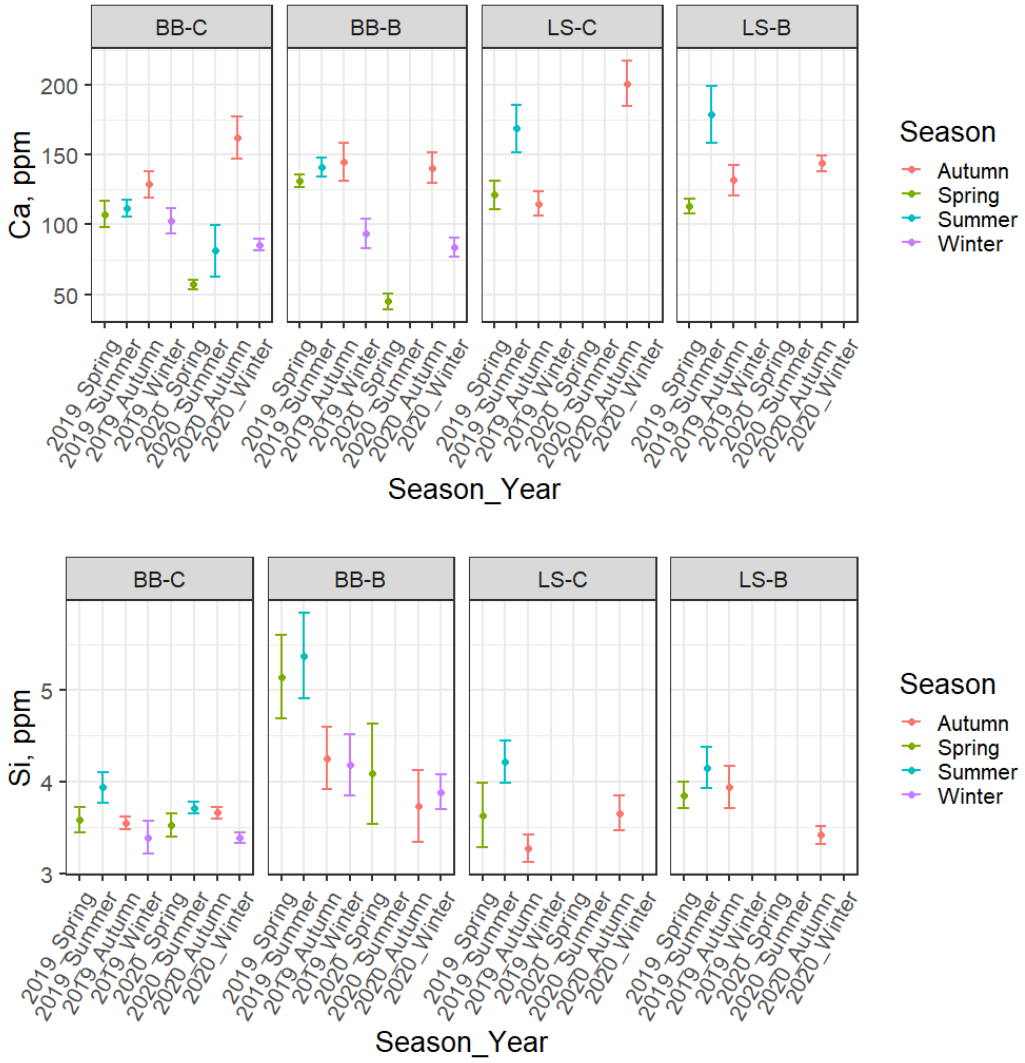

Figure E1 – Figure showing measured Ca and Si concentrations from leachate samples collected at the Flitcham Farm Field Demonstrator. Seasons are grouped into the following months: Spring: March-May, Summer: June-August, Autumn: September-November, Winter: December-February. BB = Bottom Brek, LS = Longspring Head, -C = Control, -B = Basalt-amended. Number of replicates for each site can be found in Table E1.

Table E1 – Number of replicates collected from lysimetres, used in Figure E1, E2 and E3, and in leachate equilibrium modelling (see Section 5.3.6.). Highlighted values represent the data that were used in the equilibrium modelling.

Year	Season	Site	Treatment	Count	Code
2019	Spring	Bottom Brek	Control	12	BB-C
	Summer		Control	15	BB-C
	Autumn		Control	12	BB-C
	Winter		Control	7	BB-C
	Spring		Basalt-amended	17	BB-B
	Summer		Basalt-amended	15	BB-B
	Autumn		Basalt-amended	12	BB-B
	Winter		Basalt-amended	10	BB-B
	Spring	Longspring Head	Control	9	LS-C
	Summer		Control	7	LS-C
	Autumn		Control	12	LS-C
	Spring		Basalt-amended	10	LS-B
	Summer		Basalt-amended	8	LS-B
	Autumn		Basalt-amended	15	LS-B
2020	Spring	Bottom Brek	Control	5	BB-C
	Summer		Control	2	BB-C
	Autumn		Control	6	BB-C
	Winter		Control	17	BB-C
	Spring		Basalt-amended	4	BB-B
	Autumn		Basalt-amended	15	BB-B
	Winter		Basalt-amended	20	BB-B
	Autumn	Longspring Head	Control	17	LS-C
	Autumn		Basalt-amended	18	LS-B

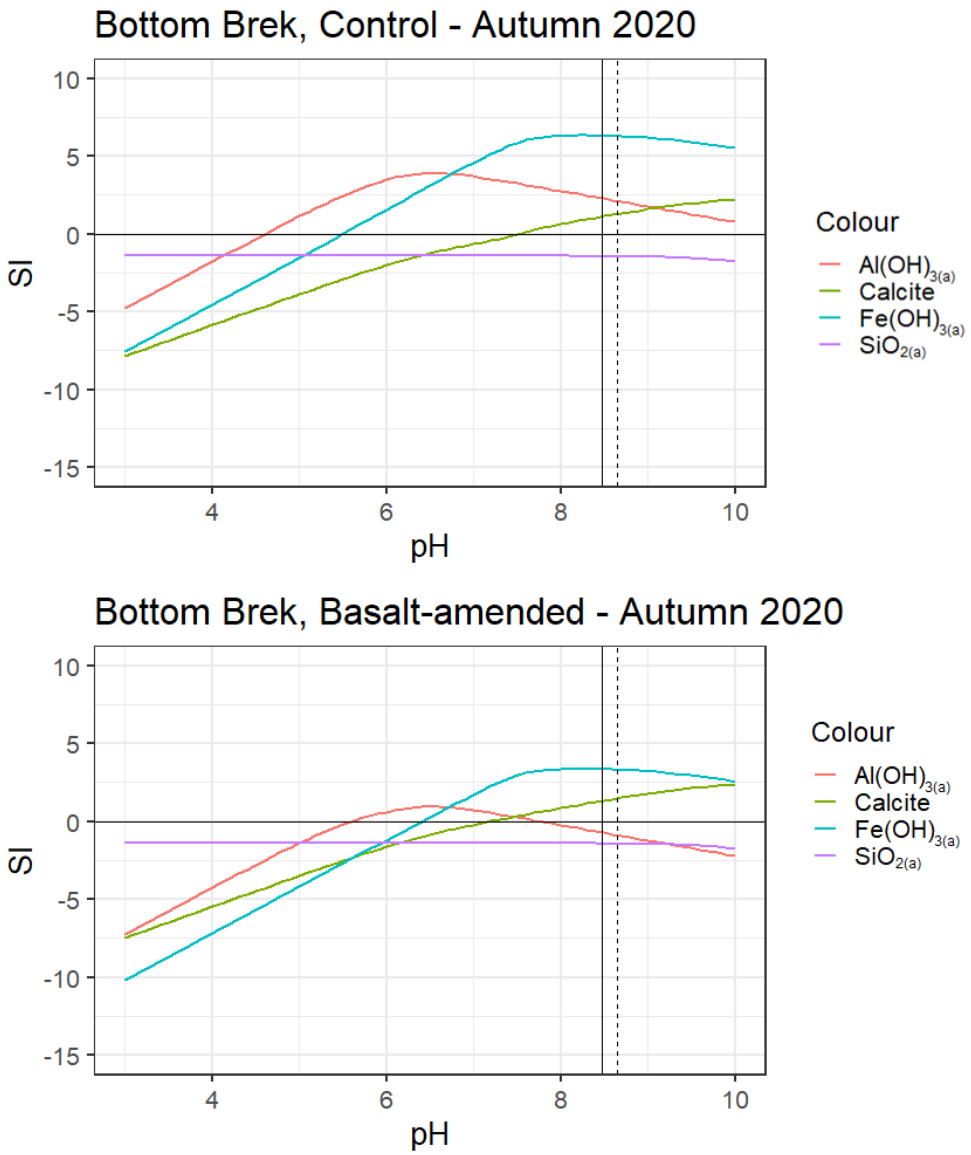

Figure E2 - Graph showing Saturation Indices (SI) of several Al, Fe, Mn, Ca and Si phases as a function of pH at both the Control and Basalt-amended plots at the Bottom Brek site in the Flitcham Farm Field Demonstrator in Autumn 2020. Vertical line represents the measured porewater pH of each respective solution. Dashed line represents the pH of the Basalt-amended treatment and solid line represents the pH of the Control treatment solution.

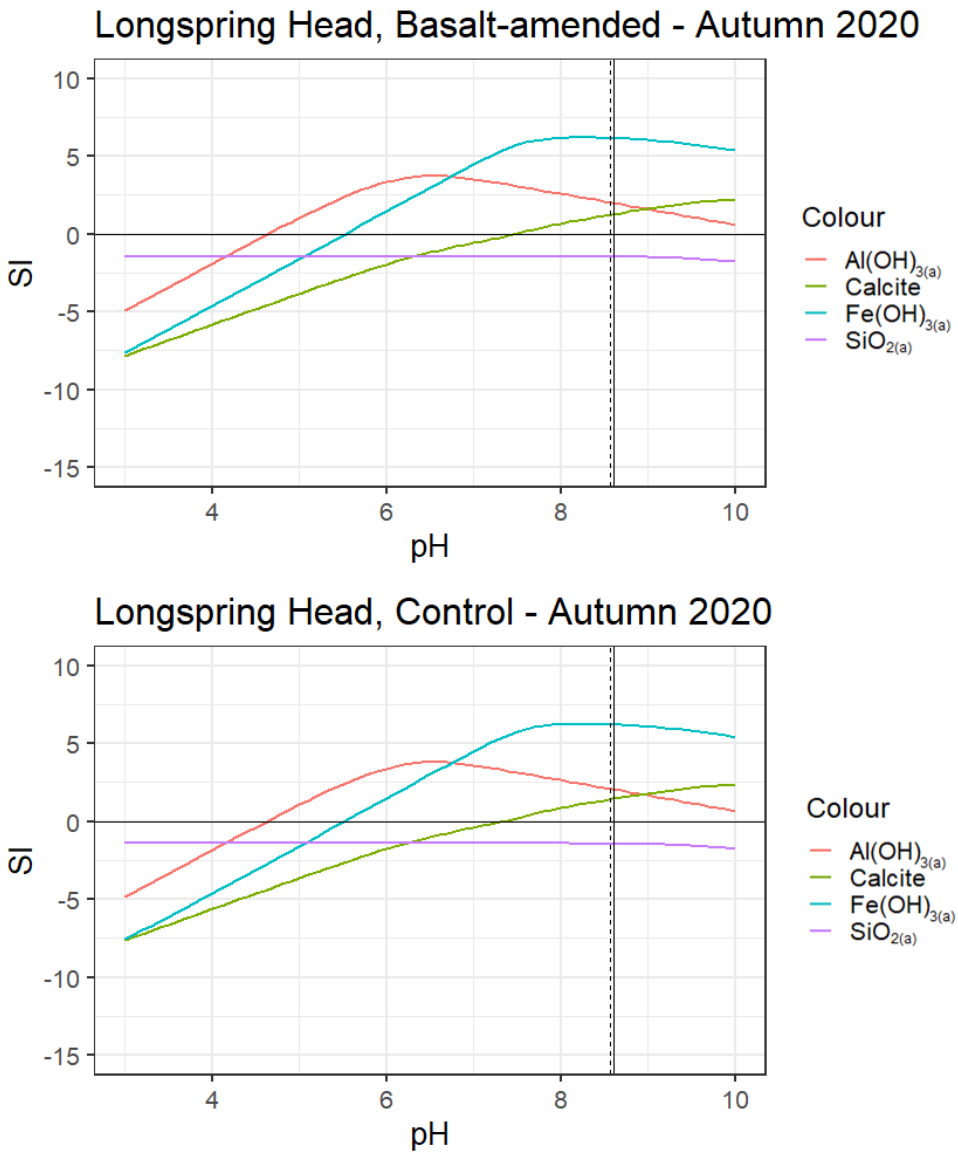

Figure E3 - Graph showing Saturation Indices (SI) of several Al, Fe, Mn, Ca and Si phases as a function of pH at both the Control and Basalt-amended plots at the Longspring Head site in the Flitcham Farm Field Demonstrator in Autumn 2020. Vertical line represents the measured porewater pH of each respective solution. Dashed line represents the pH of the Basalt-amended treatment and solid line represents the pH of the Control treatment solution.